

Analysis note

Deeply virtual Compton scattering off 4He

(EG6 run)

M. Hattawy^[1], N. Baltzell^[2,3], R. Dupré^[1], H. Egiyan^[2], L. El Fassi^[3,4],
F.-X. Girod^[2], K. Hafidi^[3], C. Moody^[3], S. Stepanyan^[2]

Review committee:

Michel Garçon^[5] (chair)

Sebastian Kuhn^[6]

Zein-Eddine Meziani^[7]

^[1]Institut de Physique Nucléaire d'Orsay, Orsay 91406, France

^[2]Jefferson Laboratory, Newport News, VA 230606, USA

^[3]Argonne National Laboratory, Argonne, IL 60439, USA

^[4]Mississippi State Univirsity, Mississippi State, MS 39762, USA

^[5]CEA-Saclay, Gif sur Yvette 91191, France

^[6]Old Dominion University, Norfolk, VA 23529, USA

^[7]Temple University, Philadelphia, PA 19122, USA

Contents

1	Introduction	5
1.1	DVCS off Helium-4	5
1.1.1	Beam-spin asymmetry	7
1.1.2	Theoretical predictions	8
1.1.3	Nuclear DVCS measurements	11
1.2	EG6 experimental setup	11
1.2.1	CLAS detector	13
1.2.2	Inner calorimeter	13
1.2.3	Solenoid	13
1.2.4	Run conditions	13
2	Radial time projection chamber	17
2.1	The EG6 RTPC	17
2.1.1	Design	17
2.1.2	Working principle	18
2.1.3	Track reconstruction	19
2.2	RTPC calibration	20
2.2.1	Event selection	21
2.2.2	Drift paths and drift speed calibration	27
2.2.3	Gain calibration	33
2.2.4	Noise rejection	36
2.3	Tracking resolution	43
2.4	RTPC efficiency	45
3	Particles reconstruction and simulation	47
3.1	Particles identification	47
3.1.1	Electron identification	47
3.1.2	Proton identification	52
3.1.3	Photon identification	54
3.1.4	Helium-4 identification	55
3.1.5	π^0 identification	57
3.2	Simulation	60
3.2.1	Event generator	61
3.2.2	GSIM	62
3.2.3	GPP	62
3.2.4	RECSIS	65
3.2.5	RTPC fastmc	65
3.3	Kinematic Corrections	66
3.3.1	Electrons	66
3.3.2	Protons	67
3.3.3	IC photons in simulation	67
3.3.4	IC photons in real data	67

4 DVCS beam-spin asymmetry extraction	75
4.1 Coherent channel	75
4.1.1 Good run list	75
4.1.2 Coherent DVCS event selection	75
4.1.3 Coherent channel checking	79
4.1.4 Comparison with simulation	79
4.2 Incoherent channel	85
4.2.1 Good run list	86
4.2.2 Proton DVCS event selection	86
4.2.3 Comparison with simulation	87
4.3 Kinematic coverages	90
4.4 Data binning	91
4.5 Background subtraction	92
4.5.1 π^0 contaminations	92
4.5.2 Accidental contaminations	94
4.6 Statistical uncertainties	97
4.7 Systematic uncertainties	97
5 Results and physics interpretations	107
5.1 Fitting the beam-spin asymmetry	107
5.2 Beam-spin asymmetry results and fit	108
5.2.1 Coherent beam-spin asymmetry	108
5.2.2 Incoherent beam-spin asymmetry	108
5.3 Helium GPD	108
5.4 Generalized EMC ratios	113
A $e^- {}^4He \rightarrow e^- {}^4He \gamma$ cross section	117
B The parametrizations for the RTPC	119
C The parametrization of the IC-photons energy corrections	123
D Exclusive π^0 events selection	125
D.1 $e^4He\pi^0$ exclusivity cuts	126
D.2 $ep\pi^0$ exclusivity cuts	129
E Tables list of the exclusive distributions	133
F A_{LU} tables	135
G Free proton beam-spin asymmetry interpolation	141
G.1 Fitting the experimentally measured asymmetries	141
G.2 Model-dependent extraction	141
G.3 Summary	141
H Investigating the Fermi motion effects on the incoherent DVCS channel	145
I Binning the incoherent DVCS data to match the free proton DVCS published data	151
Bibliography	157

Introduction

1.1 DVCS off Helium-4

Nuclear targets provide access to the measurement of two DVCS channels: the coherent and the incoherent. In the coherent channel, the target nucleus remains intact and recoils as a whole while emitting a real photon ($eA \rightarrow e'A'\gamma$). This process allows to measure the nuclear GPDs of the target, which contain information on the partons correlations and the nuclear forces in the target [1, 2]. In the incoherent channel, the nucleus breaks up and the DVCS takes place on a bound nucleon that emits the final photon ($eA \rightarrow e'N'\gamma X$). The latter allows to measure the GPDs of the bound nucleons and study the medium modifications of the nucleons in the nuclear medium. Figure 1.1 shows the diagrams of the two DVCS channels.

The GPDs depend on three variables: x , ξ and t . $x + \xi$ is the nucleon's longitudinal momentum fraction carried by the struck quark, 2ξ is the longitudinal momentum fraction of the momentum transfer Δ ($= p' - p$), and t ($= \Delta^2$) is the squared momentum transfer between the initial and the final states of the hadron target. Experimentally, only ξ and t are measurable in the DVCS reaction. At twist-2 order, ξ can be calculated as $x_B/(2 - x_B)$, where x_B is the Bjorken variable ($= Q^2/(2M_N(E - E'))$ with Q^2 is the virtuality of the exchanged photon, M_N is the mass of the nucleon and $E(E')$ is the energy of the incident (scattered) electron).

The number of GPDs needed to parametrize the partonic structure of a nucleus depends on the different configurations between the spin of the nucleus and the helicity direction of the struck quark. In principle, for a target of spin s , the number of the chiral-even GPDs is equal to $(2s + 1)^2$ for each quark flavor. For instance, at leading twist level, nine chiral-even GPDs are required to parametrize the partonic structure of the deuteron, because it has a spin one [3, 5]. This makes studying this nucleus a non-trivial task. The DVCS off spinless nuclear targets, such as ${}^4\text{He}$, ${}^{12}\text{C}$ and ${}^{16}\text{O}$, is simpler to study as only one GPD ($H_A(x, \xi, t)$) arises at leading twist to parametrize their partonic structure.

Nuclear DVCS provides a quantitative information on the nuclear medium effects, the quark confinement size of the bound nucleons, see figure 1.2. The Fourier transform of the nucleon GPDs over the momentum transfer Δ gives the transverse separation (b') between quarks in the nucleon, while the transform of the nuclear GPD ($H_A(x, \xi, t)$) gives the transverse separation (b) between the quarks in the nucleus. Knowing these two separations, one can access the transverse separation ($\beta = b - b'$) between the nucleons in a nucleus [2].

The ${}^4\text{He}$ nucleus shows a clear EMC effect. This nucleus is characterized by its spin-zero, a high density and it is a well-known few-body system. These aspects make the ${}^4\text{He}$ nucleus an ideal target to be considered for the understanding of the nuclear effects at the partonic level.

In principle, the ${}^4\text{He}$ GPD $H_A(x, \xi, t)$ characterized by:

- The universality of H_A : the H_A describes the partonic structure of the ${}^4\text{He}$ in a DVCS reaction the same way as in a DVMP reaction.
- In the forward limit ($t \rightarrow 0$), H_A is reduced to the usual PDF of ${}^4\text{He}$ that is accessible via DIS.

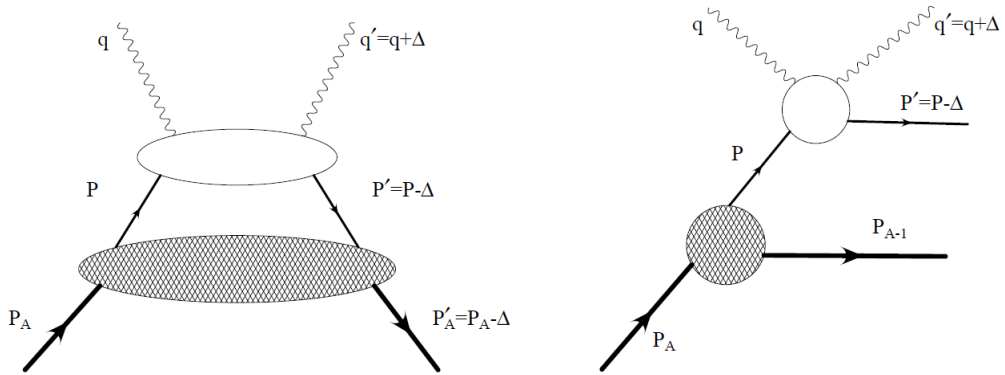


Figure 1.1: The leading twist handbag diagrams of the two DVCS channels from a nuclear target, coherent channel (on the left) and incoherent channel (on the right).

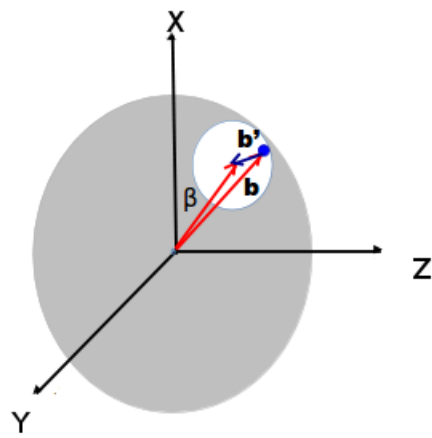


Figure 1.2: The spatial coordinates of quarks in a nucleus. See main text for definition of the variables. The figure is from [6].

- H_A can be decomposed into a polynomial in ξ .
- The first moment of H_A is the ${}^4\text{He}$ elastic electromagnetic form factor $F_A(t)$, such as:

$$\sum_q \int_{-1}^1 dx H_A^q(x, \xi, t) = F_A(t), \quad (1.1)$$

where the sum runs over all the quark flavors.

- The second moment of $H_A^q(x, \xi, t)$ reads

$$\int_{-1}^1 dx x H_A^q(x, \xi, t) = M_2^{q/A}(t) + \frac{4}{5} \xi^2 d_2^{q/A}(t) \quad (1.2)$$

where the first term of the right-hand side represents the momentum fraction carried by each quark flavor q , and the second term is encoding information about the forces experienced by partons inside the nuclei [1].

- H_A is not directly measured from experiment, but we measure its corresponding Compton form factor \mathcal{H}_A .

The ${}^4\text{He}$ DVCS amplitude can be expressed as [3]:

$$\mathcal{T}_{DVCS} \propto \sum_q e_q^2 \mathcal{P} \int_{-1}^1 dx \left(\frac{1}{x - \xi} + \frac{1}{x + \xi} \right) H_A^q(x, \xi, t) - i\pi \sum_q \left(e_q^2 [H_A^q(\xi, \xi, t) - H_A^q(-\xi, \xi, t)] \right), \quad (1.3)$$

where the first term on the right-hand side stands for the real part of the CFF \mathcal{H}_A , while the second term for the imaginary part of \mathcal{H}_A .

The coherent DVCS amplitude is enhanced through the interference with the BH process, that is calculable from the well-known elastic FF. Figure 1.3 shows the world measurements of the ${}^4\text{He}$ $F_A(t)$ along with theoretical calculations. Following the $F_A(t)$ parametrization by R. Frosch and his collaborators [7] (valid at the small values of $-t$ which are of interest in this work), figure 1.4 shows the calculated BH as a function of the azimuthal angle between the leptonic and the hadronic planes (ϕ), using a 6 GeV electron beam on a ${}^4\text{He}$ target.

The experimentally measured $e^4\text{He} \rightarrow e^4\text{He}\gamma$ cross section can be decomposed into BH, DVCS, and interference terms. The differential cross section can be written like in Appendix A, equation A.1. By generalizing the BMK model [3], the nuclear BH, DVCS and interference scattering amplitudes can be decomposed into a finite series of Fourier harmonics as can be found in Appendix A, equations A.2, A.3 and A.4.

1.1.1 Beam-spin asymmetry

It is convenient to use the beam-spin asymmetry as DVCS observable because most of the experimental normalization and acceptance issues cancel out in an asymmetry ratio. The beam-spin asymmetry is measured using a polarized lepton beam on an unpolarized target (U). JLab provides a longitudinally (L) polarized electron beam, $P_B \approx 85\%$. It is defined as:

$$A_{LU} = \frac{d^5\sigma^+ - d^5\sigma^-}{d^5\sigma^+ + d^5\sigma^-}. \quad (1.4)$$

where $d^5\sigma^+(d^5\sigma^-)$ is the DVCS differential cross section for a positive (negative) beam helicity.

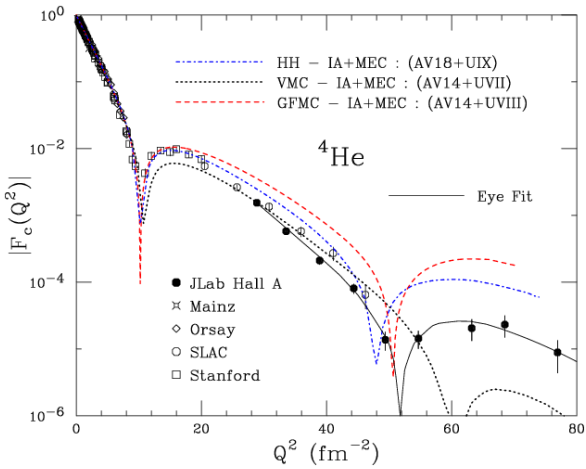


Figure 1.3: ${}^4\text{He}$ charge form factor measurements at Stanford, SLAC, Orsay, Mainz and JLab Hall A compared with theoretical calculations. The figure is from [8].

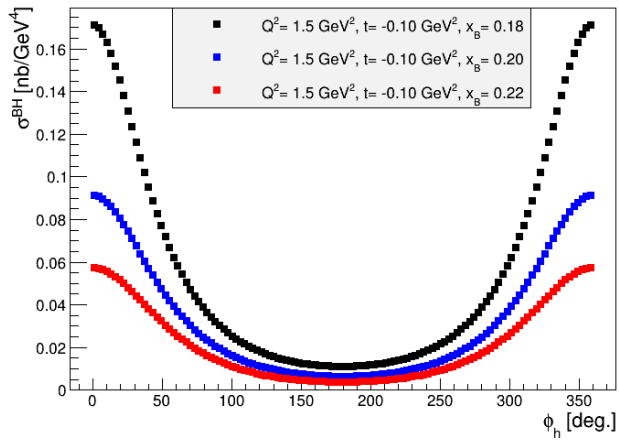


Figure 1.4: The calculated BH cross section as a function of ϕ on a ${}^4\text{He}$ target at three values of x_B and fixed values of Q^2 and t . ($t = -0.1 \text{ GeV}^2/\text{c}^2$ corresponds to $Q^2 \approx 2.57 \text{ fm}^{-2}$ on figure 1.3).

At leading twist, the beam-spin asymmetry (A_{LU}) with the two opposite helicities of a longitudinally-polarized electron beam (L) on a spin-zero target (U) can be written as:

$$A_{LU} = \frac{x_A(1+\varepsilon^2)^2}{y} s_1^{INT} \sin(\phi) \left/ \left[\sum_{n=0}^{n=2} c_n^{BH} \cos(n\phi) + \frac{x_A^2 t(1+\varepsilon^2)^2}{Q^2} P_1(\phi) P_2(\phi) c_0^{DVCS} + \frac{x_A(1+\varepsilon^2)^2}{y} \sum_{n=0}^{n=1} c_n^{INT} \cos(n\phi) \right] \right. \quad (1.5)$$

where $P_1(\phi)$ and $P_2(\phi)$ are the Bethe-Heitler propagators. The factors: $c_{0,1,2}^{BH}$, c_0^{DVCS} , $c_{0,1}^{INT}$ and s_1^{INT} are the Fourier coefficients of the BH, the DVCS and the interference amplitudes for a spin-zero target [3]. The explicit expressions of these coefficients can be found in Appendix A.

1.1.2 Theoretical predictions

On-shell calculations

The nuclear GPD H_A can be described as the sum of the individual nucleons' GPDs. In the model based on the impulse approximation of V. Guzey *et al.* [10, 11], a nucleus is assumed to consist of non-relativistic non-interacting nucleons, and these nucleons interact independently with the probe. Assuming that the nucleon GPDs H and E are the dominant GPDs in the unpolarized target scattering case, the nuclear GPD H_A for each quark flavor q can be written as:

$$H_A^q(x_A, \xi_A, t) = \frac{dx_N}{dx_A} \left[Z \left(H_p^q(x_N, \xi_N, t) + \frac{t}{4M^2} E_p^q(x_N, \xi_N, t) \right) + (A - Z) \left(H_n^q(x_N, \xi_N, t) + \frac{t}{4M^2} E_n^q(x_N, \xi_N, t) \right) \right] F_A(t), \quad (1.6)$$

where the factor dx_N/dx_A is the Jacobian for the transformation of x from the nucleonic x_N to the nuclear x_A . It is equal to $A(2 - x_A)/(2 - x_B)$ with $x_A = x_B/A$. ξ_A is defined as $x_A/(2 - x_A)$ and ξ_N is equal to $x_B/(2 - x_B)$. For free nucleons, the GPDs are constructed using the double distributions ansatz [12]. In this approximation, the GPD H with its evolution in Q^2 , can be written as:

$$H^q(x, \xi, t, Q^2) = \int_0^1 d\beta \int_{-1+|\beta|}^{1+|\beta|} d\alpha \delta(\beta + \alpha\xi - x) \pi(\beta, \alpha) \beta^{-\alpha'(1-\beta)t} q_v(\beta, Q^2), \quad (1.7)$$

where the parameters α and β are new variables that link x and ξ linearly as $x = \beta + \alpha\xi$, q_v is the valence unpolarized PDF and the profile function $\pi(\beta, \alpha)$ takes the form

$$\pi(\beta, \alpha) = \frac{3}{4} \frac{(1-\beta)^2 - \alpha^2}{(1-\beta)^3}. \quad (1.8)$$

The t -dependence of the GPD is introduced through Regge ansatz [13], with the slope α' equal to 1.105 GeV^{-2} that allows to recover the ordinary form factors of the nucleons.

This model enables to link the nuclear CFFs to the ones of the nucleons. However, it neglects the medium modifications and the binding effects between the nucleons in a nucleus. To take into account the nuclear modifications, the bound nucleons can be assumed to be modified in proportion to the corresponding bound nucleon elastic form factors [14]. That is, the GPD H of the bound proton ($H^{q/p*}$) can be written as:

$$H^{q/p*}(x, \xi, t, Q^2) = \frac{F_1^{p*}}{F_1^p} H^{q/p}(x, \xi, t, Q^2), \quad (1.9)$$

where F_1^p (F_1^{p*}) is the Dirac form factor of the free (bound) proton. The bound nucleon form factor is calculated using the Quark-Meson Coupling (QMC) model [15], that predicts a suppression as the nuclear density increases. As a result of these calculations, figure 1.5 shows the ratio of the bound (incoherent DVCS channel off ${}^4\text{He}$) to free proton beam-spin asymmetry (A_{LU}), at $\phi = 90^\circ$, as a function of x_B , using a 6-GeV longitudinally-polarized electron beam at $Q^2 = 2 \text{ GeV}^2/\text{c}^2$ and two values of the transfer momentum t . This ratio represents a generalization of the EMC effect, for t greater than zero. This model predicts an enhancement of the bound-proton beam-spin asymmetry, which increases with t .

Off-shell calculations

Another model for nuclear GPDs in the impulse approximation uses the nuclear spectral function. For a spin-zero nucleus, the GPD H^A can be written as [2]:

$$H^A(x, \zeta, t) = \sum_N \int \frac{d^2 P_\perp dY}{2(2\pi)^3} \frac{1}{A - Y} \rho^A(P^2, P'^2) \mathcal{A} \times \sqrt{\frac{Y - \zeta}{Y}} \left[H_{OFF}^N \left(\frac{x}{Y}, \frac{\zeta}{Y}, P^2, t \right) - \frac{1}{4} \frac{(\zeta/Y)^2}{1 - \zeta/Y} E_{OFF}^N \left(\frac{x}{Y}, \frac{\zeta}{Y}, P^2, t \right) \right] \quad (1.10)$$

where P and P' are the incoming and outgoing nucleons three-momenta, Y is a dynamical variable defined as $\frac{y+A\zeta}{1+\zeta}$, $\mathcal{A} = (Y - \zeta/2)(\sqrt{Y(Y - \zeta)})$ is a normalization factor with $\zeta = \frac{2\xi}{1+\xi/A}$, $\rho^A(P^2, P'^2)$ is the off-forward nuclear spectral function accounting for all configurations of the final nuclear system and the binding effects between the nucleons. In a non-relativistic approximation, ρ^A is

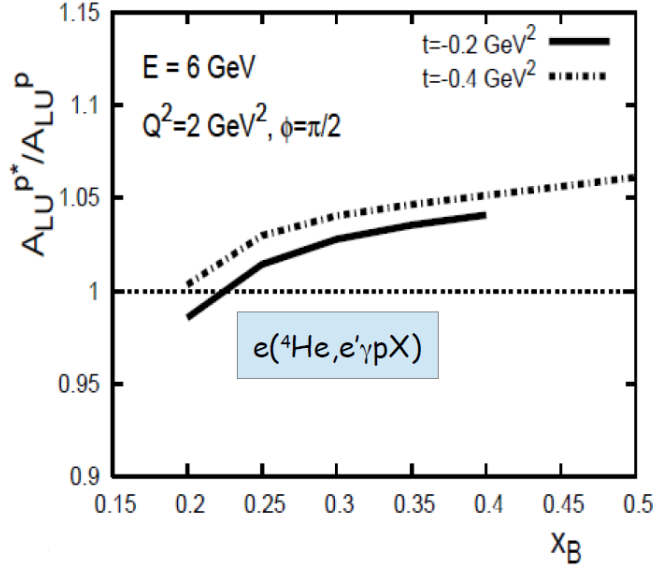


Figure 1.5: The theoretical predictions by V. Guzey [14] for the "generalized" EMC effect in terms of the beam-spin asymmetry ratio between the bound proton in ${}^4\text{He}$ and the free proton as a function of Björken variable x_B . The calculations are performed at two values of $-t$, 0.2 and 0.4 GeV^2/c^2 , with a 6 GeV electron beam and $Q^2 = 2 \text{ GeV}^2/\text{c}^2$.

defined as [16]:

$$\rho^A(P^2, P'^2) = 2\pi M_A \int dP P \Phi(P) \Phi(P') \quad (1.11)$$

with Φ the nuclear wave function in momentum space. The off-forward nucleon GPDs, H_{OFF}^N and E_{OFF}^N , are characterized by the off-shellness which is linked to P^2 . One recovers the free nucleon GPDs by disregarding this off-shellness.

The nuclear effects can be expressed with the ratio between the nuclear and the nucleon GPDs. This ratio becomes equal to the ordinary EMC ratio in the forward limit ($t = 0$). As the nuclear form factor of the ${}^4\text{He}$ has a steeper drop in t than the nucleonic one, it is more convenient to define the ratio between normalized GPDs as:

$$R_A(x, \xi, t) = \frac{H^A(x, \xi, t)/F^A(t)}{H_p^p(x, \xi, t)/F_p^1(t)} \quad (1.12)$$

where $F_p^1(t)$ is the Dirac form factor of the proton. Figure 1.6 shows the EMC ratios measured via DIS on ${}^4\text{He}$ compared to theoretical calculations. One can see that the latter calculations by S. Liuti and K. Taneja describe the EMC effect differently than the first scenario due to the off-shell effects of the nucleons associated in their calculation.

The nuclear effects can be also viewed as the beam-spin asymmetry ratio ($\frac{A_{LU}^{Incoh}}{A_{LU}^p}$) between the incoherent proton and the free proton. Figure 1.7 shows the predicted EMC effect in ${}^4\text{He}$ in terms of $\frac{A_{LU}^{Incoh}}{A_{LU}^p}$ as a function of x_B . The calculated ratio appears to be very sensitive on t , which encodes the information on the transverse degrees of freedom of the partons in the nucleon.

We conclude that nuclear DVCS is a promising field that can give more details about the nature of the nuclear forces through the study of the nuclear GPDs, and through the study of the modifications of the nucleons' GPDs in nuclei.

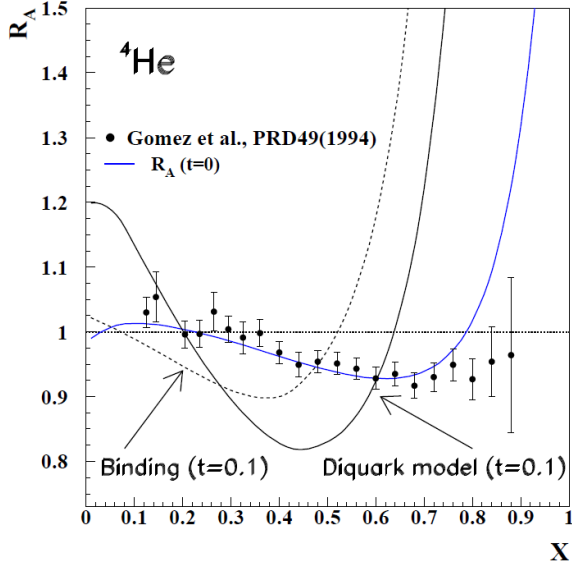


Figure 1.6: The EMC effect in ${}^4\text{He}$. The data points are the ${}^4\text{He}$ EMC ratios [17]. The black dotted and solid curves are theoretical calculations based on a binding and a diquark model respectively, at $-t = 0.1 \text{ GeV}^2/\text{c}^2$. The blue curve shows the theoretical calculation at the forward limit by Liuti and Taneja [2].

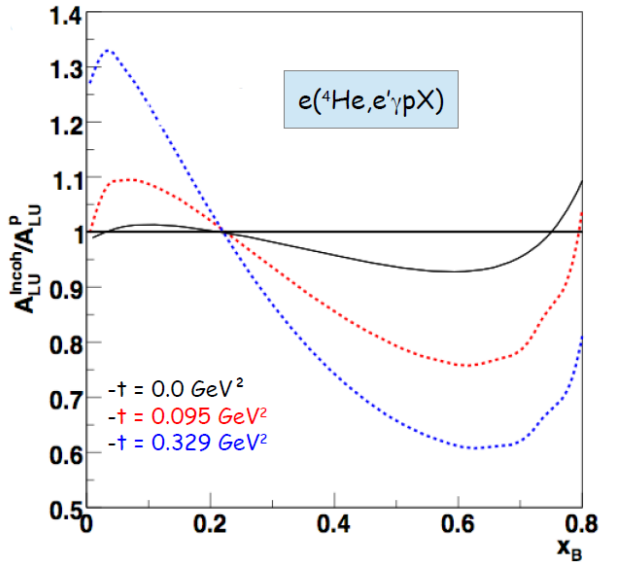


Figure 1.7: The theoretical calculations by S. Liuti and K. Taneja [2] of the beam-spin asymmetry ratio between the bound proton, in ${}^4\text{He}$, and the free proton. The ratio is plotted as a function of x at three different values of $-t$: 0, 0.095, and $0.329 \text{ GeV}^2/\text{c}^2$.

1.1.3 Nuclear DVCS measurements

The first nuclear DVCS experiments were carried out by the HERMES collaboration [18]. In these measurements, longitudinally-polarized electron and positron beams at energies equal to 27.6 GeV were scattered onto fixed nuclear targets (hydrogen, helium-4, nitrogen, neon, krypton and xenon) to study the DVCS reaction. The HERMES spectrometer did not detect the nuclear recoils. However, the exclusivity of the selected DVCS events was approximately ensured by a cut on the missing mass of the final state configuration $e\gamma X$. The separation between the coherent and the incoherent DVCS channels was made with a cut on t : the coherent channel is assumed to dominate the low t -region, while the higher t -region is assumed to be dominated by the incoherent channel on the protons and the neutrons. Figure 1.8 shows the $\sin(\phi)$ amplitude of the beam-spin asymmetries off the different targets in t -bins measured by HERMES. These asymmetries are further separated into coherent and incoherent asymmetries. Figure 1.9 shows the mass dependence of the $\sin(\phi)$ amplitude of the coherent and the incoherent beam-spin asymmetries integrated over all the data sample for each target type.

The HERMES inclusive measurements of the nuclear beam-spin asymmetries clearly suffer from a lack of statistics for a precise investigation of their physics content. Within the given uncertainties, their nuclear beam-spin asymmetries have shown neither enhancement, nor a nuclear-mass dependence.

1.2 EG6 experimental setup

The experiment described in this note has been carried out in the Hall B of the Thomas Jefferson National Accelerator Facility (JLab), Virginia, USA. Hall B houses the CEBAF Large Acceptance

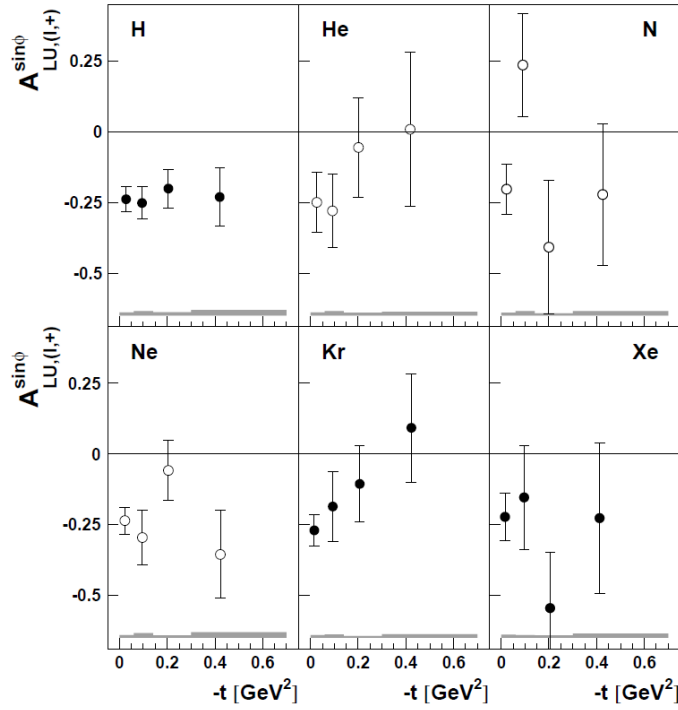


Figure 1.8: The t -dependence of the $\sin(\phi)$ amplitude of the beam-spin asymmetries measured by HERMES on different nuclear targets. The error bars show only the statistical uncertainties, while the systematic uncertainties are indicated by the bands on each plot. [18].

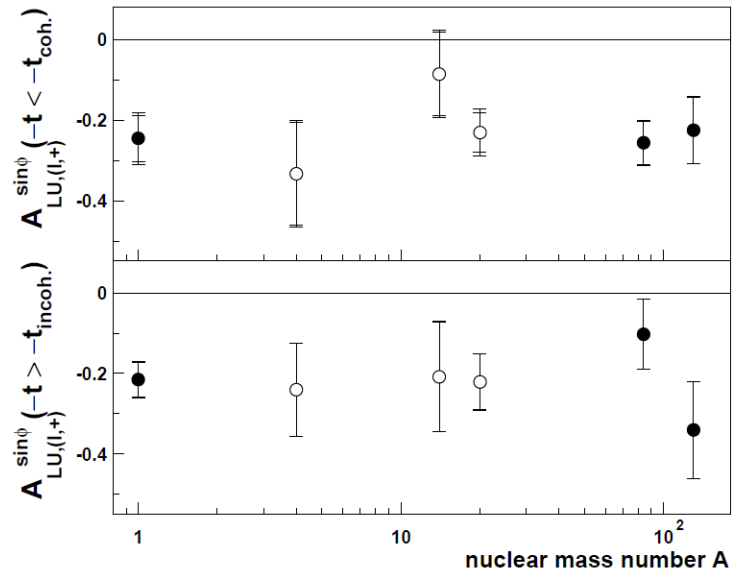


Figure 1.9: The nuclear-mass dependence of the $\sin(\phi)$ amplitude of the beam-spin asymmetries for the coherent (upper panel) and the incoherent (lower panel) data samples. The values of t_{coh} and t_{incoh} for each nuclear target were determined from Monte-Carlo simulations [18].

Spectrometer (CLAS). Our experiment was performed in 2009 with a longitudinally-polarized electron beam of 6.064 GeV scattering onto a 6 *atm* gaseous ^4He target to study the nuclear medium modifications of parton distributions using the DVCS off the target.

1.2.1 CLAS detector

To ensure the exclusivity of our reaction, the basic setup of CLAS was upgraded with a Radial Time Projection Chamber (RTPC) to detect the low-energy recoil nuclei, an additional calorimeter (IC) to detect the energetic forward-emitted real photons and a solenoid magnet to minimize the effects of Møller electrons. In the following subsections, we rapidly present the sub-detectors previously used by the collaboration, the RTPC design and calibration are detailed in the next chapter.

1.2.2 Inner calorimeter

In the basic setup of CLAS, the photons are detected by the forward electromagnetic calorimeters (EC) which cover polar angles from 8° to 45° . With a 6 GeV electron beam, a large part of the DVCS photons are produced at polar angles below 15° , where the acceptance of the EC is small. In the CLAS-E1DVCS experiment (2005), CLAS was upgraded with the addition of an Inner Calorimeter (IC). This calorimeter covers completely the polar angles between 5° and 15° . Figure 1.10 shows a schematic plot of our experimental setup. The front face of the IC is facing the downstream side of the Radial TPC (RTPC) and placed at 16 cm from the center of CLAS.

The IC is constructed from 424 lead-tungstate (PbWO_4) crystals. Each crystal is 16 cm long (corresponding to 17 radiation lengths) with a $1.33 \times 1.33 \text{ cm}^2$ front surface and a $1.6 \times 1.6 \text{ cm}^2$ back surface. The energy resolution is around 3 to 4% for photon energies between 2 GeV and 5 GeV and the angular resolution is between 3 to 5 mrad for the same energy range [24].

1.2.3 Solenoid

At occupancies greater than 4%, the efficiency of the drift chambers starts to drop and the resolution gets worse. The first region of the DCs (R1) has a higher occupancy than the other two regions (R2 and R3), mostly due to noise. This noise mainly comes from the Møller electrons, which are low-energy electrons produced in the scattering of the electron beam on the target's electrons. To reduce the effect of the noise, CLAS was upgraded by adding a solenoid that surrounds the target. The magnet provides a nominal field of 4.5 T at the center of the target. This solenoid deflects the produced Møller electrons to very forward angles preventing them from arriving to the drift chamber, the IC or the RTPC. Figure 1.11 shows a GEANT3 simulation of the Møller electrons tracks without applying the solenoid field (left), and how these electrons are bent to low polar angles, less than 4° , when the solenoid field is applied.

1.2.4 Run conditions

Table 1.1 summarizes the different beam energies used during the experimental run CLAS-EG6 with the details about the beam, the torus, and the solenoid currents.

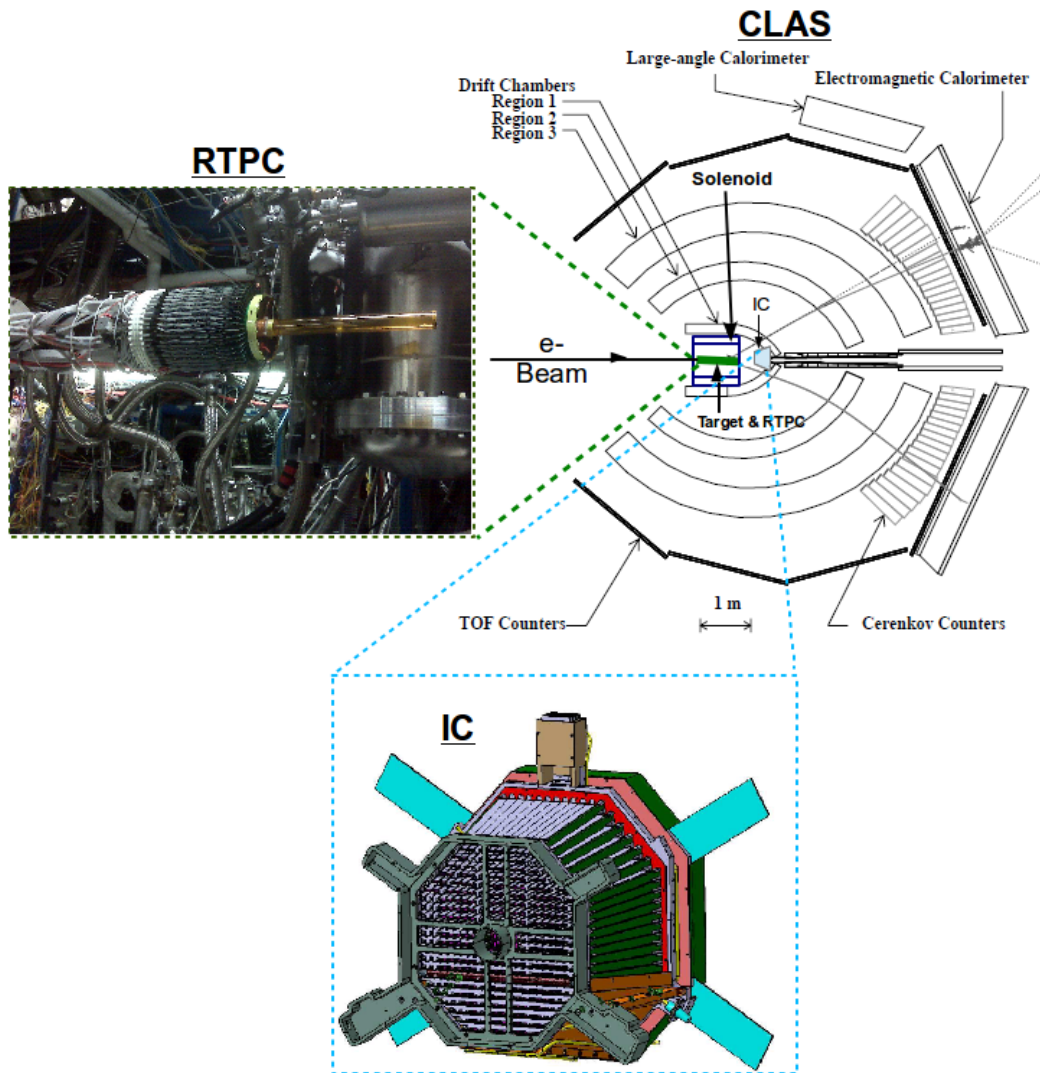


Figure 1.10: The CLAS-EG6 experimental setup in the y-z plane. The basic apparatus of CLAS is shown in the right top plot, a zoom on the IC is shown on the bottom plot, and a photo of the RTPC and the target are shown in the left top plot. The RTPC is surrounded by a solenoid (in blue).

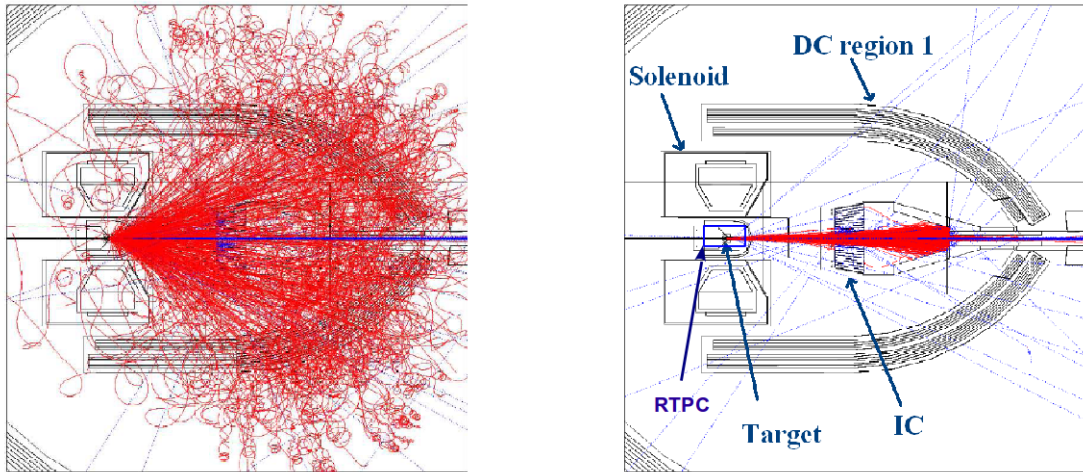


Figure 1.11: The tracks of the produced Møller electrons (in red) without applying the solenoid field (left) and with it (right) [24].

beam energy [GeV]	Beam current [nA]	Torus current [A]	Solenoid current [A]
1.204	150	2100	450
5.7	100	1900	450
6.064	120-150	2100	450
1.269	100	1900	450

Table 1.1: The different beam energies used during the experimental run period CLAS-EG6 with the currents in the beam, torus, and the solenoid.

Radial time projection chamber

2.1 The EG6 RTPC

At 6 GeV incident electron beam energy, the recoil 4He nuclei from the coherent DVCS channel, have an average momentum around 200 MeV/c. CLAS cannot detect such low energy particles, for example protons are detected with a threshold of about 250 MeV/c, which will be even higher for helium. In order to detect such low-energy recoils a Radial TPC (RTPC), similar to the one used during the BoNuS run [25], was added to CLAS. In 2009, the CLAS-EG6 group [9] has built this RTPC, figure 2.1 shows a close photo of the RTPC, while figure 2.2 shows a schematic drawing of its internal structure. It is a 200 mm-long and 150 mm-diameter TPC, composed of two electronically separated modules, each covering about 150° of the azimuthal angle. The RTPC tracks the charged particles through the ionization centers they leave in the gas-filled detection volume. Then, the ionized electrons drift under the effect of an electric field and are amplified by a gas electron multiplier system before to be detected on collection pads.

2.1.1 Design

The RTPC has the following substructure, from the beam axis to the exterior:

- The target extends along the RTPC's central z-axis, with a diameter of 6 mm. It is enclosed in a $27\text{-}\mu\text{m}$ -thick Kapton wall.
- The first gas gap extends from 3 mm to 20 mm radial distances. It is filled with 4He gas at one atmospheric pressure. This region is swarmed with Møller electrons induced by the beam, but filling this region with a light gas like 4He at low pressure minimizes their secondary interactions, while the magnetic field of the solenoid keeps them away from the sensitive drift region. This gap is surrounded by a grounded window made of $4\text{-}\mu\text{m}$ -thick aluminized mylar.
- The second gas gap extends from 20 mm to 30 mm radial distances and is filled with a gas mixture of 80% Neon (Ne) and 20% Dimethyl Ether (DME: C_2H_6O). This drift gas fills all the following gaps up to the external shell.
- The cathode foil, which is made of $4\text{-}\mu\text{m}$ -thick aluminized mylar, surrounds the second gas gap. It is connected to a voltage of 4.3 kV to generate an electric field in the drift region.
- The drift region is filled with the Ne-DME gas mixture. It extends from the cathode, 30 mm from the beam line, to the first gas electron multiplier layer, 60 mm from the beam line.
- The amplification system is composed of three Gas Electron Multiplier (GEM) layers located at radii of 60 mm, 63 mm, and 66 mm.
- The electron collection system has an internal radius of 69 mm and collects the charges. The data are then pre-amplified and transmitted to the data acquisition system.

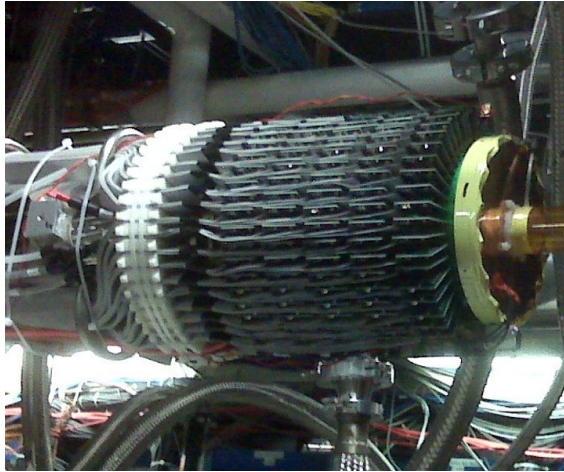


Figure 2.1: A view of the RTPC before insertion into the solenoid. The incident electron beam comes from the left.

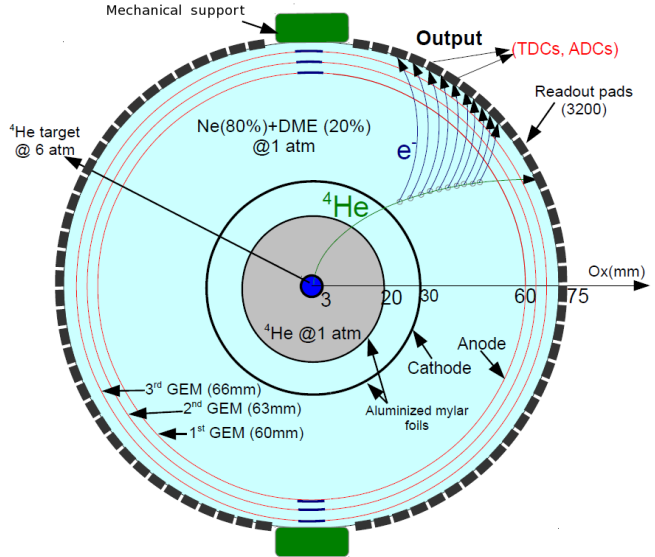


Figure 2.2: A cross section of the RTPC taken on a plane perpendicular to the beam line, with a typical ${}^4\text{He}$ track crossing the drift volume.

The Ne-DME gas mixture has been chosen as the drift gas because of its low-diffusion characteristics and small Lorentz angles (the angles between the drift direction of electrons under the influence of magnetic field and the direction of the electric field). These characteristics minimize the changes in the drift velocity of the ionization electrons [26].

The GEMs amplify the ionized electrons to produce measurable signals. Figure 2.3 shows a microscopic photo of a GEM. It is made from an insulator (Kapton) sandwiched between two copper layers. The mesh of each GEM layer is chemically etched with $50\text{-}\mu\text{m}$ -diameter holes in double-conical cross section shapes, as can be seen from the schematic plot on the right.

The electrons amplification is achieved through the holes via the strong electric field, that is generated by a 400-V potential difference between the two copper layers. Such a strong field leads to high ionization of the initial electrons and therefore amplification of the signals. Furthermore, an additional potential difference of 150 V is set between each two successive GEM layers to push the amplified electrons towards the readout board. In this configuration, the gain of each GEM layer is of the order of 100.

The RTPC electron collection system has 3200 readout pads. Each module of the RTPC has 40 rows and 40 columns of readout pads, each is 5 mm long and 4.45 mm wide. Each group of 16 pads is connected to a pre-amplifier before the recorded signals are carried to the acquisition electronics. There are 20 rows and 5 columns of pre-amplifiers per module. This readout system records the charge information in time bins, in which the charge is measured in Analog-to-Digital-Converter (ADC) units, while the 114 ns width of the time bins will be referred as Time-to-Digital-Converter (TDC) units. From this measurement, we deduce the time taken by the electrons to drift from the ionization point to the readout board.

2.1.2 Working principle

When a charged particle traverses a gas, it ionizes the gas-atoms along its trajectory. In a TPC, the electrons released in the ionization drift towards the readout board under the effect of an

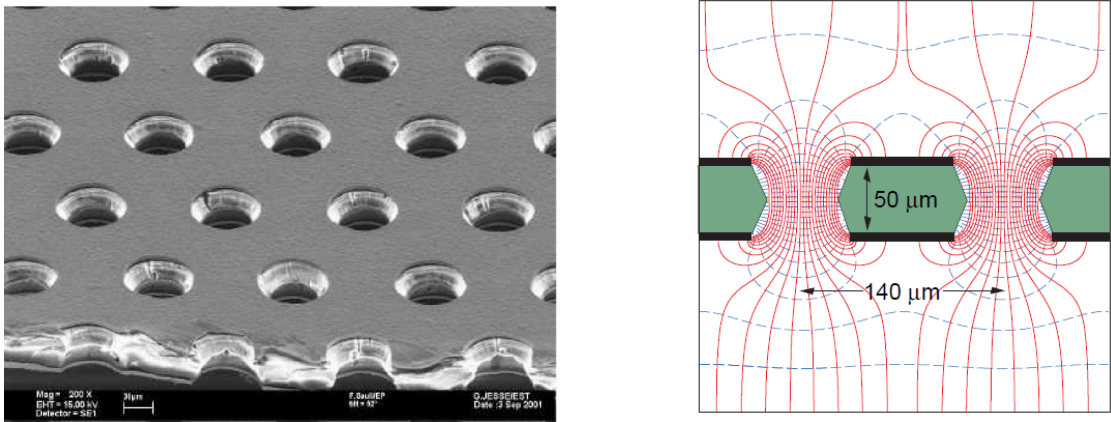


Figure 2.3: On the left: A microscopic image of a GEM shows the amplification holes, and the two copper layers, separated by a Kapton insulator. This figure is from [27]. On the right: Schematic of the hole structure in the GEMs with the electric field lines (solid red) and the equipotentials (dashed blue). This figure is from [28].

applied electric field. The drift velocity depends on the gas mixture, and on the electric (\vec{E}) and magnetic (\vec{B}) fields. The recorded time of the electrons provides information on how far the initial ionizations happened in the drift region, leading to reconstruct the original points of ionization, while the recorded ADCs give the deposited energy.

In our TPC the cathode and the anode are two cylinders. Thus, the generated \vec{E} field in the drift region has a purely radial components, perpendicular to the beam line, with a magnitude around 500 V/cm. However, the two-cylinders configuration produces small gradient components at the sides of the RTPC. This issue was solved by installing field cages at the ends of the RTPC to keep a regular \vec{E} field. These caused some high voltage issues and were disconnected during the experiment, partly justifying the time dependent calibration described below.

The \vec{B} field is generated by the solenoid. Figure 2.4 shows the magnetic field vectors in the different regions of the RTPC. The presence of the magnetic field enables us to deduce the momentum of a charged particle from the curvature of its track and the known magnetic field.

2.1.3 Track reconstruction

In order to reconstruct tracks we must first select the good hits. The first step is the rejection of out-of-time hits and the noise reduction, as will be explained in section 2.2.4. The second step is the spatial reconstruction of the hits, using the extracted drift speed and drift paths. For each registered hit, the position of the initial ionization is obtained from the recorded time (TDC) and from the position of its pad. In the third step, the reconstructed nearby hits are linked together in chains. The maximum distance between two adjacent hits must be less than 10.5 mm to chain them. Then, the number of hits per chain is required to be greater than 10 hits in order to proceed to the fitting step.

A fit to a chain of hits is performed in two iterations. In the first iteration, the hits of the chain are fitted with a helix. The helix fit is based on a circle fit in the $x - y$ plane followed by a linear fit in the $s - z$ plane for the hits of the chain, where $s = \sqrt{x^2 + y^2}$. In the second iteration, the residual between the fit and each hit is calculated. If the hit's residual is greater than 5 mm, the hit is excluded from the chain. Then the hits are re-fitted with the same previous helix fit giving five final parameters for each track's chain. From these five parameters, one can

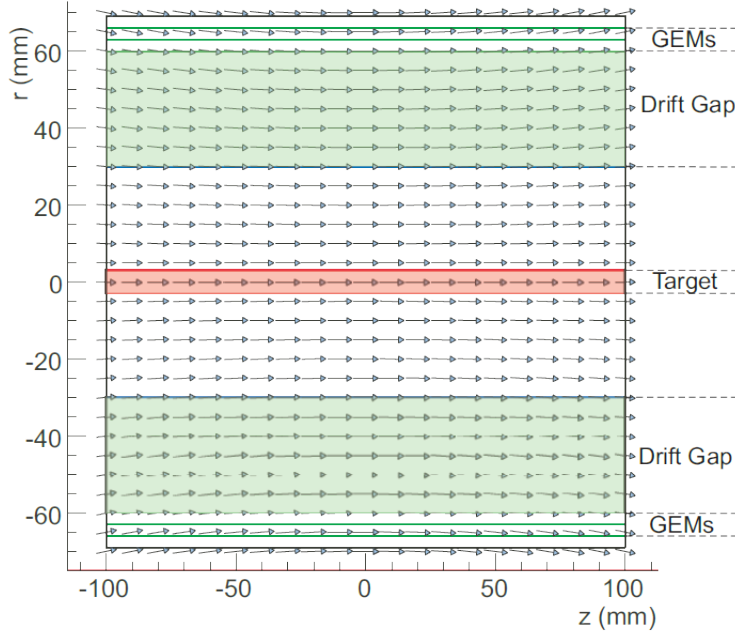


Figure 2.4: The solenoid magnetic field vectors in the RTPC, shown in the $r - z$ plane, where r is the radial distance from the central axis and z represents the longitudinal distance along the RTPC.

reconstruct all the parameters of a track. For example, one can calculate the momentum from the known longitudinal magnetic field (\vec{B}_z), the radius of curvature of the track (r_0) and the polar angle (θ), like:

$$p_{tot} = \sqrt{p_{\parallel}^2 + p_{\perp}^2}, \quad (2.1)$$

with $p_{\perp} = 0.3 \cdot q \cdot B_z \cdot |r_0|$ and $p_{\parallel} = p_{\perp} / \tan(\theta)$,

where p is in GeV/c unit, q is the elementary charge, B_z is in Tesla (T) and r_0 is in meters (m). For example, In a magnetic field of 4.5 T, the recoil ${}^4\text{He}$ nuclei from DVCS (elastic) reaction have kinetic energies in the range [10, 25] ([17, 35]) MeV, from momenta of [260, 450] ([360, 550]) MeV and r_0 [70, 150] ([130, 180]) mm.

2.2 RTPC calibration

Reconstructing a trajectory from the recorded time information of the electrons requires a good knowledge of their drift speed and drift paths. Also, the gains of the readout pads are required to calculate $\frac{dE}{dx}$ from the recorded ADCs. The determination of the drift paths and the gain calibration of the RTPC require well identified events, so we decided to use elastic scattering ($e {}^4\text{He} \rightarrow e {}^4\text{He}$). However, the cross section of the elastic process at detectable angles is highly suppressed at higher beam energy, so we had specific calibration runs with 1-pass beam energies of 1.024 and 1.269 GeV.

A GEANT4 simulation for the RTPC has been developed to help reproduce these events in order to properly extract the drift paths and the gains. Their extractions are based on comparing the experimentally identified ${}^4\text{He}$ elastic tracks to the GEANT4 simulated ones. Indeed, the kinematics of each elastic ${}^4\text{He}$ can be calculated from the electron measured in CLAS and then

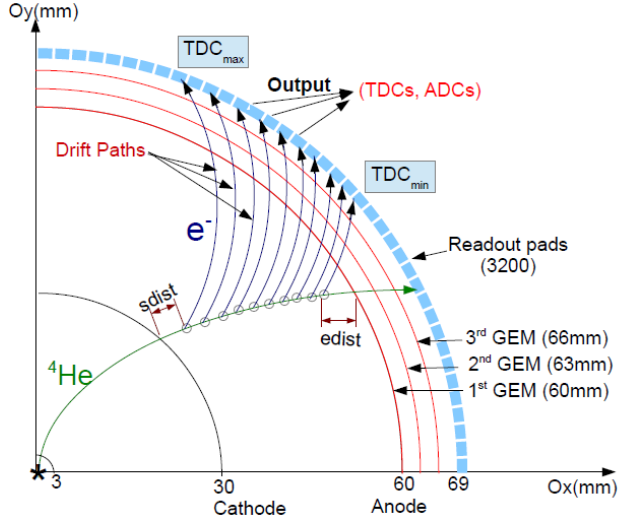


Figure 2.5: Schematic of a segment of the RTPC in a plane perpendicular to the beam line, with a ${}^4\text{He}$ track (in green) crossing the volume. See the text for description of the various elements and notations. $sdist$ and $edist$ are distances between first and last hits and boundaries of the RTPC as shown in this sketch.

simulated in GEANT4. The output of the simulation gives an expected trajectory that we then match to the measured signals to determine the drift paths.

This process is iterative since good tracks need to be identified at the beginning of the process and as the calibration improves, more good tracks are identified. For this analysis, we started from a MAGBOLTZ calibration, which was then improved with the method described above with several iterations. In particular, it is important that the alignment of the RTPC with respect to the beamline is properly implemented (see details in CLAS-NOTE [46]). As the process evolved and was improved over time, we present in the following subsections only the method used for the last iteration of our calibration process.

2.2.1 Event selection

Figure 2.5 shows a drawing of a segment of the RTPC, where a ${}^4\text{He}$ track (in green) crosses the volume of the RTPC, producing a chain of ionization points within the drift gas. The released electrons follow the drift paths (in black) towards the readout board under the effect of the electromagnetic field between the anode and the cathode. The electrons released close to the cathode take the maximum drift time (TDC_{max}) to reach the readout pads, while the electrons released close to the anode take the minimum time ($TDC_{min} = 15$ the trigger time), also called time offset, which is identical for all readout channels. In our convention, the distance between the first ionization point in the chain and the cathode is labelled as $sdist$, while the distance between the last point and the anode is labelled as $edist$.

Because the two modules of the RTPC are electronically separated, we will sometimes show their distributions separately. In our angular convention, the right module of the RTPC covers the azimuthal angles between 90° and 270° , while the left-side module covers the rest of the azimuthal angles.

2.2.1.1 RTPC good track requirements

A good RTPC track passes the following requirements:

- The number of active pads in the track is greater than 3.

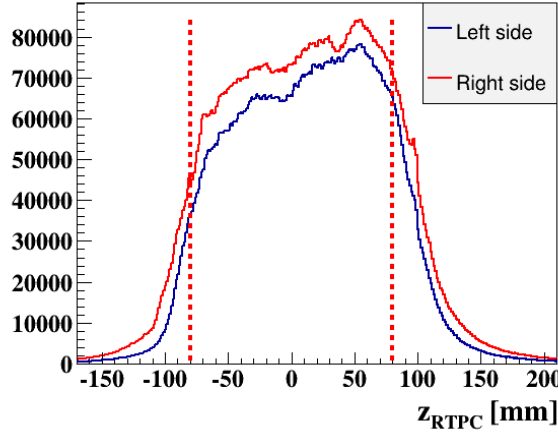


Figure 2.6: The z-vertex distributions for the reconstructed tracks in the RTPC.

- The vertex position in z is in the RTPC volume, i.e. $z \in [-80,80]$ mm, as illustrated in figure 2.6.
- The radius of curvature is positive ($r_0 > 0$): the ${}^4\text{He}$ is a positively charged nucleus and the reconstructed track in the RTPC must have positive radius of curvature. In other words, it travels in a clockwise direction if one looks into the electron beam. The curvature distribution of the collected RTPC tracks is shown in figure 2.7.
- The helix fit is well reconstructed with a $\chi^2 < 3.5$. The quality of the fit (χ^2) being defined as:

$$\chi^2 = \frac{\left(\frac{DOCA}{\sigma_r}\right)^2 + \sum_{i=1}^{N_{pts}} \left(\frac{r_i^{pt} - r_i^{helix}}{\sigma_r}\right)^2 + \left(\frac{\phi_i^{pt} - \phi_i^{helix}}{\sigma_\phi}\right)^2 + \left(\frac{z_i^{pt} - z_i^{helix}}{\sigma_z}\right)^2}{N_{pts} - 4} \quad (2.2)$$

where $\frac{DOCA}{\sigma_r}$ is the beam-spot constraint, r_i^{pt} , ϕ_i^{pt} , z_i^{pt} are the radial, azimuthal, longitudinal coordinates of each reconstructed hit "i". $(r_i^{helix}, \phi_i^{helix}, z_i^{helix})$ is the point on the helix fit that is closest to the reconstructed hit i . The resolutions are defined as $(\sigma_r, \sigma_\phi, \sigma_z) = (0.53 \text{ mm}, 2^\circ, 1.2 \text{ mm})$ based only on the size of the readout pads and were kept identical for all calibration iterations. These resolutions were derived by CLAS-BoNuS experiment [25]. N_{pts} is the total number of the hits in the chain. Figure 2.8 shows the χ^2 distributions for the positive tracks which originate within the RTPC.

- $sdist$ ($\in [-2.0, 2.0]$ mm) and $edist$ ($\in [-1.5]$ mm): these cuts are applied to ensure that a track is on time, i.e. the first ionization point is close to the cathode and the last point is close to the anode. For both $sdist$ and $edist$, positive values correspond to tracking points inside the drift region, while negatives are outside the drift region. So, in terms of the path length of the track starting from the vertex, $sdist$ and $edist$ have opposite signs. The $sdist$ and $edist$ distributions are shown in figures 2.9 and 2.10 respectively¹.

¹The long tail on the positive side of the $edist$ distribution is mostly due to electronic noise. Note that after applying all the elastic He-4 selection cuts, we observe that most of the tails for both $edist$ and $sdist$ are removed.

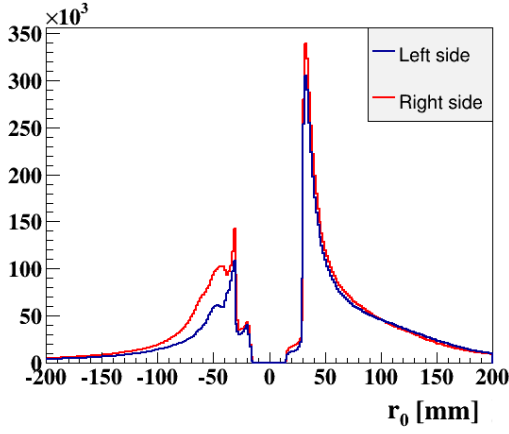


Figure 2.7: The radius of curvature of the reconstructed tracks in the RTPC.

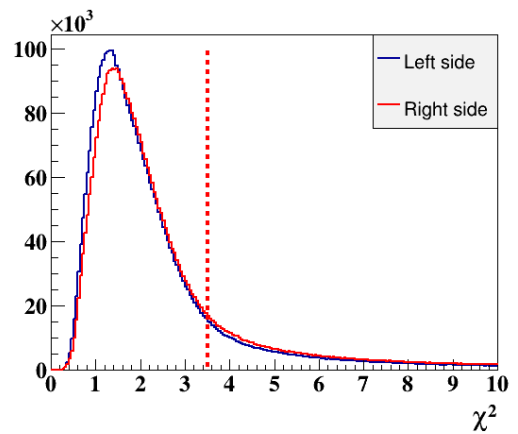


Figure 2.8: The χ^2 distribution for the positive tracks in the RTPC. The red line represents the cut we apply to select good tracks.

- Vertex correspondence: the track reconstructed in the RTPC has to originate from the same place as the electron that triggered the event. We define Δz as the difference between the electron z-vertex and the z-vertex of the RTPC track. Due to variations in the electric and the magnetic fields along the 200 cm of length of the RTPC, Δz shows a dependence on the longitudinal position along the RTPC (z_{RTPC}). This can be seen in figure 2.11. These distributions are fitted to extract the mean and the width of Δz as a function of z_{RTPC} . We then apply a 2σ cut around the mean to select the RTPC good tracks. The parametrizations of the mean (μ) and the width (σ) of Δz can be found in Appendix B.

2.2.1.2 Elastic scattering event selection

The elastic process on 4He is defined as:

$$e(k) + {}^4He(p) \rightarrow e(k') + {}^4He(p') \quad (2.3)$$

with the symbols in parenthesis representing the four-momenta of the particles.

In addition to the good-track requirements described above, to select elastic events we impose further constraints. The co-planarity between the scattered electron and the recoil 4He is ensured using a $\Delta\phi$ ($=\phi_e - \phi_{{}^4He}$) cut as shown in Figure 2.12. Like for Δz , the $\Delta\phi$ 2σ cut is dependent on z to account for systematic variations. Our final parametrizations can be found in Appendix B as well.

An additional elastic cut is performed by comparing the measured 4He polar angle to the calculated one, based on the measured electron in CLAS. Indeed, from momentum conservation the 4He polar angle can be calculated as:

$$\theta_{cal}^{{}^4He} = \sin^{-1} \left(\frac{p_{e'}^{}}{p_{cal}^{}} \cdot \sqrt{1 - \cos^2 \theta_{e'}} \right) \quad (2.4)$$

$$\text{with } p_{cal}^{{}^4He} = \sqrt{(E_b + M_{{}^4He} - p_{e'})^2 - M_{{}^4He}^2} \quad (2.5)$$

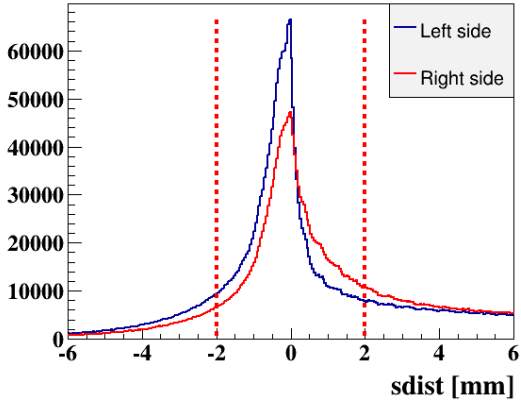


Figure 2.9: $sdist$ distribution for the positive tracks in the RTPC. We set $|sdist| < 2.0$ mm to select good tracks.

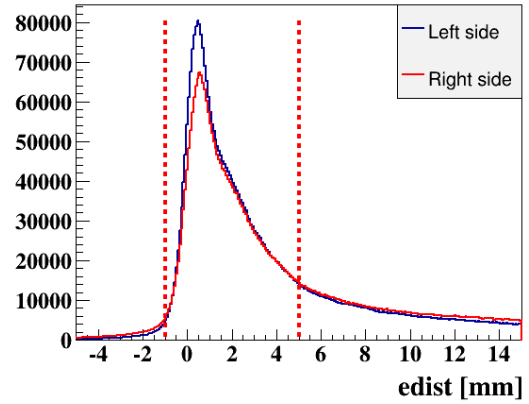


Figure 2.10: $edist$ distribution for the positive tracks in the RTPC. We require $-1.0 < edist < 5.0$ mm to select the good tracks.

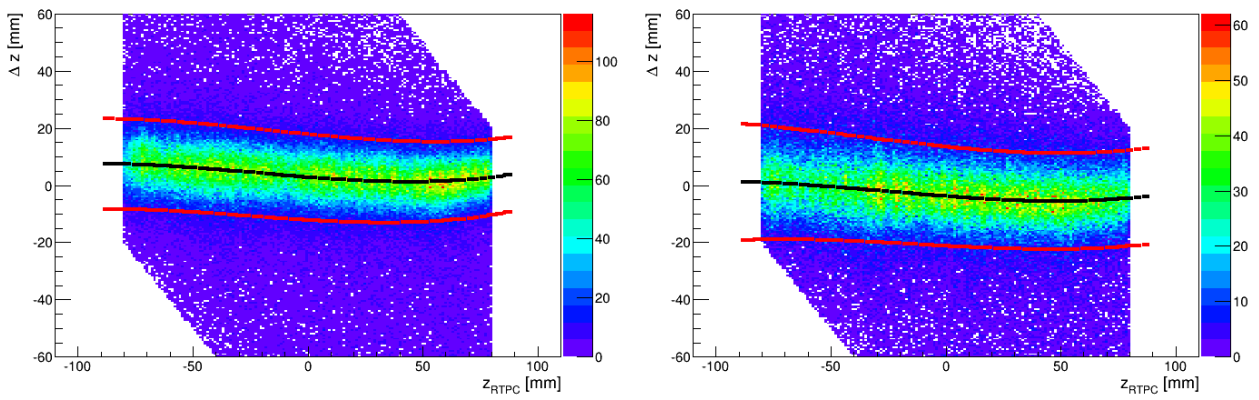


Figure 2.11: The Δz distribution versus the RTPC longitudinal position (z_{RTPC}) for the left and the right modules of the RTPC, respectively. The black lines represent the mean value of Δz as a function of z_{RTPC} , while the red lines are 2σ cuts around the mean.

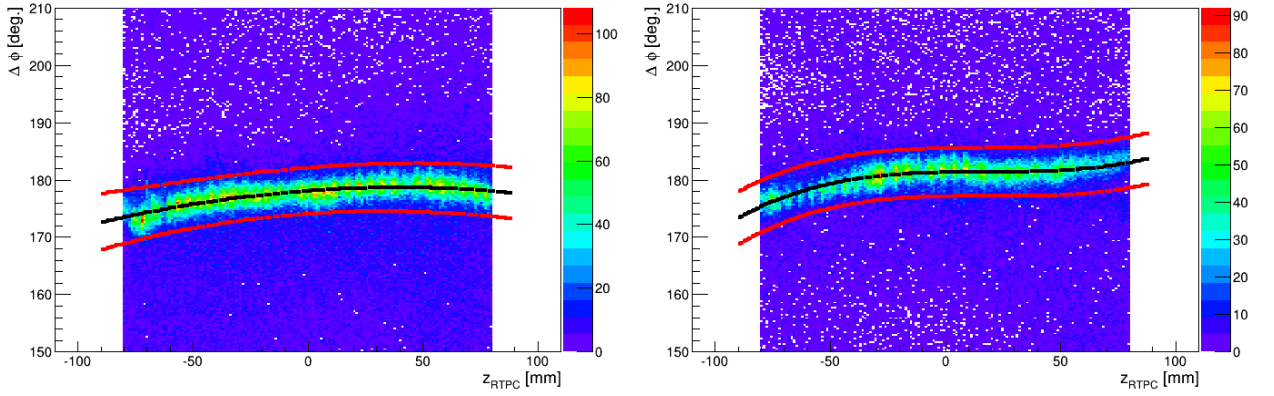


Figure 2.12: The distributions of $\Delta\phi$ as a function of z along the RTPC for the selected good tracks in the RTPC, for the two halves of the RTPC respectively. In each plot, the black line is the mean of $\Delta\phi$ and the red lines are 2σ cuts to select the elastic events.

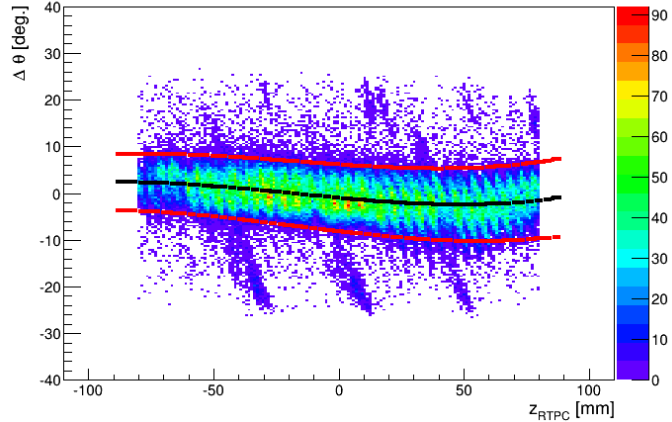


Figure 2.13: The $\Delta\theta$ distribution, for the selected events after the $\Delta\phi$ cut, as a function of z along the RTPC. The black line represents the mean, while the red lines are 2σ cuts around the mean to select the elastic 4He events.

where $p_{e'}$ and $\theta_{e'}$ are the electron's measured momentum and polar angle, E_b is the beam energy and $M_{{}^4He}$ is the helium mass (3.727 GeV/c²). Figure 2.13 shows the $\Delta\theta$ ($\theta_{cal}^{{}^4He} - \theta_{meas}^{{}^4He}$) distribution versus the 4He z-vertex. No significant difference was observed between the two modules regarding this quantity. The obtained parametrization of the mean and the width of the $\Delta\theta$ distribution can be found in Appendix B.

Constructing the invariant mass is one way to verify the efficiency of the previously described selection procedures. For a helium target, the invariant mass (W) is:

$$W = \sqrt{-2E_b p_{e'} (1 - \cos(\theta_{e'})) + M_{{}^4He}^2 + 2(E_b - p_{e'}) M_{{}^4He}}. \quad (2.6)$$

with the conventions for the variables as in equation 2.5. Figure 2.14 shows the W distribution of the events that have a good track in the RTPC and the identified elastic events. One can see the good agreement between the helium-4 real mass and the mean value of the identified elastic events. The difference in width is related to differences in resolution in CLAS. The large effect is due to the reaction products being emitted back to back resulting in a small overall acceptance for

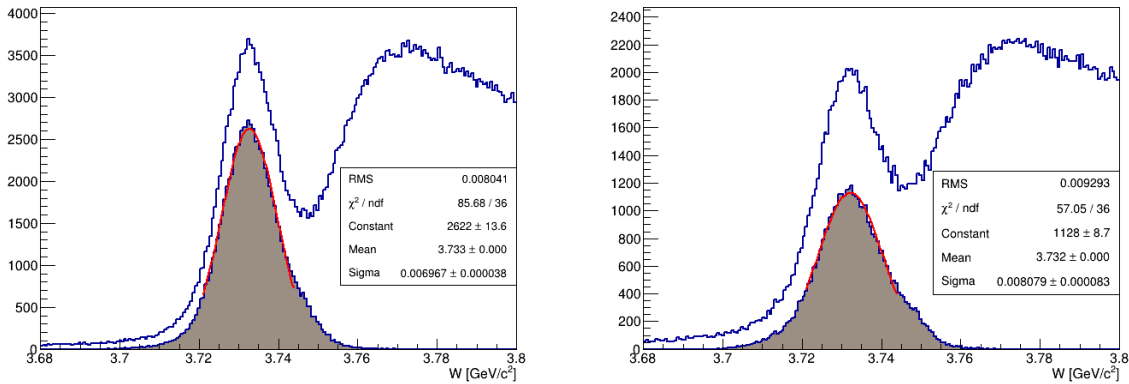


Figure 2.14: The invariant mass distributions for events with one good RTPC track (in blue) and the events passing the elastic cuts (in shaded) for each of the two modules of the RTPC, respectively.

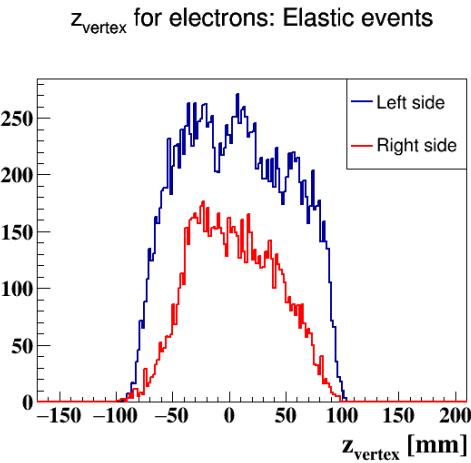


Figure 2.15: z-vertex distributions for the electrons of the identified elastic events in the two modules of the RTPC.

the process. This result is therefore very sensitive to the local variations of the resolution, which can be rather important in CLAS.

The figures presented for Δz and $\Delta\phi$ distributions in this section are shown after all the calibration and detector alignments (RTPC alignment is described in CLAS-NOTE-2013-008). The observed remaining dependences are not fully understood and probably arise from field misalignment and variations in the electric and magnetic fields within the chamber.

2.2.1.3 Checking the initial good track requirements

In this section, we study some of the good track requirements presented in section 2.2.1.1. We apply here all the good track and elastic requirements but the one related to the plotted variable.

Figure 2.15 presents the z-vertex distributions of the elastic events. One sees that the initial [-80:80] mm cuts on the helium z-vertex appear to be suitable cuts to ensure that the reconstructed tracks are within the physical volume of the RTPC.

In figure 2.16, we show the distribution of the radius of curvature for the identified elastic tracks in the RTPC. One sees that applying the other good track and elastic conditions eliminate

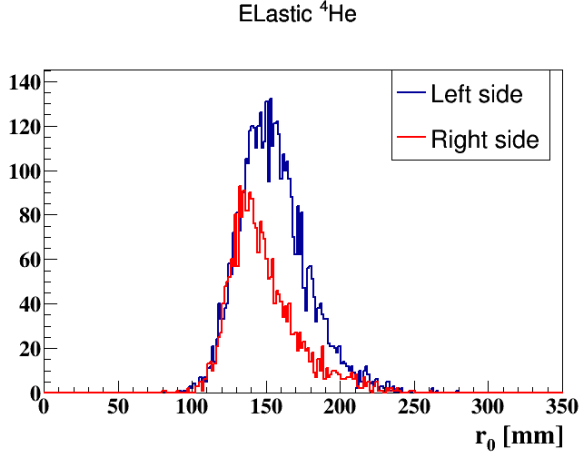


Figure 2.16: The radius of curvature distributions of the identified elastic ${}^4\text{He}$ tracks in the two modules of the RTPC after applying the other good track and elastic events

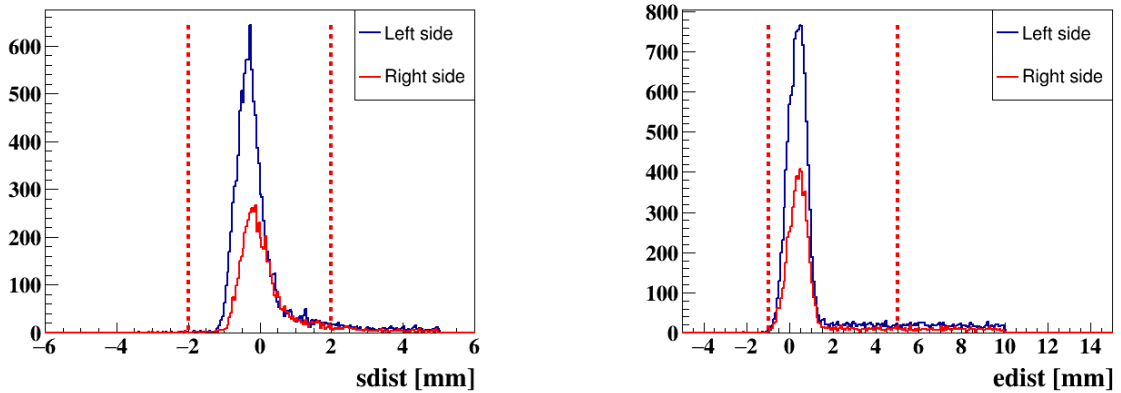


Figure 2.17: $sdist$ (on left) and $edist$ (on right) distributions for the identified ${}^4\text{He}$ elastic tracks in the two modules of the RTPC after applying the other cuts. The vertical dashed red lines indicate the initial cuts were applied to select the good tracks.

all the negative tracks as well as the tracks with r_0 less than 30 mm.

The distributions of $sdist$ and $edist$ for the identified elastic ${}^4\text{He}$ elastic tracks, figure 2.17, show that the tails, which are mostly due to electronic noise, are removed. Therefore, making tighter cuts would not cause significant changes in the calibration as the tail regions are cleaned by the other good track and elastic cuts.

2.2.2 Drift paths and drift speed calibration

2.2.2.1 Drift speed parametrization

The electrons follow their drift paths with a certain speed, named drift speed. This speed is affected by the experimental conditions, such as the variations in the magnetic field or in the gas composition. We can measure this speed using the tracks detected in the RTPC, as it is explained in this section.

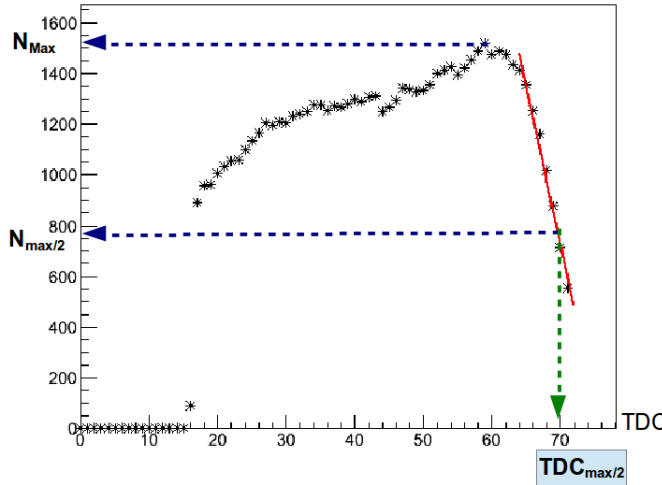


Figure 2.18: Time profile of the collected hits for the RTPC good tracks in one experimental run, run 61511, integrated over the full longitudinal length (z) of the RTPC. The $\text{TDC}_{\text{max}/2}$ is the time at which the dropping edge passes half the maximum number of hits.

In our TPC, the electrons released close to the cathode take the maximum drift time (TDC_{max}) to reach the readout pads while the geometrical symmetry along the RTPC ensures that these electrons always travel the same distance. Therefore, by identifying the TDC_{max} , the drift speed can be deduced. Figure 2.18 shows the time profile of the collected hits for the detected good tracks. The experimental drift time ranges between the trigger time ($\text{TDC}_{\text{min}} = 15$ TDCs) to 75 TDCs. The time profile shows an expected dropping edge at high TDCs due to the geometrical constraints. In order to avoid the statistical effects in determining the TDC_{max} , we define a value named as $\text{TDC}_{\text{max}/2}$ at which the dropping edge passes to half of the maximum number of hits in each hits-time profile. $\text{TDC}_{\text{max}/2}$ is inversely proportional to the drift speed.

We measure the $\text{TDC}_{\text{max}/2}$ along the length of the RTPC to take into account the variations in the electric and magnetic fields. The results can be seen in figure 2.19, where a clear variation of the drift speed along the RTPC was observed.

We also monitor the $\text{TDC}_{\text{max}/2}$ evolution during the time of the experiment, to take into account variations. The EG6 experiment has recorded data with different electron-beam energies: 1.204, 5.7, 6.064 and 1.269 GeV. The 5.7 and 6.064 data sets have low elastic cross sections compared to the 1.206 and 1.269 data sets. For this reason, we use all the RTPC good tracks and not only the elastic ones for these. Before checking the stability of $\text{TDC}_{\text{max}/2}$ over the experimental running period, we want to check the feasibility of using all good tracks for the purpose of parametrizing the drift speed. In this check, the $\text{TDC}_{\text{max}/2}$ identified using the good tracks of the 1.206-GeV data set is compared to the one identified from the elastic events of the same data sets. The result is shown in figure 2.20, in which the ratio between the two $\text{TDC}_{\text{max}/2}$ is plotted as a function of the longitudinal position along the RTPC. This ratio is consistent with 1, within 1%. Thus we can conclude that using the hits of the collected good tracks is a good approximation.

The variations with time of $\text{TDC}_{\text{max}/2}$ are shown in figure 2.21, in which each point is a run of about two hours of data taking. One can see a non-negligible variation over the three months of data taking due to the changes in the experimental conditions. The main cause of these variations is probably the variation of proportions in the drift gas mixture which was not perfectly under control due to leaks in the parts of the detector where the gas is contained by very thin aluminized mylar.

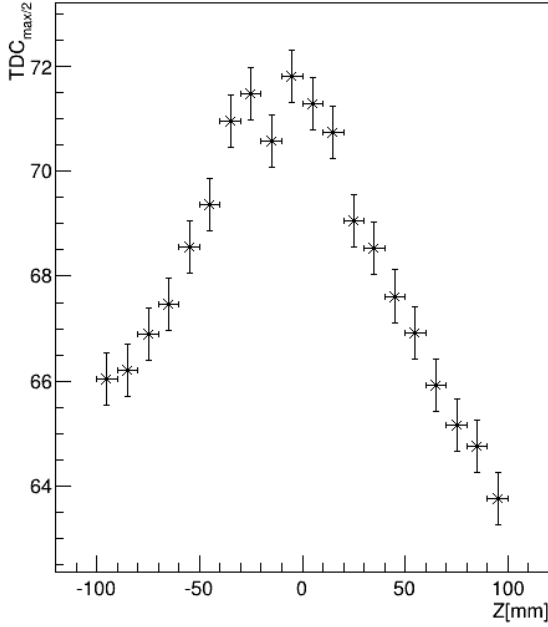


Figure 2.19: $TDC_{max/2}$ variation as a function of the longitudinal position along the RTPC, z position of the hit, in one experimental run, 61510.

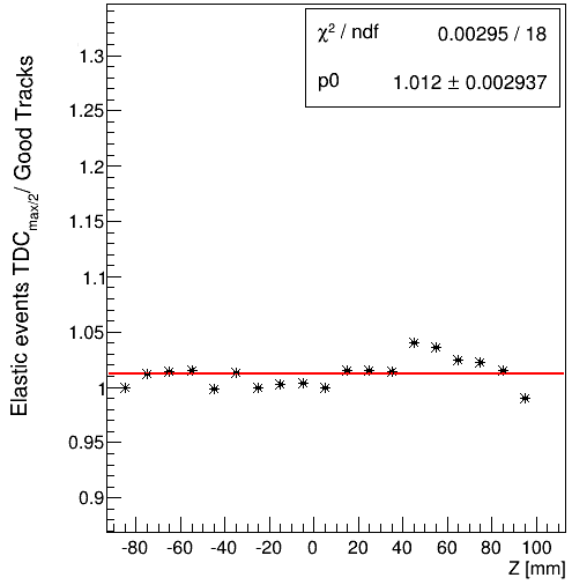


Figure 2.20: Ratio between $TDC_{max/2}$ extracted using the RTPC good tracks and the one extracted using the clean elastic events, both from the 1.204-GeV dataset, as function of the hit position (z).

As $TDC_{max/2} - 15$ ($= \frac{\text{Drift path length}}{\text{Drift speed}}$) varies with both run number (time) and the geometry of the RTPC (z along the RTPC). We parametrize the dependence on z , hit (pad) position, for each run in the form:

$$TDC_{max/2}(z) = p_0 + p_1 * e^{p_2 * (z - p_3)^2}. \quad (2.7)$$

Then fits are performed for these parameters as functions of the run number, such that the drift speed parametrization depends on the run and z along the RTPC. The numeric parametrizations of p_0 , p_1 , p_2 , and p_3 can be found in Appendix B, table B.1.

The implementation of these parametrizations of the drift speed in our reconstruction codes resulted in more good tracks and elastic events identified comparing to the previous calibration sets. Figure 2.21 also shows these gain percentages of good tracks (GT) and elastic events (El) for a few runs. The gradual improvement with time is due to the improvement on the parameters of the reconstructed tracks ($sdist$, $edist$... etc), which are then more likely to pass the selection requirements.

2.2.2.2 Drift paths parametrization

A drift path is the trajectory that an electron follows after being released in the drift region. The standard software to calculate these paths is the MAGBOLTZ program [29]. This program requires precise knowledge of the experimental conditions, such as the detector's geometry, the exact composition of the drift gas and the applied electric and magnetic fields. Thus any variation in these conditions would give inaccurate calculated drift paths. In the EG6 experiment, MAGBOLTZ has been used to calculate a first set of drift paths, but it was found rapidly that our lack of knowledge on some of the RTPC's conditions was limiting the precision of the calculation.

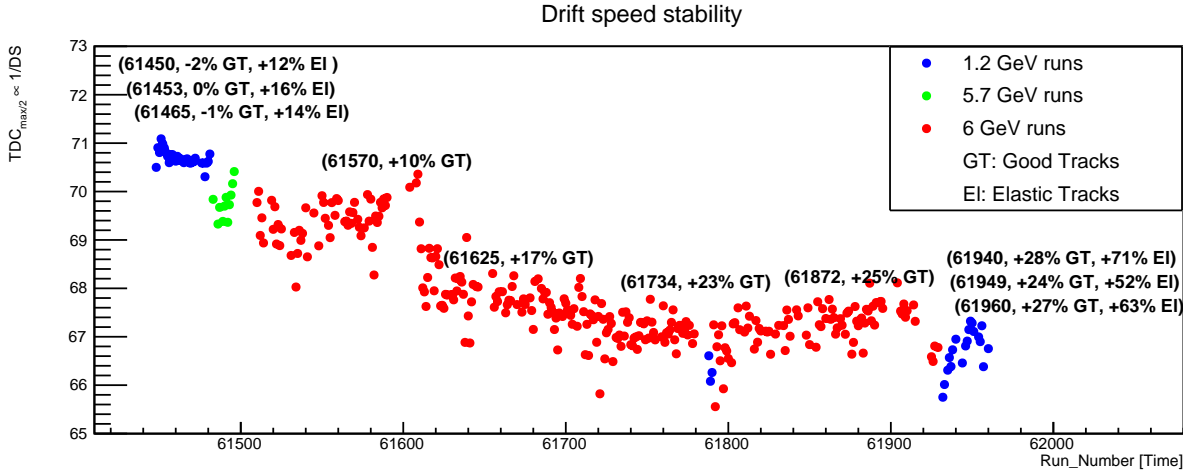


Figure 2.21: The integrated $TDC_{max/2}$ over the full z-RTPC as a function of run number. The gain after calibration in the collected good tracks (GT) and elastic events (El) are shown for a sample of runs.

For this reason, we chose to further calibrate the drift paths with a method that does not require an exact knowledge of the conditions in the chamber and is instead based on the experimental data.

In this alternative method, we use the identified elastic ($e^- {}^4He \rightarrow e^- {}^4He$) events to extract the drift paths. For these events, the kinematic of the recoil 4He is calculated from the scattered electron. Then the electrons' drift paths are extracted by comparing event by event the experimentally measured hits in the RTPC to the trajectory of the corresponding simulated 4He . With this technique, the drift paths are obtained with limited impact from our knowledge of the conditions in the RTPC, in particular the method is completely independent from both electric field and gas mixture.

We perform the drift paths' extraction in two passes. In the first pass, we assume a linear correlation between the radius of emission R (we work here in radial coordinates: R and ϕ) and the drift time to link GEANT4 hits along the trajectory to actually measured hits. Based on this association, we obtain a $\Delta\phi$ distribution as function of time. $\Delta\phi$ is the difference between the ϕ observed in GEANT4 and the ϕ of the pad which actually measured a correlated hit. Assuming we have an axial symmetry of the drift path, $\Delta\phi$ as a function of time indicates how much the electron drifted because of the magnetic field for any hit. This is therefore the relevant information to reconstruct the origin of the hits measured in the detector. However, the actual correlation between time and radius is not exactly linear. So we perform a second pass, in which we refine the initial correlation between the radius and the time using the drift paths obtained in the first pass. We then repeat the procedure of the first pass to extract the final drift paths. Because of the variations in the magnetic field along the detector, the extraction is made in z bins.

The detailed steps of the procedure are as follow:

- We first select a sample of well identified elastic events in our experimental data. Using the kinematics of the scattered electrons in these events, we generate in GEANT4 a sample of events identical to the measured ones.
- For each couple of events (the experimental one and its simulated equivalent) we make a linear correlation between R , from simulation, and TDC from real data, to link the GEANT4 hits to the measured ones. In our TPC, the maximum R equals 60 mm (close to the anode) at the trigger time, ($TDC_{min} = 15$ TDCs), and the minimum R equals 30 mm (close to the

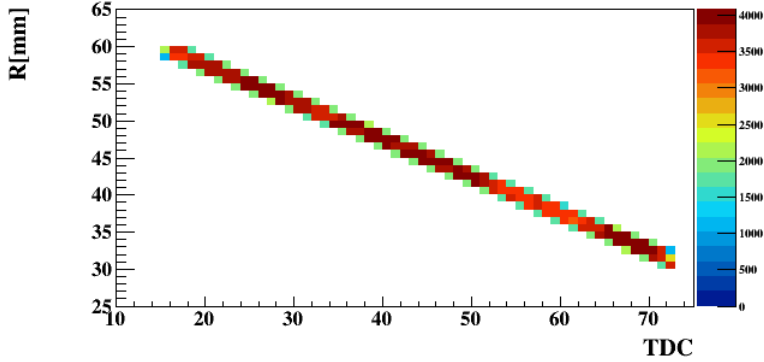


Figure 2.22: (First pass). Distribution of R as a function of time (in TDC) for the simulated hits located in one z bin. The width of the bin is 10 mm, with the center at $z = 5$ mm.

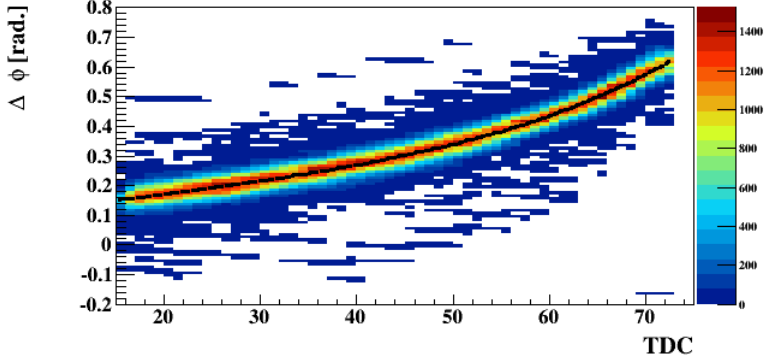


Figure 2.23: (First pass). Distribution of $\Delta\phi$ as a function of time (in TDC) for in one z bin. The width of the bin is 10 mm, with the center at $z = 5$ mm. The black line represents a fit for $\Delta\phi$.

cathode) at maximum TDC (TDC_{max}). Thus, the linear correlations can be written as:

$$R(TDC) = \frac{60 - 30}{15 - TDC_{max}}(TDC - 15) + 60. \quad (2.8)$$

We apply 3 TDCs-wide windows around the linear R-TDC correlation to associate the GEANT4 simulated hits to measured hits. Figure 2.22 shows the distribution of R versus TDC for to select the matched hits.

- From these selected matched hits, we obtain $\Delta\phi$ ($= \phi_{sim.} - \phi_{hit_pad}$) as a function of time. The results can be seen in figure 2.23². This figure is fitted to obtain the parameterization of the drift path.
- The correlation between R and the time is then refined using the extracted $\Delta\phi$ as a function

² $\Delta\phi$ at the anode ($TDC = 15$) is not equal to zero because there is a drift in ϕ between the anode (the first GEM layer at radial distance equal to 60 mm) and the readout pads (at radial distance equal to 69mm).

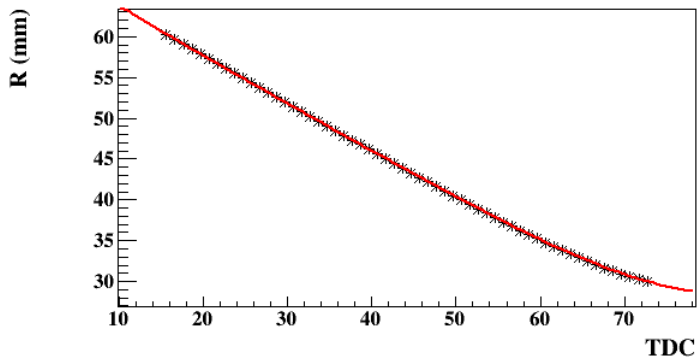


Figure 2.24: (Second pass). The calculated R as a function of time (in TDC) is corrected by the $\Delta\phi$ relation extracted from the first pass.

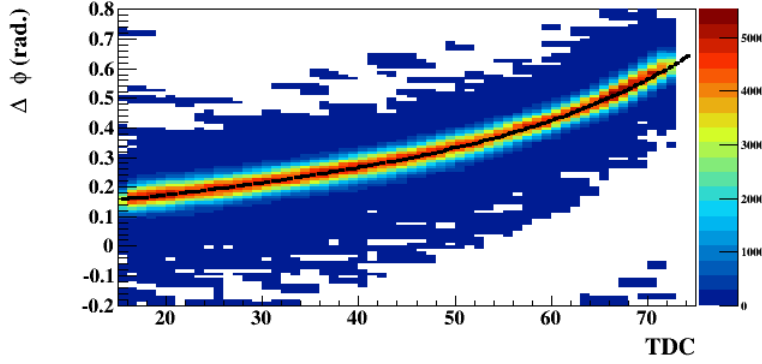


Figure 2.25: (Second pass). Distribution of $\Delta\phi$ as a function of time (in TDC) located in the same z bin shown in figure 2.23. The black line represents the final drift paths.

of time as:

$$R(TDC) = R_{min} + \left[\sum_{i=TDC_{Max}}^{TDC} \sqrt{DS^2 - R^2(i)} \cdot \left(\frac{\partial \Delta\phi}{\partial TDC}(i) \right)^2 \right] \cdot TDC, \quad (2.9)$$

where DS is the average drift speed, equal to 0.7 mm/TDC (6.14 $\mu\text{m}/\text{ns}$), R_{min} equals to 30 mm, $R(i)$ is the linear correlation defined in equation 2.8 and $\Delta\phi(i)$ is the fit in figure 2.23. The sum is multiplied by a TDC unit (=114 ns). The calculated R , figure 2.24, is almost linear, indicating that only two iterations are probably enough.

- In the second pass, we use the newly found $R(TDC)$ relation to construct new $\Delta\phi$ distributions, see figure 2.25 for our final result.

We performed a third pass in which the $R(TDC)$ correlation is refined using the drift paths from the second pass. As a result, we observed no difference between the drift paths of the second and the third passes. In other words, extracting the drift paths from two iterations gives us stable results.

The first drift paths were extracted using the elastic events from the early 1.204 GeV dataset. In order to ensure the consistency of these drift paths over the experimental running period, we

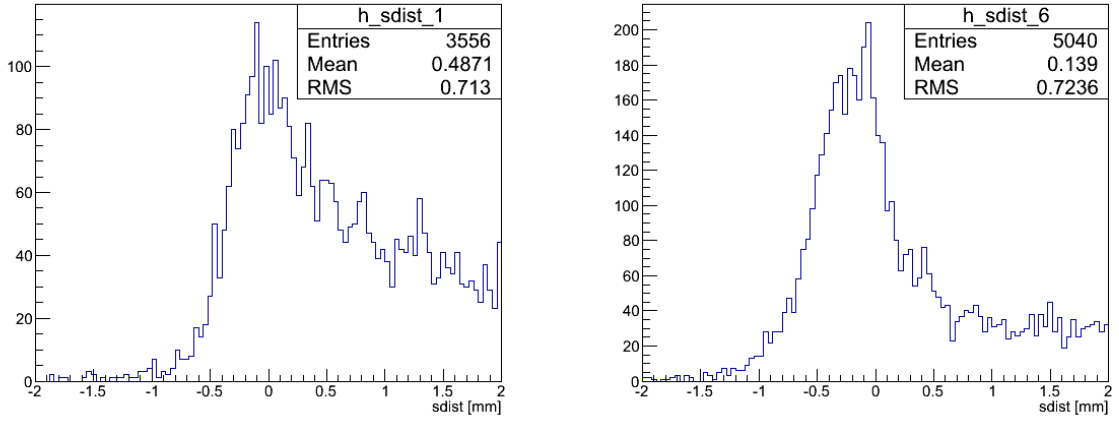


Figure 2.26: The $sdist$ distribution for the collected tracks in the RTPC using the same initial collected data with an old set of drift paths, on the left, and a newer set, on the right.

extracted another set of drift paths using the elastic events of the 1.269 GeV dataset. We observed no difference between the two sets of the drift paths, ensuring the stability over the experimental period. The final drift paths are extracted using both datasets, 1.204 and 1.269 GeV. They take the form:

$$\Delta\phi(TDC, z) = \sum_{i=0}^4 p_i(z) * TDC^i, \quad (2.10)$$

where the parameters, p_0 , p_1 , p_2 , p_3 and p_4 are functions of z , as can be seen in Appendix B, table B.2. The final drift paths are implemented in our reconstruction codes such that the reconstructed position of each hit becomes:

$$\phi_{exp}(z, TDC) = \phi_{hit_pad} - \Delta\phi(z, TDC). \quad (2.11)$$

It is important to note that the drift paths have shown strong sensitivity to the other RTPC calibrations. Therefore, we performed iterative extractions of the drift paths and, as a result, obtained more good tracks with a signal to background ratio largely improved. Figure 2.26 shows an illustration of the improvements in terms of the $sdist$ parameter using the same initial collected data with an old drift paths and a newer set.

2.2.2.3 Summary

The drift paths and drift speed were first extracted using the MAGBOLTZ Monte Carlo simulation. One can find the detailed procedure of a similar extraction in the BoNuS analysis note [28]. Then, we improved this first result with many iterations after each change that would affect the drift paths, such as the beam-offset and gain calibrations of the RTPC. Moreover after each pass, the number of elastic events used for calibration increased, justifying by itself a new calibration. Overall, this was a long process that evolved and improved over the years and we concentrated in the note on the description of the final iteration of this calibration.

2.2.3 Gain calibration

The second important calibration is the amplitude of the signal provided in ADC units. Since each charged particle deposits a certain amount of energy ($\frac{dE}{dX}$) when crossing a material, we can

identify particles based on this variable. The ($\frac{dE}{dX}$) depends on the characteristics of the particle, such as its energy, mass and charge, and the nature of the medium as well.

$\frac{dE}{dX}$ can be calculated using the Bethe-Bloch formula [32]:

$$\left\langle \frac{dE}{dX} \right\rangle = \rho K z^2 \frac{Z}{A} \frac{1}{\beta^2} \left[\frac{1}{2} \ln \left(\frac{2m_e c^2 \beta^2 \gamma^2 T_{max}}{I_{max}} \right) - \beta^2 - \frac{\delta \beta \gamma}{2} \right] \quad (2.12)$$

$$\text{with } T_{max} = \frac{2m_e c^2 \beta^2 \gamma^2}{1 + 2\gamma m_e / M + (m_e / M)^2} \quad (2.13)$$

where T_{max} is the maximum kinetic energy of a free electron in a single collision, and z , M , β are the charge, mass and speed ($= p / \sqrt{M^2 + p^2}$, where p is the momentum) of the particle, respectively. m_e is the electron mass and the constant K is equal to $4\pi N_A r_e^2 m_e c^2 = 0.307075$ MeV mol⁻¹ cm². Z , A , I , ρ are the effective charge, atomic number, mean excitation energy and mass density of the medium. In the RTPC, these constants are equal to 66, 126.79 mg mol⁻¹, 99.79 eV and 1.03 mg/cm³, respectively.

Experimentally, $\frac{dE}{dX}$ can be calculated from the collected ADCs as:

$$\left\langle \frac{dE}{dX} \right\rangle = \frac{\sum_i \frac{ADC_i}{G_i}}{vtl}, \quad (2.14)$$

where the sum runs over all the pads contributing to a track. ADC_i is the recorded amplitude in each pad i , and G_i is its gain. The vtl is the total visible length of the track in the active drift volume. This is of course assuming the energy loss in the drift region is small in regard to the total energy of the particle, which is true except close to our detection threshold.

The electron collection system of the RTPC has 3200 readout pads. The gain of each pad is the ratio between the deposited energy and the output recorded value. We extracted the gains using two techniques. The first one is by comparing the experimental recorded $\frac{dE}{dX}$ to the expected values calculated from the Bethe-Bloch formula. The second technique is based on comparing the experimental ADCs to the GEANT4 simulated ones, track by track. We latter refined this second method by comparing the ADCs of each pad to the average ADCs of the other pads in the same track.

The two techniques were investigated for the EG6 experiment using the elastic events from the 1.206 GeV data set. The first method involves a series of equations to be solved to obtain the gains.

The second method requires improvements in the simulation, in order to match the real experiment. In summary, these improvements are:

- Implementation in the simulation of the previously extracted parametrizations of the drift speed and the drift paths.
- Global ADC normalization to give reasonable simulated values. In the left module, 1 ADC is equal to 17 eV, while it is equal to 21 eV in the right module. These normalizations were extracted from the comparison of the data to the GEANT4 simulation.
- Rejection of the signals from bad pads. During the experiment, the readout system of the RTPC suffered from 555 dead or noisy pads. These pads are marked by the dotted squares in figure 2.30.
- Smearing the position of the simulated hits. Experimentally, the average number of hits per track is around 80 while the initially reconstructed mean value from the simulation is

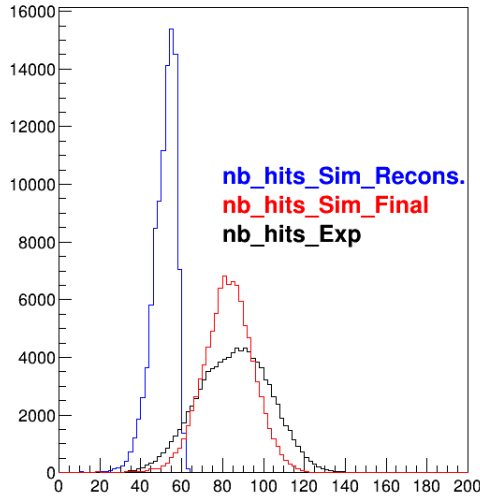


Figure 2.27: The distributions of the number of hits per track. The black, the blue and the red distributions are the number of hits per track for respectively, the experimental data, simulation before smearing and the simulation with smearing.

around 50. We apply a Gaussian smearing on the position of the simulated hits to make the simulation more realistic, see figure 2.27.

- Application of the TPC’s DAQ cut on the simulated data. Experimentally, each pad must have at least 3 consecutive time bins, with ADC values above the threshold, 35 ADCs, in order to be recorded. Then, the hits of three neighboring bins on each side of the above threshold bins are also recorded, while the other hits are not.

To illustrate the procedure of comparing simulated tracks with real tracks, we show in Figure 2.28 the simulated and the experimental ADCs as a function of the TDCs for the same track. Then, the gain of each pad is defined as the ratio between the mean recorded experimental ADCs to the mean simulated ADCs in the same track. Then for each pad, the gain ratios were collected from all the identified elastic tracks and these gains were fitted by a Landau function to give a first pass gain for each pad as the most probable value of the fit.

To make sure that the recorded ADCs by a given pad are similar to the recorded ADCs by other pads in the same track, we refined this calibration after the extracted gains were applied to the experimental data. At this step, we compared the mean ADCs of each pad to the mean ADCs of the whole track. This ratio is collected from all the elastic events and a gain correction factor is extracted and applied to get a final gain for each pad, labeled as second pass gain in figure 2.29.

As the two modules of the RTPC are electronically separated, we look at their calibrations separately. Figure 2.29 shows the ratio between the calculated $\frac{dE}{dX}$, using the gains extracted from first and the second (both passes) methods, and the GEANT4 simulated $\frac{dE}{dX}$ for the elastic events in the two modules of the RTPC. From the latter figure, one can see improvements obtained by using this method to fine tune the gains extracted only by comparing data to simulation. We conclude that extracting the gains from comparing data to simulation in terms of the ADCs of the individual tracks gives more precise gains than solving the series of equations. Figure 2.30 shows the gains from the second method, where the dotted squares refer to the dead or noisy pads. These are the ones that are implemented in the EG6 reconstruction codes.

In the left module of the RTPC, on the bottom panel of figure 2.29, one notices an additional

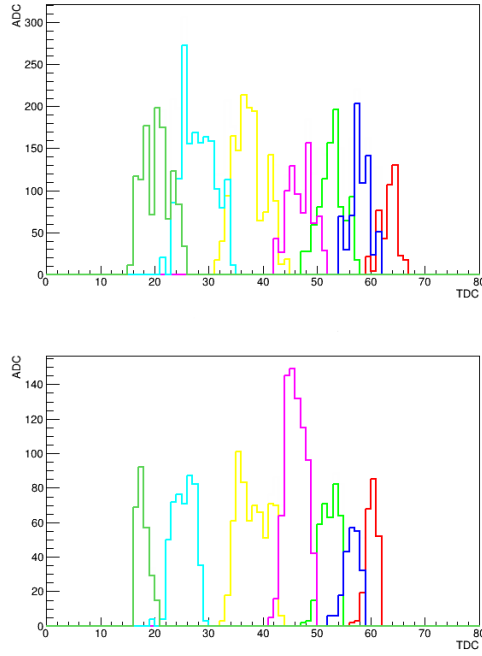


Figure 2.28: The simulated (top) and the experimental (bottom) ADCs versus TDC distributions for the same track. The same colors indicate hits that were registered in the same channel for the simulation and the experiment.

unexpected lower peak ($dE/dx_{exp}/dE/dx_{sim} \sim 0.3$). These events pass all the elastic requirements but for some reasons they have lower ADC values. They represent around 7% of all the elastic events. After extended studies, the nature of these particles is not identified yet. We note that this is a global phenomenon in the left module as 94% of the left module's pads are involved in both some low and high dE/dx events. For instance, figure 2.31 shows the average ADC versus TDC distributions for the recorded hits in one of these pads in the left module. For the calibration procedures, the events with low dE/dx were excluded as we do not fully understand their nature, see figure 2.32.

To check the validity of the extracted gains, we show $\frac{dE}{dX}$ versus the momentum (per charge unit) measured in the RTPC for all the collected tracks of the 1.206 GeV data set. In the plots, we add the theoretical lines derived from the Bethe-Bloch formula for possible detected particles: 4He , 3He , 3H , Deuterium (d) and the protons. One can see the different bands corresponding to the different detected particles. Even though the bands are very wide, the $\frac{dE}{dX}$ can be used to perform particles identification for large data set and different physics processes. In this analysis, the $\frac{dE}{dX}$ is not used to identify the recoil 4He in the coherent DVCS event selection, as the set of exclusivity cuts that will be presented in chapter 4 appears to be strict enough.

2.2.4 Noise rejection

The RTPC was designed to reduce noise and contribution from Møller electrons via the first and second 1 atm gas gaps. During data taking, the readout thresholds of the RTPC were set low to avoid efficiency problems, with the effect of recording more electronic noise. The latter effect is illustrated by the large occupancies in the top panel of figure 2.37.

Two independent noise signatures were found, and event-based algorithms were implemented to significantly reduce them offline. This resulted in improved track quality, increased track

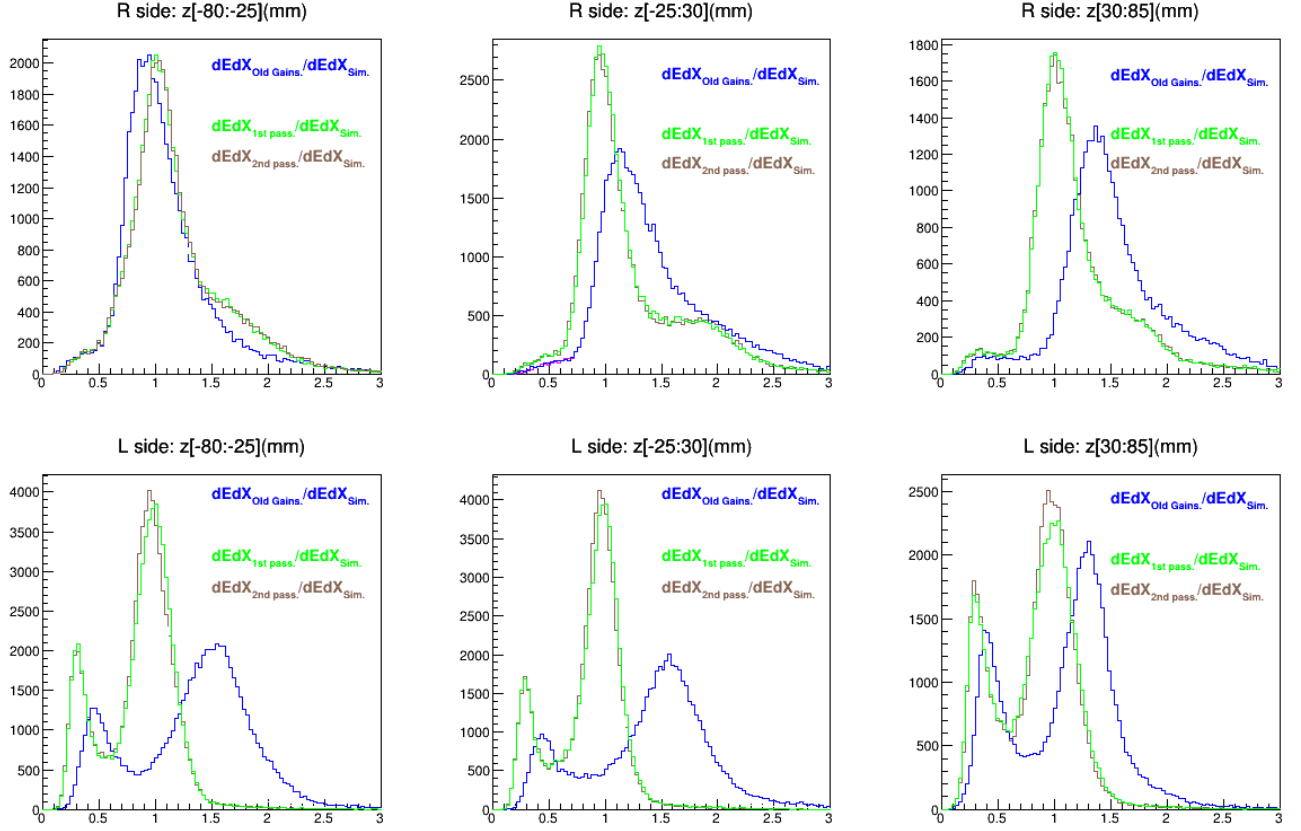


Figure 2.29: The ratio between the experimental dEdx and the simulated ones for different regions along z for the two modules of the RTPC, right module on top panel and left module on bottom panel. The blue lines are using the first method of extracting the gains (comparing the experimental recorded dEdx to the expected values calculated from the Bethe-Block formula). The green lines are using the fist pass of the second method (comparing simulation to data only) with all the elastic event sample. The brown lines are using the final gains extracted from the second method (both passes).

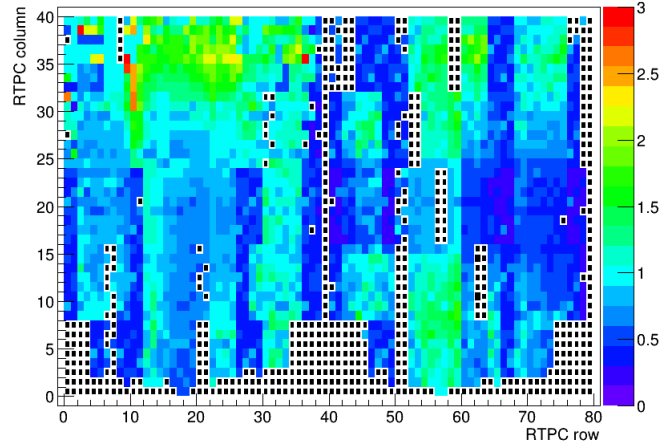


Figure 2.30: The extracted gains from the second method. The dotted squares refer to the position of the excluded pads.

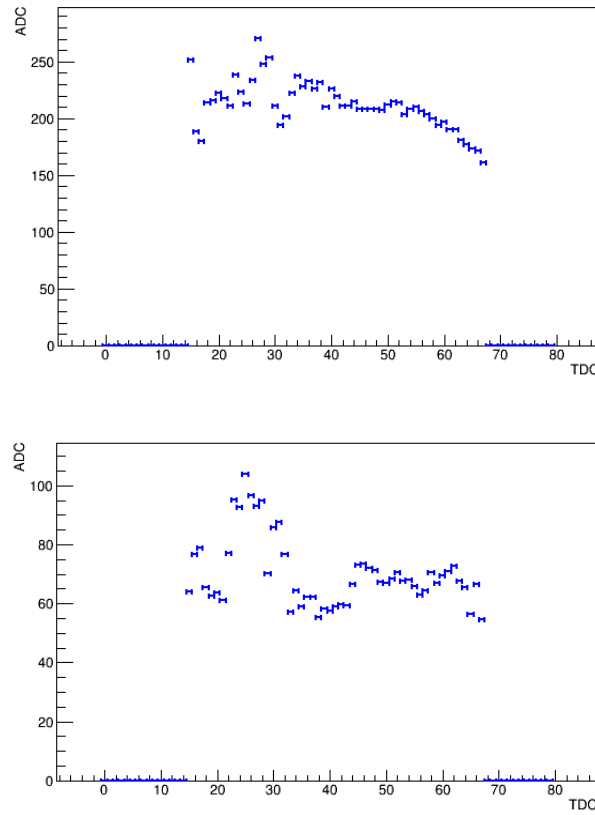


Figure 2.31: The average ADC vs. TDC distributions of the experimental hits recorded for the elastic events in one pad of the left module, pad number 706. On the top: the distribution for the elastic tracks in the region where $dEdx_{exp}/dEdx_{sim} \sim 1$. On the bottom: the distribution for the elastic tracks that exhibit $dEdx_{exp}/dEdx_{sim} \sim 0.3$.

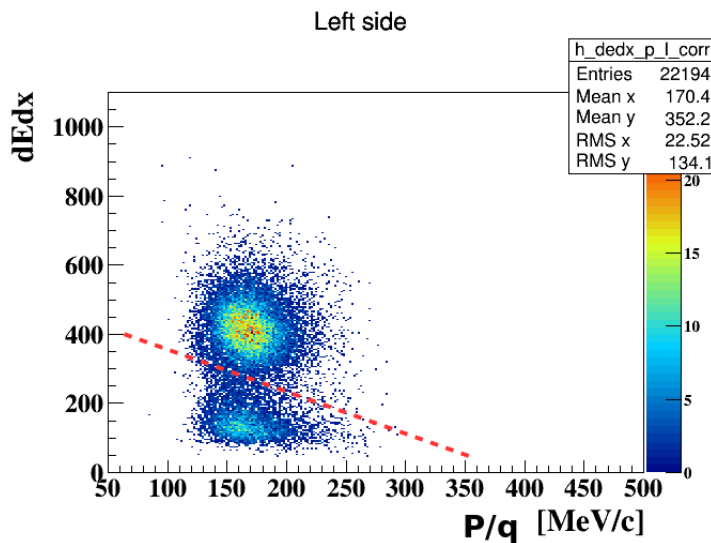


Figure 2.32: DEdx as a function of the measured momentum inside the left module of the RTPC for a sample of the identified elastic 4He tracks. The red dashed line represents the cut we applied to exclude the low dEdX events from usage for the calibration purposes explained earlier in this chapter.

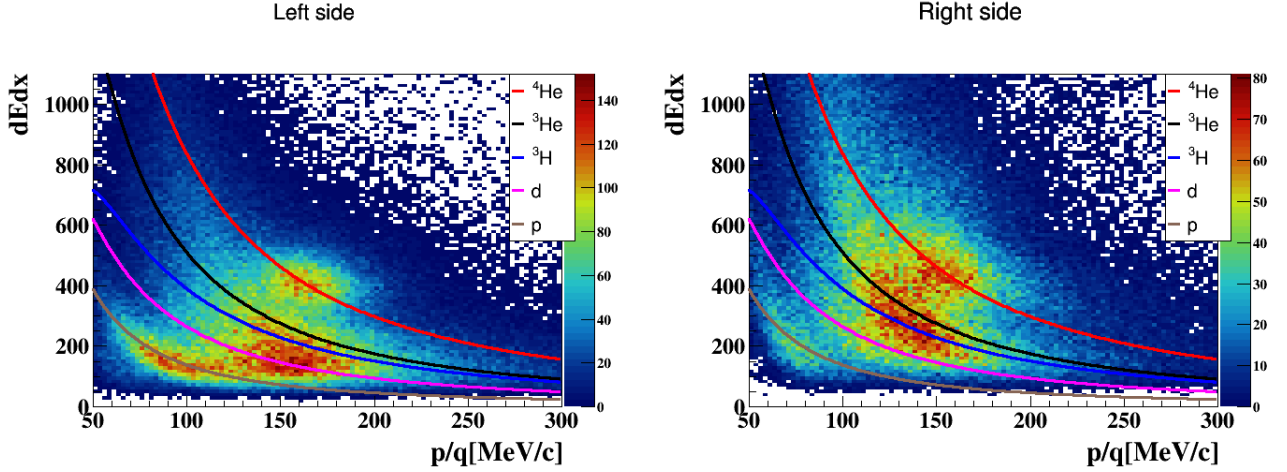


Figure 2.33: The experimental $\frac{dE}{dX}$ calculated using the second method gains versus p/q of all the collected good tracks in the RTPC in the early 1.204 GeV dataset.

efficiency, and the opportunity to reintroduce channels otherwise determined to be too noisy. This also resulted in more uniform occupancy, shown in the bottom panel of figure 2.37.

Here we describe the methods and their specific effects. These are implemented in EG6's pass2 reconstruction in `$CLAS_PACK/gem/noisypads.c`.

2.2.4.1 Oscillatory Noise

An oscillatory noise signature was found for many RTPC readout pads, and is attributed largely to the electronics. The signature is a series of hits falling on a fixed ADC vs TDC curve for TDC less than 30. About 18% of the active pads have very strong contributions from this type of noise, which previously resulted in many of them being marked as "bad" due to high occupancies.

An algorithm was developed to remove hits corresponding to this noise without suppressing good hits. First, the ADC vs TDC noise curve was parameterized. Next, for every event and channel independently, the number of hits falling on this curve is counted. If a significant number of hits lie far above or below the noise curve, no rejection is performed. If most of the hits below TDC=30 fall on the noise curve, all hits below TDC=30 are rejected for that channel. Figure 2.34 shows the effect of this noise reduction for one very noisy pad. The result of this algorithm is 5% more good tracks reconstructed, with improved signal to background ratio, as can be seen in figure 2.35. Further, this allowed to recover 40 channels that had previously been ignored due to high occupancies before this noise rejection.

2.2.4.2 Readout Group Noise

Another noise signature is isolated to particular readout boards, corresponding to 8x2 channel groups. Initially many of these 8x2 groups were ignored in reconstruction due to very high occupancy (see figure 2.37). Upon further analysis, we found many events where these groups behaved normally and measured good tracks, while in other events the whole 8x2 channel group fired. In other words, the noise level of channels within the groups is correlated in time.

An event-based method was implemented to treat this noise by computing an event pedestal for the entire group for cases when there exist neighboring hits. Hits in the 8x2 with no neighboring hits outside the group were used to calculate an event pedestal for the group. That pedestal

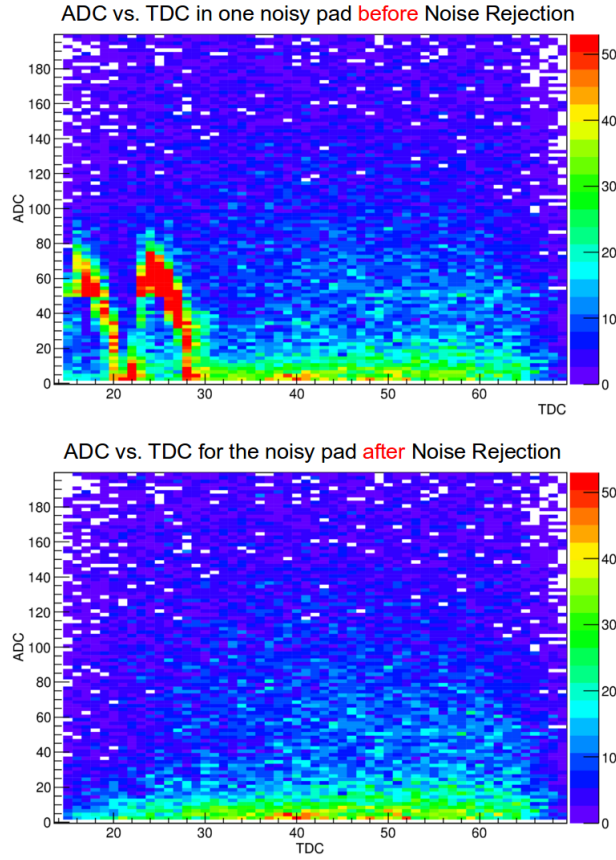


Figure 2.34: The integrated ADC vs. TDC of the hits for good tracks before (left) and after (right) the oscillatory noise reduction, for a particular pad with strong noise. The color scale on the z-axis is for the hit yield and identical in both plots as well as the event sample.

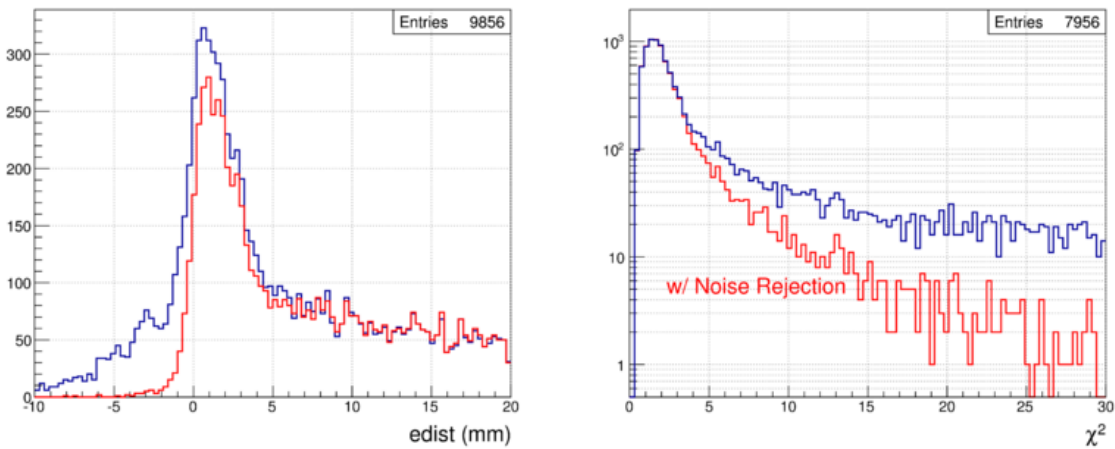


Figure 2.35: The $edist$ (left) and the χ^2 (right) distributions for all the tracks collected in the RTPC before (blue) and after (red) the oscillatory noise rejection. The event sample and color scales are identical in both plots.

is subtracted off all hits in the board in that event. If there are no neighboring hits outside the 8×2 group, the whole group is rejected in that event.

The effect of this algorithm on a couple reconstructed tracks is shown in figure 2.36. The overall result was another 5% increase in good tracks, and this noise subtraction also allowed to recover 32 more channels previously ignored due to high occupancy.

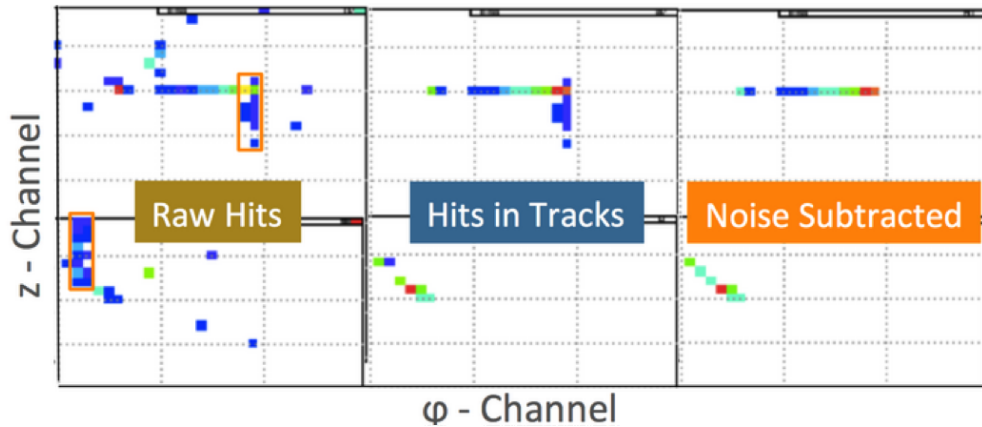


Figure 2.36: Example effects of readout board noise subtraction for tracks in two events (corresponding to the two rows in the figure). The known hot 8×2 readout groups are shown in the orange rectangle in the leftmost column. Color scale is ADC.

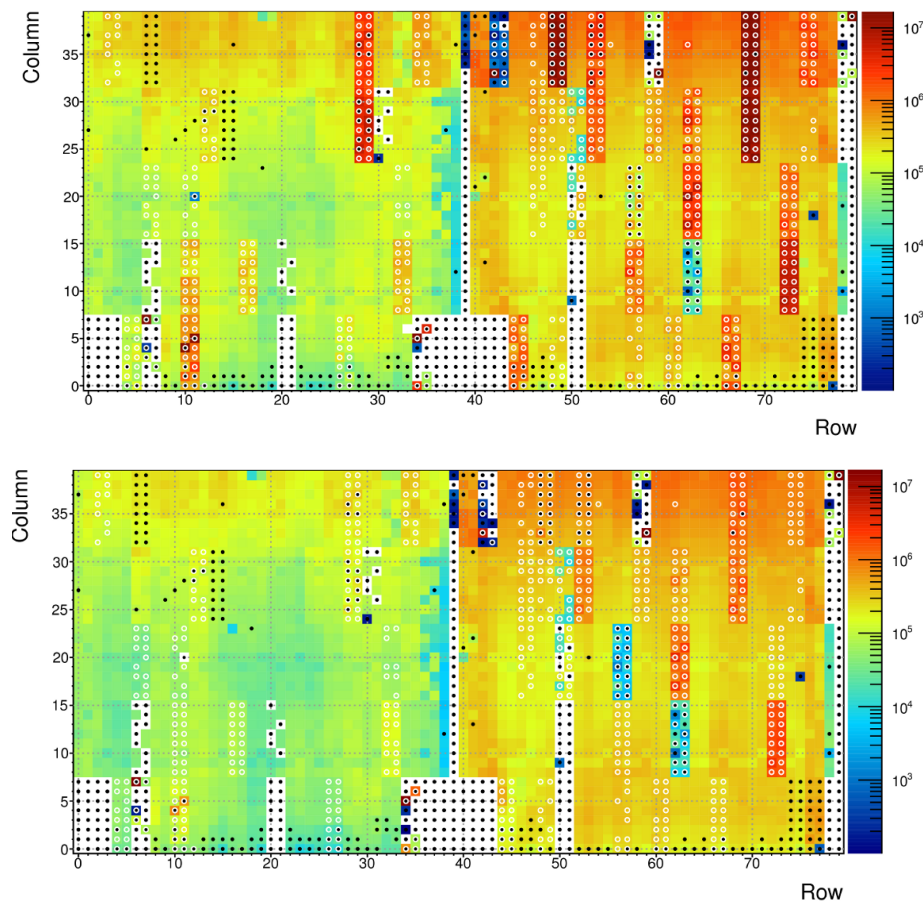


Figure 2.37: Occupancies before (top) and after (bottom) the two noise reduction algorithms. The event sample and occupancy color scales are identical in the two plots.

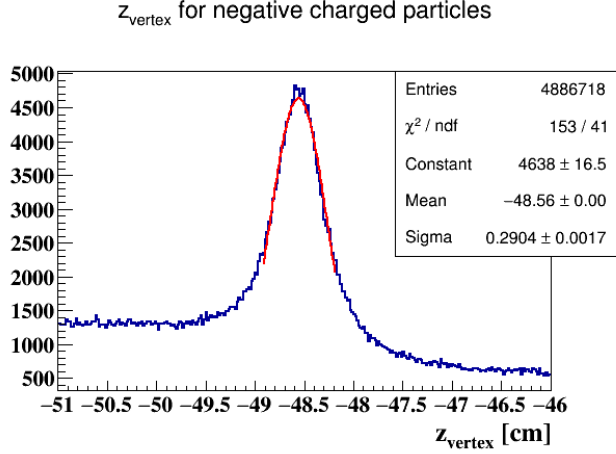


Figure 2.38: z -vertex of scattered electrons from the downstream window of the target. The z -vertex resolution of CLAS here is about 3 mm.

RTPC's module	σ_z	σ_ϕ	σ_θ	σ_p
Left module	6.03 mm	1.93°	3.78°	9%
Right module	7.40 mm	1.94°	4.02°	8 %

Table 2.1: The resolutions of the two modules of the RTPC.

2.3 Tracking resolution

The RTPC tracking resolution is defined as the spread of the reconstructed track vertex, angles and momentum with respect to their true values. In the EG6 experiment, we use the cleanly identified elastic events to estimate the RTPC resolutions. The CLAS detector nominally provides electron detection with an angular resolution around 1 and 4 mrad in θ and ϕ , and a momentum resolution ($\frac{\Delta p}{p}$) around 0.5% [19]. The z -vertex resolution is about 3 mm for an extended target in the presence of the solenoid, as can be observed experimentally from the target window, figure 2.38.

With such electron resolutions, one can extract the RTPC resolutions by comparing the calculated kinematics of the recoil elastic 4He nuclei with the measured experimental values, as shown in figures 2.39, 2.40, 2.41, 2.42 for the two halves of the RTPC separately. The distributions are fitted with a Gaussian and the extracted widths are listed in table 2.1. One can see that for the resolution, the two modules of the RTPC show almost the same performance. These resolutions will be used to match the simulated data to the experimental ones, as will be shown in the following chapter.

One notices slight shifts in Δz , $\Delta\phi$, and $\Delta\theta$ distributions. The reason of the shifts may rise from our non-perfect knowledge of the exact conditions in the chamber, such as the magnetic field, that affect the reconstructed parameters of the tracks. The reconstructed momenta show 10-15% systematic shifts compared to the calculated values.

2.4 RTPC efficiency

The previous distributions have shown that the two modules of the RTPC have slightly different yield, however this yield should not be linked to a different performance of the RTPC. The differences are mainly due to complicated convolution of CLAS and the RTPC acceptance. We

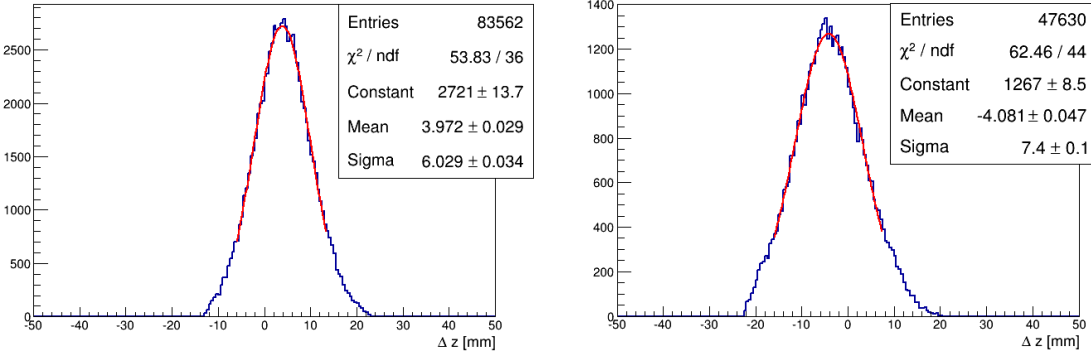


Figure 2.39: The z-vertex resolution of the two modules of the RTPC, respectively.

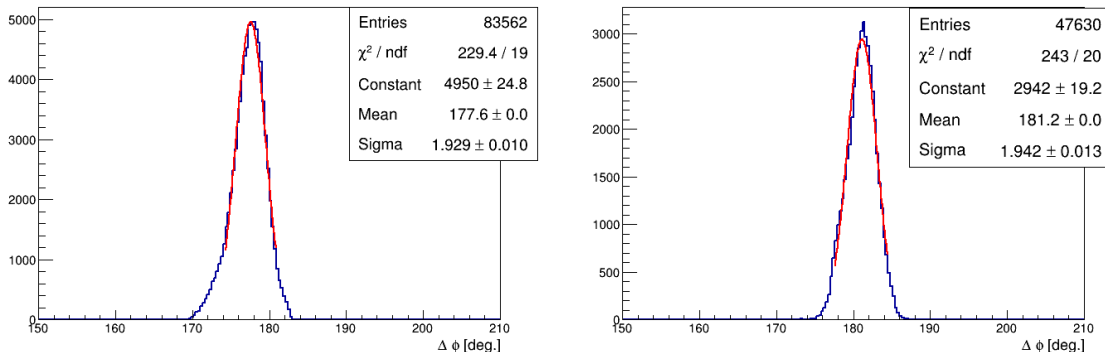


Figure 2.40: The azimuthal angle resolution of the two modules of the RTPC, respectively.

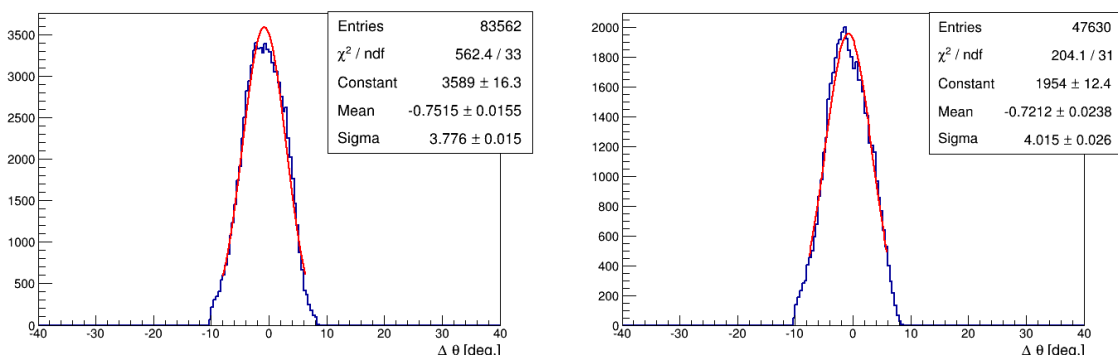


Figure 2.41: The polar angle resolution of the two modules of the RTPC, respectively.

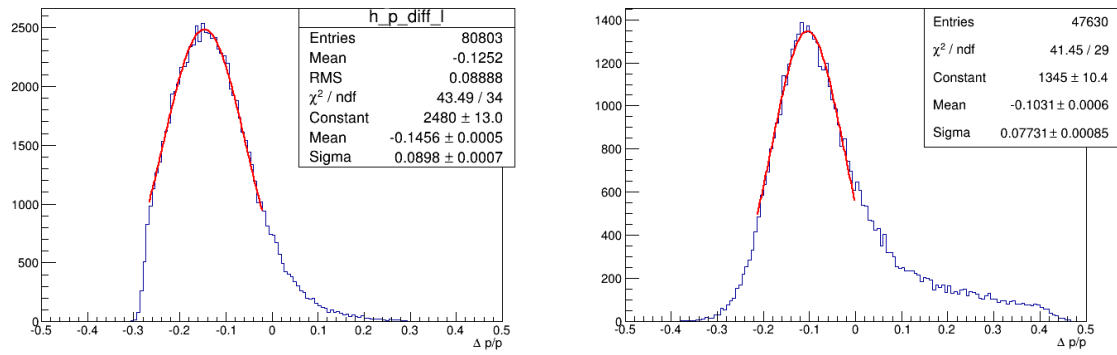


Figure 2.42: The momentum resolution of the two modules of the RTPC, respectively.

measured the efficiency of the RTPC using the elastic scattering, and a result found that the left and the right modules have similar efficiencies except near the target windows, as shown in figure 2.43.

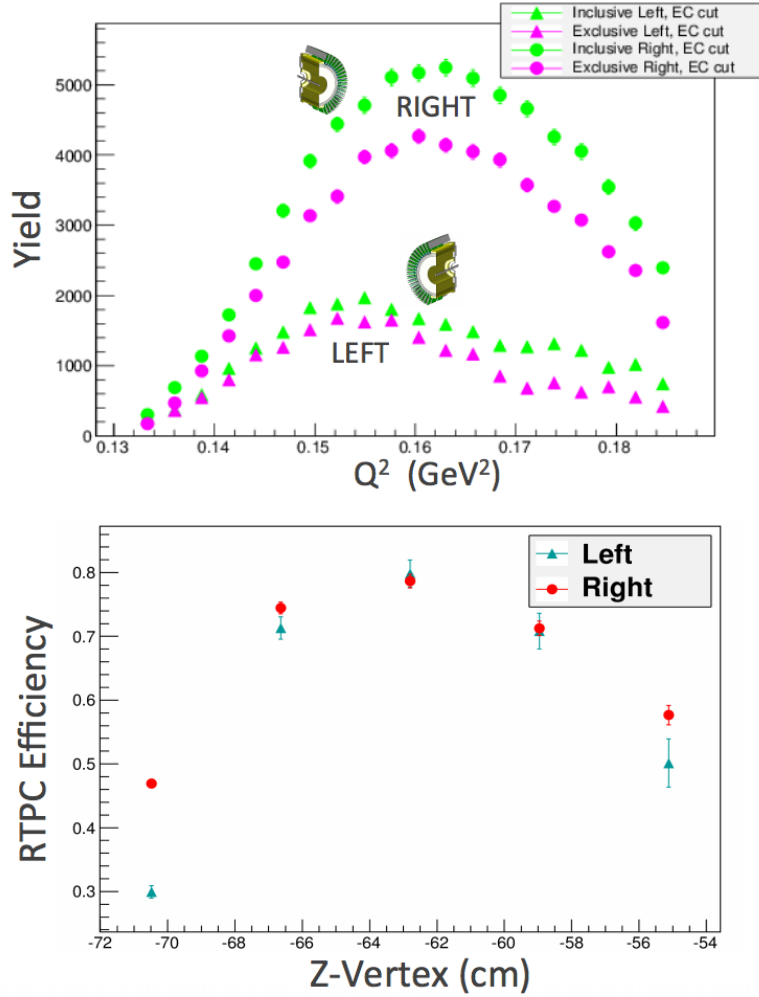


Figure 2.43: On top is the inclusive and exclusive elastic yields separated into the two RTPC halves (LEFT/RIGHT). Here the inclusive yields are the number of electrons in the elastic W-peak whose corresponding elastically scattered ${}^4\text{He}$ would have been in the acceptance of the RTPC, and the exclusive yields require the additional detection of the ${}^4\text{He}$. On bottom is the RTPC ${}^4\text{He}$ efficiency calculated from the ratio of exclusive and inclusive elastic yields.

Particles reconstruction and simulation

The final state of a coherent (incoherent) DVCS event consists of three particles: an electron, a ^4He (a proton), and a real photon. To identify the DVCS events, we first identify, individually, the different particles of interest. Then, events with three detected final-state particles will be further filtered by imposing the energy-momentum conservation laws, as will be presented in the following chapter.

Even after imposing the conservation laws, the DVCS sample will not have 100% truly DVCS events. In our kinematical region, the main contamination to our DVCS channels comes from the electroproduction of neutral pions. For instance, in the coherent π^0 -electroproduction, when one of the two-photon decay of the π^0 passes the DVCS requirements, it will be counted as a DVCS event. Thus, these events have to be subtracted before looking to any DVCS observable. For this purpose, we perform a technique in which we combine the measured exclusive π^0 -electroproduction data sample with a Monte-Carlo simulation to evaluate the background in the selected DVCS sample. For this technique, we need to identify the experimental π^0 s that come in the coherent and the incoherent π^0 -electroproduction channels.

In this chapter, we presents the procedures carried out to identify the final-state particles of interest, the Monte-Carlo simulation we used, and the kinematic corrections we applied on the particles.

3.1 Particles identification

3.1.1 Electron identification

The electron detection triggers the data acquisition system to record data from all the sub-detectors of CLAS. In this analysis, a particle which passes the following set of criteria is assumed to be a good electron.

Initial requirements

- Negative charge: the torus magnet generates a field which has mainly azimuthal components. Hence, the trajectory of a negative particle will be bent towards the beam line direction without changing azimuth. Consequently, information on its charge is accessible from the curvature of its trajectory.
- $(DC_{stat}, EC_{stat}, SC_{stat}, CC_{stat}) > 0$: these status variables are linked to the number of hits and the thresholds in the different sub-detectors of CLAS. Thus, we select the electrons which have positive status in the different sub-detectors as a first step to reduce the noise in the data sample.
- $stat > 0$: this variable is positive if the trajectory of a particle passes the two steps of the tracking in the DCs, Hit-Based Tracking (HBT) and Time-Based Tracking (TBT).

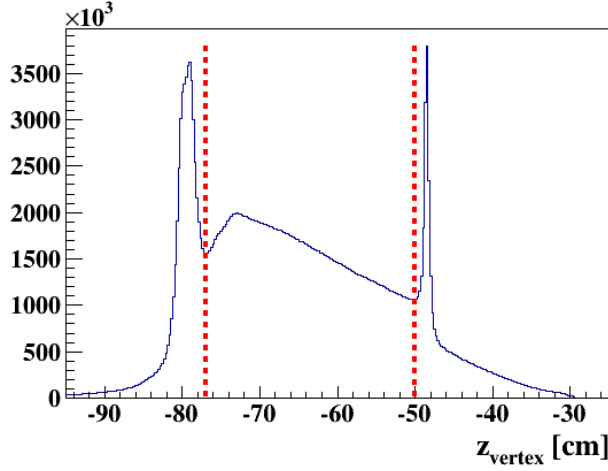


Figure 3.1: The reconstructed longitudinal vertex of the collected negative particles. The two dashed red lines represent the chosen cut, $-77 \text{ cm} < z_{\text{vertex}} < -50 \text{ cm}$, to eliminate the particles which originate from the windows and outside the target.

- Momentum cut ($p_{e^-} > 0.8 \text{ GeV}/c$): during the data acquisition, the EC threshold was set to 200 mV corresponding to electrons having a minimum momentum of about 0.7 GeV/c. In this analysis, we apply a conservative cut of 0.8 GeV/c to be above this threshold.
- Vertex cut: the target is centered at -64 cm with respect to the center of CLAS. Figure 3.1 shows the reconstructed z-vertices for the collected negative particles. One sees two sharp peaks corresponding to the two aluminum windows at the ends of the target. These particles have to be rejected as they originate from outside the target. As will be emphasized later, we need an accurate determination of the electron's vertex to ensure the correspondence between the final-state particles, which all have to originate from the same point.

Fiducial cuts

Some regions of CLAS have to be excluded from the analysis to ensure an accurate detection of the different particles. For instance, an electron that hits the edge of the EC will have only part of its electromagnetic shower contained within the detector. Also, the structure of the torus magnet divides CLAS into six separate sectors, which makes edge effects non-negligible. For this reason, the following set of fiducial cuts is applied:

- EC fiducial cut: each EC has a triangular shape with its three sides labelled as U,V and W. We apply a set of cuts ($60 \text{ cm} < U, V < 360 \text{ cm}, W < 390 \text{ cm}$) to reject the electrons which hit the EC close to the edges, as shown in figure 3.2.
- CC fiducial cut: in reference [21], G. Adams *et al.* have studied the efficiency of the CCs. They found that within the fiducial regions, which are defined by the edges of the CCs mirrors, the detection efficiency is stable and is around 98%. Outside the fiducial regions, the efficiency shows strong variations. In reference [31], M. Osipenko *et al.* have developed a coordinate system to represent the CC hits with respect to the center

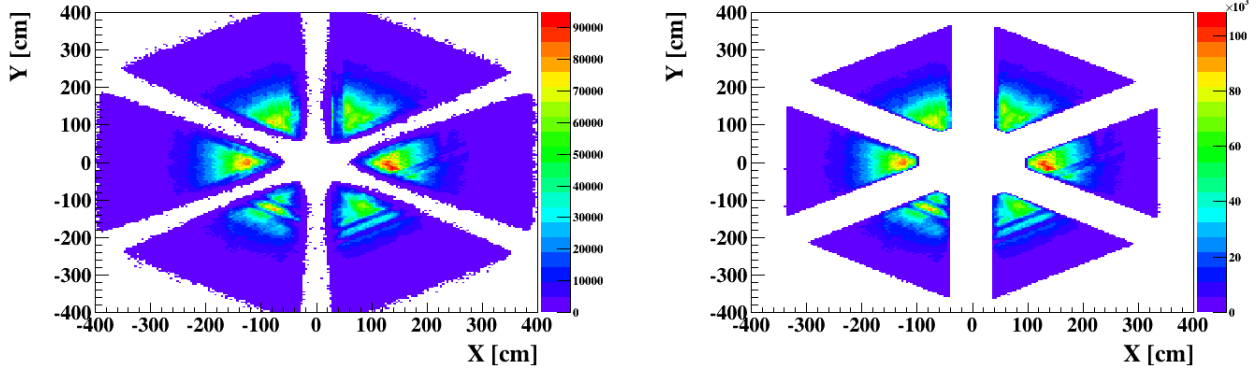


Figure 3.2: On the left: XY distribution for the negative particles in the EC before the U , V and W cuts. On the right: the same distribution is plotted after the cuts. X and Y are the coordinates in the EC with respect to the center of CLAS.

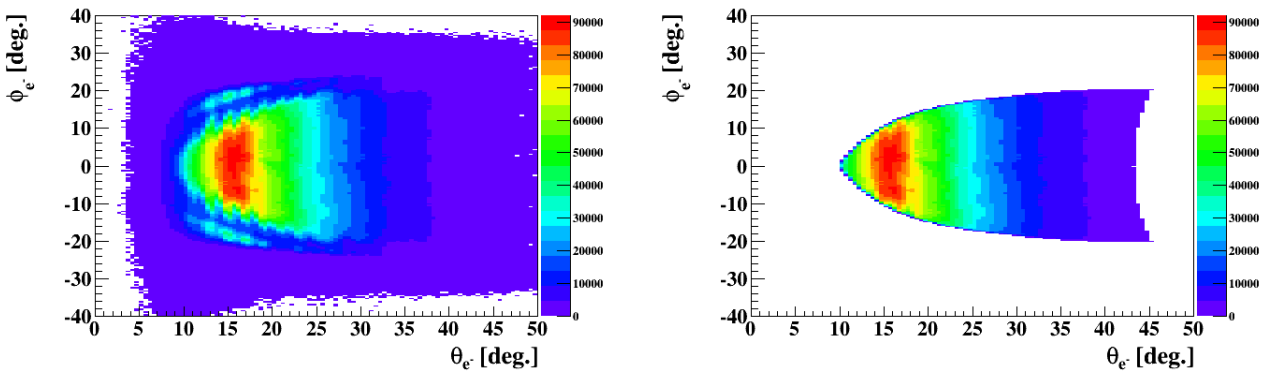


Figure 3.3: Azimuthal angle as a function of polar angle for the negative particles before (left) and after (right) applying the CC fiducial cut. The angles are calculated with respect to the center of each sector in CLAS.

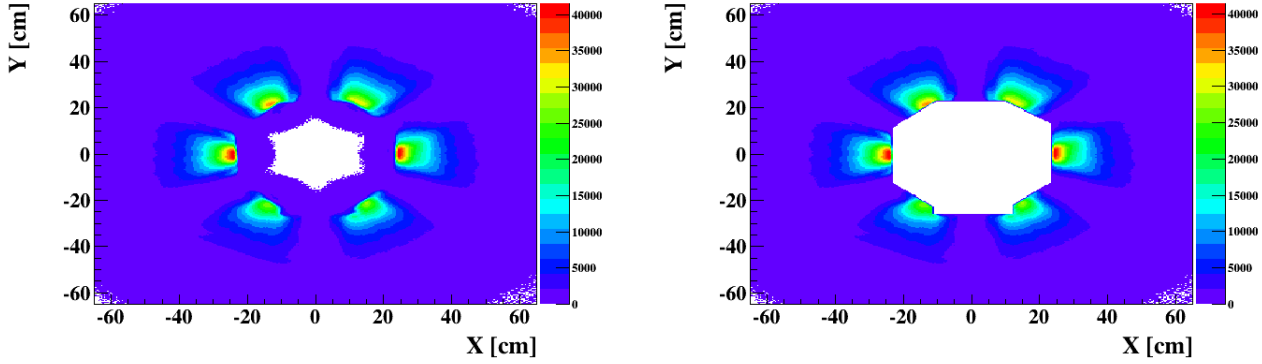


Figure 3.4: On the left: XY distribution for all the negative particles in the first region of the DC before applying the IC shadow cut. On the right: the same distribution after the cut.

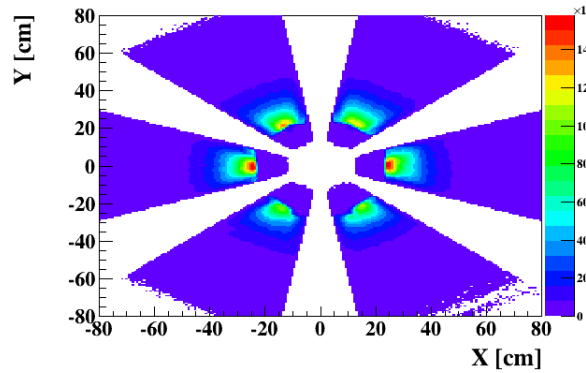


Figure 3.5: XY distribution for all the negative particles in DC1 after applying the DC fiducial cut.

of each sector in CLAS. In this frame, the CCs mirror edges can be defined as:

$$\begin{aligned} \phi_e = & -63.32792 + 11.05609 \cdot \theta_e - 0.6344957 \cdot \theta_e^2 + 1.873895 * 10^{-2} \cdot \theta_e^3 \\ & - 2.762131 * 10^{-2} \cdot \theta_e^4 + 1.604035 * 10^{-2} \cdot \theta_e^5. \end{aligned} \quad (3.1)$$

Based on these works, we reject all the hits located outside the mirror edges. Figure 3.3 shows an illustration of this cut.

- IC shadow cut: this cut originates from the location of the IC in front of the innermost part of the DCs. The electrons which are produced at polar angles lower than 14° will hit the IC. The left plot of figure 3.4 illustrates this effect, and the right plot shows the effect of the cut we apply.
- DC fiducial cut: the DCs have low detection efficiency at the edges because only part of the tracks are detected [20]. So we apply a fiducial cut to reject the particles at the edges. The left plot of figure 3.4 shows the XY distribution of all the negative particles in DC1. The result of applying the DC fiducial cut can be seen in figure 3.5.

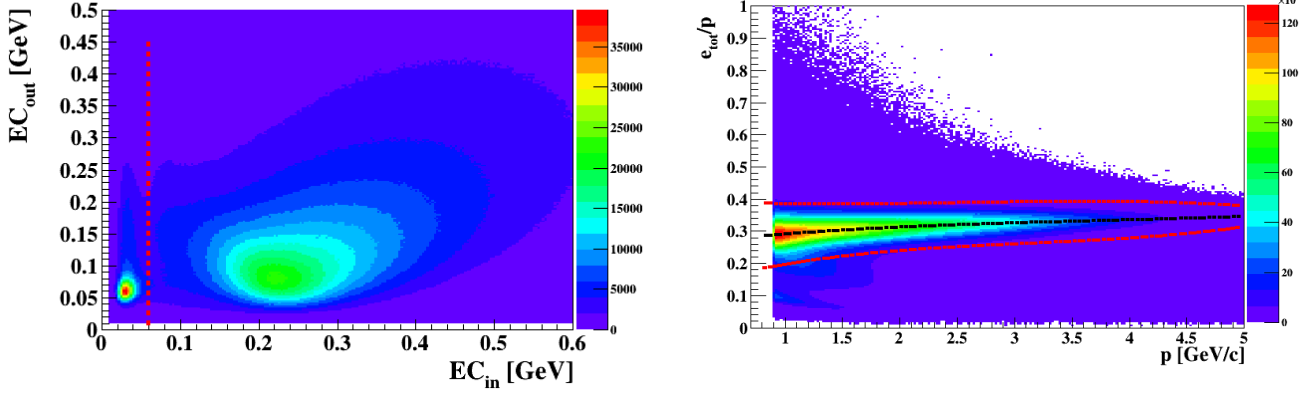


Figure 3.6: Deposited energies in the EC: E_{out} as a function of E_{in} . The dashed red line represents a 60 MeV cut on EC_{in} to reject the π^- s.

Figure 3.7: E_{tot}/p as a function of p . The black dashed line represents the mean value of E_{tot}/p as a function of p . The red dashed lines represent the 2.5σ cuts.

EC energy cuts

The Minimum Ionizing particles (MIPs), such as pions, deposit constant amounts of energy per distance while traversing the EC. In contrast, the showering particles, such as electrons and photons, deposit energies proportional to their momenta. We use two energy cuts to clean the electrons from the main contamination, i.e. π^- s.

- Minimum deposited energy: the inner and the outer parts of the EC have thicknesses 15 cm and 24 cm, respectively. The simulations show that pions deposit a constant energy amount of 2 MeV/cm, independently of their momenta. Figure 3.6 shows the deposited energy in the outer part of the EC (EC_{out}) as a function of the energy deposited in the inner part (EC_{in}), after the fiducial cuts. On the x-axis, one can see a clear region, around 30 MeV, that comes mainly from the negative pions, which deposit 2 MeV/cm along the 15 cm thickness of the inner EC. We use a cut of 60 MeV on EC_{in} to reject these particles.
- An additional cut, correlating the measured deposited energy and the momentum, is applied. Figure 3.7 shows the ratio of the total deposited energy in the ECs ($EC_{tot} = EC_{in} + EC_{out}$) to the momentum (p) as a function of p . One notices that EC_{tot}/p varies slightly with the momentum due to variations in the efficiencies of the DC and EC. We apply 2.5σ cuts around the mean (μ) to select the good electrons, using to the following parametrizations of the mean (μ) and the width (σ):

$$\mu(p) = 0.256084 + 0.0432374 \cdot p - 0.00914180 \cdot p^2 + 0.00081589 \cdot p^3 \quad (3.2)$$

$$\sigma(p) = 0.0572976 - 0.0272689 \cdot p + 0.008576 \cdot p^2 - 0.00097998 \cdot p^3 \quad (3.3)$$

CC cut

The Cherenkov counters have been designed to separate electrons from pions below 2.5 GeV/c momentum. In this region, the pions are not supposed to produce photoelectrons. However, low momentum δ -electrons can be produced from the diffusion of the pions in the Cherenkov gas. These δ -electrons produce a small number of photoelectrons. Figure 3.8

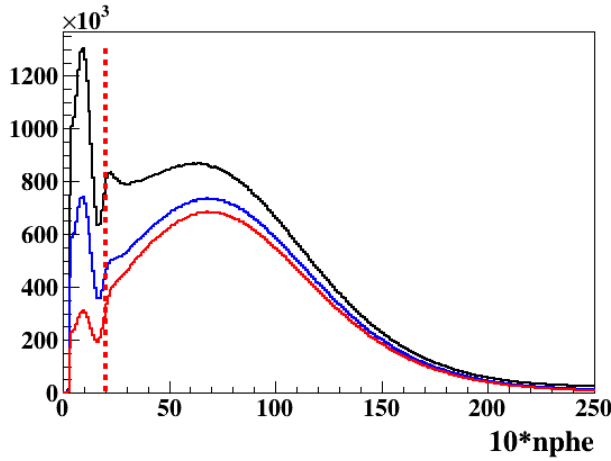


Figure 3.8: Distribution of number of photoelectrons emitted by negative particles in the CC ($nphe \cdot 10$). The black curve represents the distribution after the initial cuts, the blue curve is after the geometrical cuts and the red curve is after applying all the cuts including the EC energy cuts. The dashed red line represents the cut we apply ($nphe > 2$) to select the good electrons.

shows the distributions of the number of photoelectrons ($nphe$) produced by the negative particles for three different stages of the electron selection.

One sees from figure 3.8 that the single-photoelectron peak is strongly reduced after applying the energy cuts. We conclude that the particles causing the single-photoelectrons peak are linked to particles with low deposited energy in the EC_{in} , figure 3.6. We apply a final cut on the red distribution in figure 3.8 ($nphe > 2$), and we assume that the negative particles which pass all the previous requirements and produce more than 2 photoelectrons in the CC are good electrons.

3.1.2 Proton identification

Similarly to the electrons, the protons are affected by the geometry and the efficacy of the different sub-detectors of CLAS. The following conditions are applied to select the good protons.

- Coincidence with one and only one good electron.
- Initial track requirements: the positive charge of the proton results in bending its trajectory away from the beam line direction. Thus, a positive charge is required from the curvature of the track. Like for the electrons, the proton candidates must pass the two steps of the tracking in the DCs, have signal above the threshold in the SCs ($SC_{stat} > 0$) and originate from a vertex within the target ($-77 \text{ cm} < z_{vertex} < -50 \text{ cm}$).
- Fiducial cuts: the tracks of the protons detected close to the edges of the DC can only be partially reconstructed. As for the electrons, the protons which are recoiled at polar angles smaller than 14° hit the IC. We apply the previously presented (in section 3.1.1) DC and IC shadow fiducial cuts to avoid these effects. Figure 3.9 shows the XY projection in the DC1 for the collected positive particles which passed the initial track requirements, before and after these two fiducial cuts.

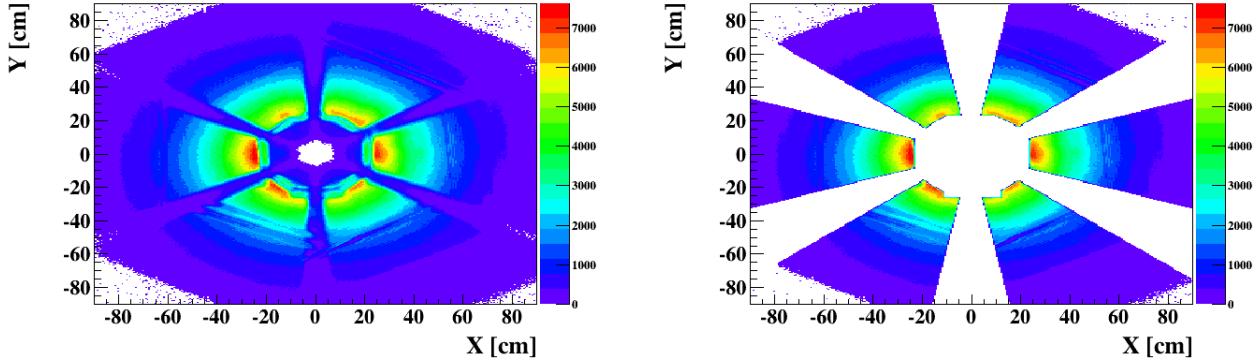


Figure 3.9: XY plane projection in DC1 for the positive particles before (left) and after (right) IC shadow and DC fiducial cuts.

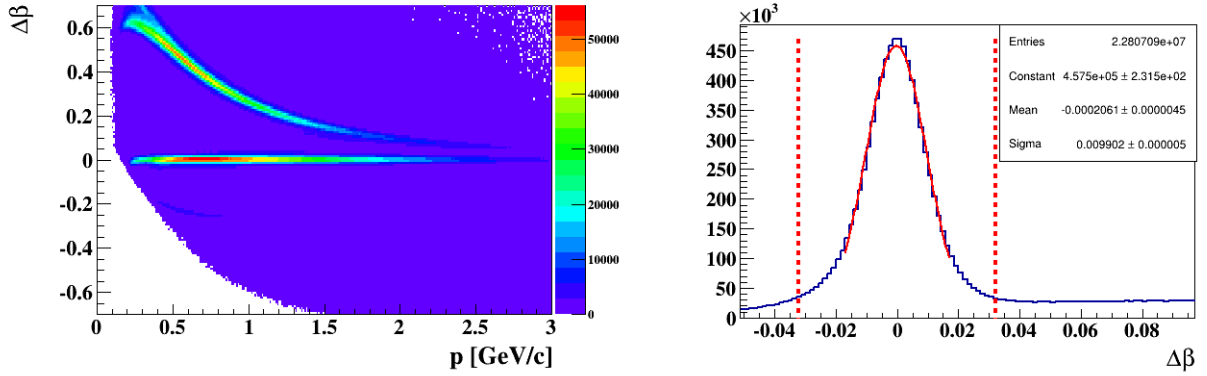


Figure 3.10: On the left: $\Delta\beta$ as a function of p for the detected positive particles after the fiducial cuts. On the right: one-dimensional distribution of $\Delta\beta$ zoomed in the region of the protons. The red dashed lines represent $\pm 3\sigma$ cuts around the mean to select good reconstructed protons.

- Velocity ($\Delta\beta$) cut: the previous cuts do not separate the protons from other positive particles, such as positive pions and kaons. A very clear separation can be obtained by associating the information from the SCs and the DCs. The velocity of a charged particle can be calculated by using the momentum (p) reconstructed in the DCs and the Time-Of-Flight (t_{TOF}) measured by the SCs. We define:

$$\Delta\beta = \beta_{SC} - \beta_{DC} = \frac{l_{track}}{c \cdot t_{TOF}} - \frac{p}{\sqrt{p^2 + m_p^2}}, \quad (3.4)$$

where l_{track} is the measured track length and m_p is the proton mass. On the left plot of figure 3.10, $\Delta\beta$ is plotted as function of momentum. One can see two main trends in this plot: the region around zero corresponds to the protons, while the one above corresponds to the positive pions (π^+). The right plot shows a one-dimensional distribution of $\Delta\beta$ zoomed in the region of the protons.

- Vertex matching: the last cut is the correspondence between the longitudinal vertices of the detected electron and proton. Figure 3.11 shows the difference $\Delta z = z_e - z_p$ and the chosen

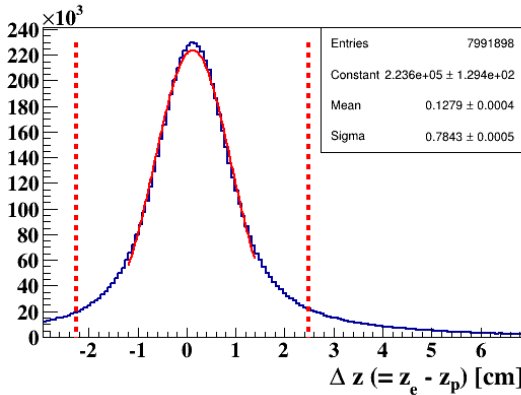


Figure 3.11: Δz distribution. The red dashed lines indicate $\pm 3\sigma$ cuts around the mean.

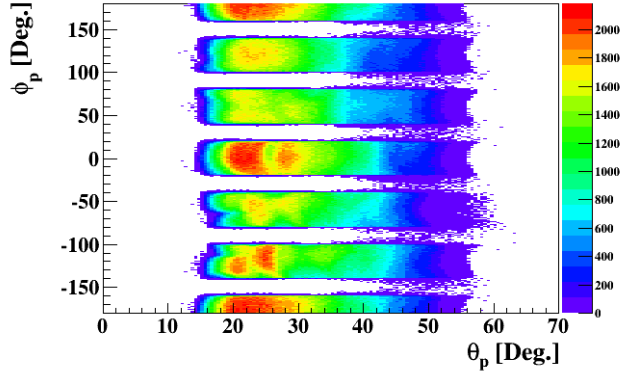


Figure 3.12: ϕ vs. θ for the selected protons.

cuts (red dashed lines).

Finally, figure 3.12 shows the azimuthal angle as a function of the polar angle distribution for the identified protons after all the selection cuts. One notices that the population of the protons is different from one sector to another, which comes from the dead regions in some sectors.

3.1.3 Photon identification

CLAS is equipped with two calorimeters that can detect photons: the IC, covering polar angles from 4° to 14° , and the EC, covering polar angles from 8° to 45° . Like for the other particles, in addition to the coincidence with one good electron, we require a set of criteria to ensure the quality of the detected photons. Due to the efficiency constraints in both calorimeters, we restrict the energy of the selected photons to be greater than 300 MeV. Further requirements are applied depending on each detector.

EC photons

A particle has to pass the following conditions in order to be considered a good photon:

- Neutral charge: this condition is achievable via the information from the drift chambers. A photon candidate in the EC must not be associated with a track in the DCs.
- EC fiducial cut: like for the electrons, this requirement is made to reject the photons which are detected at the edges of the EC. Figure 3.13 shows the XY plane distribution of EC neutral particles. We use the cuts: $100 \text{ cm} < U, V < 360 \text{ cm}$, and $W < 390 \text{ cm}$, to select the EC photons.
- Velocity (β) cut: the scattered electron and its associated photon originate from the same vertex. Knowing the electron vertex (\vec{V}_e) and the photon hit position in the EC (\vec{R}_γ), one can calculate the photon velocity β as:

$$\beta_\gamma = \frac{l}{ct} = \frac{|\vec{R}_\gamma - \vec{V}_e|}{c(t_{EC} - t_{trg})} \quad (3.5)$$

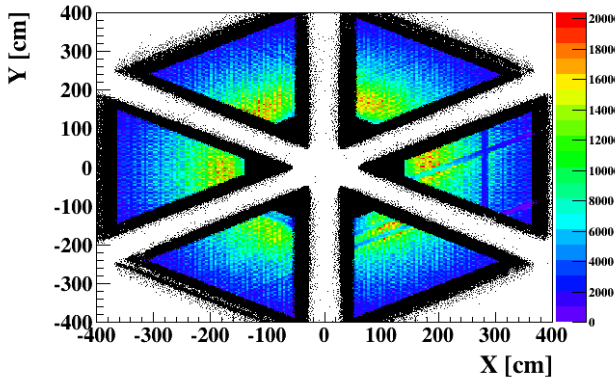


Figure 3.13: XY projection of the neutral particles in the EC. The coloured regions represent photons which passed the EC fiducial cuts, while the black regions are out of the fiducial cuts.

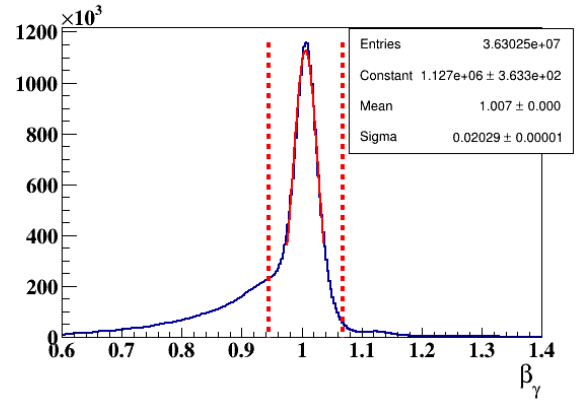


Figure 3.14: β distribution of neutral particles in the EC. The two vertical lines represent $\pm 3\sigma$ cuts around $\beta = 1$ to select photons.

where l is the traveled distance from the vertex to the hit point in the EC. The traveling time (t) is calculable from the relative difference between the trigger time (t_{trg}) and the EC timing (t_{EC}). Figure 3.14 shows the β distribution of the neutral particles in the EC.

IC photons

For IC photons, we use the following cuts:

- IC fiducial cuts: the photons which hit the edges of the IC deposit only part of their energies within the calorimeter. For this reason, we reject the photons which hit the innermost or the outermost rings of the IC. Figure 3.15 illustrates this cut [33].
- Møller electrons reduction: a two-dimensional plot of photon polar angles as a function of the energy shows an overcrowded region at low θ and low energy. This can be seen in figure 3.16. This region is mostly populated by the Møller electrons and must be excluded from the analysis. We optimized a linear cut for this region, shown by the black dashed line. The vertical extension of this line shows the minimum energy cut ($E_\gamma > 300$ MeV).
- We do not apply any timing cut to select the photons in the IC because its timing is not functioning properly for certain channels. Therefore, applying a timing cut would add inefficient regions in the detector that we wanted to avoid. Therefore, we rely mainly on exclusivity cuts to remove any potential contamination.

To summarize the photon selection, the two-dimensional distribution of azimuthal angle as a function of polar angle for IC and EC photons is shown in figure 3.17.

3.1.4 Helium-4 identification

Details on the RTPC's structure and the definition of the different variables were given in chapter 2, section 2. In the following, we show the cuts to select the RTPC good tracks with a 6-GeV beam energy. The distributions will be shown for the two independent modules of the RTPC separately, labelled as left and right sides. The cuts are:

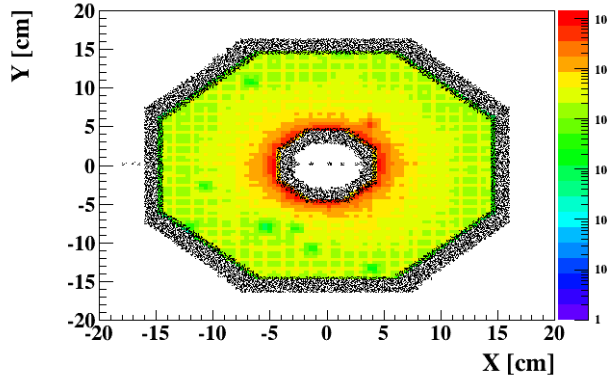


Figure 3.15: XY distribution for the IC photons. The photons which hit the black innermost and outer regions are excluded from this analysis.

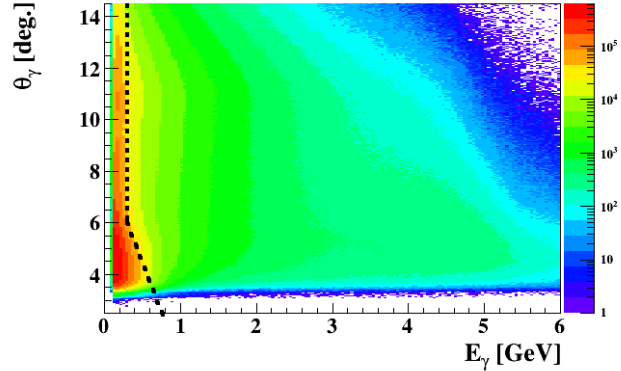


Figure 3.16: θ versus E for the IC photons which passed the fiducial cuts. The black dashed line represents the cut to reject the Møller electrons.

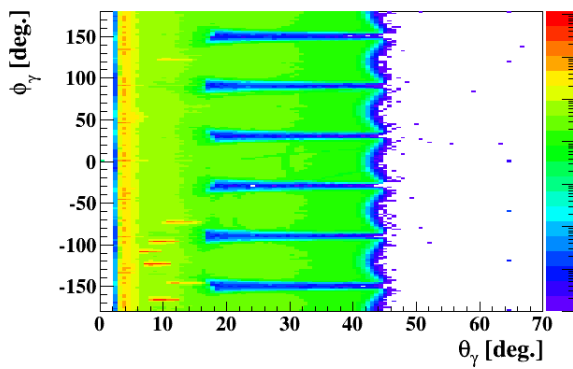
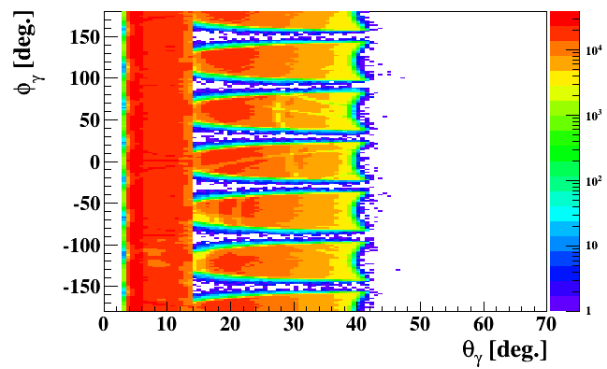


Figure 3.17: On the left: ϕ versus θ for all the neutral particles before the cuts. On the right: ϕ vs. θ for the selected photons.



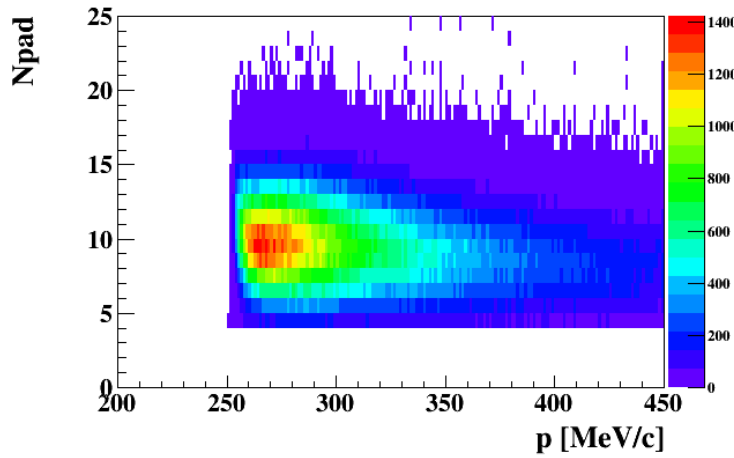


Figure 3.18: The number of active pads versus the measured p for the good tracks collected using 6 GeV electron beam energy.

- Coincidence with one and only one good electron.
- Number of active pads greater than 3: the track has to have recorded hits from at least four different readout pads. Figure 3.18 shows the distribution of the number of active pads as a function of the total momentum measured in the RTPC for the identified good tracks using 6 GeV electron beam energy.
- Positive radius of curvature.
- Vertex cut: figure 3.19 shows the z-vertices of the positive-curvature tracks.
- Track helix-fit quality: figure 3.20 shows the χ^2 distributions for the positive tracks originating within the RTPC. We apply $\chi^2 < 3.0$ to select good ${}^4\text{He}$ tracks.
- *sdist* and *edist* cuts: figures 3.21 and 3.22 show the *sdist* and *edist* distributions, for the positive tracks, originated within the RTPC, and having good χ^2 values.
- Z-vertex cut: like for the protons, the RTPC's reconstructed track has to originate from the same electron vertex. Figure 3.23 shows the difference between the z of the reconstructed vertices of the electron and the associated RTPC tracks.
- Fiducial cuts: Figure 3.24 illustrates the effect of the fiducial cuts we apply on the azimuthal angles.
- In this work, due to the wide bands in dEdx distributions, we do not use this quantity to select the recoil ${}^4\text{He}$ nuclei. We claim that the kinematic exclusivity cuts, that are presented in chapter 4, are sufficient to select coherent ${}^4\text{He}$ DVCS events. A systematic check about this question is presented in chapter 4.

3.1.5 π^0 identification

In this analysis, we identify the π^0 's with the goal of DVCS background subtraction as will be addressed in section 4.5. The π^0 identification is based on its two real photons decay mode ($\pi^0 \rightarrow$

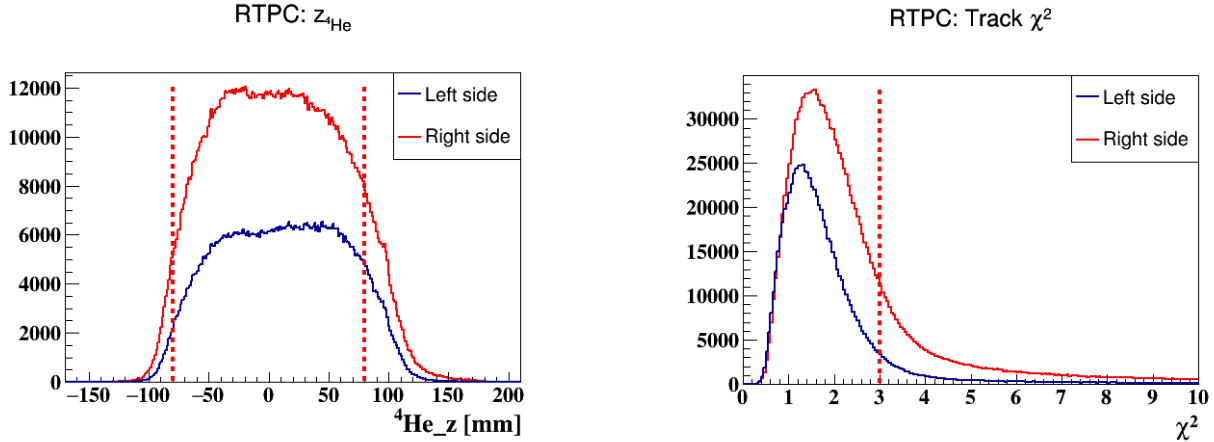


Figure 3.19: z -vertices for the reconstructed positive tracks with respect to the RTPC center (-64 cm with respect to the CLAS center), in the two modules of the RTPC. We chose the cut $-80 \text{ mm} < z < 80 \text{ mm}$ to select good tracks.

Figure 3.20: χ^2 distribution for the tracks in the two modules of the RTPC, with the cut we require to select good tracks: $\chi^2 < 3$.

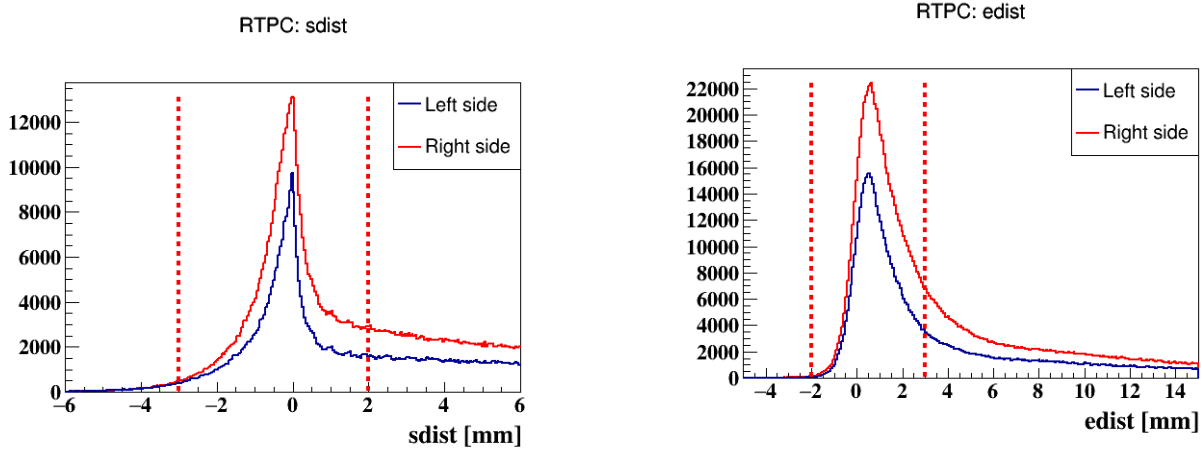


Figure 3.21: $sdist$ distribution for the positive tracks in the RTPC. $-3 < sdist < 2.0 \text{ mm}$ cut is applied to select good tracks.

Figure 3.22: $edist$ distribution for the positive tracks in the RTPC. We require $-2.0 \text{ mm} < edist < 3.0 \text{ mm}$ to select good tracks.

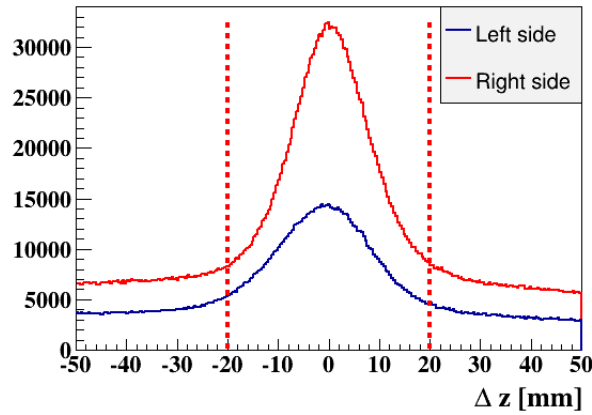


Figure 3.23: The correspondence between the z-vertices of the detected electron and the good track in the RTPC. We require the absolute value of Δz to be less than 20 mm.

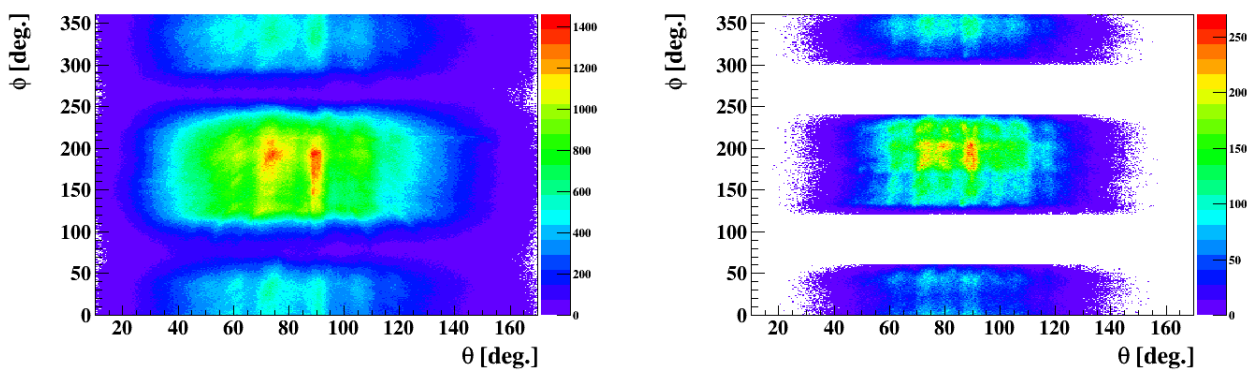


Figure 3.24: On the left: ϕ vs. θ for the positive-curvature tracks in the RTPC before the cuts. On the right: the same distribution after all the cuts.

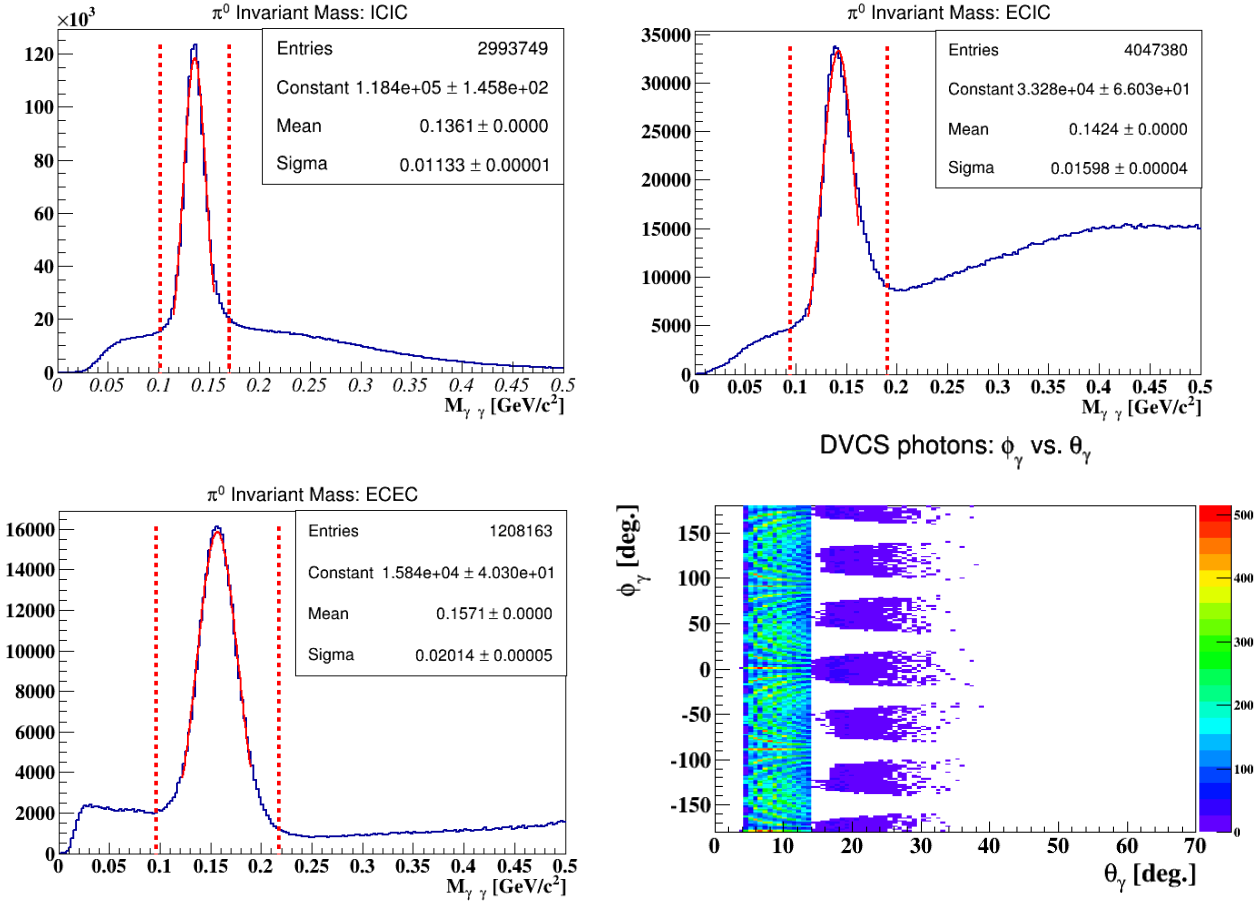


Figure 3.25: The reconstructed invariant mass of the photon pairs in the three topologies: ICIC, ECIC and ECEC. On the bottom-right: ϕ vs. θ distribution for the simulated DVCS photons, shown that most of the DVCS photons are located in the IC.

$\gamma\gamma$), with a branching ratio around 98.8%. In our experimental configuration, the reconstructed neutral pions can be categorized into three topologies: ICIC (the two photons are detected in the IC), ICEC (one photon in the IC and the second in the EC), and ECEC (the two photons are detected in the EC). The nominal mass of the π^0 is 0.135 GeV/c². The reconstructed invariant mass of the detected pair of photons can be seen in figure 3.25, for the three topologies. One can see clear peaks corresponding to the neutral pions in the three distributions.

One can conclude from the mean and sigma values of the distributions in figure 3.25 that the IC has a better energy resolution than the EC. About 97% of the simulated DVCS events, as can be seen in the bottom-right plot, have the real photon emitted at very forward angles covered by IC. For these reasons, we chose to exclude the DVCS events which have their photons in the EC. Hence we are left with the two π^0 topologies, ICIC and ICEC, for the background subtraction as will be addressed later in this chapter.

3.2 Simulation

The Monte-Carlo simulation is used in this analysis for two goals: understanding the behaviour of the particles of interest in the detectors, and computing the acceptance for the DVCS background subtraction. The key stages of the simulation are summarized in figure 3.26: Monte-Carlo generated events pass in a GEANT3 simulation (GSIM) for the CLAS detector, then are processed

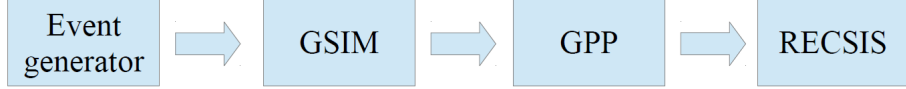


Figure 3.26: The scheme shows the main simulation steps.

Parameter	$e^4He\gamma$	$e^4He\pi^0$	$ep\gamma$	$ep\pi^0$
Q_0^2	$1.0 \text{ GeV}^2/\text{c}^2$	$1.0 \text{ GeV}^2/\text{c}^2$	$1.0 \text{ GeV}^2/\text{c}^2$	$1.0 \text{ GeV}^2/\text{c}^2$
α	2.5	3.0	1.5	1.5
b	$-11.0 \text{ GeV}^2/\text{c}^2$	$-8.8 \text{ GeV}^2/\text{c}^2$	$-1.408 \text{ GeV}^2/\text{c}^2$	$-1.408 \text{ GeV}^2/\text{c}^2$
β	12.0	7.3	4.0	1.5
x_c	0.2	0.3	0.2	0.5
c	0.2	0.3	0.2	0.5
d	0.4	0	0.4	0

Table 3.1: Values of the parameters adapted in our event generator.

with a package called GPP to add resolution and efficiency effects, and finally are reconstructed by a package named RECSIS, from which we obtain the physical quantities of each particle, like it is done for real data. In the following, each simulation stage will be briefly presented.

3.2.1 Event generator

Events are generated in the measured ranges of Q^2 , x_B , t , and ϕ following a parametrization of the cross section which roughly reproduces the DVCS and exclusive π^0 electroproduction data [33]:

$$\frac{d^4\sigma}{dQ^2dx_Bdt d\phi} \propto \left(\frac{Q_0^2}{Q^2}\right)^\alpha * \frac{1}{1 + (\frac{x_B - x_c}{c})^2} * \frac{1}{(1 + bt)^\beta} * (1 - d(1 - \cos(\phi))). \quad (3.6)$$

This parametrization is the product of four factors which reproduce the DVCS and π^0 , characteristics as follows:

- the Q^2 -dependent term accounts for the depth of the interaction: Q_0^2 is the minimum allowed value and the α is a parameter which controls the shape of the distribution.
- the x_B term accounts for the dependence of the cross section on the parton distribution functions, with x_c the mean value of the Bjorken variable x_B .
- the t term accounts for the t-dependence of the elastic form factors of the helium and of the proton, via the parameters b and β .
- the ϕ term accounts for the cross section dependence on this angle, via the parameter d . The DVCS and the BH have a different behaviour than the π^0 exclusive events.

Table 3.1 shows the values of the parameters used for the cross section parametrization of the four channels of interest: $e^4He\gamma$, $e^4He\pi^0$, $ep\gamma$, and $ep\pi^0$.

Regarding the protons in $ep\gamma$ and $ep\pi^0$ channels, we apply the Fermi motion on the initial protons based on the parametrization of C. Ciofi degli Atii and S. Simula [34]. Figure 3.27 shows the Fermi momentum distributions of the nucleons inside 4He , where we apply a cut on the high-momentum tail at 0.3 GeV/c, higher momentum should not contribute to the final DVCS sample because of our exclusive cuts presented in the following chapter.

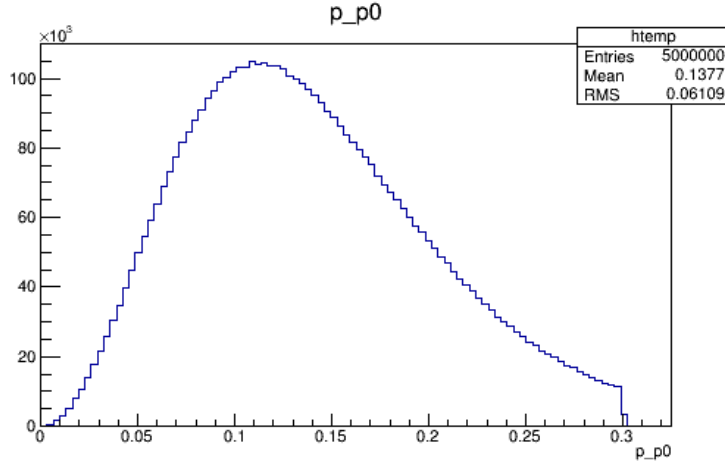


Figure 3.27: Fermi momentum distribution of the nucleons inside ${}^4\text{He}$, in GeV/c .

3.2.2 GSIM

GSIM is a GEANT3-based simulation of the CLAS detector, developed by the CLAS collaboration [35]. This simulation takes into account all the experimental environment, such as the target's position, materials, and geometry, and also the various sub-detectors' materials and geometries, to reproduce the behaviour of particles traversing the detector. *Nota Bene* the reconstruction in the RTPC is not implemented in GSIM, however its material is present.

3.2.3 GPP

For the purpose of making the simulation more realistic, the output of GSIM is fed to the GSIM Post-Processing (GPP) package. This package applies resolution effects on the different measured quantities, and also reads efficiency maps to match the simulation to the real experiment. The resolutions are categorized into three groups, time, position, and energy resolution. In the following, we present the techniques used in this work to extract the smearing factors for the simulation.

SC time smearing

The GPP takes a single factor to smear the time in a Gaussian form. Figure 3.28 shows an illustration of the time smearing effects, in which $\Delta\beta$ for the protons ($\Delta\beta = \beta_{\text{measured}} - \beta_{\text{calculated}}$) is compared for data and simulation. The chosen SC smearing factor is 2.1.

DCs position smearing

The GPP uses three factors to smear the positions of the hits in the DCs, in a Gaussian form. These smearing factors are extracted from comparing simulation to data in terms of the Time-Based Tracking (TBT) residual distributions, i.e. the deviation of the hits in the DCs from the fitted track. Figure 3.29 shows the experimental, initial simulated, and smeared simulated residual distributions for the collected good electrons and protons. The extracted smearing factors are: $(a, b, c) = (1.1, 0.85, 1.1)$, where the factor a stands for smearing of DC1, b for DC2, and c for DC3. One can see the smearing effects by looking to the values of σ from the fit in each Super-Layer (SL). We conclude that these factors match the simulation to the data.

IC energy smearing

An energy smearing for the IC photons is also needed. The GPP software uses three factors to

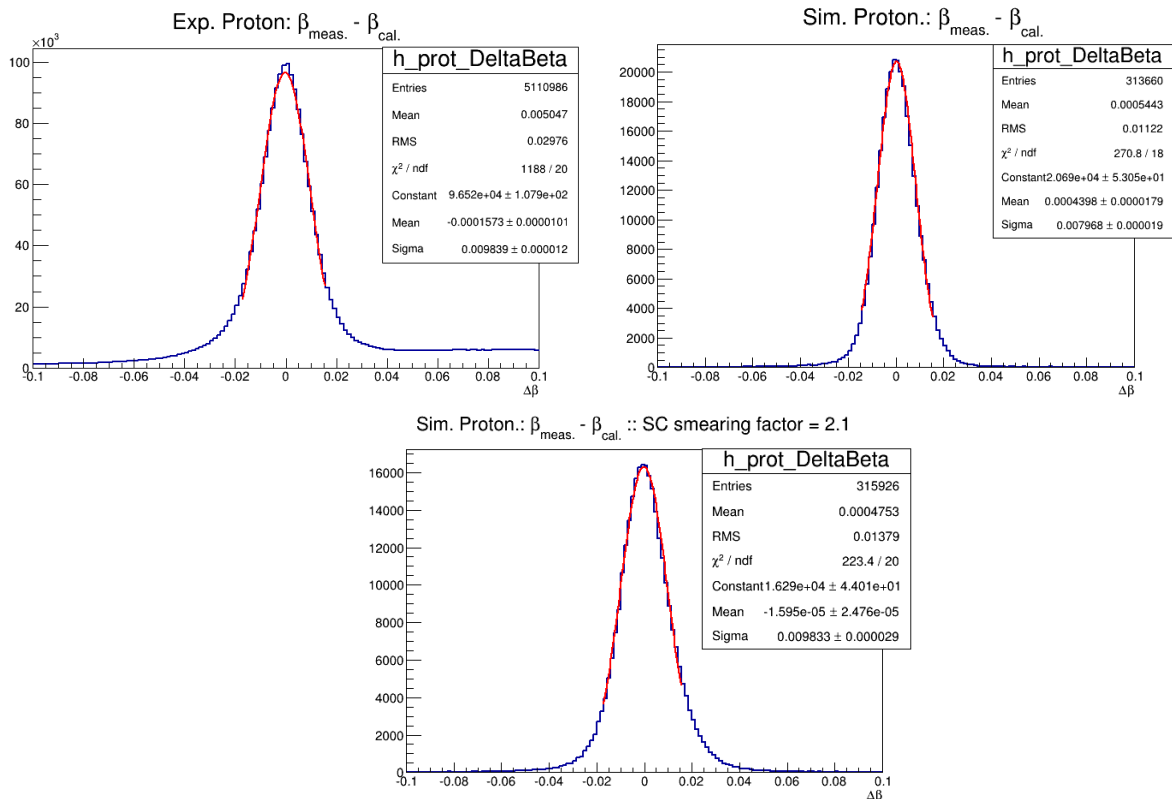


Figure 3.28: Illustration of the SC time smearing via the $\Delta\beta$ distributions for the protons. On the top left: $\Delta\beta$ distribution of the experimental data. On the top right: the simulated data without smearing. On the bottom: the simulated data after SC time smearing with a factor equal to 2.1.

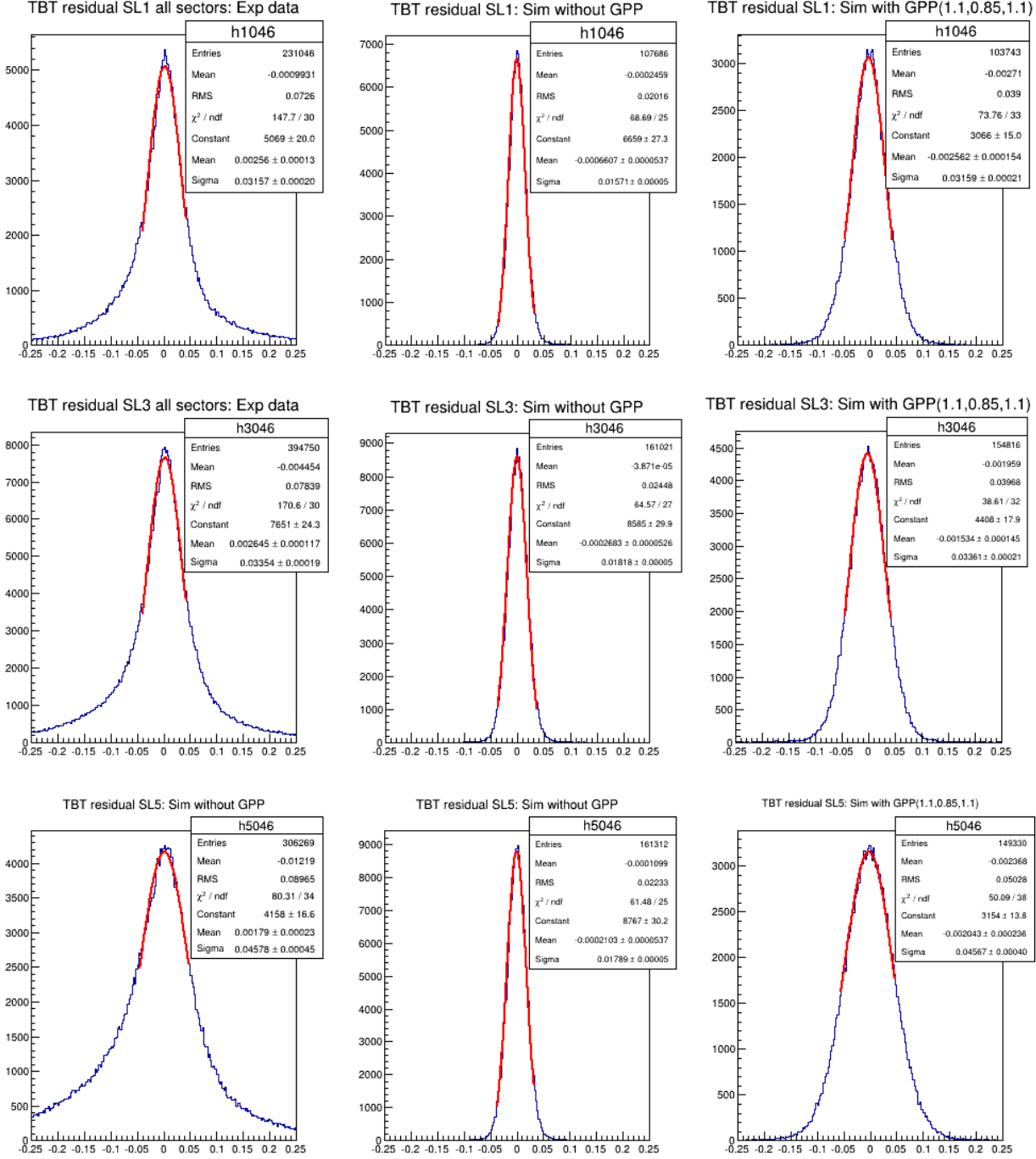


Figure 3.29: Time-Based Tracking (TBT) residual distributions for the electrons and the protons in the first super-layer (top panel), the second super-layer (middle panel) and the third super-layer (bottom panel) of the experimental data (first column), of the simulation without GPP (second column), and the simulation with GPP DC-position smearing factors: 1.1, 0.85, and 1.1 for a , b , and c respectively.

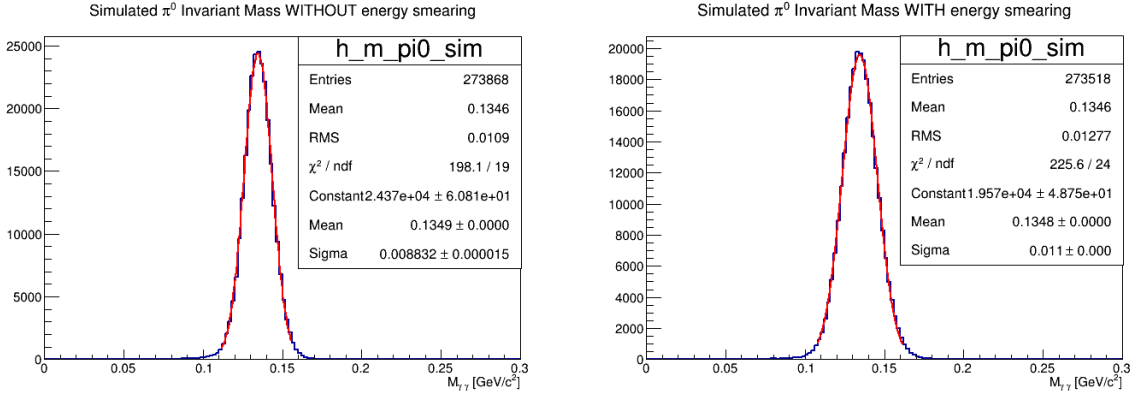


Figure 3.30: The invariant mass of the Monte-Carlo simulated π^0 without IC energy smearing, on the left, and with smearing, on the right.

perform this smearing: *ic_a*, *ic_b*, and *ic_c*, where *ic_a* accounts for the smearing of the width of the noise around zero using a Gaussian, while *ic_b* and *ic_c* are the smearing factors for the ADC values, using Gaussians as well. Our parameters are: 0.008, 0.036, and 0.024 respectively. Figure 3.30 shows the effect of these smearing factors on the simulated invariant mass of the π^0 . The associated experimental distribution can be seen on the top left plot of figure 3.25. One notices that the smeared width of the simulated distribution matches the measured experimental one.

3.2.4 RECSIS

RECSIS is the reconstruction package of CLAS which is used for both data and simulation. The detector responses, in terms of ADCs and TDCs, are converted by RECSIS into physical meaningful physical quantities, such as momentum, using lookup tables. In this process, the thresholds on the different detectors (DCs, CCs, ECs, SCs, IC, and RTPC) are applied to filter the signals before the reconstruction procedures. After this reconstruction, the outputs of RECSIS for the experimental and the simulated events can be compared directly, as will be presented in the next section.

3.2.5 RTPC fastmc

All the sub-detectors of CLAS are implemented in the GSIM GEANT3 simulation, however the RTPC is only there as dead material. As it is a more recent detector it has been fully simulated using a stand alone GEANT4 simulation. As a first step, we replace this RTPC's simulation by a fast Monte-Carlo (fastmc) package at the level of the event generator to make the simulated ${}^4\text{He}$ more realistic and matching the data. This fastmc smears the ${}^4\text{He}$ kinematics and applies the RTPC's acceptance. Regarding the smearing, the momentum, polar angle, azimuthal angle and z-vertex of the ${}^4\text{He}$ are smeared with Gaussians using the observed tracking resolutions of the RTPC (see chapter 2, section 3). For the acceptance, the fastmc:

- ensures that the ${}^4\text{He}$ track intersects the cathode and the gems of the RTPC.
- removes the tracks which pass in the dead area between the two modules of the RTPC.
- removes the track if it goes to the upstream end of the target's holder.
- applies the RTPC's thresholds on the momentum and the polar angle.

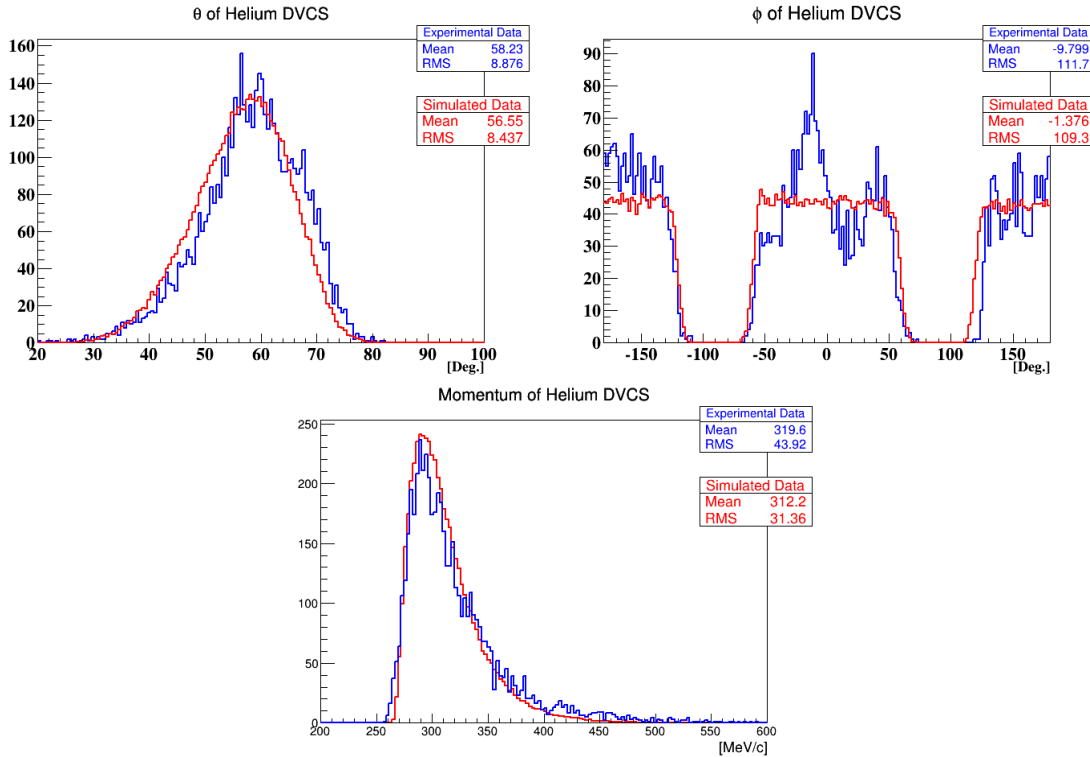


Figure 3.31: Comparison between experimental (blue) and simulated (red) DVCS ${}^4\text{He}$ nuclei in terms of polar angle, azimuthal angle and momentum.

The fastmc is applied to the Monte-Carlo generated ${}^4\text{He}$ for the channels $e^4\text{He}\gamma$ and $e^4\text{He}\pi^0$. We do not specifically apply energy loss and multiple scattering in our fastmc, but we do apply resolution effects based on experimental data that include both effects. The plots in figure 3.31 show the comparison between data and simulation in terms of θ , ϕ and momentum of the ${}^4\text{He}$ DVCS nuclei, that will presented in details in the following chapter. The other particles, (e^- , p , γ), are fed to GSIM through the previously mentioned simulation-reconstruction chain procedures.

3.3 Kinematic Corrections

The simulation enables us to extract kinematic corrections for the different particles, by comparing the reconstructed physical quantities from the simulation to the initially generated ones. In general, the reconstructed azimuthal angles of all the particles are consistent with the generated ones, while the reconstructed polar angles and momenta show some deviations. Therefore, corrections are required. In the following, the electron and the proton corrections are applied on both data and simulation, while the simulated photons are corrected differently from the experimental ones, as will be explained and justified.

3.3.1 Electrons

The reconstructed kinematics of the simulated electrons are roughly consistent with the generated quantities, as can be seen in figure 3.32. Nevertheless, we extracted and applied corrections on the electrons to achieve a higher precision. The corrected polar angles and momenta take the

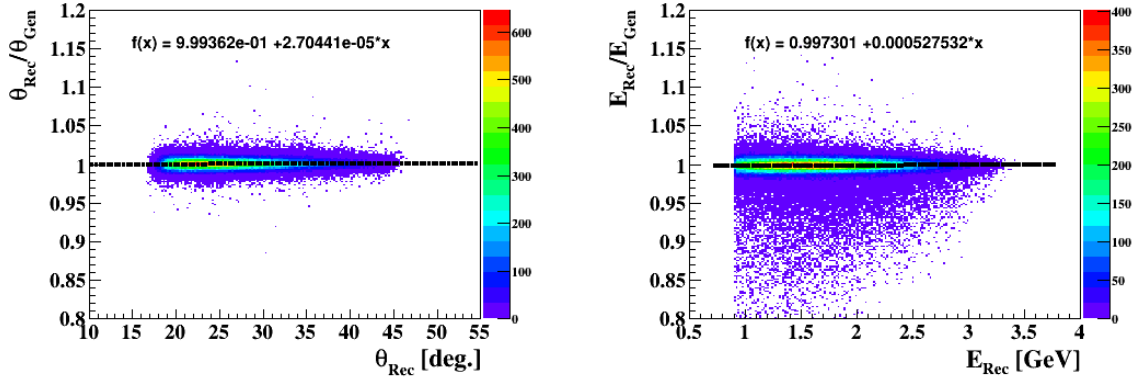


Figure 3.32: Electron corrections. On the left: The ratio of the reconstructed to the generated electron polar angles is plotted as a function of the reconstructed polar angle. The mean of the distribution is parametrized by the black curve. On the right: the momentum ratio (Rec/Gen) is plotted as a function of the reconstructed momentum and parametrized by the black curve .

form:

$$\theta_{corr.} = \frac{\theta_{rec.}}{f(\theta_{rec.})} \quad p_{corr.} = \frac{p_{rec.}}{f(p_{rec.})} \quad (3.7)$$

where $f(\theta_{Rec.})$ and $f(p_{Rec.})$ are the functions shown, respectively, on the left and right plots of figure 3.32.

3.3.2 Protons

The same procedures for the extraction of the kinematic corrections of the electrons have been carried out for the protons. The results can be seen in figure 3.33. The corrected polar angles and momenta are obtained using equations 3.7 and the functions shown on each plot of figure 3.33.

3.3.3 IC photons in simulation

The simulated IC photons shows non-negligible polar angle and energy deviations from the expected kinematics. This can be seen in figure 3.34. These deviations are almost systematic shifts, in which the polar angle deviation might be coming from badly defined geometrical values within GSIM. For these photons, we followed the same techniques of comparing the reconstructed quantities to the generated ones in order to extract the correction functions.

As an illustration of the corrections, figure 3.35 shows the squared $e\gamma X$ missing mass distribution for the simulated $ep\gamma$ DVCS events before the corrections, on the left, and after the corrections, on the right. In this configuration, the missing particle is the proton, such that the expected mean value should be the mass squared of the proton ($0.938^2 = 0.8798$). The right value is obtained after the corrections.

3.3.4 IC photons in real data

For the experimental IC photons, we used the reconstructed invariant mass of the π^0 in the ICIC topology to ensure the consistency of the IC calibration over the acceptance of the detector and the experimental running time. In this investigation, we require each π^0 photon to have a minimum energy of 500 MeV in order to avoid low efficiency effects of the IC.

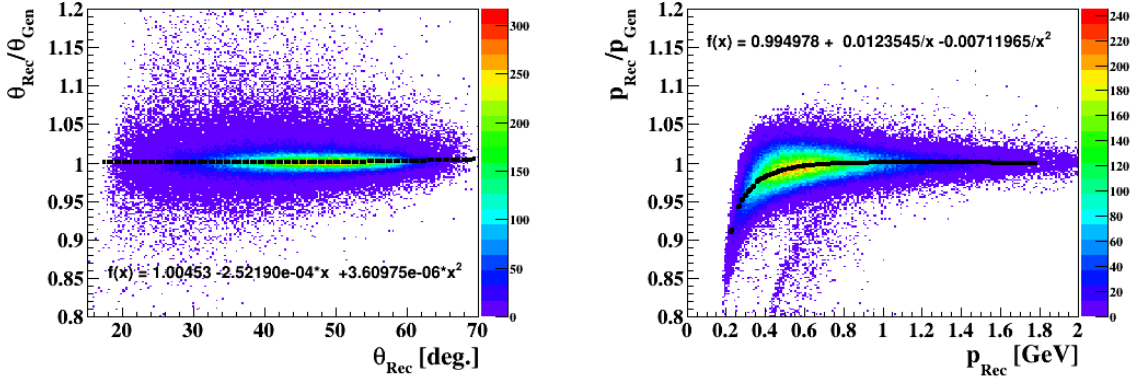


Figure 3.33: Proton corrections. On the left: the reconstructed-generated polar angle ratio is plotted as a function of the reconstructed angle and fitted with the black curve. On the right: the momentum ratio is plotted as a function of the reconstructed momentum.

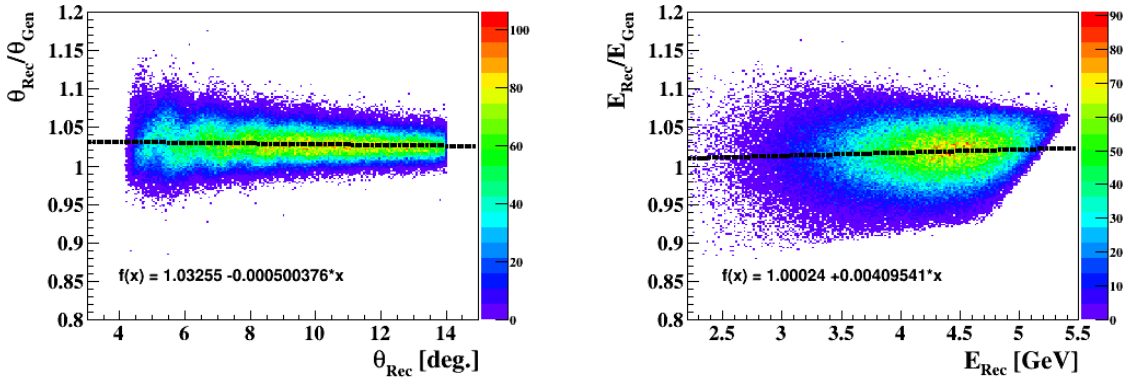


Figure 3.34: Corrections for the simulated IC photons. On the left: the reconstructed-generated polar angle's ratio is plotted as a function of the reconstructed polar angles. On the right: the energy ratio is plotted.

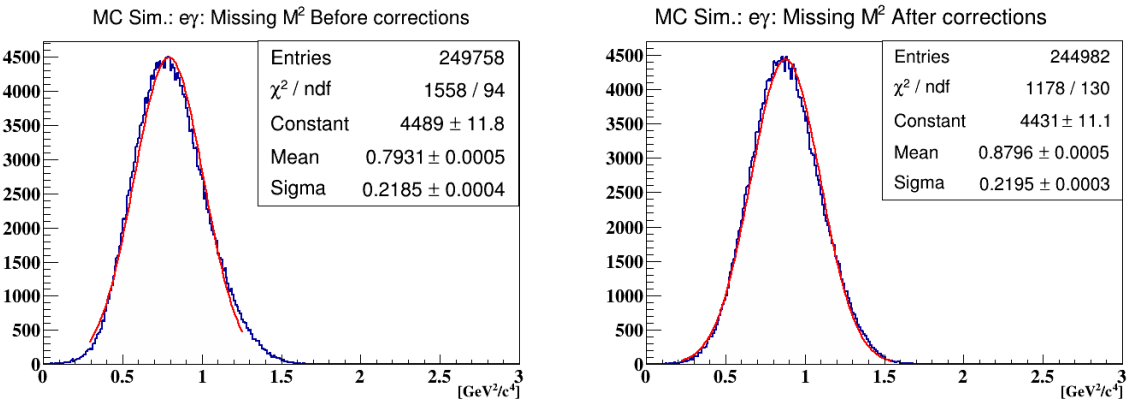


Figure 3.35: An illustration of the corrections in terms of the squared $e\gamma X$ missing mass distribution for the $e\gamma\gamma$ simulated DVCS events.

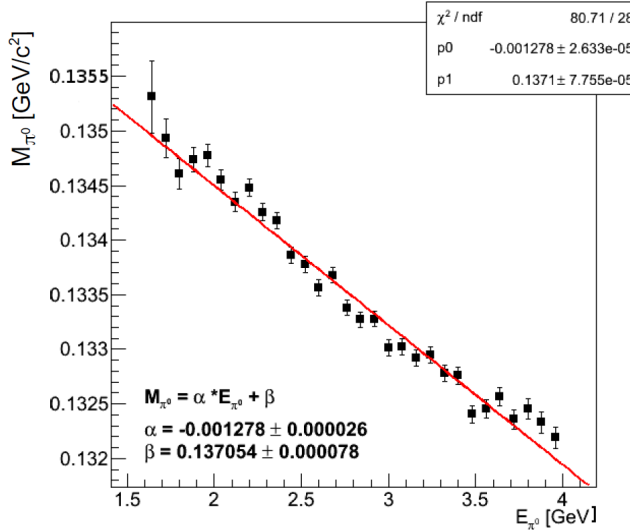


Figure 3.36: The invariant mass of the reconstructed π^0 as a function of its energy. The red line represents a linear fit.

3.3.4.1 Run-dependent energy correction

In the CLAS-EG6 experiment, the reconstructed mass of the π^0 displays a linear dependence on the energy, as can be seen in figure 3.36. In order to ensure the consistency of the calibration over time, we extracted this mass-energy dependence for the individual runs. Figure 3.37 shows the extracted slope (α) and offset (β), from the linear fits of the mass versus the energy of π^0 , as a function of run number. One notices a non-negligible variation over the experimental running period due to changes in the experimental conditions, such as changes in trigger requirements and beam position.

To extract energy corrections for IC photons, the two distributions of figure 3.37 have been parametrized by piecewise functions of the form:

$$\alpha(x) = c_0 + c_2 \left[e^{-c_3(x-c_1)} - e^{-c_4(x-c_1)} \right], \quad (3.8)$$

$$\beta(x) = p_0 + p_2 \left[e^{-p_3(x-p_1)} - e^{-p_4(x-p_1)} \right], \quad (3.9)$$

where the values of the parameters of α and β can be found in Appendix C (tables C.1 and C.2 respectively). The requirement of a 500 MeV maximum difference between the two photons allows to assume that the two photons have approximately the same energy ($E_{\pi^0} = 2E_\gamma$). Then, the correction take the form:

$$\frac{E_{corr}^{\pi^0}}{M_{Theoretical}^{\pi^0} = 0.135 GeV} = \frac{E_{uncorr}^{\pi^0}}{M_{uncorr}^{\pi^0}} \quad (3.10)$$

$$\implies E_{corr}^\gamma = \frac{0.135 * E_{uncorr}^\gamma}{\alpha(run) * 2 * E_{uncorr}^\gamma + \beta(run)} \quad (3.11)$$

which takes as input the measured uncorrected photon energy (E_{uncorr}^γ), and the α and β parameters, which depend on the run number. It then returns the corrected energy (E_{corr}^γ).

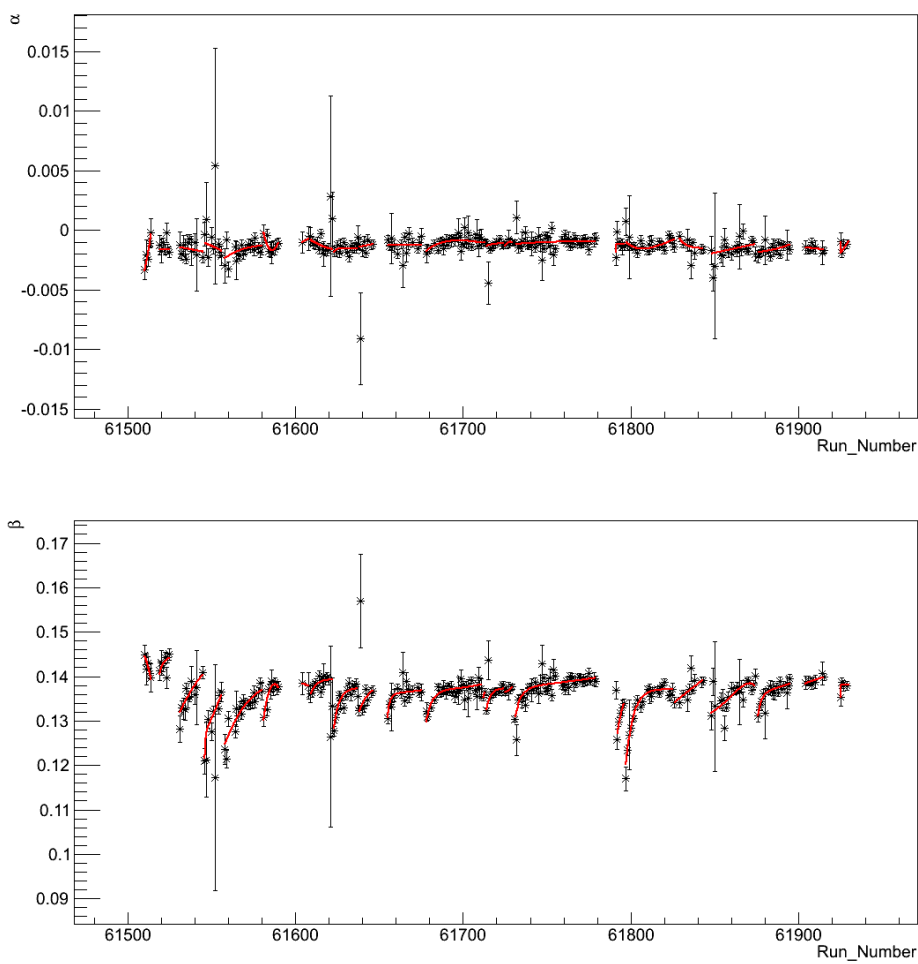


Figure 3.37: The slope (α) and the offset (β) from linear fits of M_π^0 vs. E_π^0 , as a function of run number. The red lines represent the fitting functions.

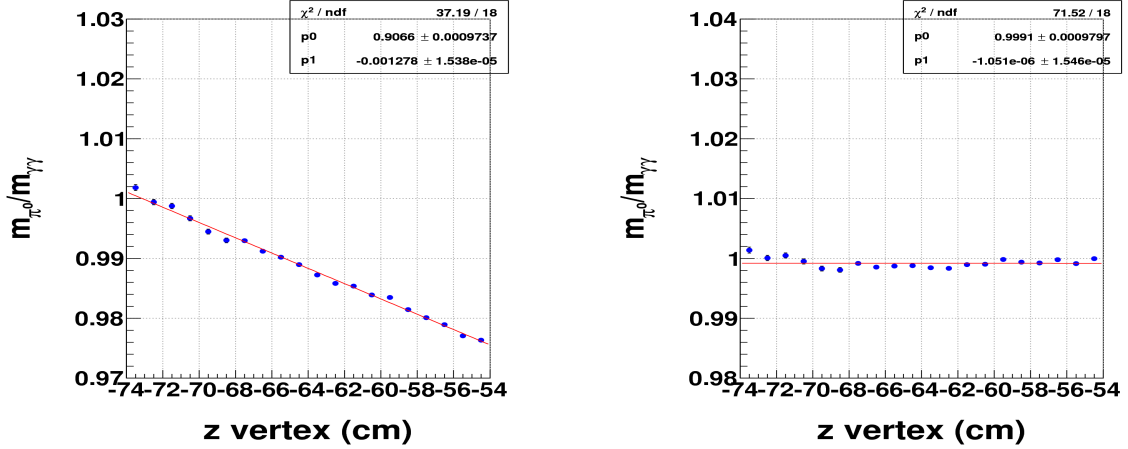


Figure 3.38: The measured fractional invariant mass of ICIC π^0 as a function of the electron z -vertex before (left) and after (right) cluster position corrections for shower depth.

3.3.4.2 Position correction

Cluster position is reconstructed as a weighted average of its hits' positions. Those hit positions are taken as the center of the front face of their corresponding crystal. However, the energy deposition of the shower occurs at some depth into the crystal. Due to the roughly focusing design of the calorimeter, this effect is negligible for photons originating from a vertex near the crystals' focal point. However, for an extended target, and EG6 has the longest target used to date with this calorimeter, this effect is significant and a correction necessary.

The focusing nature of this calorimeter allows us to treat this correction as only a shift in the radius of the cluster position, δr (although other conventions could have been chosen, e.g. only a shift in cluster z -position). This is essentially a geometric projection effect, and it can be parameterized in terms of shower depth d , and the angle of the photon θ_γ with respect to that of the crystal's longitudinal axis, θ_C :

$$\delta r = \frac{d \sin(\theta_C - \theta_\gamma)}{\cos \theta_C} \quad (3.12)$$

Each photon's angle is calculated from its cluster's position (x, y) and the corresponding electron's z -vertex (or RTPC vertex in the case of EG6's neutral trigger). The crystal angles are parameterized in terms of cluster position based on the calorimeter design drawings (where 78.3 cm is the focal length):

$$\tan \theta_C = \frac{\sqrt{x^2 + y^2}}{78.3 \text{ cm}} \quad (3.13)$$

The shower depth parameter d was treated as a free parameter and fit to the slope of $\sin(\theta_\gamma - \theta_C)$ versus $\cos \theta_C$, where δr was determined by the PDG π^0 mass. Energy-dependence of shower depth was investigated but empirically found to be insignificant. The depth parameter was further tuned to minimize the z -dependence of the reconstructed π^0 mass peak, since z is the most relevant reconstructed quantity least correlated with photon energy.

The resulting shower depth d was estimated to be 5.56 cm in equation 3.12. The effect of this correction in terms of z -dependence is illustrated in figure 3.38.

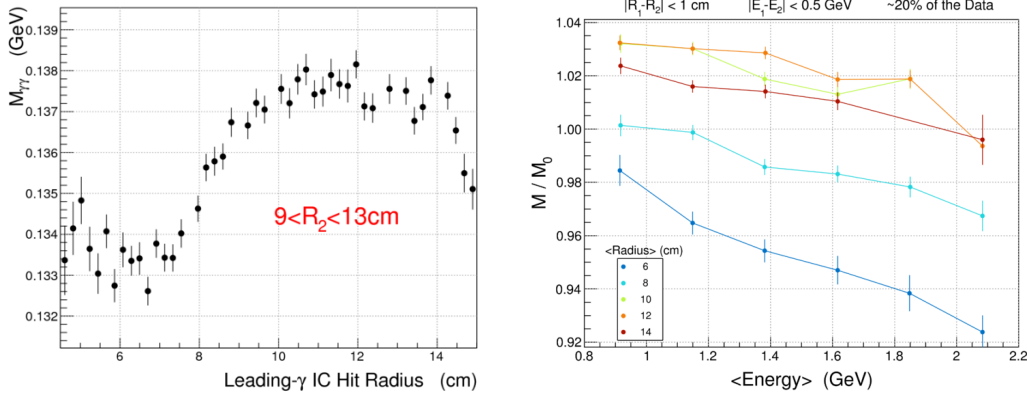


Figure 3.39: IC radial dependence of measured π^0 mass after all corrections prior to section 3.3.4.3 (left). Multidimensional dependence of π^0 mass on radius and energy for a subset of the data (right).

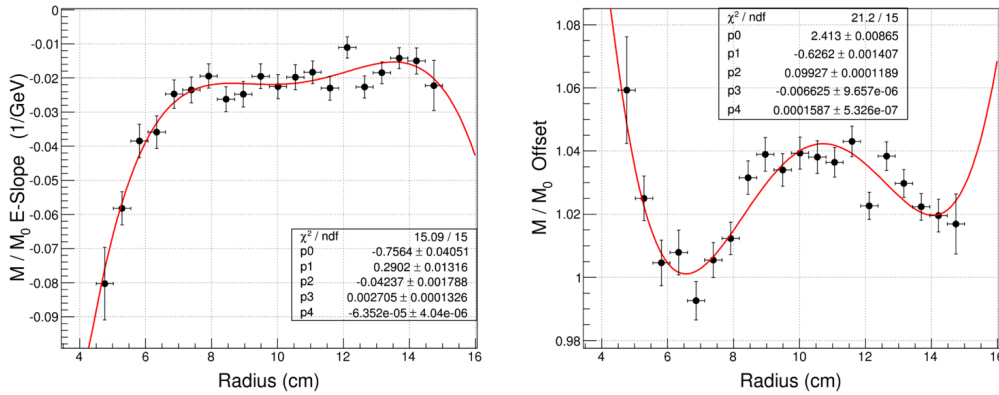


Figure 3.40: The slope (left) and offset (right) resulting from the linear fits of the distributions in figure 3.39. Note that fiducial cuts naturally reject radii below 4.3 cm and above 14.5 cm.

3.3.4.3 Radial-dependent energy correction

After the previous corrections, we observed a remaining radial dependence of the reconstructed π^0 mass [37], where “radial” refers to the distance of the cluster from the beamline. This can be seen in the left panel of figure 3.39. This is most likely attributed to a systematic error in the original π^0 -based gain calibration, which may not have fully accounted for correlations between crystals and the strong variation in rates with radius. It is worth noting that this effect has also been observed in the eg1-dvcs experiment in $e\gamma$ missing mass [45].

To extract a correction for this behavior, photon pairs are selected with cluster radii differing by less than 1 cm and energies differing by less than 500 MeV. Then the π^0 mass peak was fit in multidimensional bins of radius and energy. The result was a clear linear dependence on energy within each radial bin; an example is shown in the right panel of figure 3.39. By fitting the linear energy-dependence for each radial bin, with results illustrated in figure 3.40, a correction function is derived:

$$E_{\text{final}}^\gamma = \frac{E_{\text{corr}}^\gamma}{2 * S(r) * E_{\text{corr}}^\gamma + O(r)}, \quad (3.14)$$

where $S(r)$ and $O(r)$ are the fitted slope and offset, and E_{corr}^γ is the output of equation 3.11.

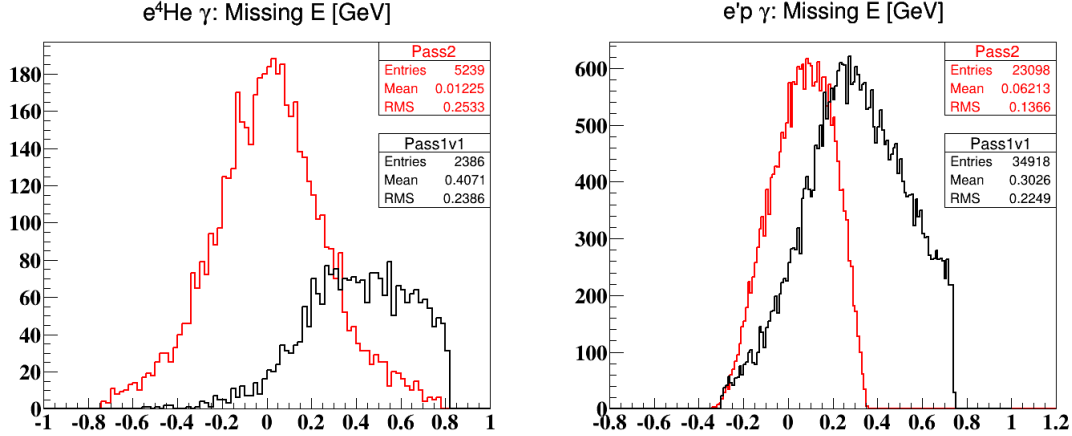


Figure 3.41: The distributions in black are without the IC photon corrections and in red with the corrections. On the left: the missing energy distribution of $e^4He\gamma$ DVCS events for data. On the right: the missing energy distribution of $e^p\gamma$ DVCS events for data.

3.3.4.4 IC Correction Summary

These corrections for IC photons in real EG6 data have been implemented in pass2 reconstruction in `$CLAS_PACK/icf/eg6iccorr.c` and have been applied to the ICPB bank and used in this analysis.

By construction they put the measured π^0 mass at 135 MeV over all kinematics and detector acceptance. But large improvements are also seen in exclusive DVCS analyses, both coherent and incoherent. Their missing energy distributions are shown in Figure 3.41 before and after these π^0 -based IC photon energy corrections. One sees that correcting few percent deviations of π^0 mass from the true mass caused few hundreds MeV shifts in missing energy of the DVCS events. This large shift in missing energy is due to the fact that the corrections are measured in the range of E_γ available in the IC from $\pi^0 \rightarrow \gamma\gamma$ decays, which is about 0.8 to 2.5 GeV. To apply the correction on a photon, its radius is used to get the linear energy dependence, and then that is extrapolated to the measured energy of the photon. For the DVCS photons, this goes well above the measured range of photon energies used to derive these corrections, energy range is about 2 to 5 GeV.

DVCS beam-spin asymmetry extraction

In the previous chapter, the events were filtered to select the ones which have one and only one good electron, and other good particles in coincidence with the electron. This chapter explains the procedure we used to extract the beam-spin asymmetry observable following this order: clean the DVCS data sample by choosing good run list, ensure the exclusivity of the selected events by imposing the conservation laws, subtract the background by combining data with simulation, and binning the identified DVCS events. This chapter contains also an estimation of the systematic uncertainty contribution from each source on the measured beam-spin asymmetry.

In the following, the selection procedures of the coherent DVCS events is detailed and generalized to the cases of incoherent DVCS, the coherent π^0 , and the incoherent π^0 channels.

4.1 Coherent channel

4.1.1 Good run list

In principle, with constant beam luminosity, target density and pressure, the event rate has to be constant over the experimental time. Due to the changes in the experimental conditions, such as changing a trigger in a detector, a slight shift in the beam position or a system failure somewhere, this rate changes. We minimize the effects of these changes on the reconstructed events by selecting the good runs. To this aim, we monitor the ratio of the number of the good tracks reconstructed in the RTPC to number of the detected good electrons in CLAS ($\langle tpc/e \rangle$) as a function of run number. Furthermore, we also look at this ratio in the six sectors of CLAS, as they are independent of each other and their performances might be different.

In this work, after the PID procedures, a run is considered good if:

- The integrated $\langle tpc/e \rangle$ rate over the six sectors of CLAS is consistent with the neighboring runs.
- The six sectors show small fluctuations for each run.

Figure 4.1 shows the integrated and the sector-dependence of $\langle tpc/e \rangle$ for the individual runs. One notices a universal variation of this ratio over the three months of data taking. This can be attributed to changes in the RTPC. In particular, we had leaks in our gas system that appeared during the run. This probably caused gas contamination, changing the properties of the detector.

4.1.2 Coherent DVCS event selection

Events with one and only one good electron, one and only one good RTPC track and at least one good photon are considered good coherent DVCS candidates. Even though the DVCS reaction has only one real photon in the final state, events with more than one good photon are not discarded at this stage. This is motivated by the fact that some photons correspond to random coincidences and discarding these events results in losing good events. Then, events with one or more π^0 are removed from the coherent DVCS sample. After that, the most energetic photon

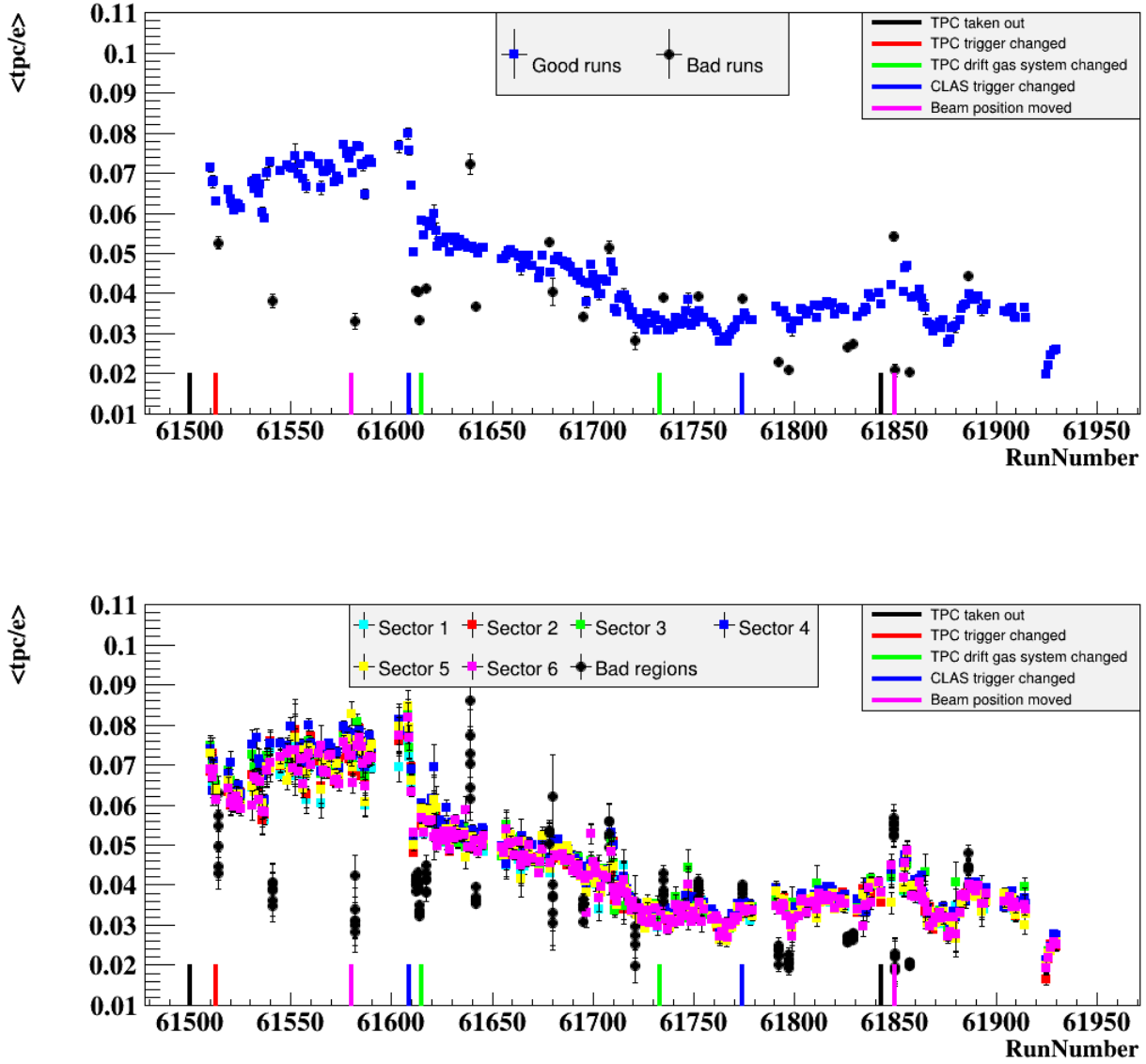


Figure 4.1: On the top: The integrated $\langle tpc/e \rangle$ ratio (over the six sectors of CLAS) for the individual runs. The blue points refer to the good runs, while the black ones are the rejected ones. On the bottom: the $\langle tpc/e \rangle$ ratio is shown for each sector of CLAS. The colored points indicate the different sectors for each good run, while the black ones are the rejected runs without color difference between the sectors. In both plots, the experimental setting changes that might cause a change in the event rate are indicated with vertical colored lines.

in each remaining event is chosen as the DVCS photon. Next, to consider an event as a clean 4He DVCS, it has to pass respectively two sets of requirements: DVCS characteristic cuts and exclusivity cuts.

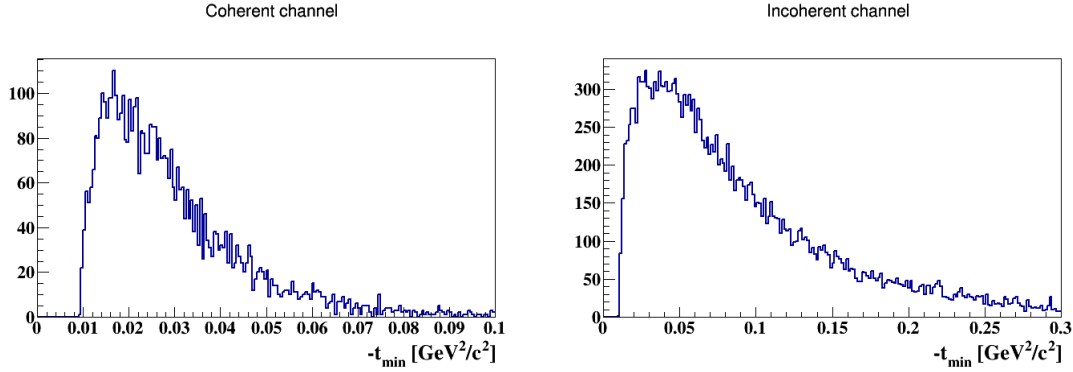


Figure 4.2: Coherent (left) and incoherent (right) $-t_{min}$ distributions calculated for the experimentally selected DVCS events. We use the experimental Q^2 and x_B of the individual events.

DVCS characteristics

- $Q^2 > 1 \text{ GeV}^2$: to ensure that the interaction occurs at the partonic level and the applicability of the factorization in the DVCS handbag diagram.
- $-t > -t_{min}$: the transferred momentum squared to the recoil ${}^4\text{He}$ has to be greater than a minimum value defined by the kinematics of the beam and the scattered electron as:

$$t_{min} = -Q^2 \frac{2(1-x_A)(1-\sqrt{1+\varepsilon^2}) + \varepsilon^2}{4x_A(1-x_A) + \varepsilon^2}, \quad (4.1)$$

where $\varepsilon^2 = \frac{4M_{{}^4\text{He}}^2 x_A^2}{Q^2}$, $x_A = \frac{M_p \cdot x_B}{M_{{}^4\text{He}}}$ and M_p ($M_{{}^4\text{He}}$) is the proton (${}^4\text{He}$) mass.

In the case of the proton DVCS, the variable x_A is replaced by the Bjorken x_B in the formula for t_{min} . Figure 4.2 presents t_{min} distributions for both DVCS channels.

- In the case of the incoherent DVCS channel, we apply a cut on the invariant mass of the virtual photon and the target proton system to be greater than $2 \text{ GeV}/c^2$. This cut avoids the region of excitation of the proton to resonances.
- $E_\gamma > 2 \text{ GeV}$. This is a cleaning cut applied to reduce the background in the DVCS sample as the simulation indicates that no DVCS events are expected with photon energy less than 2 GeV. Figure 4.3 shows the energy distributions of the simulated coherent and incoherent DVCS events.

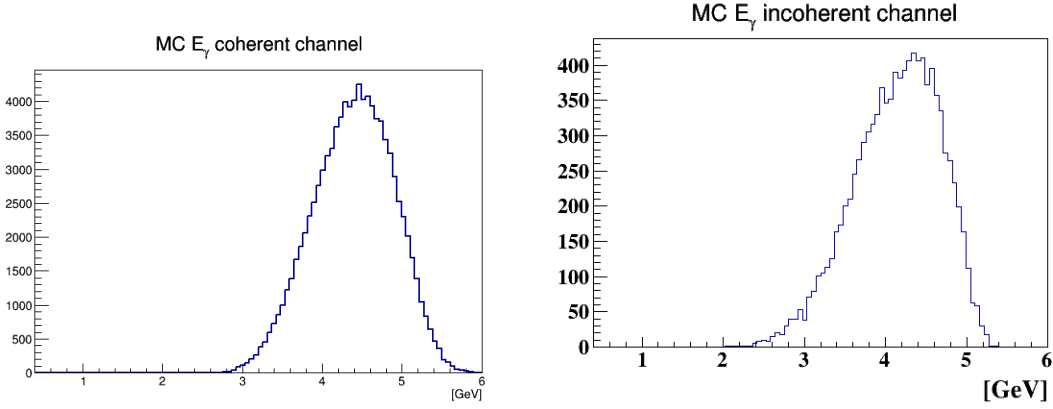


Figure 4.3: The energy distribution of the simulated coherent (left) and incoherent (right) DVCS photons.

Exclusivity cuts

The coherent DVCS reaction is:

$$e(\mathbf{P}_e) + {}^4He(\mathbf{P}_{{}^4He}) \rightarrow e'(\mathbf{P}_{e'}) + {}^4He'(\mathbf{P}_{{}^4He'}) + \gamma(\mathbf{P}_\gamma) \quad (4.2)$$

where the symbols in the parentheses are the energy-momentum four-vectors. We define the additional four-vectors:

$$\text{virtual photon vector } (\mathbf{P}_{\gamma^*}) = \mathbf{P}_e - \mathbf{P}_{e'} \quad (4.3)$$

$$\mathbf{P}_X^{e^4He\gamma} = \mathbf{P}_{\gamma^*} + \mathbf{P}_{{}^4He} - (\mathbf{P}_\gamma + \mathbf{P}_{{}^4He'}) \quad (4.4)$$

$$\mathbf{P}_X^{e^4He} = \mathbf{P}_{\gamma^*} + \mathbf{P}_{{}^4He} - \mathbf{P}_{{}^4He'} \quad (4.5)$$

$$\mathbf{P}_X^{e\gamma} = \mathbf{P}_{\gamma^*} + \mathbf{P}_{{}^4He} - \mathbf{P}_\gamma \quad (4.6)$$

The exclusivity of the coherent DVCS reaction is ensured by imposing the following conservation laws:

- The co-planarity cut ($\Delta\phi$). In principle, the virtual photon, the emitted real photon and the recoil helium lie in the same plane, which is called the hadronic plane. Thus the DVCS events must have $\Delta\phi$ values around zero. The hadronic plane can be defined in three ways:

$$\overrightarrow{HP}_1 = \overrightarrow{\mathbf{P}}_{{}^4He'} \times \overrightarrow{\mathbf{P}}_{\gamma^*} \quad (4.7)$$

$$\overrightarrow{HP}_2 = \overrightarrow{\mathbf{P}}_{{}^4He'} \times \overrightarrow{\mathbf{P}}_\gamma \quad (4.8)$$

$$\overrightarrow{HP}_3 = \overrightarrow{\mathbf{P}}_{\gamma^*} \times \overrightarrow{\mathbf{P}}_\gamma \quad (4.9)$$

$\Delta\phi$ is defined to be the ϕ difference between these planes and is calculable from three combinations: $(\overrightarrow{HP}_1, \overrightarrow{HP}_2)$, $(\overrightarrow{HP}_1, \overrightarrow{HP}_3)$ and $(\overrightarrow{HP}_2, \overrightarrow{HP}_3)$. We investigated the three combinations and we decided to use the second one as it gives better resolution.

- Missing energy, mass and transverse momentum ($p_X^T = \sqrt{(p_X^x)^2 + (p_X^y)^2}$) cuts on $\mathbf{P}_X^{e^4He\gamma}$.
- Missing mass cuts on the e^4HeX and $e\gamma X$ systems, which are defined as $(P_X^{e^4He})^2$ and $(P_X^{e\gamma})^2$ respectively.

- Cone angle cut between the measured real photon and the missing particle in the e^4HeX configuration. It is defined as:

$$\theta(\gamma, e^4HeX) = \cos^{-1} \left(\frac{\vec{P}_\gamma \cdot \vec{P}_X^{e^4He}}{|\vec{P}_\gamma| |\vec{P}_X^{e^4He}|} \right). \quad (4.10)$$

Figure 4.4 summarizes all the exclusivity cuts. In these plots, the black distributions represent the coherent events after the DVCS characteristic cuts and before all the exclusivity cuts. The shaded distributions stand for the events which passed all the exclusivity cuts except the one on the quantity plotted. We fitted each shaded distribution by a Gaussian and then we applied 3σ cuts around the mean value of each distribution except the missing energy distribution for which a final [-0.45:0.5] GeV cut is applied to remove the tails and reduce the background. The events which pass these cuts are assumed to be good 4He DVCS events.

4.1.3 Coherent channel checking

4.1.3.1 Checking 4He PID

In this analysis We claim that kinematic exclusivity cuts are sufficient to cleanly select coherent 4He DVCS events without the need for $\frac{dE}{dx}$ cuts. We performed few checks regarding applying a PID cut, where the full data was analyzed in the following three sets:

- Processing all the reconstructed tracks in each event with the exclusivity cuts.
- Processing events with only one good track in the RTPC being reconstructed.
- Processing events with only one track that passes a dedx cut.

The results are shown in figure 4.5 in terms of the exclusive variables for the identified coherent DVCS events. One can see that applying a PID cut would only change the statistics and not the width of distributions. On the other hand, figure 4.6 shows a comparison between the reconstructed beam-spin asymmetries with and without applying a PID cut. The two sets of asymmetries are compatible within the given statistical error bars. From these two observations, we deduce that a PID cut on the Helium would not reduce any background contribution.

4.1.3.2 Left/Right modules of the RTPC

The two modules of the RTPC have shown different yields in terms of the identified good track, see Section 3.1.4. This different yields should not affect the DVCS distributions neither the reconstructed beam-spin asymmetries. In this section, we carry out the analysis for the coherent channel based on the Left/Right modules of the RTPC to ensure that the reconstructed asymmetries for the two modules of the RTPC are compatible. Figure 4.7 shows the RTPC module dependent exclusive distributions for the identified coherent DVCS events. Figure 4.8 shows the integrated coherent beam-spin asymmetries for the two modules separately, and for the two half together. To conclude, the two modules of the RTPC show a very similar performances in terms of the DVCS exclusive distributions and the module-dependent asymmetries are compatible.

4.1.4 Comparison with simulation

Coherent DVCS events were simulated according to the procedures described in section 3.2.1. Then, events are selected following the same identification criteria as for the experimental data.

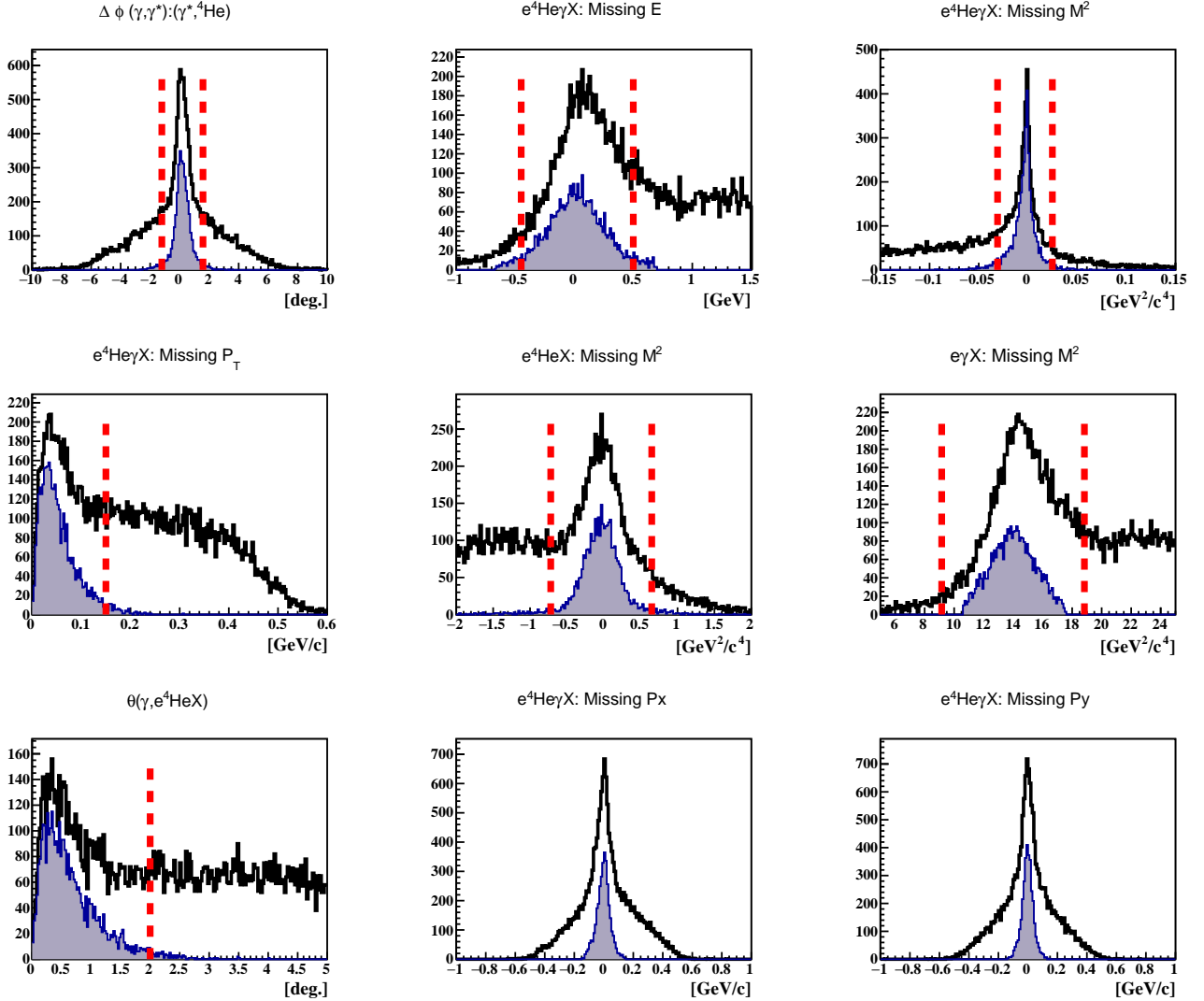


Figure 4.4: The coherent DVCS exclusivity cuts. The blue distributions represent the coherent DVCS events candidate. The shaded distributions represent the events which passed all the exclusivity cuts except the quantity plotted. The vertical red lines represent 3σ cuts on all the distribution except the missing energy distribution for which [-0.45:0.5] GeV cut is applied. The missing momentum in x and y directions in the configuration $e^4\text{He}\gamma X$, are shown for information. The mean and the sigma values of each quantity can be found in Appendix E, table E.1.

Finally, We apply similar exclusivity cuts as presented for the experimental coherent DVCS events. That is each exclusive distribution is fitted by a Gaussian and a 3σ cut is applied. So the cut are not identical, but obtained with the same method. This is done to avoid issues on variables where the peak is not in the exact same place in simulation and in data.

Figure 4.9 shows the comparison between the experimental and the simulated DVCS events as a function of the kinematic variables: Q^2 , x_B , $-t$, and ϕ . Figure 4.10 shows the comparison as a function of the quantities used for the exclusivity cuts. The distributions in the latter two figures show a satisfying match between the experimental and the simulated data.

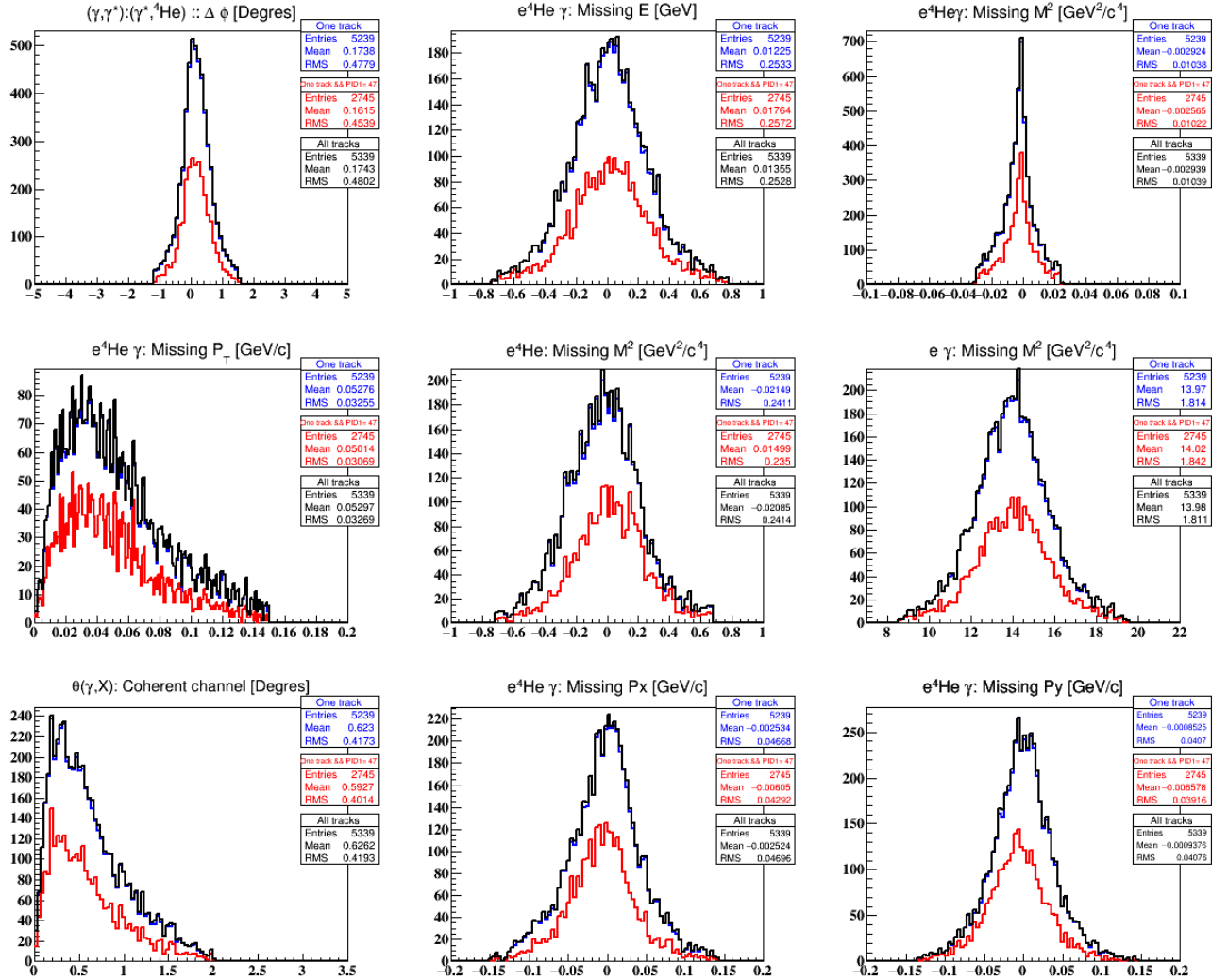


Figure 4.5: Distributions of the exclusive variable for the identified DVCS events with only one track in the RTPC (blue), one track and PID1 is equal to 47 (red), and processing all the tracks in each event with the exclusivity variables (black).

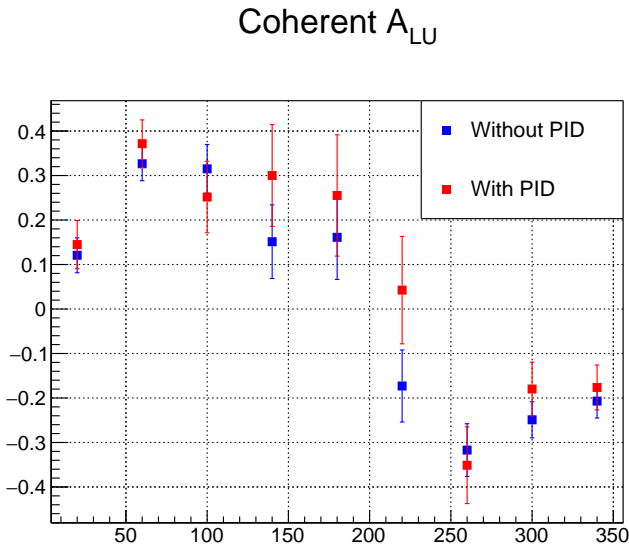


Figure 4.6: The integrated coherent beam-spin asymmetries as a function of ϕ with (red) and without (blue) applying a PID cut on Helium tracks.

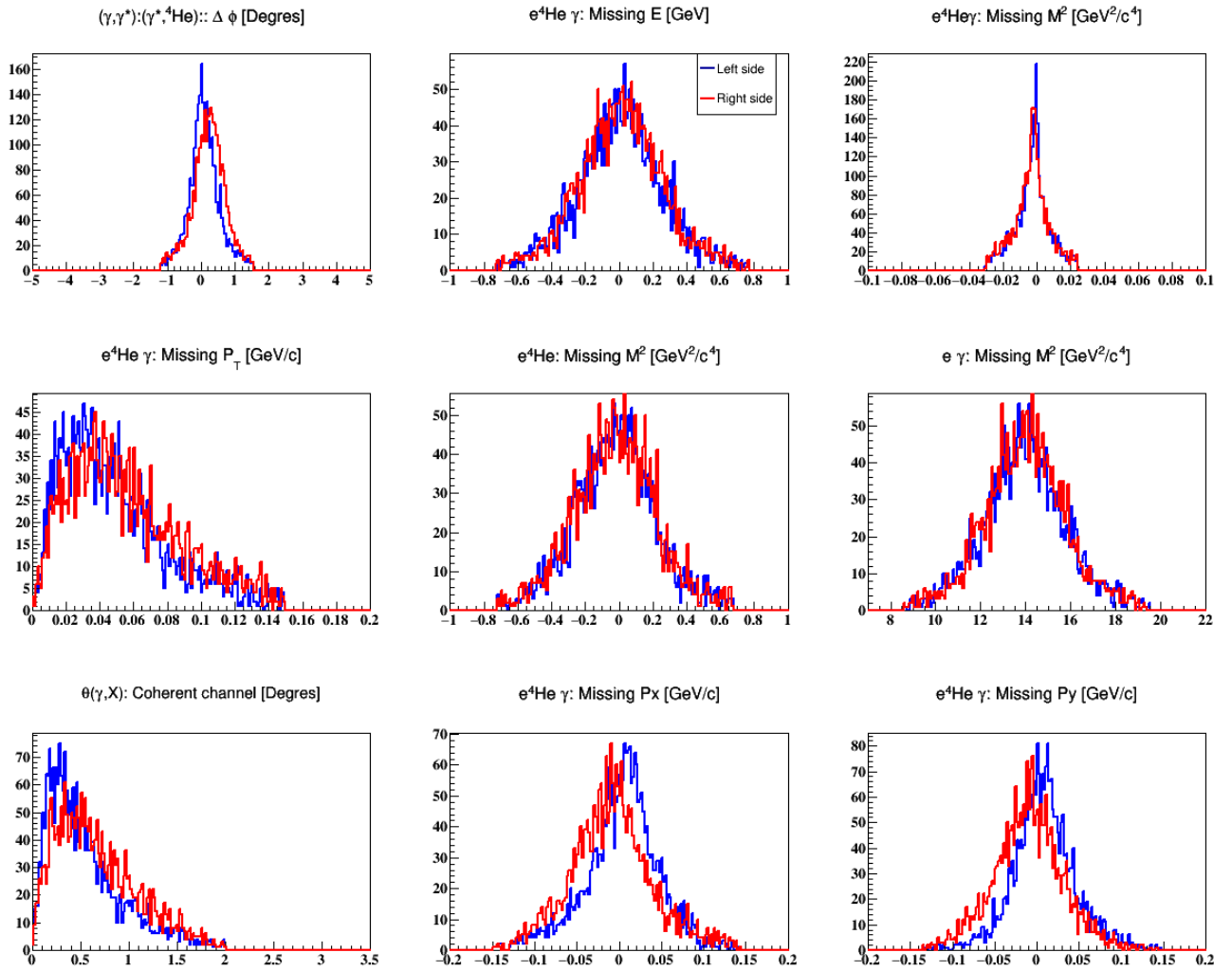


Figure 4.7: The distributions of the exclusive variables for the identified coherent DVCS events in the individual modules of the RTPC, Left module in blue and Right module in red.

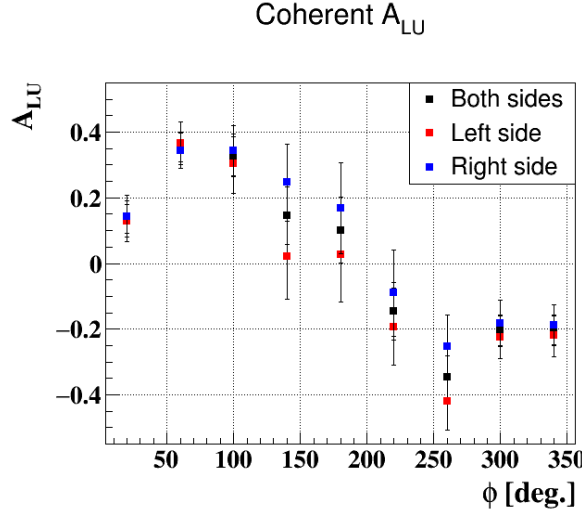


Figure 4.8: The reconstructed integrated-over-full-data beam-spin asymmetries as a function of the hadronic angle ϕ in the two modules of the RTPC separately, and the integrated signal over the whole RTPC.

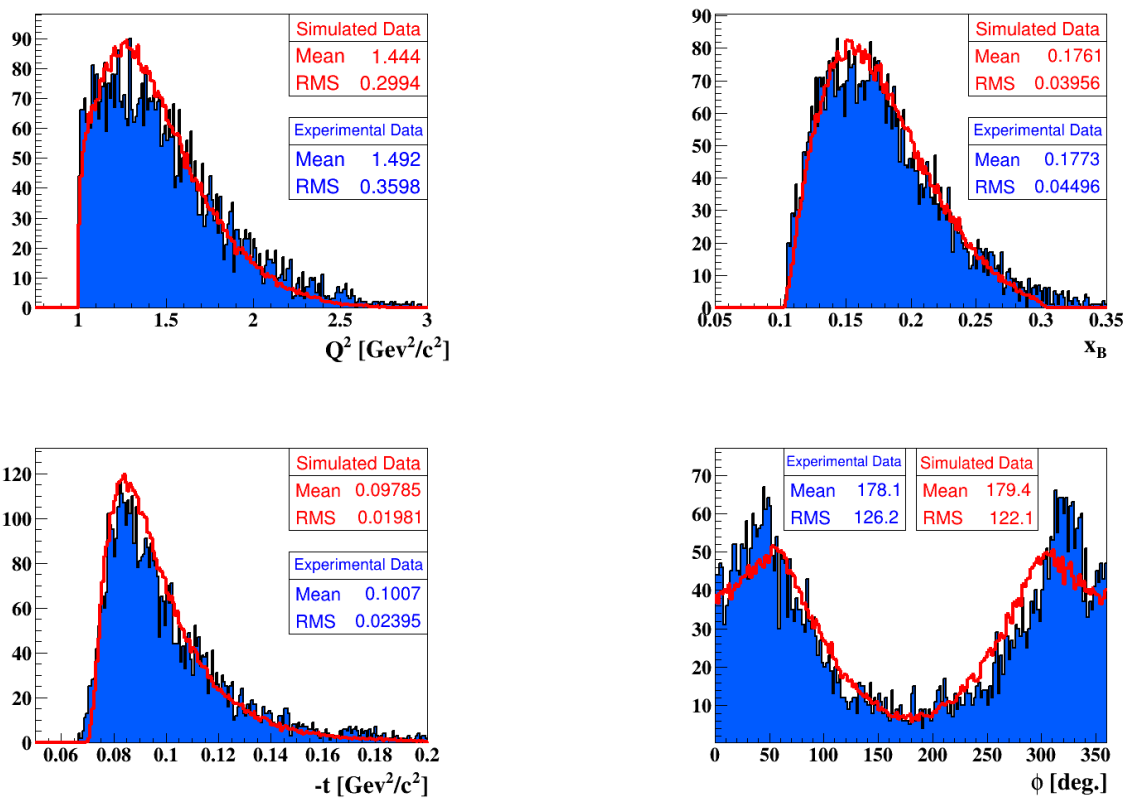


Figure 4.9: Comparison between the simulated $e^4He\gamma$ DVCS events (in red lines) and the experimental DVCS events (in shaded blue) as a function of the kinematic variables: Q^2 , x_B , $-t$, and ϕ .

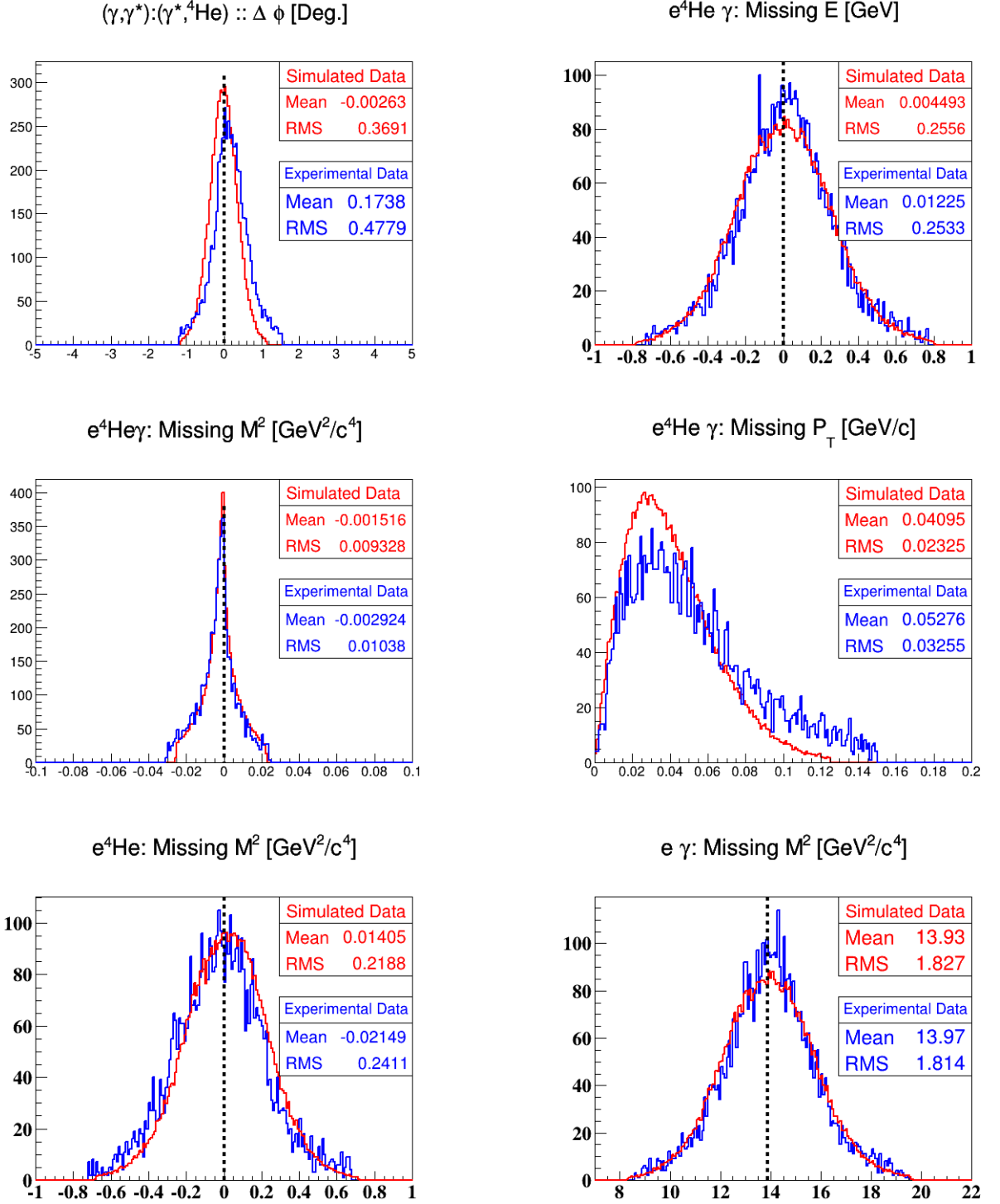


Figure 4.10: Comparison between simulated and experimental $e^4\text{He}\gamma$ DVCS events. The distributions from left to right and from top to bottom are: Co-planarity cut, missing energy, missing mass squared and missing transverse momentum in the configuration of detecting all the three final-state particles, missing mass squared in the $e^4\text{He}X$ and $e\gamma X$ configurations respectively. The vertical black lines indicate the theoretically expected value for each quantity.

4.2 Incoherent channel

In this channel, the DVCS process happens on a bound proton. Thus, the final state has a recoil proton instead of the helium nucleus. Therefore, events with one good electron, one recoil proton,

and at least one real photon are the good candidates here. For the rest, we follow the same steps that were introduced for the coherent DVCS selection.

4.2.1 Good run list

The events rate stability is verified by looking at the rate of the detected number of protons to the detected electrons ($\langle p/e \rangle$). Like for the coherent channel, the same technique for the determination of the good run list is followed herein. The results are presented in figure 4.11.

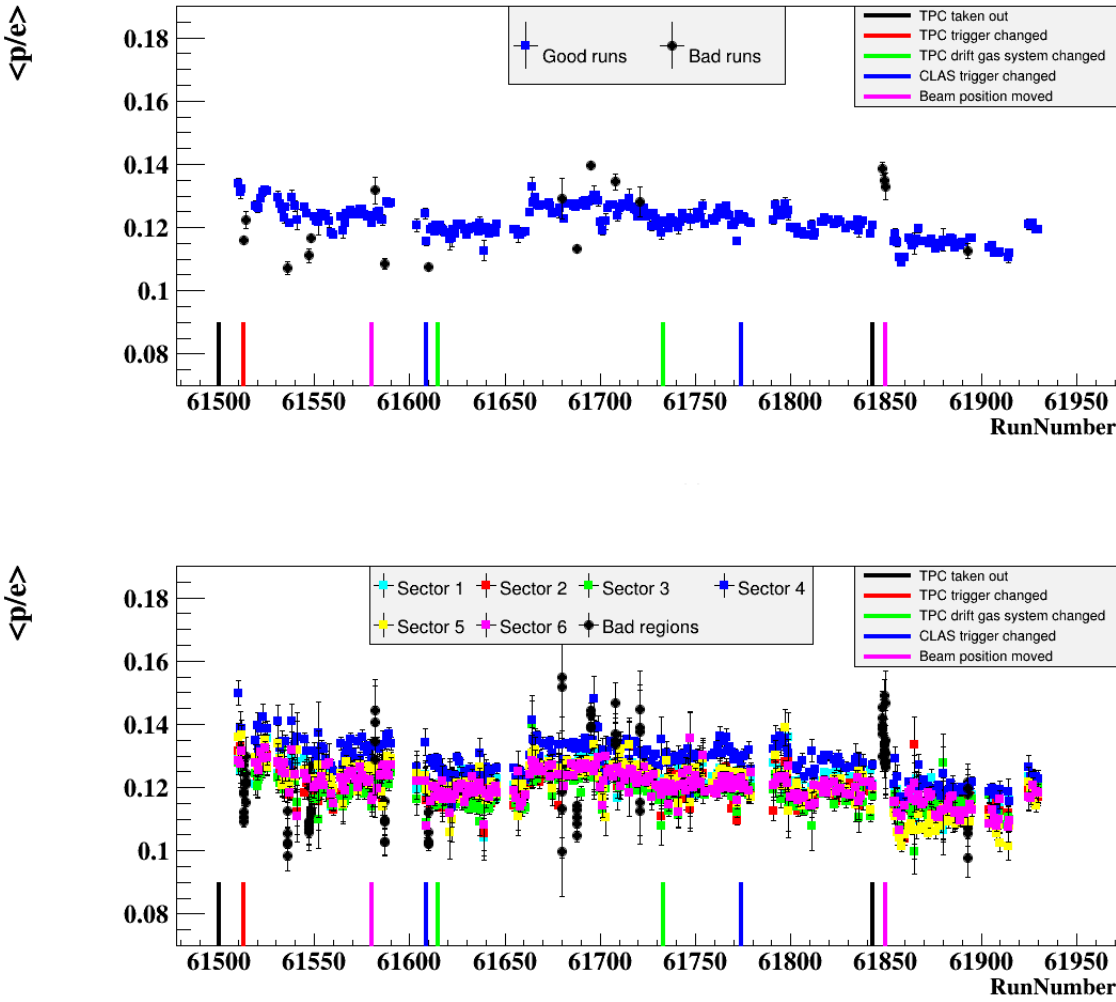


Figure 4.11: On the top: the integrated $\langle p/e \rangle$ ratio as a function of run number. The blue points refer to the good runs, while the black points are the rejected ones. On the bottom: the same ratio for each run, is shown for each sector of CLAS. The colored points indicate the six sectors, while the black points are the sectors of the rejected runs.

4.2.2 Proton DVCS event selection

To certify that an event is a proton DVCS one, we require the same DVCS kinematic cuts as those presented for the coherent DVCS selection. Then, the exclusivity of the DVCS reaction is ensured

by applying an equivalent set of exclusivity with taking a proton at rest as the target, instead of ^4He . Figure 4.12 summarizes these exclusivity cuts.

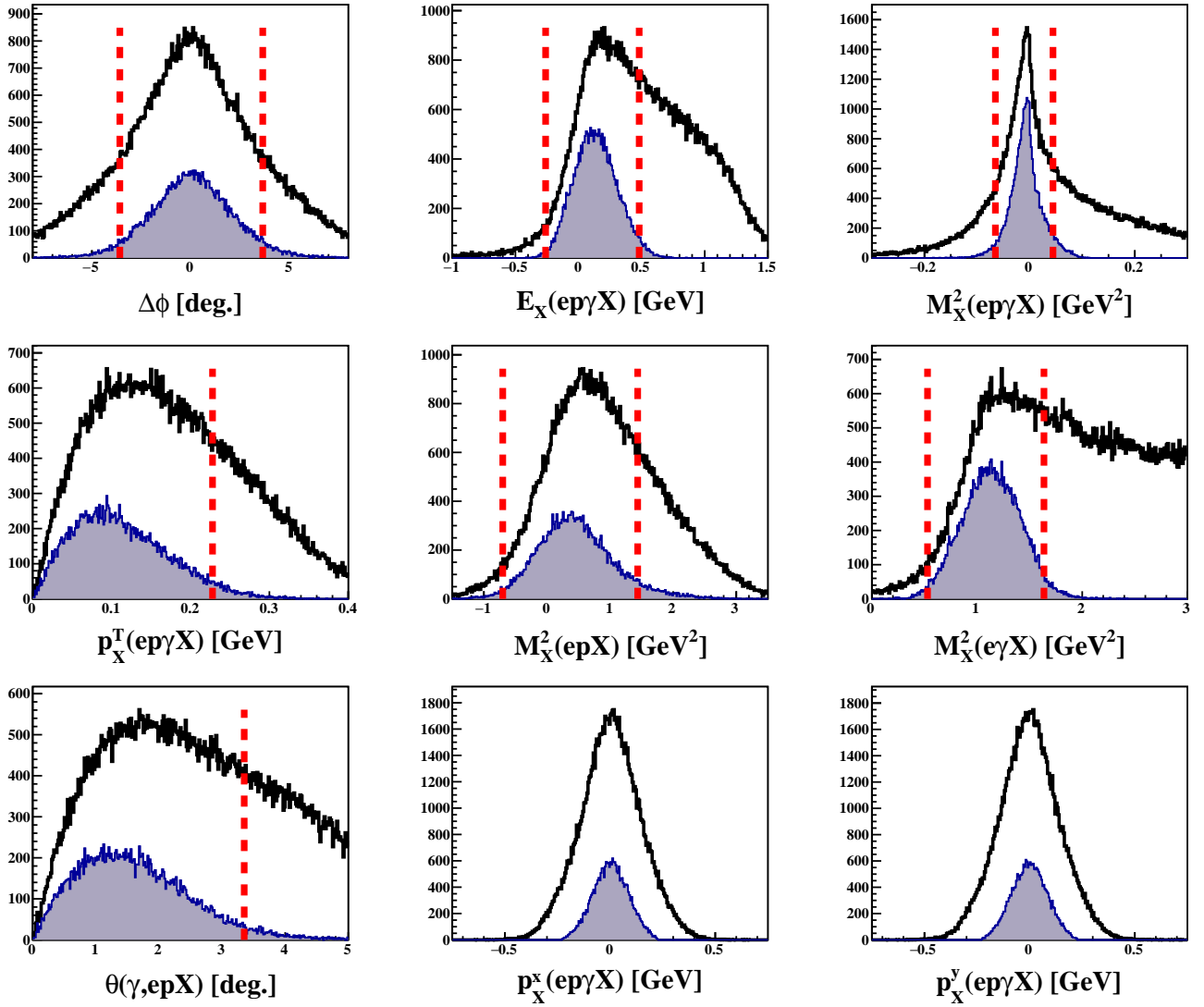


Figure 4.12: The incoherent DVCS exclusivity cuts. The black distributions represent all the events with one good electron, one good proton, and at least one photon in the IC. The shaded brown distributions show the incoherent DVCS events which passed all the exclusivity cuts except the one on the quantity drawn. The distributions from left to right and from top to bottom are: the proton-photon coplanarity, the missing energy, missing mass squared, missing transverse momentum from $\text{ep}\gamma X$, the missing mass squared $\text{ep}X$ and the missing mass squared $\text{e}\gamma X$, the angle between the missing particle in $\text{ep}X$ and the measured photon, the missing P_x and P_y in $\text{ep}\gamma X$. The vertical red lines represent 3σ cuts. The mean and sigma values of each shaded distribution are listed in table E.3.

4.2.3 Comparison with simulation

The three particles of the simulated $\text{ep}\gamma$ DVCS events are selected applying the previously described identification requirements. The events with three identified particles (e, p, γ) are required to pass a set of exclusivity cuts such as the ones of the experimental incoherent DVCS events. In this section, a comparison between the experimental and the simulated data is carried out.

Figure 4.13 shows the comparison between the simulated (red lines) and the experimental (shaded blue) incoherent DVCS events as a function of the four kinematic variables: Q^2 , x_B , $-t$, and ϕ . Figure 4.14 shows the comparison as a function of the variables used to select exclusive DVCS events.

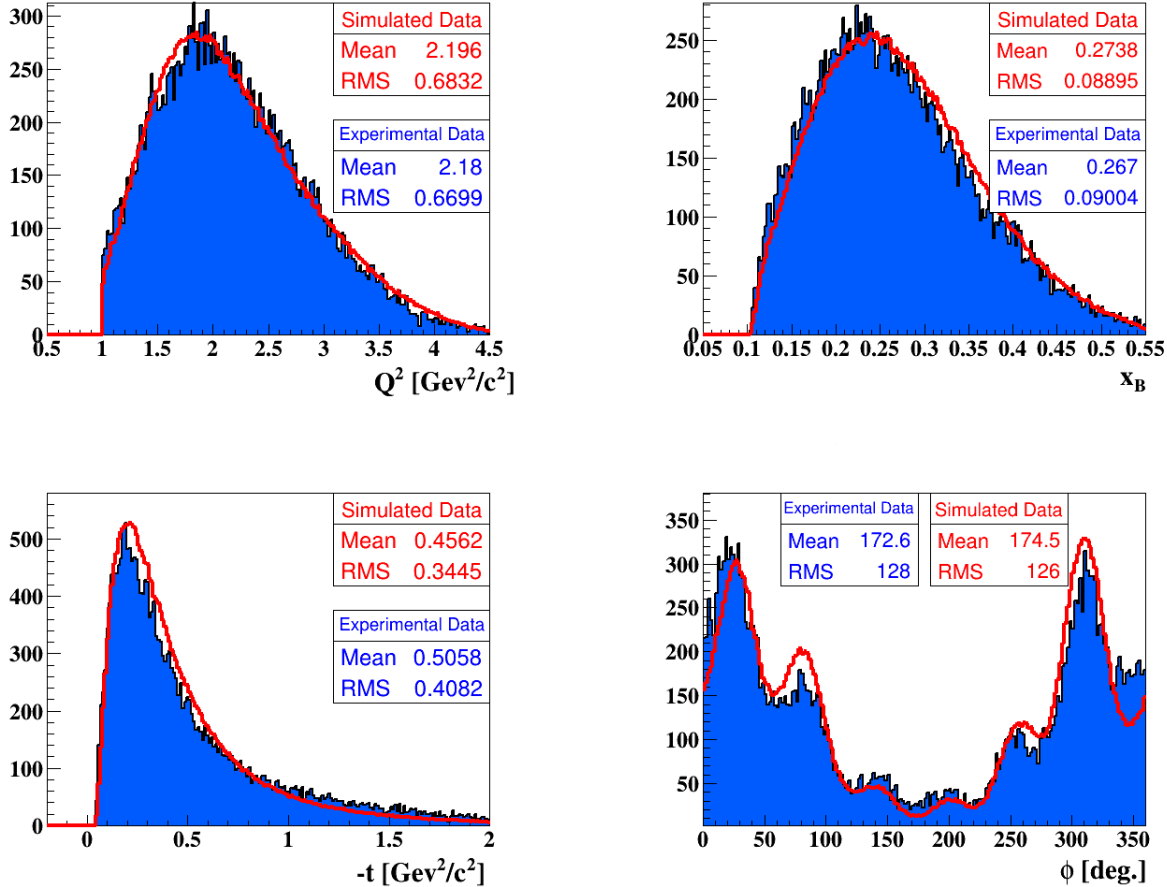


Figure 4.13: Comparison between the Monte-Carlo simulated $e p \gamma$ DVCS events (red lines) and the experimental ones (blue shaded distributions) in terms of the kinematics: Q^2 , x_B , $-t$, and ϕ , respectively from left to right and from top to bottom.

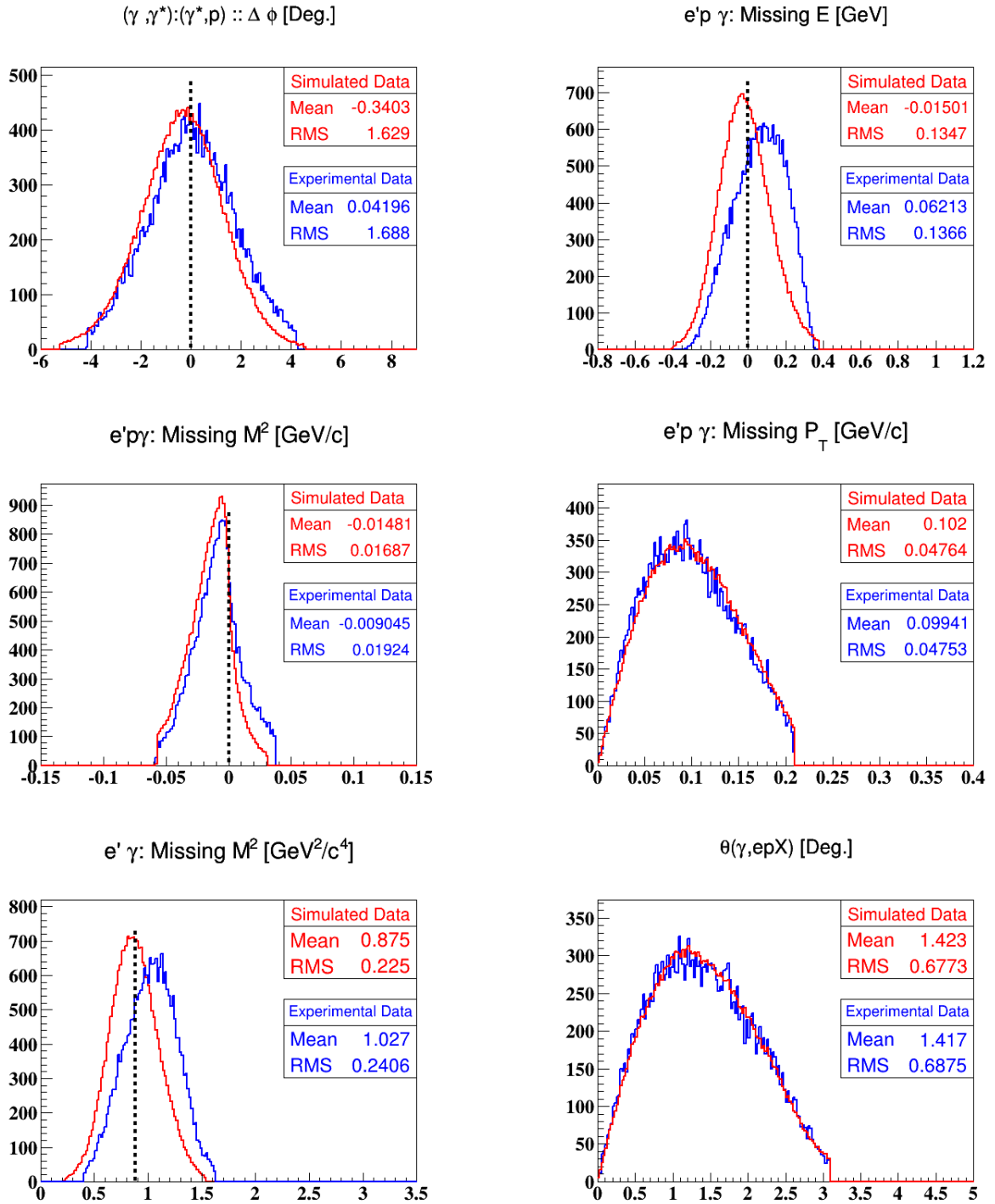


Figure 4.14: Comparison between simulated and experimental $ep\gamma$ DVCS events in terms of the variables used for exclusivity cuts. The vertical black lines indicate the theoretically expected values for each exclusive quantity.

4.3 Kinematic coverages

The one-dimensional distributions of explored kinematical regions can be seen in figure 4.9 for the coherent, and in figure 4.13 for the incoherent DVCS channels. In figure 4.15, we show two-dimensional distributions of these variables to display the correlations between them.

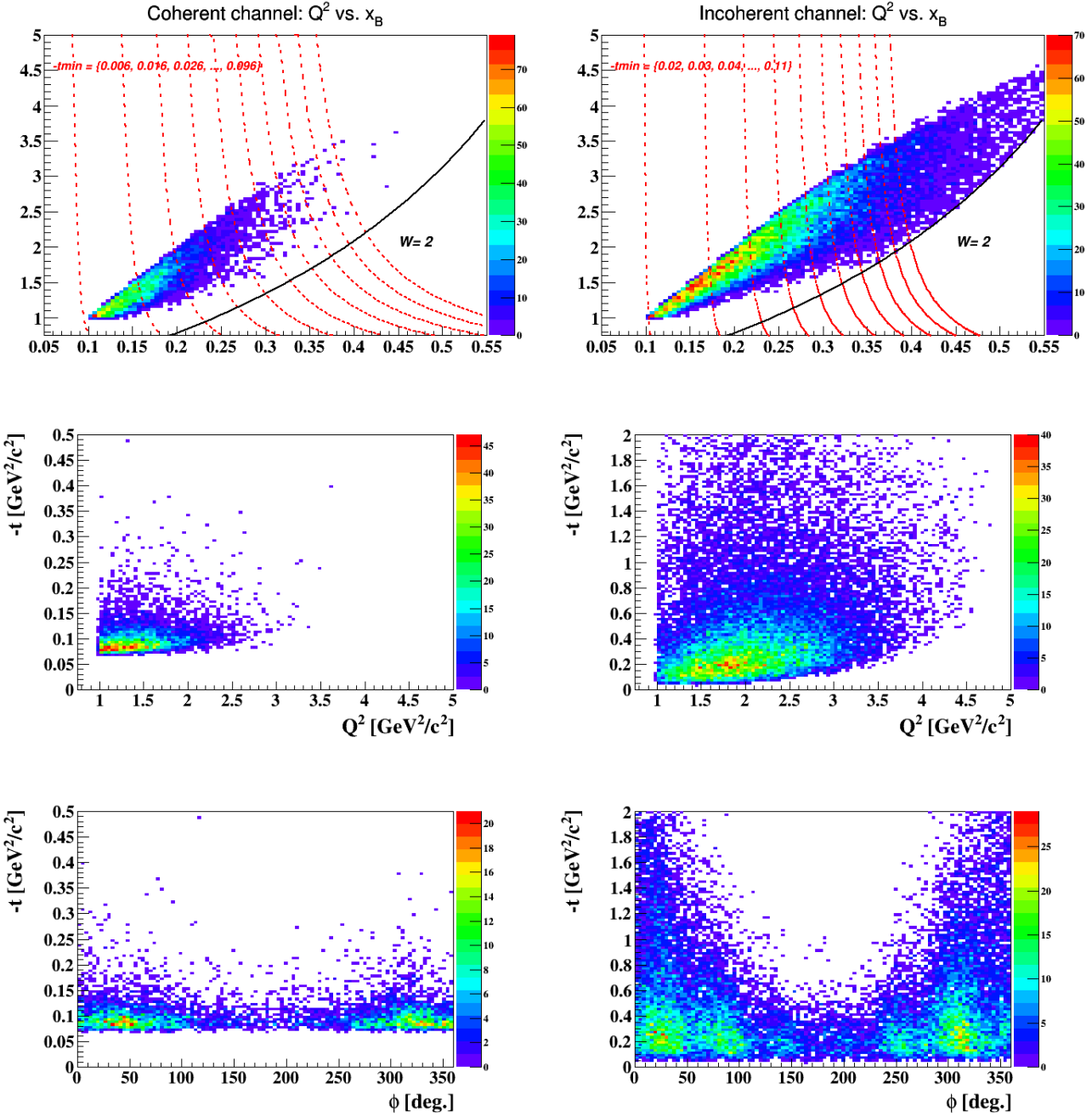


Figure 4.15: The distributions of the identified coherent DVCS are on the left panel, while on the right are the incoherent ones. On the top panel: Q^2 as a function of x_B with W and fixed $-t_{min}$ value cuts in $Q^2 - x_B$ plane. On the middle panel: $-t$ as a function of Q^2 . On the bottom panel: $-t$ as a function of ϕ .

4.4 Data binning

The DVCS cross section and A_{LU} , equations 1.4 to 5.1, depend on the four kinematic variables: Q^2 , x_B , t , and ϕ . The number of identified coherent (incoherent) DVCS events is about 5000 (30k). Due to our limited statistics only, a two-dimensional binning is carried out in this analysis. The strongest dependence of A_{LU} is on the azimuthal angle between the leptonic and the hadronic planes (ϕ). Thus, we construct the two-dimensional bins as follows: the coherent (incoherent) measured ranges of Q^2 , x_B and $-t$ are binned statistically into three (four) bins. Then, the identified DVCS events in each Q^2 , x_B and $-t$ bin, are binned into nine bins in ϕ . Therefore, we are left with Q^2 - ϕ bins integrated over the full ranges of x_B and $-t$, x_B - ϕ bins integrated over Q^2 and $-t$, and $-t$ - ϕ bins integrated over Q^2 and x_B . For instance, figure 4.16 shows the one-dimensional bins in Q^2 and the associated bins in ϕ .

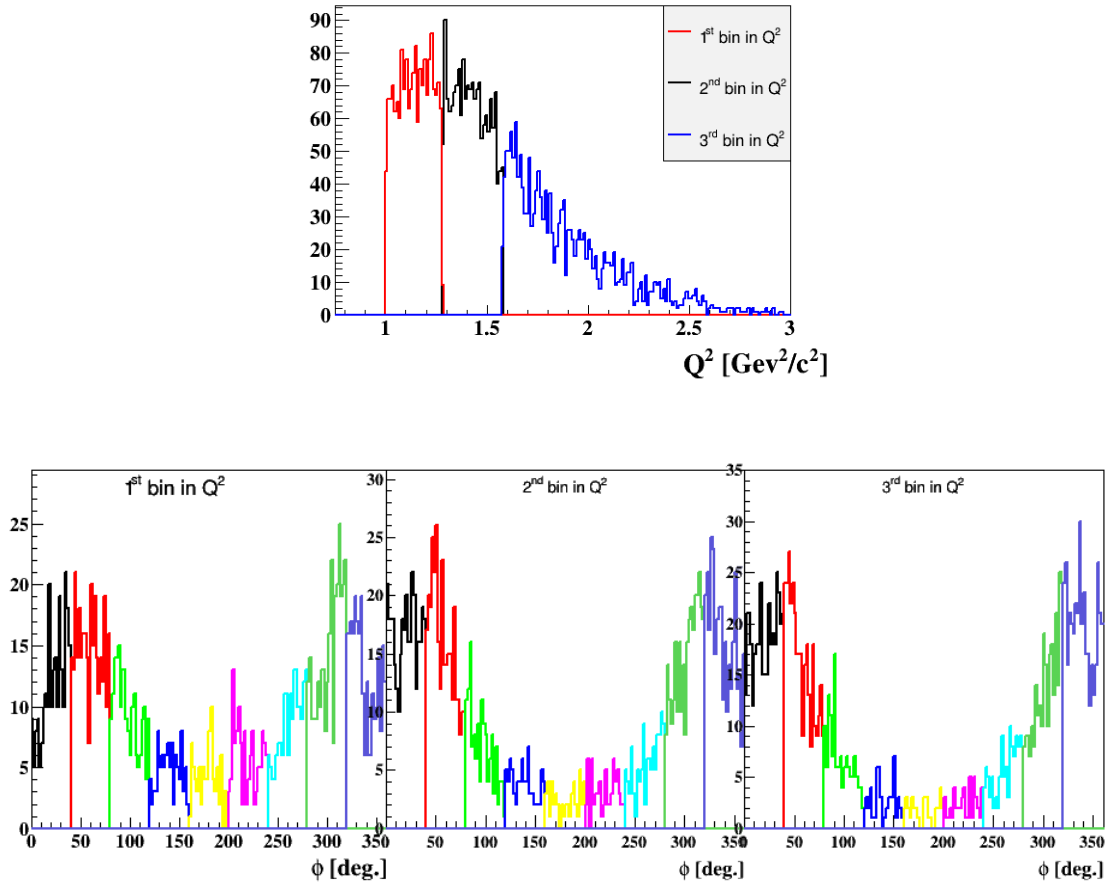


Figure 4.16: On the top: the Q^2 distribution of the collected coherent DVCS events. The different colors indicate the different bins in Q^2 integrated over the full ranges of $-t$ and x_B . On the bottom: the ϕ distributions of the coherent DVCS events for the bins in Q^2 , which are shown in the top plot. The different colors in each ϕ distribution represent the nine bins in ϕ .

4.5 Background subtraction

4.5.1 π^0 contaminations

Even with all cuts applied to select the selected DVCS events, the events are not all DVCS events. In our kinematic region, the main contamination comes from the exclusive electroproduction of π^0 ($e^4He \rightarrow e^4He\pi^0 \rightarrow e^4He\gamma\gamma$, $ep \rightarrow ep\pi^0 \rightarrow ep\gamma\gamma$), in which one of the two photons of the π^0 decay passes the requirements of the DVCS. Thus, the event is counted as a DVCS event. These events contaminate the DVCS sample and have to be subtracted to obtain the true number of DVCS events. In the case of the coherent channel, this can be formulated as:

$$N_{e^4He\gamma}^{True} = N_{e^4He\gamma}^{Exp.} - N_{e^4He\pi^0(\gamma)}^{Exp.}, \quad (4.11)$$

where $N_{e^4He\gamma}^{True}$, $N_{e^4He\gamma}^{Exp.}$ and $N_{e^4He\pi^0(\gamma)}^{Exp.}$ are the true number of coherent DVCS events, the experimentally measured number of $e^4He\gamma$ events and the contamination number, respectively. The contamination can be calculated by using real data and simulation. We define, for each kinematic bin and for each beam helicity state

$$N_{e^4He\pi^0(\gamma)}^{Exp.} = \frac{N_{e^4He\pi^0(\gamma)}^{Sim.}}{N_{e^4He\pi^0(\gamma\gamma)}^{Sim.}} * N_{e^4He\pi^0(\gamma\gamma)}^{Exp.} \quad (4.12)$$

where $N_{e^4He\pi^0(\gamma\gamma)}^{Exp.}$ is the number of measured $e^4He\pi^0$ events, for which both photons of the π^0 have been detected. The quantity $\frac{N_{e^4He\pi^0(\gamma)}^{Sim.}}{N_{e^4He\pi^0(\gamma\gamma)}^{Sim.}}$ is the acceptance ratio for detecting a $e^4He\gamma$ event that originates from an $e^4He\pi^0$ event. It can be derived from Monte-Carlo simulations by generating and simulating $e^4He\pi^0$. $N_{e^4He\pi^0(\gamma)}^{Sim.}$ is the number of such events passing the DVCS requirements, while $N_{e^4He\pi^0(\gamma\gamma)}^{Sim.}$ is the number of simulated $e^4He\pi^0$ events passing the exclusivity cuts for $e^4He\pi^0$ events.

The previous formulas apply to the case of the coherent DVCS. The same procedures hold for the incoherent case by replacing the 4He with the proton.

The selection of the exclusive $e^4He\pi^0$ and $ep\pi^0$ events requires the detection of one good electron, one good π^0 in the topology ICIC or ICEC, and one good 4He track in the coherent case, or one good proton in the incoherent case. In order to ensure that this is a deep process, we apply the same kinematic cuts as DVCS. These cuts and the comparisons with simulation can be found in Appendix D.

Figure 4.17 shows the coherent acceptance ratio as a function of each of the four kinematic variables (Q^2 , x_B , $-t$, ϕ_h). These distributions are one-dimensional, i.e. the data are integrated over all kinematical ranges except for the quantity which is binned (along the x-axis). The results for the incoherent channel can be found in figure 4.18. The mean value of the acceptance ratio for the coherent channel is around 25%, with some dependence on x_B and ϕ , and almost no dependence on Q^2 and $-t$. For the incoherent channel, the mean acceptance ratio is around 20% with some dependence on the four kinematic variables.

Figure 4.19 presents the measured coherent and incoherent π^0 contamination with respect to the measured DVCS events. On both channels, the contamination increases strongly with $-t$, with a mean of 2% (6%) for the coherent (incoherent) channel.

As presented in the previous section, we construct two-dimensional bins: Q^2 - ϕ , x_B - ϕ and $-t$ - ϕ . Thus, for each bin in Q^2 , x_B and $-t$, we assume that the acceptance ratio does not change a lot within the bin range and we construct the one-dimensional acceptance ratio as a function of ϕ .

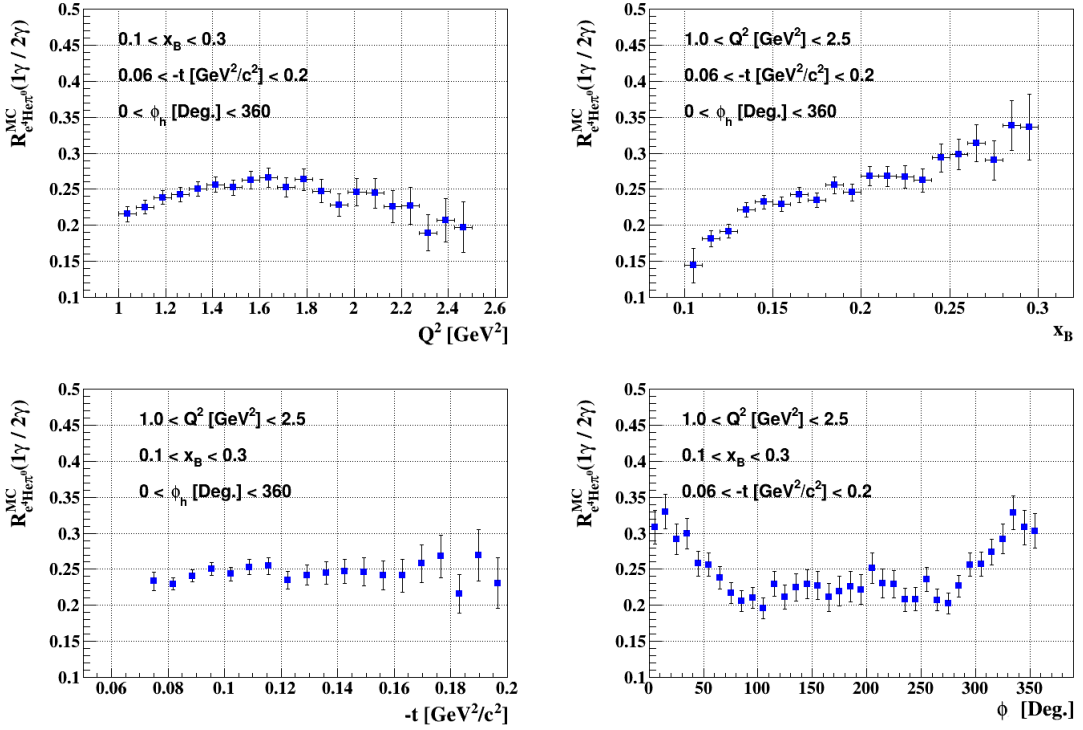


Figure 4.17: The coherent channel acceptance ratios as a function of the kinematic variables: Q^2 (top left), x_B (top right), $-t$ (bottom left), and ϕ (bottom right).

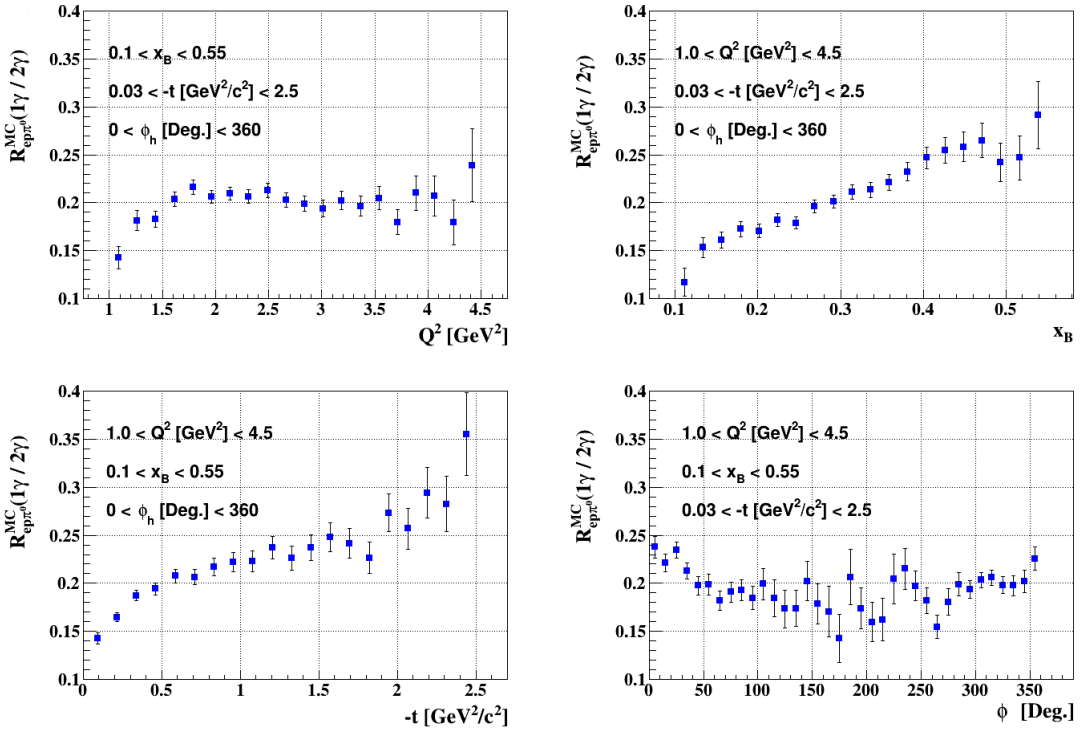


Figure 4.18: The incoherent channel acceptance ratios as a function of the kinematic variables: Q^2 (top left), x_B (top right), $-t$ (bottom left), and ϕ (bottom right).

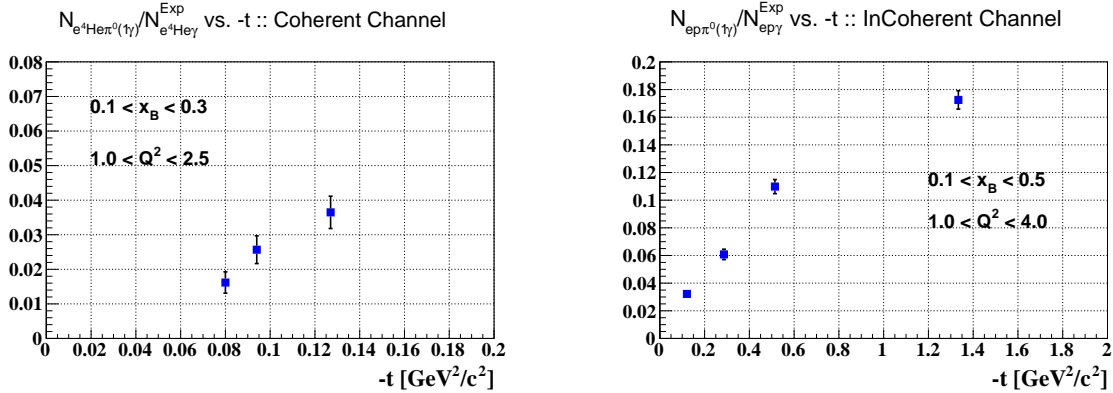


Figure 4.19: The experimental coherent (left) and incoherent (right) π^0 contamination with respect to the experimental DVCS events as a function of the transferred momentum squared $-t$. The data is integrated over the kinematical variables Q^2 , x_B , and ϕ .

We also carried out four-dimensional background subtraction, in which the acceptance ratio has been extracted from simulation as a function of Q^2 , x_B , $-t$, and ϕ . The difference between the reconstructed beam-spin asymmetries using two-dimensional and four-dimensional background subtraction are presented in figures 4.20 and 4.21 for the coherent and the incoherent DVCS channels. Even though the two-dimensional subtraction is a good approximation, a four-dimensional subtraction is applied on the final results presented next chapter.

Regarding other backgrounds, the procedures carried out in this work followed the same guidelines as for DVCS analysis on the nucleon. The neutral pion production occurs "without threshold" as seen from the $eHe\gamma$ sample, meaning that the contamination from $eHe\pi^0$ with one photon lost is distributed all the way down to the DVCS, in the limit where the second photon energy becomes negligible in the lab. Single charged pion production occurs with a small threshold but is inconsistent with the already detected particles (e and 4He). Two pion production is entirely cleaned up by the exclusivity cuts. Scattering from the windows is excluded by the vertex cuts. As far as accidental, we correct for that as presented in the following section.

4.5.2 Accidental contaminations

The Δz distributions between the recoil hadrons and the scattered electrons, see figures 3.23 and 3.11, indicate that accidental background events are contributing inside the exclusive DVCS. In order to estimate and correct this background contribution, we processed our dataset with the previously presented exclusive requirements without any constraints on the z-vertex of the final state particle nor on the correspondence between them, Δz . The results for the identified coherent DVCS events are presented in figure 4.22. This guides us to correct for these accidentals in our asymmetries in the form: $A_{LU \text{ corr.}} = \frac{1}{1-\text{contamination}} A_{LU}$, with a 4.1% global accidental contamination for the coherent DVCS channel (see numbers in table 4.1). The same procedures were performed on the incoherent channel, and a global contamination of 6.5% has been observed.

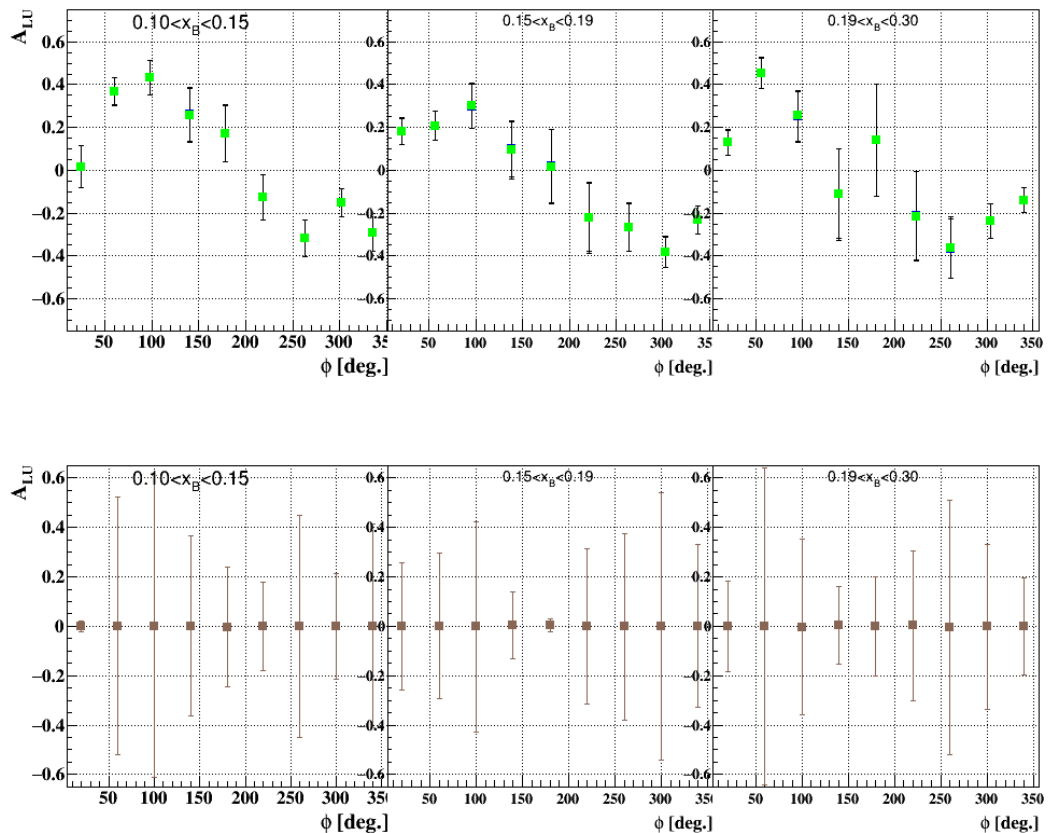


Figure 4.20: On top: the reconstruct coherent beam-spin asymmetries as a function of ϕ in x_B bins using two-dimensional (in blue) and four-dimensional (in green) background subtraction. On bottom: the difference between the two asymmetries as a function of ϕ .

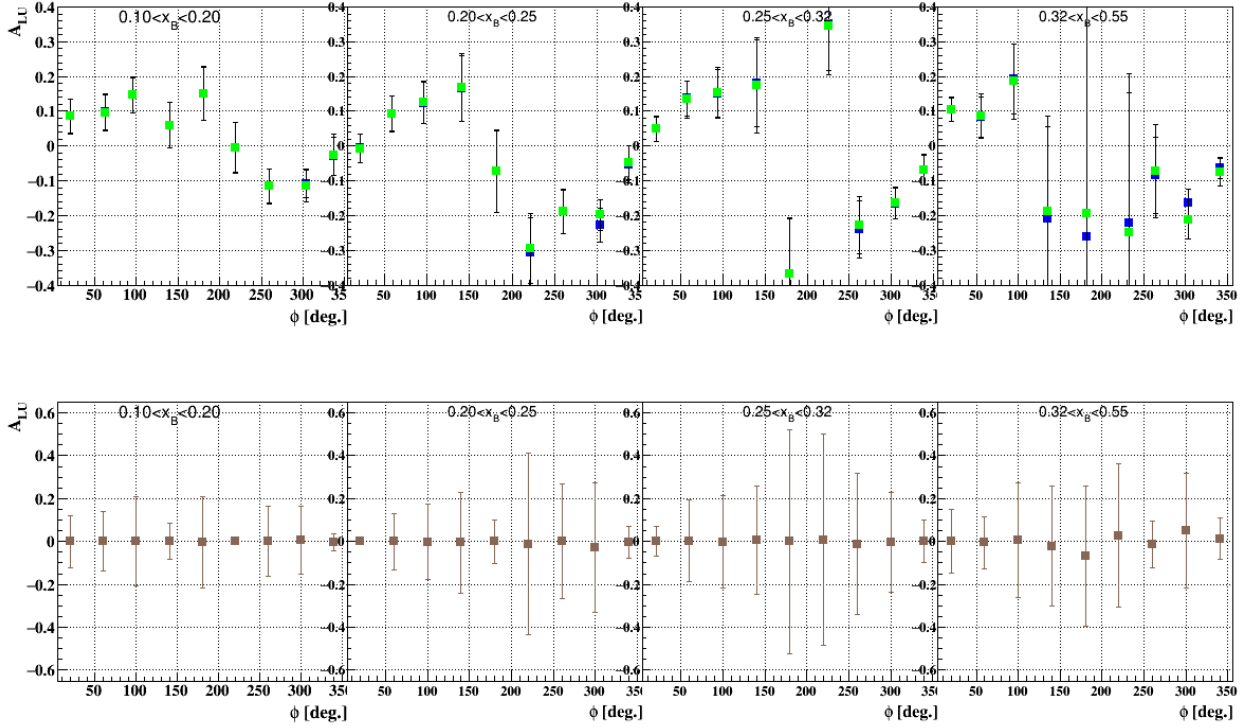


Figure 4.21: On top: the reconstruct incoherent beam-spin asymmetries using two-dimensional (in blue) and four-dimensional (in green) background subtraction. On bottom: the difference between the two asymmetries as a function of ϕ .

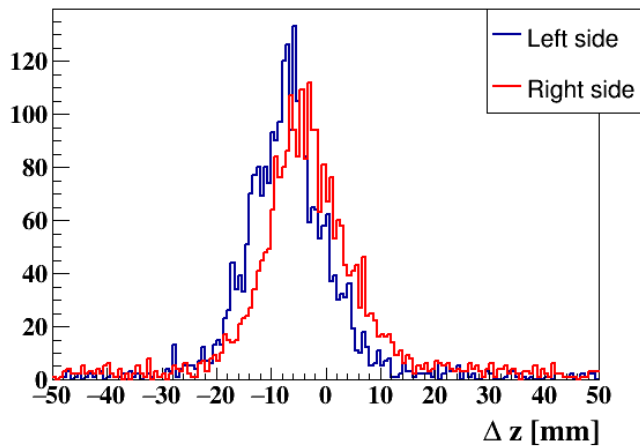


Figure 4.22: The z-vertex correspondence between the scattered electron and the recoil 4He for the identified coherent DVCS events after the exclusivity cuts in the two modules of the RTPC separately without any initial constrains on z-vertices of the individual particles. Table 4.1 summarizes the cut numerically.

Number of coherent DVCS events		
Δz [mm]	Left module	Right module
[-50:-30]	42	77
[-20:20]	2741	2856
[30:50]	34	78
Contamination percentage	2.7%	5.4%

Table 4.1: The numbers of the identified coherent DVCS events in the different regions in Δz for the two modules of the RTPC.

4.6 Statistical uncertainties

In terms of the collected number of events in each beam-helicity state (N^+ , N^-), A_{LU} can be expressed as:

$$A_{LU} = \frac{1}{P_B} \frac{N^+ - N^-}{N^+ + N^-}. \quad (4.13)$$

where P_B is the beam polarization, N^+ and N^- are the background-subtracted yields of DVCS events. The statistical uncertainties on the measured A_{LU} can be derived as:

$$\Delta A = \frac{1}{P_B} \sqrt{\left(\frac{\partial A}{\partial N^+} \right)^2 (\Delta N^+)^2 + \left(\frac{\partial A}{\partial N^-} \right)^2 (\Delta N^-)^2} = \frac{1}{P_B} \sqrt{\frac{(2N^- \Delta N^+)^2 + (2N^- \Delta N^+)^2}{(N^+ + N^-)^4}}, \quad (4.14)$$

where N^+ and N^- are

$$N^\pm = N_{e^4He\gamma}^\pm - R N_{e^4He\pi^0}^\pm, \quad (4.15)$$

and R is the calculated background acceptance ratio from the simulation. The statistical uncertainty on the counts (N^\pm) is

$$(\Delta N^\pm)^2 = (\Delta N_{e^4He\gamma}^\pm)^2 + (R \Delta N_{e^4He\pi^0}^\pm)^2 = N_{e^4He\gamma}^\pm + R^2 N_{e^4He\pi^0}^\pm. \quad (4.16)$$

The errors on P_B and R are not considered statistical errors. They contribute in the systematic uncertainties, as will be discussed in the following section. This derivation is valid for the coherent and the incoherent DVCS channels.

4.7 Systematic uncertainties

It is particularly convenient to use the A_{LU} as a DVCS observable, because most of the experimental systematic uncertainties, such as normalization and efficiencies that appear in the cross sections cancel out in the asymmetry ratio. However, some sources still affect this asymmetry and contribute in the systematic uncertainties on the measured A_{LU} . The main known sources of systematic errors are: the DVCS selection cuts, the fitting sensitivity to our binning, the beam polarization, the background acceptance ratio and the radiative corrections. In the following, we present an estimation of the contribution from each source.

DVCS selection cuts

In order to evaluate the systematic uncertainties stemming from the DVCS selection cuts, the analysis was repeated changing cuts. As it can be seen in figure 4.4, the 3σ cuts cover up to 97% of the events in all the distributions except the $e^4He\gamma$ missing mass distribution. In order to

investigate the effect of taking different cuts on the reconstructed A_{LU} , we fix the 3σ cuts on all the exclusive quantities except for the cut on $e^4He\gamma$ missing mass. For the incoherent channel, the same procedure is carried out on the $ep\gamma$ missing mass distribution. The results can be seen in figure 4.23. The maximum variation that has been observed on the A_{LU} observable between 3σ cut and the other cuts ($\frac{\Delta A_{LU}^{sys,cuts}}{A_{LU}}$) is equal to 8% for the coherent channel and to 6% for the incoherent channel at $\phi = 90^\circ$ extracted from a fit, in the form of $\frac{\alpha \sin(\phi)}{1 + \beta \cos(\phi) + \eta \cos(2\phi)}$, to $A_{LU}(\phi)$ distribution. The fit parameters are plotted as functions of the cut widths in figures 4.24 to 4.28.

Fitting sensitivity to our binning

In order to evaluate how sensitive are the fit results to our binning, we binned the data into 11 bins in ϕ and we compared the reconstructed asymmetries to the results from our 9 binning. Figure 4.29 shows the coherent reconstructed A_{LU} as a function of ϕ in Q^2 , x_B and $-t$ bins. The coherent, figure 4.30, and the incoherent, figure 4.31, measured A_{LU} at $\phi = 90^\circ$ are showing an overall average of 5.1% and 7.1% systematic uncertainties respectively, which will be added to our estimated uncertainties for the extracted asymmetries at $\phi = 90^\circ$.

Beam polarization

The beam polarization has been measured regularly during the CLAS-EG6 data taking period by using the Hall B Møller polarimeter. This polarimeter measures the angular distribution of the Møller electrons to obtain the beam polarization. Figure 4.32 shows the Møller measurements taken during the EG6 experiment. A linear fit to these measurements yields a mean polarization value of 0.8367. The precision of the Hall B Møller polarimeter ($\frac{\Delta P}{P}$) was measured to be around 3.5% [42]. We assume therefore a 3.5% systematic uncertainty on the measured asymmetries ($\frac{\Delta A_{LU}^{sys,p}}{A_{LU}} = \frac{\Delta P}{P}$).

Acceptance ratio

Predominantly, two techniques are used to estimate the systematic uncertainty associated with the calculated acceptance ratio (R). The first is via repeating the analysis by implementing R differently, while the second technique is by using two generating models to calculate R.

Both methods were investigated in this work. Regarding the first method, the analysis was repeated by taking three different values for R: 0.8^*R , R and 1.2^*R . The beam-spin asymmetries at $\phi = 90^\circ$ were extracted and compared, see figure 4.33. A maximum variation of 2% (0.6%) has been observed on the incoherent (coherent) A_{LU} at $\phi = 90^\circ$.

For the second technique, in fact there is only one event generator available, presented in section 3.2.1. Nevertheless, one can still use this method by generating events with or without the cross section parametrization. In the absence of the parametrization, the generated events are flat in the four kinematic variables (Q^2 , $-t$, x_B , ϕ). The calculated coherent and incoherent acceptance ratios (R) with and without the cross section parametrization are shown in figure 4.34. One can see that the difference between the calculated acceptance ratios is almost constant. Thus, we can conclude that the first method of taking $\pm 20\%$ on R is an adequate way to obtain an estimation of the systematic uncertainty associated to the calculated acceptance ratios.

Radiative corrections

In this analysis, we have assumed that the beam-spin asymmetry arises from the leading twist DVCS amplitude and its interference with the BH process. However, there are higher-order electromagnetic corrections which can affect the beam-spin asymmetry. Andrei V. Afanasev and

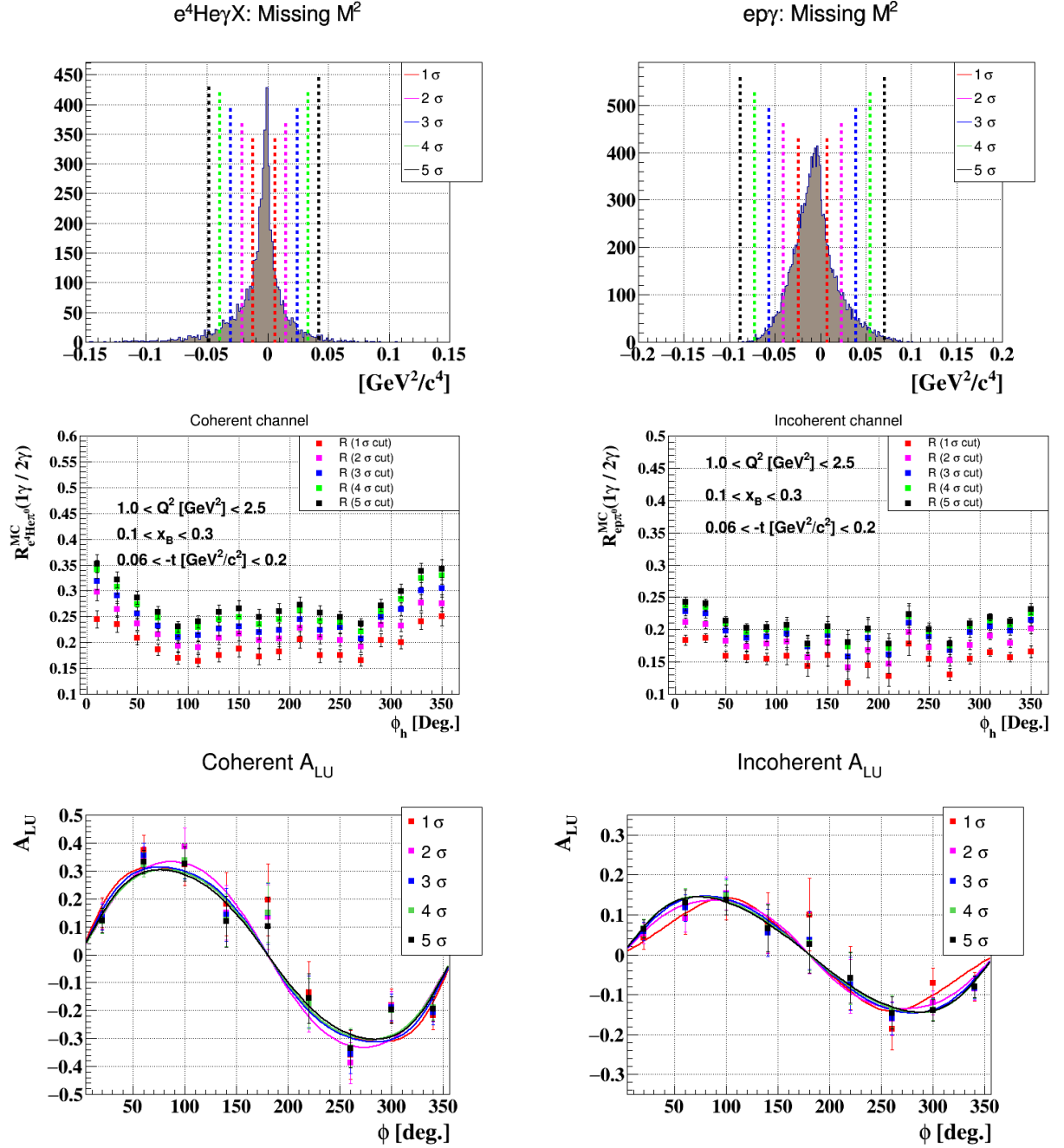


Figure 4.23: The systematic uncertainties stemming from the DVCS selection cuts in the coherent (left column) and the incoherent (right column) channels. On the top: the missing mass squared of $e^4He\gamma$ and $ep\gamma$. The different vertical coloured lines indicate the different cuts: 1σ , 2σ , ... 5σ . In the middle: the coherent (incoherent) acceptance ratios versus ϕ for the different configurations of the cuts. On the bottom: the reconstructed A_{LU} as a function of ϕ_h for the different cut widths.

his collaborators have estimated the corrections to A_{LU} which arise from such effects in a model-independent way [43]. They have performed one-loop corrections on the outgoing electron as only the radiation from it affects the A_{LU} . They found that the correction does not exceed 0.1% at a 4.25 GeV electron beam energy and $Q^2=1.25 \text{ GeV}^2$. In our case, as the radiative emission is inversely proportional to the mass of the radiating particle, the helium and the proton contributions are negligible compared to the leptonic one. Therefore, we can still take the result of Afanasev as a

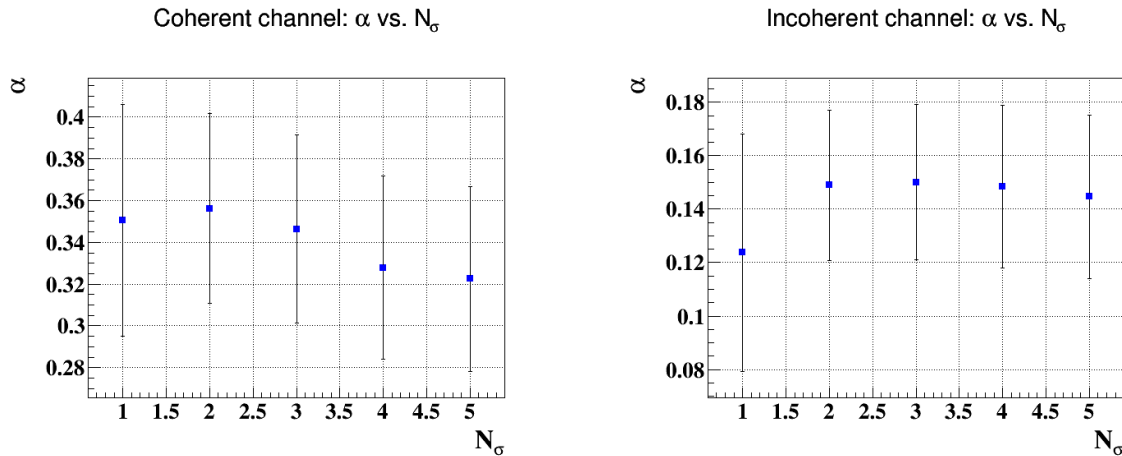


Figure 4.24: The coherent (left) and incoherent (right) α parameter of the fits as a function of cut width.

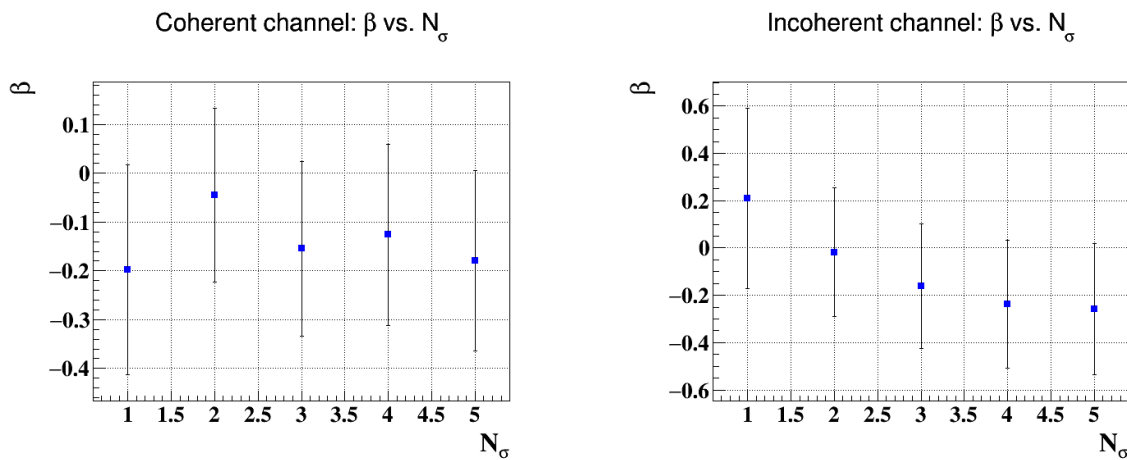


Figure 4.25: The coherent (left) and incoherent (right) β parameter of the fits as a function of cut width.

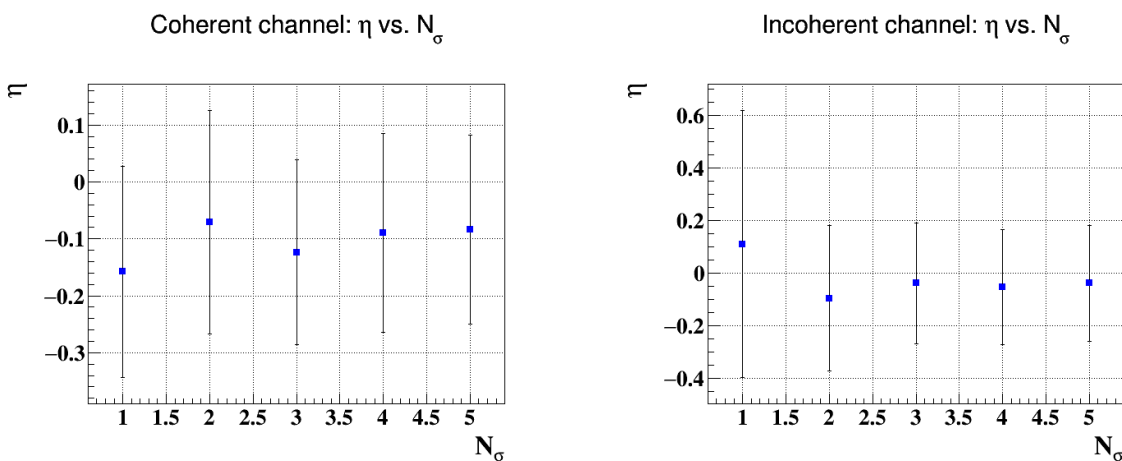


Figure 4.26: The coherent (left) and incoherent (right) η parameter of the fits as a function of cut width.

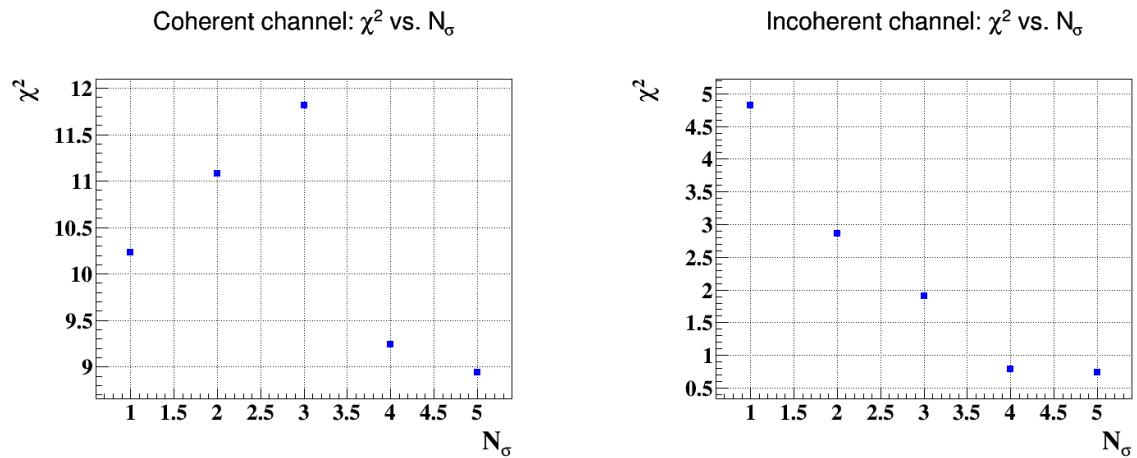


Figure 4.27: The coherent (left) and incoherent (right) χ^2 parameter of the fits as a function of cut width.

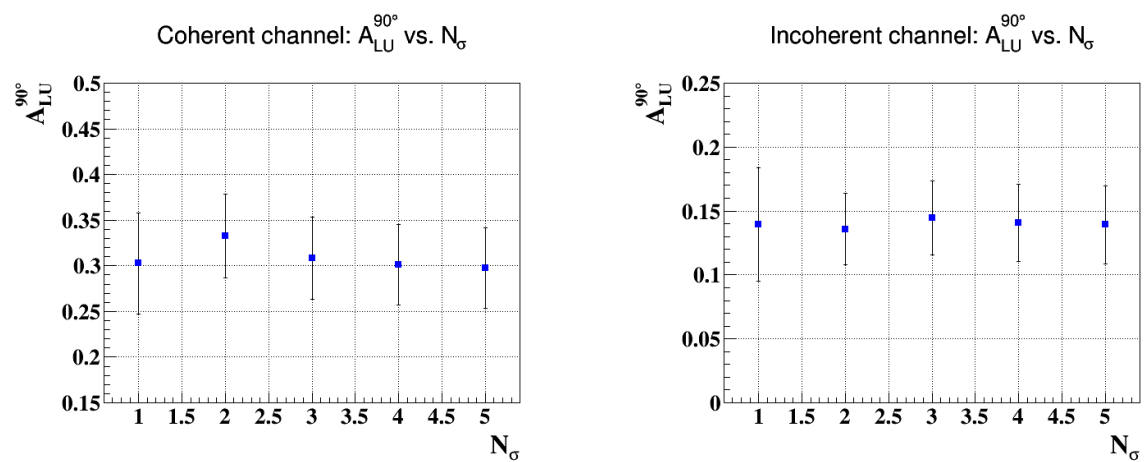


Figure 4.28: The coherent (left) and incoherent (right) beam-spin asymmetry at $\phi = 90^\circ$.

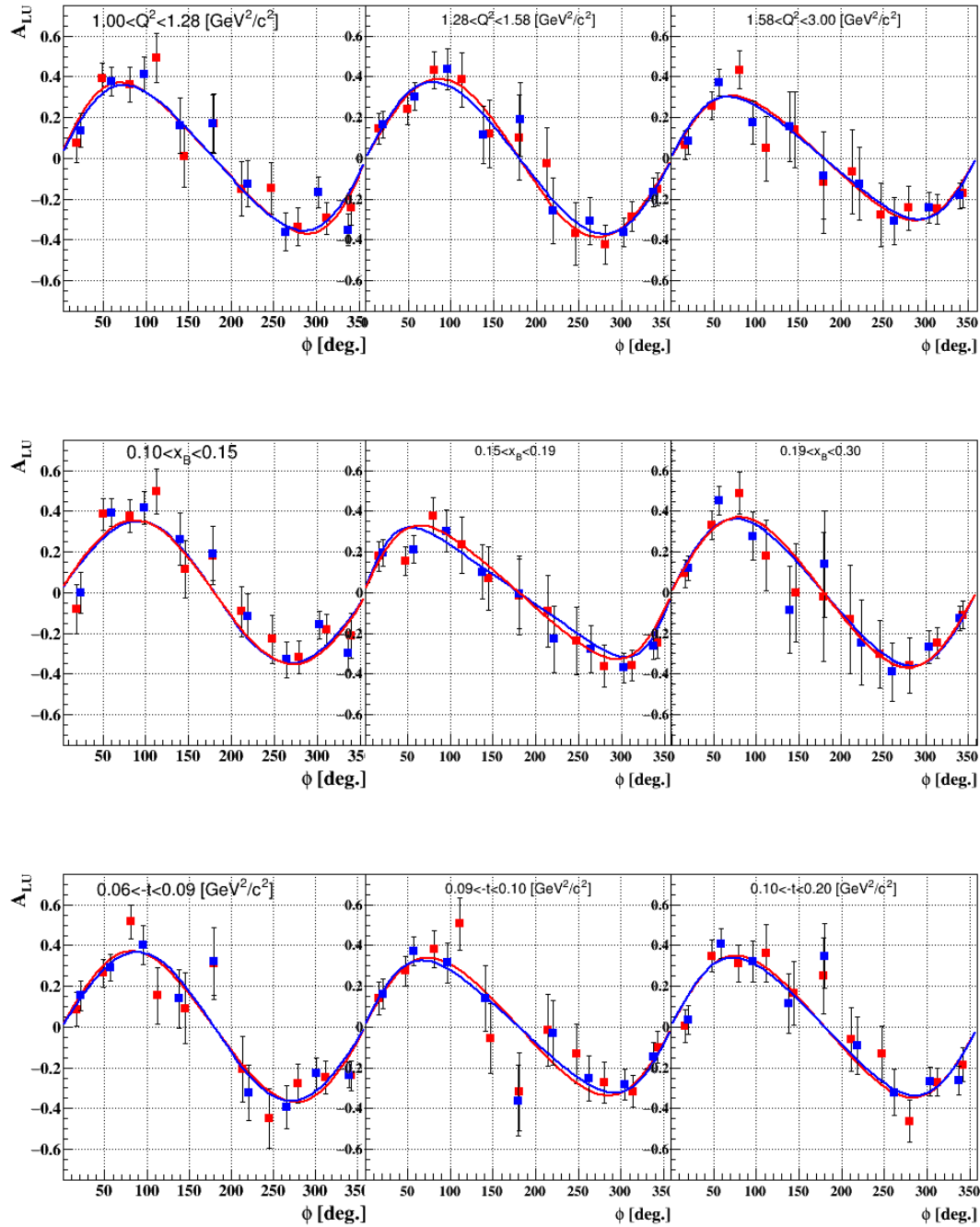


Figure 4.29: The measured coherent beam-spin asymmetry as a function of ϕ in Q^2 , x_B and $-t$ bins, using two binning sets in ϕ : 9 bins (in blue) and 11 bins (in red).

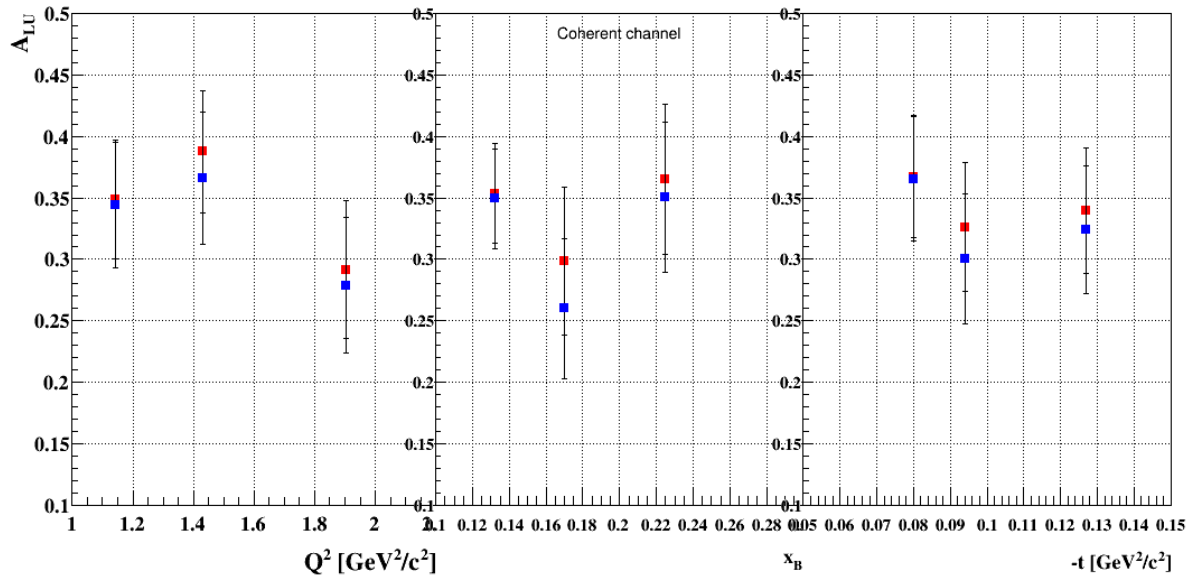


Figure 4.30: The coherent $A_{LU}(\phi = 90^\circ)$, from the fit, as a function of Q^2 , x_B and $-t$, using 9 (in blue) and 11 (in red) bins in ϕ .

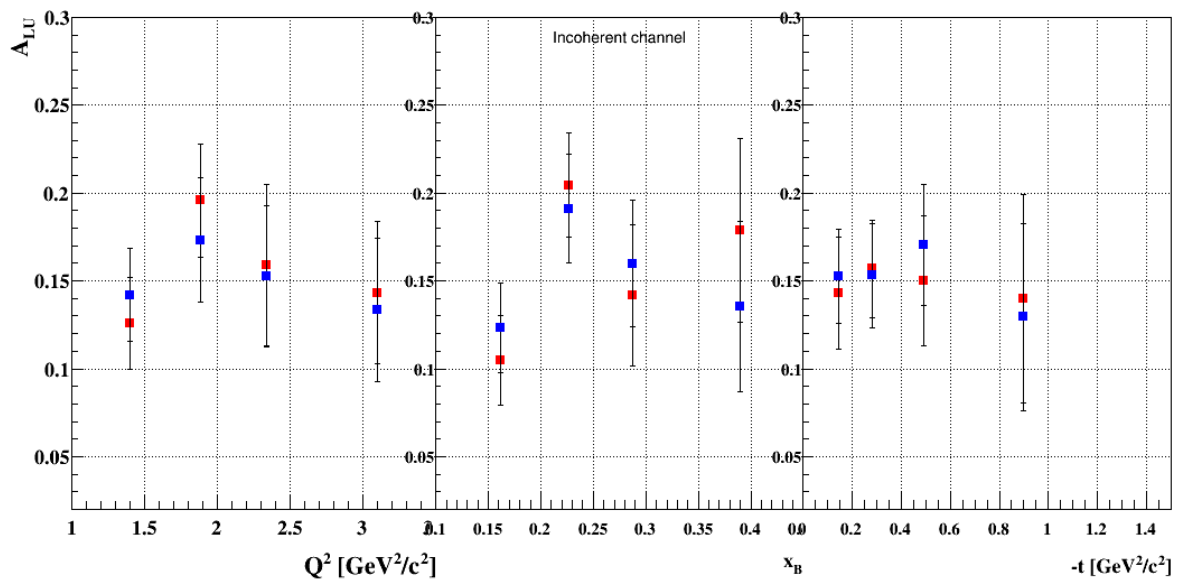


Figure 4.31: The incoherent $A_{LU}(\phi = 90^\circ)$, from the fit, as a function of Q^2 , x_B and $-t$, using 9 (in blue) and 11 (in red) bins in ϕ .

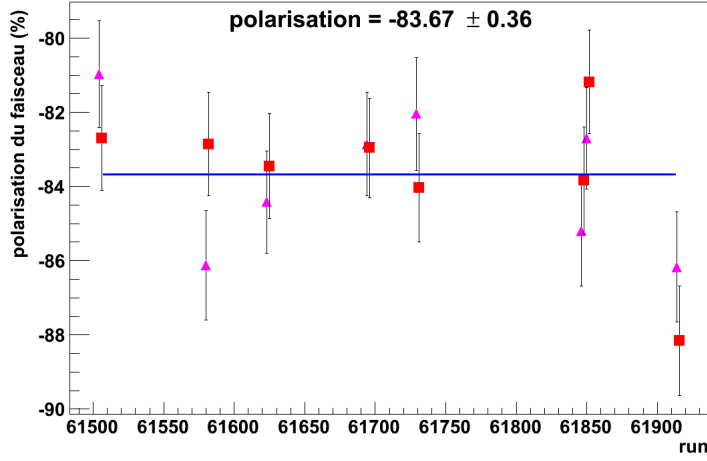


Figure 4.32: Beam polarization measurements during the CLAS-EG6 running period. The red squares are the measurements with a negative current in the Helmholtz coils of the Møller polarimeter and the purple triangles are these with a positive current. The figure is taken from [36].

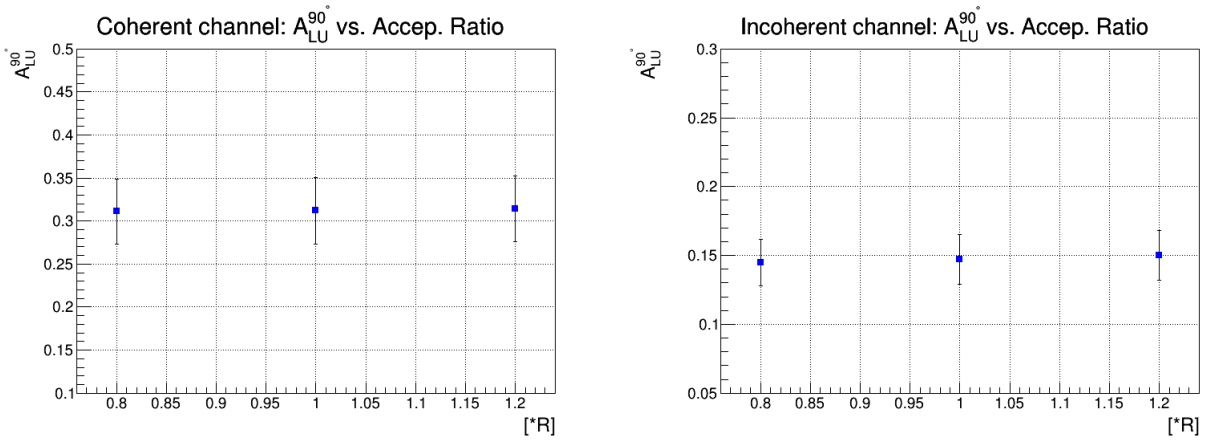


Figure 4.33: The extracted beam-spin asymmetries at $\phi = 90^\circ$ as a function of three sets of the calculated acceptance ratios: 0.8^*R , 1.0^*R and 1.2^*R , for the coherent (on the left) and the incoherent (on the right) DVCS channels.

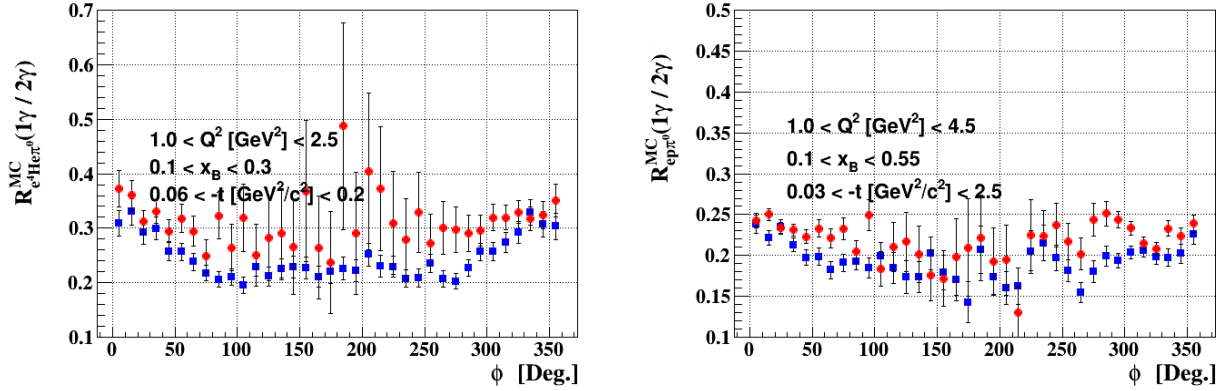


Figure 4.34: The coherent (on the left) and the incoherent (on the right) acceptance ratios (R) as function of the angle ϕ . In both plots, the blue (red) points are the ratios with (without) the cross section parametrization.

good estimation for the radiative effects on our measured A_{LU} .

Systematic uncertainty summary

The total systematic uncertainty is the quadratic sum of the previously described individual uncertainties. Table 4.2 summarizes the sources of systematic uncertainty and their contributions on the measured A_{LU} at $\phi = 90^\circ$, that will be added quadratically to the statistical uncertainties on A_{LU} .

Systematic source	Coherent channel	Incoherent channel	Type of systematic error
DVCS cuts	8 %	6 %	bin to bin
Data binning	5.1%	7.1%	bin to bin
Beam polarization	3.5%	3.5%	Normalization
Acceptance ratio	0.6%	2.0%	bin to bin
Radiative corrections	0.1%	0.1%	bin to bin
Total	10.1%	10.1%	bin to bin

Table 4.2: The systematic uncertainties on the measured coherent and incoherent beam-spin asymmetries at $\phi = 90^\circ$.

In addition to evaluating the systematic uncertainties on A_{LU} at $\phi = 90^\circ$, we performed bin by bin, in ϕ , extraction of these uncertainties. For instance, regarding the bin extraction from the source 'data binning' listed in table 4.2, the uncertainty is calculated as the difference between the two reconstructed asymmetries. Similar procedures have been carried out for the other studies, and finally all the contributions were added quadratically. These systematic uncertainties will be shown with the final asymmetry results in the following chapter.

Results and physics interpretations

In this chapter, we present our results after all corrections discussed above and including all systematic errors. In order to discuss these results, we first present the functional forms we will use to fit them, which are different for the coherent and incoherent channels. For the coherent channel, we use exact formula from [38] to extract the real and imaginary parts of the CFF \mathcal{H}_A at twist-2. For the incoherent channel, we use a simplified form and only extract the asymmetry at 90° . Then we present the beam-spin asymmetry measurements for both DVCS channels with their aforementioned fits and draw some first conclusions. Finally we present ratios of our asymmetry to free proton results from CLAS (E1-DVCS part-1 [38, 48]).

5.1 Fitting the beam-spin asymmetry

For a spin-zero target at leading twist, the beam-spin asymmetry (A_{LU}) can be expressed as follow [4]

$$A_{LU}(\phi) = \frac{\alpha_0(\phi) \Im m(\mathcal{H}_A)}{\alpha_1(\phi) + \alpha_2(\phi) \Re e(\mathcal{H}_A) + \alpha_3(\phi) (\Re e(\mathcal{H}_A)^2 + \Im m(\mathcal{H}_A)^2)} \quad (5.1)$$

where $\Im m(\mathcal{H}_A)$ and $\Re e(\mathcal{H}_A)$ are the imaginary and real parts of the CFF \mathcal{H}_A associated to the GPD H_A . The α_i 's are ϕ -dependent kinematical factors that depend on the nuclear form factor F_A and the independent variables Q^2 , x_B and t . These factors are simplified as:

$$\alpha_0(\phi) = \frac{x_A(1+\varepsilon^2)^2}{y} S_{++}(1) \sin(\phi) \quad (5.2)$$

$$\alpha_1(\phi) = c_0^{BH} + c_1^{BH} \cos(\phi) + c_2^{BH} \cos(2\phi) \quad (5.3)$$

$$\alpha_2(\phi) = \frac{x_A(1+\varepsilon^2)^2}{y} (C_{++}(0) + C_{++}(1) \cos(\phi)) \quad (5.4)$$

$$\alpha_3(\phi) = \frac{x_A^2 t (1+\varepsilon^2)^2}{y} \mathcal{P}_1(\phi) \mathcal{P}_2(\phi) \cdot 2 \frac{2 - 2y + y^2 + \frac{\varepsilon^2}{2} y^2}{1 + \varepsilon^2} \quad (5.5)$$

Where $S_{++}(1)$, $C_{++}(0)$, and $C_{++}(1)$ are the Fourier harmonics in the leptonic tensor. Their explicit expressions can be found in Appendix A.

Using the α_i factors, one can obtain in a model-independent way $\Im m(\mathcal{H}_A)$ and $\Re e(\mathcal{H}_A)$ from fitting the experimental A_{LU} as a function of ϕ for given values of Q^2 , x_B and t . Equation 5.1 is the functional form we use to fit the coherent asymmetries presented in this analysis.

Regarding the incoherent channel, the beam-spin asymmetry signals will be fitted by the simple form $\frac{\alpha \sin(\phi)}{1 + \beta \cos(\phi)}$, which has been used for DVCS on free proton, see reference [38, 48], and allows an easy extraction of $A_{LU}^{90^\circ}$.

5.2 Beam-spin asymmetry results and fit

In this section, the beam-spin asymmetries will be compared to the theoretical calculations based on the two models that were presented in section 1.1.2.

5.2.1 Coherent beam-spin asymmetry

Figure 5.1 shows the coherent A_{LU} for the three sets of two-dimensional bins. The asymmetries are fitted with the form of equation 5.1, where the real and the imaginary part of the CFF \mathcal{H}_A are the free parameters in the fit.

Figure 5.2 shows the Q^2 , x_B , and $-t$ -dependencies of the α term of A_{LU} . The x_B and $-t$ -dependencies are compared to theoretical calculations performed by S. Liuti and K. Taneja. Their model relies on the impulse approximation and uses advanced spectral function of the nuclei to calculate the nuclear GPDs and then the observables. The calculations were carried out at slightly different kinematics than ours but provide already some guidance. The experimental results appear to have larger asymmetries compared to the calculations. These differences may arise from nuclear effects which are not taken into account in the model, such as long-range interactions [16]. Our measurements also agree with those of HERMES, considering their large uncertainties.

5.2.2 Incoherent beam-spin asymmetry

Figure H.5 shows our measured incoherent beam-spin asymmetries, for the three sets of the two-dimensional bins as for the incoherent channel. The Q^2 , x_B , and $-t$ -dependencies of A_{LU} at $\phi = 90^\circ$ (the α parameter of the fit) are shown in figure H.6.

The theoretical calculations from S. Liuti and K. Taneja are carried out at slightly different kinematics than our experimental measured values. Nevertheless, one can see that our incoherent asymmetries are not well described by these calculations. For instance, in the top right plot of figure H.6, even though our asymmetries (at $-t = 0.2 \text{ GeV}^2/\text{c}^2$) are located between the model's predictions, which are carried out at $-t = 0.095$ and $0.329 \text{ GeV}^2/\text{c}^2$, they do not show the drop in $\langle x_B \rangle$, as the model predicted. Similar observation can be seen as a function of $-t$ from the bottom plot.

5.3 Helium GPD

As shown at the beginning of this chapter, one can extract both real and imaginary parts of the ${}^4\text{He}$ CFF \mathcal{H}_A from fitting the beam-spin asymmetry signals. This extraction is fully model independent and, in contrast with the proton's GPD extraction, does not make any assumption on additional GPDs. In this work, we performed the first experimental extraction of \mathcal{H}_A from exclusive measurements of the reaction. The results are presented in figure 5.5 as function of Q^2 , x_B , and $-t$.

Within the given uncertainties, our results show a slight dependence on Q^2 , x_B , and $-t$, which are in agreement with the theoretical calculations for \mathcal{H}_A . One can see a difference between the precision of the extracted real and imaginary parts, indicating the fact that the beam-spin asymmetry is mostly sensitive to the imaginary part of the CFF \mathcal{H}_A .

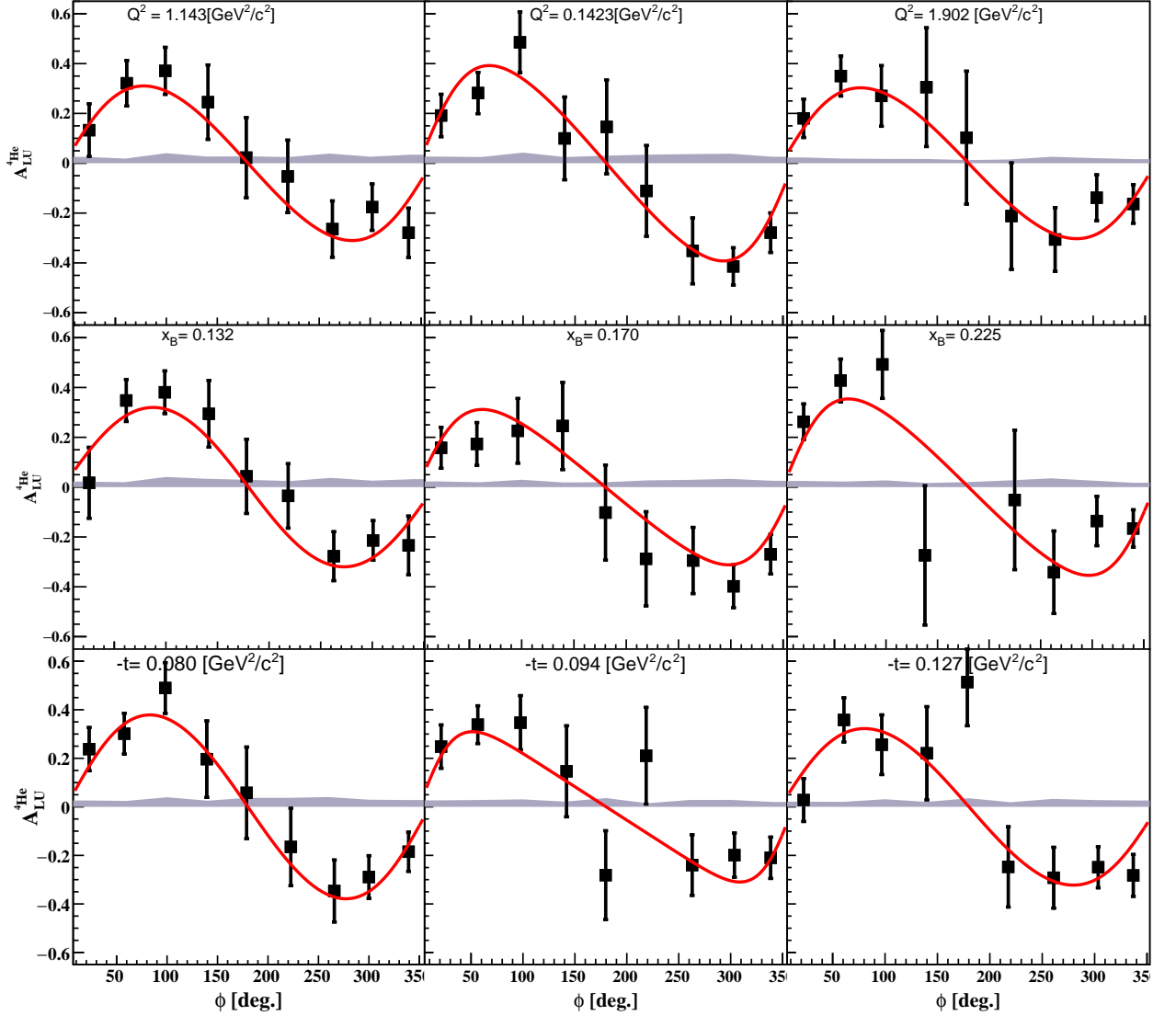


Figure 5.1: The coherent A_{LU} as a function of ϕ and Q^2 (top panel), x_B (middle panel), and $-t$ (bottom panel) bins. The black error bars represent the statistical uncertainties. The bluish-gray bands represent the systematic uncertainties, including the normalisation systematic uncertainties. The red curves represent fits, in the form of equation 5.1, for the asymmetries with the statistical and the systematic uncertainties added quadratically.

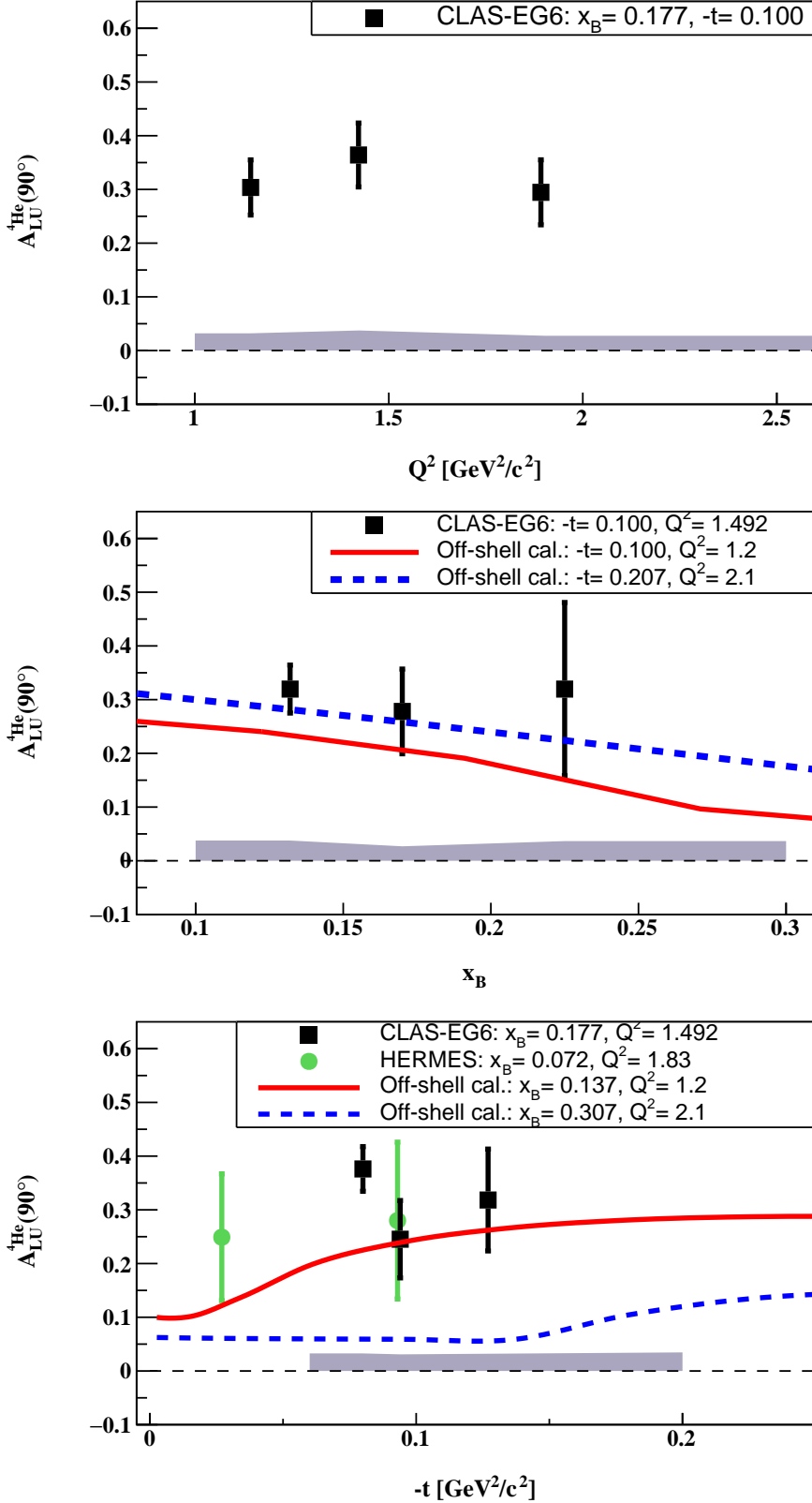


Figure 5.2: The Q^2 -dependence (on the top), the x_B -dependence (on the middle), and the t -dependence (on the bottom) of the fitted coherent A_{LU} signals at $\phi = 90^\circ$ (black squares). On the middle: the red and the blue curves are theoretical predictions from [16] at two values of $-t$. On the bottom: the green circles are the HERMES $-A_{LU}$ (positron beam was used) inclusive measurements [18], and the colored curves represent theoretical predictions from [16].

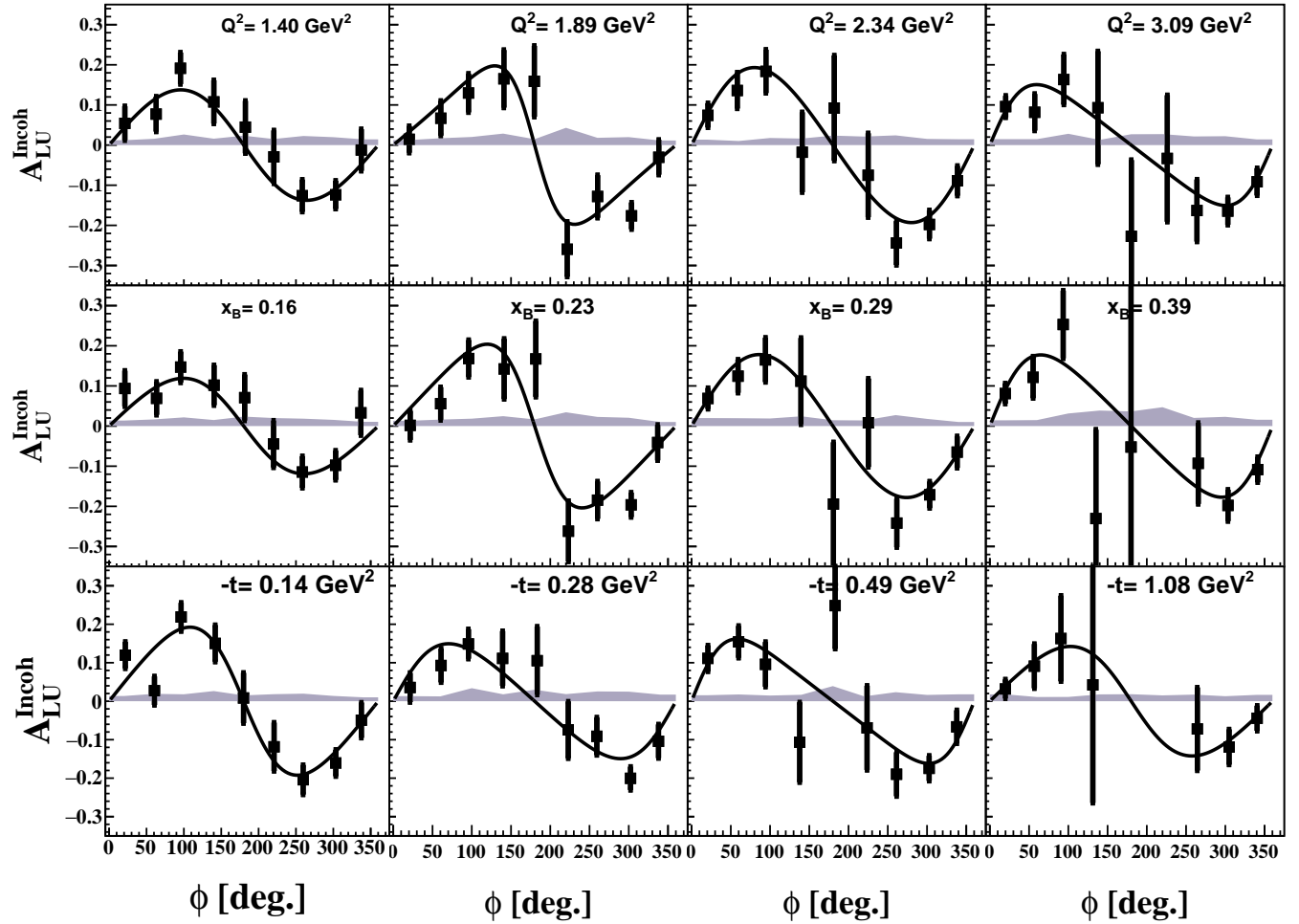


Figure 5.3: The incoherent A_{LU} as a function of the angle ϕ in Q^2 , x_B , and $-t$ bins, respectively from top to bottom. See the caption of figure 5.1 for the color indications. The red lines represent fits to the $\frac{\alpha \sin(\phi)}{1 + \beta \cos(\phi)}$ function.

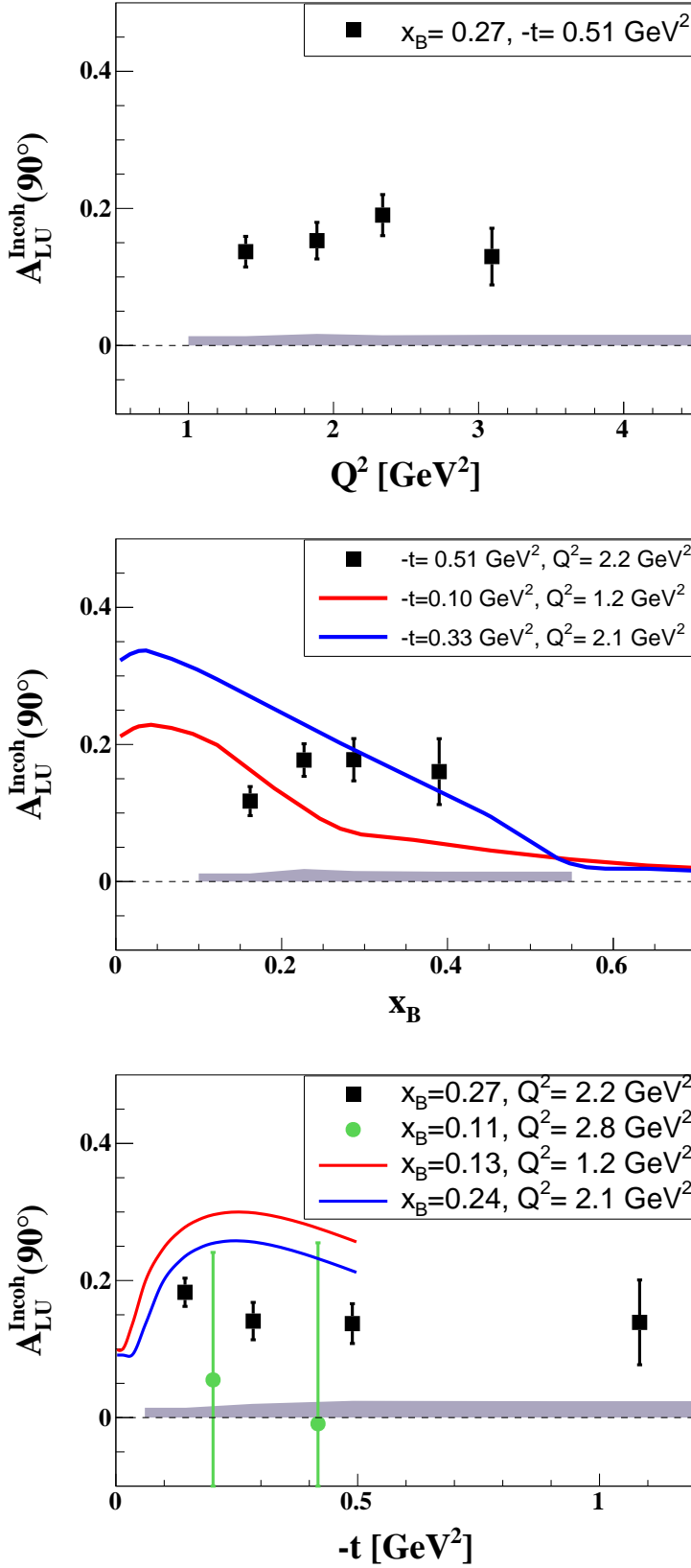


Figure 5.4: The Q^2 (top), x_B (middle), and $-t$ -dependencies (bottom) of the incoherent A_{LU} at $\phi = 90^\circ$ (black squares). Middle panel: the red and the blue curves are theoretical calculations from [16]. On the bottom: the green circles are the HERMES $-A_{LU}$ (positron beam was used) inclusive measurements [18], the colored curves represent theoretical calculations from [16].

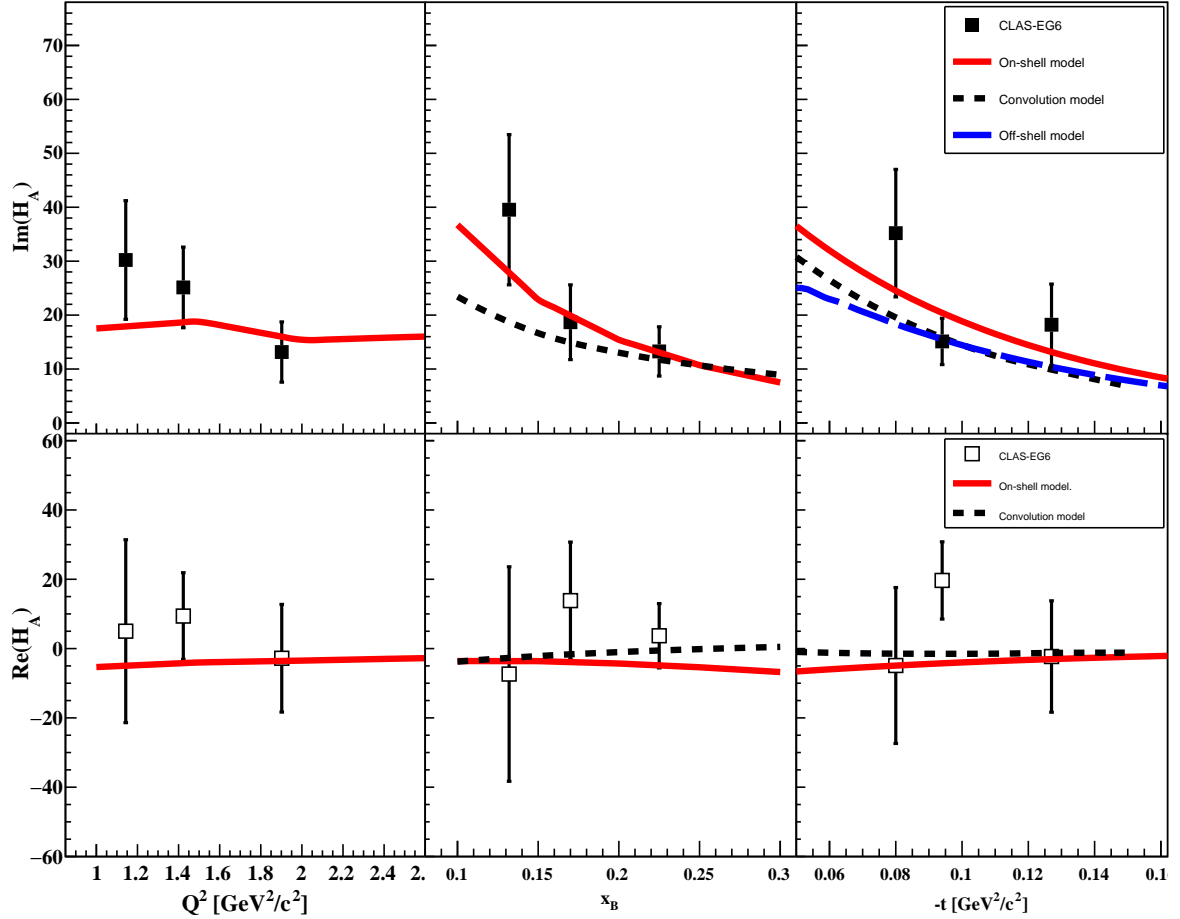


Figure 5.5: The model-independent extraction of the imaginary (black full squares in the top panel plots) and real (empty black squares in the bottom panel plots) parts of the ${}^4\text{He}$ CFF \mathcal{H}_A , as functions of Q^2 (on the left), x_B (on the middle), and t (on the right). The full red curves are calculations based on the impulse approximation from [49]. The black dashed curves are calculations from a convolution model based on the VGG model for the nucleon's GPDs [50]. The blue long-dashed curve on the top-right plot is from the off-shell calculations presented in section 1.1.2 based on reference [51].

5.4 Generalized EMC ratios

Comparing our measured DVCS channels to the free-proton DVCS reaction allows us to investigate the nuclear medium effects at the GPD level. For this we use analyzes performed on free-proton with the DVCS data sets taken by the CLAS collaboration, during the E1-DVCS experiment (parts 1 and 2). The results of part 1 are already published [38, 39]. Herein, our coherent and incoherent beam-spin asymmetries are compared to the results of free proton asymmetries from this publication.

The explored kinematical ranges of Q^2 , x_B and $-t$ of the free-proton data are similar to the ones of the incoherent channel, and the two data sets were recorded using similar electron-beam energies and experimental setup. Therefore, we construct A_{LU} ratios based on choosing the free proton bins which have similar Q^2 , x_B and $-t$ values as our bins. The incoherent A_{LU} ratios at $\phi = 90^\circ$ are shown in figure I.4 as functions of Q^2 , x_B , and $-t$, along with theoretical predictions at similar kinematical values.

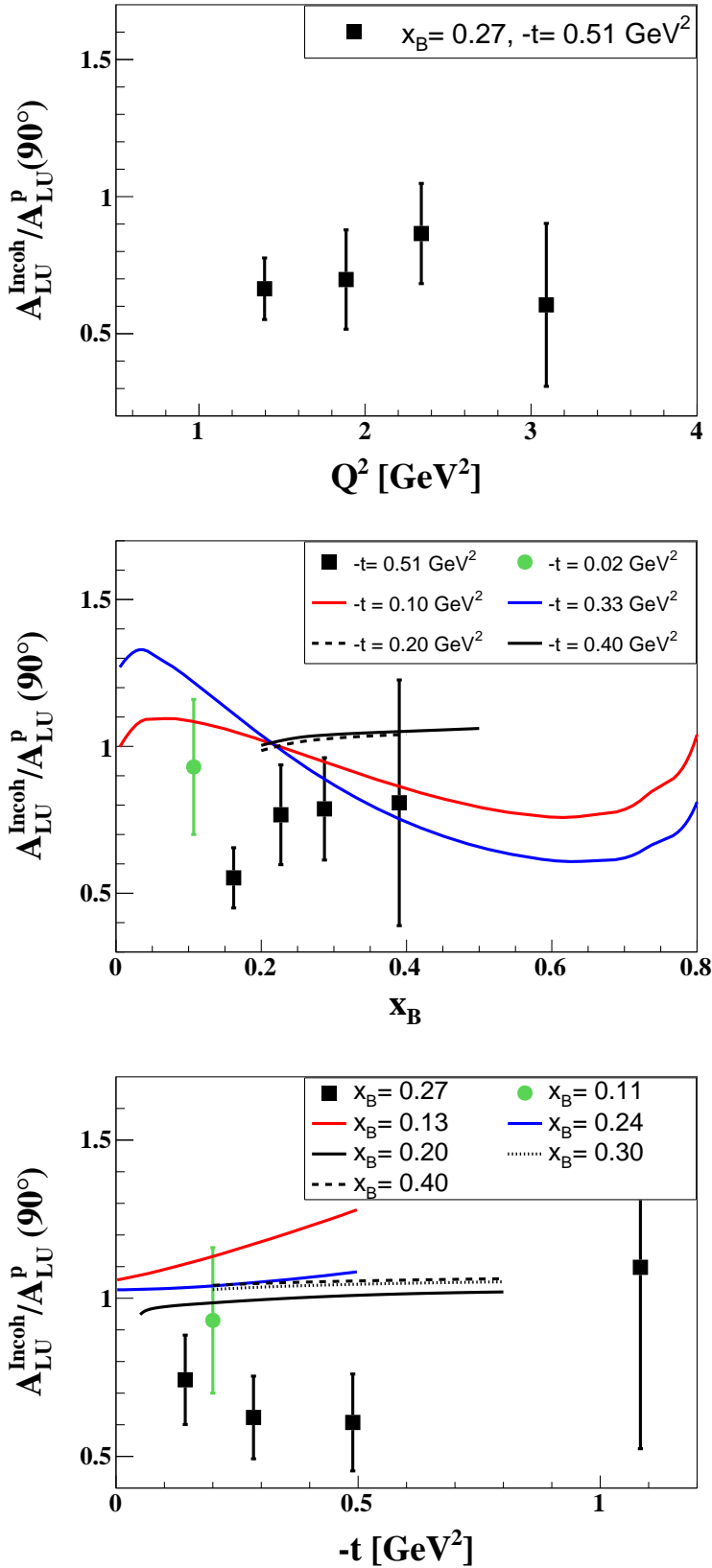


Figure 5.6: The A_{LU} ratio between the bound and the free proton at $\phi = 90^\circ$, as a function of Q^2 (on the top), x_B (on the middle), and t (on the bottom). The black squares are our results, the green circles are the HERMES inclusive measurement [18] results. The blue and red curves are from an on-shell calculations from S. Liuti and K. Taneja [16]. The solid and dashed black curves are from the off-shell calculations [14].

Overall the A_{LU} ratios, one can see that the bound protons have 20-40% smaller beam spin asymmetries than the free protons. These measurements disagree with the enhancement predicted by the simple impulse approximation of V. Guzey [14], as can be seen in chapter 1, figure 1.5. The calculations of S. Liuti and K. Taneja [16] also overshoot the data indicating a trend. In particular, the anti-shadowing region seems to be absent in terms of the A_{LU} ratio, while it was predicted by the calculation. Before to draw any strong conclusions on the structure of bound protons, it remains to be understood what parasitic effects can create such a decrease. In particular, final state interactions need to be evaluated, as they could dilute the signal. Within the given uncertainties, our measured ratios are compatible with the previous measured single point from HERMES.

More attention is needed in constructing the coherent A_{LU} ratio between ${}^4\text{He}$ and the free proton. One can see from figure 4.15 that the coherent experimental ranges of Q^2 , x_B and $-t$ are limited compared to the incoherent channel especially in the $-t$ -domain. The latter is due to the fact that the nuclear form factor of the ${}^4\text{He}$ has a steeper drop in $-t$ than the nucleonic one. Our coherent DVCS data set was binned in 3 bins in Q^2 to show Q^2 -dependence of the coherent A_{LU} ratio. Similar procedures were performed to shows the x_B -dependence. For the dependence on $-t$, the data are integrated to one bin to optimize a more precise ratio. The results are presented in figure 5.7 along with the available theoretical predictions for this ratio. Our measurements shows a nuclear beam-spin asymmetry enhancement compared to the free proton. The measured ratios are not matching the measurement of HERMES collaboration [18], pausing the question of weather they actually measured coherent DVCS. It is also in conflict with the calculations of Liuti and K. Taneja [16], which is missing the large observed increase. On the other hand, our measurements seems to agree with the enhancement predicted by V. Guzey [44]. Moreover, A. Kirchner and D. Mueller (KM model) [3], using their formalism of GPDs factorization, have predicted a beam-spin asymmetry ratio of 1.4 (0.35/0.25) for all different spin-zero nuclei at $x_B=0.3$, $E_b=6\text{GeV}$, $-t=0.25\text{ GeV}^2$, and $Q^2=2.5\text{ GeV}^2$.

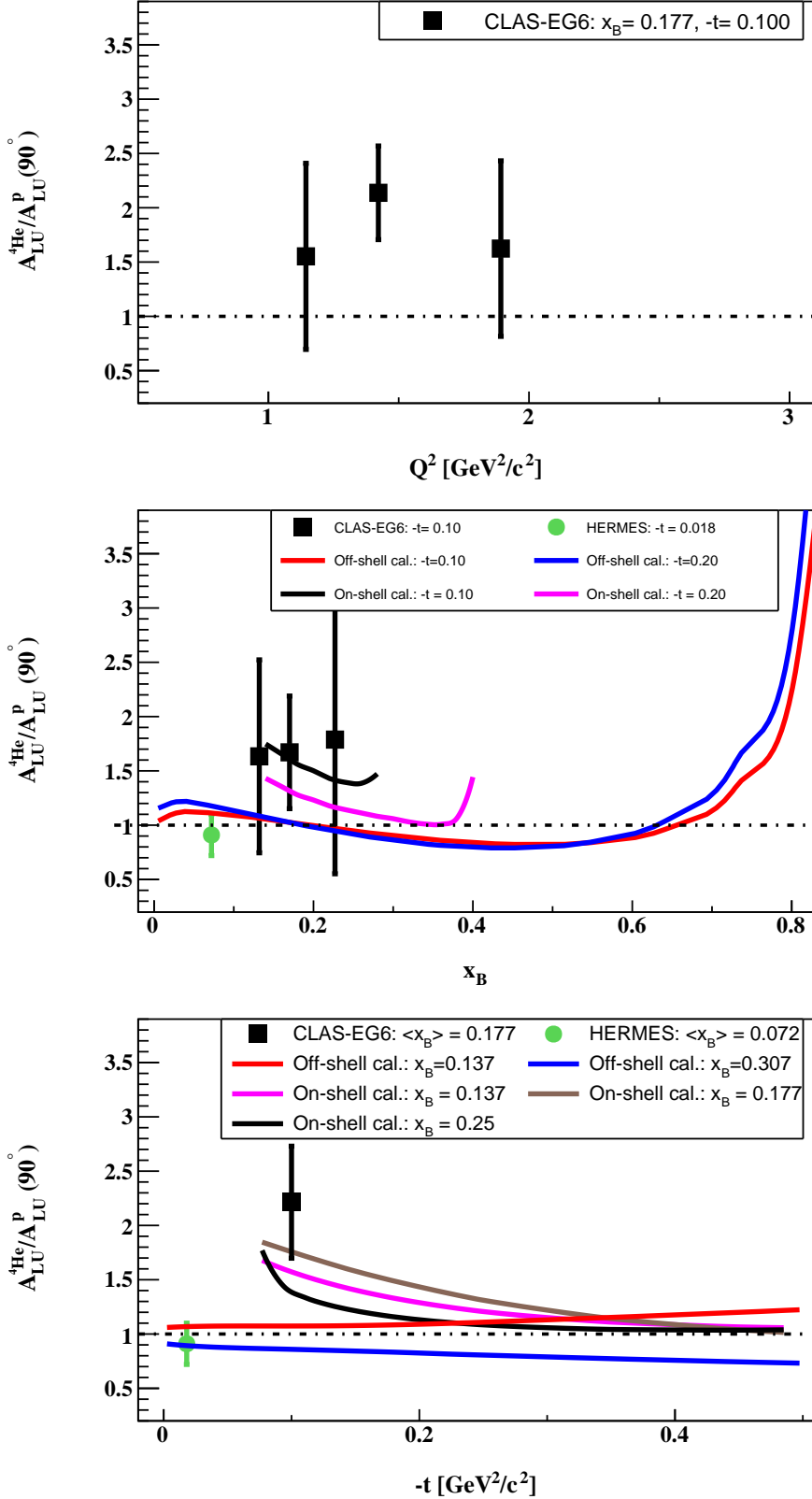


Figure 5.7: The A_{LU} ratio between ${}^4\text{He}$ and free proton at $\phi = 90^\circ$, as a function of Q^2 (on the top), x_B (on the middle), and $-t$ (on the bottom). The black squares represent the results of this work and the green circles are the HERMES measurements [18]. These measurements are compared to theoretical predictions from S. Liuti and K. Taneja [16], the red and the blue curves, and the model predictions from V. Guzey et al. based on the off-shell calculations [44], in black, purple and brown curves.

APPENDIX A

$e^- {}^4He \rightarrow e^- {}^4He \gamma$ cross section

The differential cross section for a longitudinally-polarized electron beam (λ) and an unpolarized 4He target can be written as:

$$\frac{d^5\sigma_\lambda}{dx_A dQ^2 dt d\phi_e d\phi} = \frac{\alpha^3}{16\pi^2} \frac{x_A y^2}{Q^4 \sqrt{1+\varepsilon^2}} \frac{|\mathcal{T}_{BH}|^2 + |\mathcal{T}_{DVCS}^\lambda|^2 + \mathcal{I}_{BH*DVCS}^\lambda}{e^6} \quad (\text{A.1})$$

where $y = \frac{p \cdot q}{p \cdot k}$, $\varepsilon = \frac{2x_A M_A}{Q}$ and $x_A = \frac{Q^2}{2p \cdot q}$. The different amplitudes can be written as [4]:

$$|\mathcal{T}_{BH}|^2 = \frac{e^6(1+\varepsilon^2)^{-2}}{x_A^2 y^2 t \mathcal{P}_1(\phi) \mathcal{P}_2(\phi)} \left[c_0^{BH} + c_1^{BH} \cos(\phi) + c_2^{BH} \cos(2\phi) \right] \quad (\text{A.2})$$

$$|\mathcal{T}_{DVCS}|^2 = \frac{e^6}{y^2 Q^2} \left[c_0^{DVCS} + \sum_{n=1}^2 \left(c_n^{DVCS} \cos(n\phi) + \lambda s_n^{DVCS} \sin(n\phi) \right) \right] \quad (\text{A.3})$$

$$\mathcal{I}_{BH*DVCS} = \frac{\pm e^6}{x_A y^3 t \mathcal{P}_1(\phi) \mathcal{P}_2(\phi)} \left[c_0^I + \sum_{n=0}^3 \left(c_n^I \cos(n\phi) + \lambda s_n^I \sin(n\phi) \right) \right] \quad (\text{A.4})$$

where $\mathcal{P}_1(\phi)$ and $\mathcal{P}_2(\phi)$ are BH propagators and defined as:

$$\mathcal{P}_1(\phi) = \frac{(k - q')^2}{Q^2} = -\frac{1}{y(1+\varepsilon^2)} [J + 2K \cos(\phi)] \quad (\text{A.5})$$

$$\mathcal{P}_2(\phi) = \frac{(k - \Delta)^2}{Q^2} = 1 + \frac{t}{Q^2} + \frac{1}{y(1+\varepsilon^2)} [J + 2K \cos(\phi)] \quad (\text{A.6})$$

with,

$$J = \left(1 - y - \frac{y\varepsilon^2}{2} \right) \left(1 + \frac{t}{Q^2} \right) - (1 - x_A)(2 - y) \frac{t}{Q^2} \quad (\text{A.7})$$

$$K^2 = -\delta t (1 - x_A) \left(1 - y - \frac{y^2 \varepsilon^2}{4} \right) \left\{ \sqrt{1 + \varepsilon^2} + \frac{4x_A(1 - x_A) + \varepsilon^2}{4(1 - x_A)} \delta t \right\} \quad (\text{A.8})$$

$$\delta t = \frac{t - t_{min}}{Q^2} = \frac{t}{Q^2} + \frac{2(1 - x_A) \left(1 - \sqrt{1 + \varepsilon^2} \right) + \varepsilon^2}{4x_A(1 - x_A) + \varepsilon^2} \quad (\text{A.9})$$

where t_{min} represents the kinematic boundary of the process and defined as:

$$t_{min} = Q^2 \frac{2(1 - x_A)(1 - \sqrt{1 + \varepsilon^2}) + \varepsilon^2}{4x_A(1 - x_A) + \varepsilon^2} \quad (\text{A.10})$$

The Fourier coefficients, in equations A.2, A.3 and A.4, of a spin-0 target are defined as:

$$\begin{aligned} c_0^{BH} = & \left[\left\{ (2-y)^2 + y^2(1+\varepsilon^2)^2 \right\} \left\{ \frac{\varepsilon^2 Q^2}{t} + 4(1-x_A) + (4x_A + \varepsilon^2) \frac{t}{Q^2} \right\} \right. \\ & \left. + 2\varepsilon^2 \left\{ 4(1-y)(3+2\varepsilon^2) + y^2(2-\varepsilon^4) \right\} - 4x_A^2(2-y)^2(2+\varepsilon^2) \frac{t}{Q^2} \right. \\ & \left. + 8K^2 \frac{\varepsilon^2 Q^2}{t} \right] F_A^2(t) \end{aligned} \quad (\text{A.11})$$

$$c_1^{BH} = -8(2-y)K \left\{ 2x_A + \varepsilon^2 - \frac{\varepsilon^2 Q^2}{t} \right\} F_A^2(t) \quad (\text{A.12})$$

$$c_2^{BH} = 8K^2 \frac{\varepsilon^2 Q^2}{t} F_A^2(t) \quad (\text{A.13})$$

where $F_A(t)$ is the electromagnetic form factor of the ${}^4\text{He}$. At leading twist, the $|\mathcal{T}_{DVCS}|^2$ writes as a function of only one CFF according to

$$c_0^{DVCS} = 2 \frac{2-2y+y^2+\frac{\varepsilon^2}{2}y^2}{1+\varepsilon^2} \mathcal{H}_A \mathcal{H}_A^\star \quad (\text{A.14})$$

and the interference amplitude coefficients are written as:

$$s_1^{INT} = F_A(t) \Im m(\mathcal{H}_A) S_{++}(1), \quad (\text{A.15})$$

with

$$S_{++}(1) = \frac{-8K(2-y)y}{1+\varepsilon^2} \left(1 + \frac{1-x_A + \frac{\sqrt{1+\varepsilon^2}-1}{2}}{1+\varepsilon^2} \frac{t-t_{min}}{Q^2} \right) \quad (\text{A.16})$$

$$c_0^{INT} = F_A(t) \Re e(\mathcal{H}_A) C_{++}(0), \quad (\text{A.17})$$

with

$$\begin{aligned} C_{++}(0) = & \frac{-4(2-y)(1+\sqrt{1+\varepsilon^2})}{(1+\varepsilon^2)^2} \left\{ \frac{\tilde{K}^2}{Q^2} \frac{(2-y)^2}{\sqrt{1+\varepsilon^2}} \right. \\ & \left. + \frac{t}{Q^2} \left(1-y - \frac{\varepsilon^2}{4}y^2 \right) (2-x_A) \left(1 + \frac{2x_A(2-x_A + \frac{\sqrt{1+\varepsilon^2}-1}{2} + \frac{\varepsilon^2}{2x_A}) \frac{t}{Q^2} + \varepsilon^2}{(2-x_A)(1+\sqrt{1+\varepsilon^2})} \right) \right\} \end{aligned} \quad (\text{A.18})$$

$$c_1^{INT} = F_A(t) \Re e(\mathcal{H}_A) C_{++}(1), \quad (\text{A.19})$$

with

$$\begin{aligned} C_{++}(1) = & \frac{-16K(1-y+\frac{\varepsilon^2}{4}y^2)}{(1+\varepsilon^2)^{5/2}} \left\{ \left(1 + (1-x_A) \frac{\sqrt{1+\varepsilon^2}-1}{2x_A} + \frac{\varepsilon^2}{4x_A} \right) \frac{x_A t}{Q^2} - \frac{3\varepsilon^2}{4.0} \right\} \\ & - 4K \left(2-2y+y^2 + \frac{\varepsilon^2}{2}y^2 \right) \frac{1+\sqrt{1+\varepsilon^2}-\varepsilon^2}{(1+\varepsilon^2)^{5/2}} \left\{ 1 - (1-3x_A) \frac{t}{Q^2} \right. \\ & \left. + \frac{1-\sqrt{1+\varepsilon^2}+3\varepsilon^2}{1+\sqrt{1+\varepsilon^2}-\varepsilon^2} \frac{x_A * t}{Q^2} \right\} \end{aligned} \quad (\text{A.20})$$

APPENDIX B

The parametrizations for the RTPC

- The parametrizations of the mean (μ) and the width (σ) of Δz distributions shown in figure 2.11, with L and R stand for the left and the right modules of the RTPC, and z in mm:

$$\mu_{\Delta z}^L(z) = 2.80051 - 0.0624556 * z + 0.00035567 * z^2 + 5.25789e - 06 * z^3 \quad (\text{B.1})$$

$$\sigma_{\Delta z}^L(z) = 7.48614 - 0.00776678 * z - 3.66892e - 05 * z^2 \quad (\text{B.2})$$

$$\mu_{\Delta z}^R(z) = -3.85725 - 0.061265 * z + 0.000324528 * z^2 + 4.28801e - 06 * z^3 \quad (\text{B.3})$$

$$\sigma_{\Delta z}^R(z) = 8.67335 - 0.00975138 * z + 8.01378e - 05 * z^2 \quad (\text{B.4})$$

- The parametrizations of the mean (μ) and the width (σ) of $\Delta\phi$ distributions shown in figure 2.12 are:

$$\mu_{\Delta\phi}^L(z) = 178.053 + 0.0298072 * z - 0.000362634 * z^2 - 2.32442e - 07 * z^3 \quad (\text{B.5})$$

$$\sigma_{\Delta\phi}^L(z) = 2.00365 + 0.0011081 * z + 4.1589e - 05 * z^2 - 2.95347e - 07 * z^3 \quad (\text{B.6})$$

$$\mu_{\Delta\phi}^R(z) = 181.3 + 0.00749361 * z - 0.000338728 * z^2 + 6.37882e - 06 * z^3 \quad (\text{B.7})$$

$$\sigma_{\Delta\phi}^R(z) = 2.0939 + 9.59331e - 05 * z + 2.16727e - 05 * z^2 - 5.69296e - 08 * z^3 \quad (\text{B.8})$$

- The parametrizations of the mean (μ) and the width (σ) of $\Delta\theta$ distribution shown in figure 2.13 are:

$$\mu_{\Delta\theta}(z) = -1.02349 - 0.0487393 * z + 0.000219641 * z^2 + 3.84156e - 06 * z^3 \quad (\text{B.9})$$

$$\sigma_{\Delta\theta}(z) = 3.57854 + 0.00639663 * z \quad (\text{B.10})$$

- The drift speed parametrization:

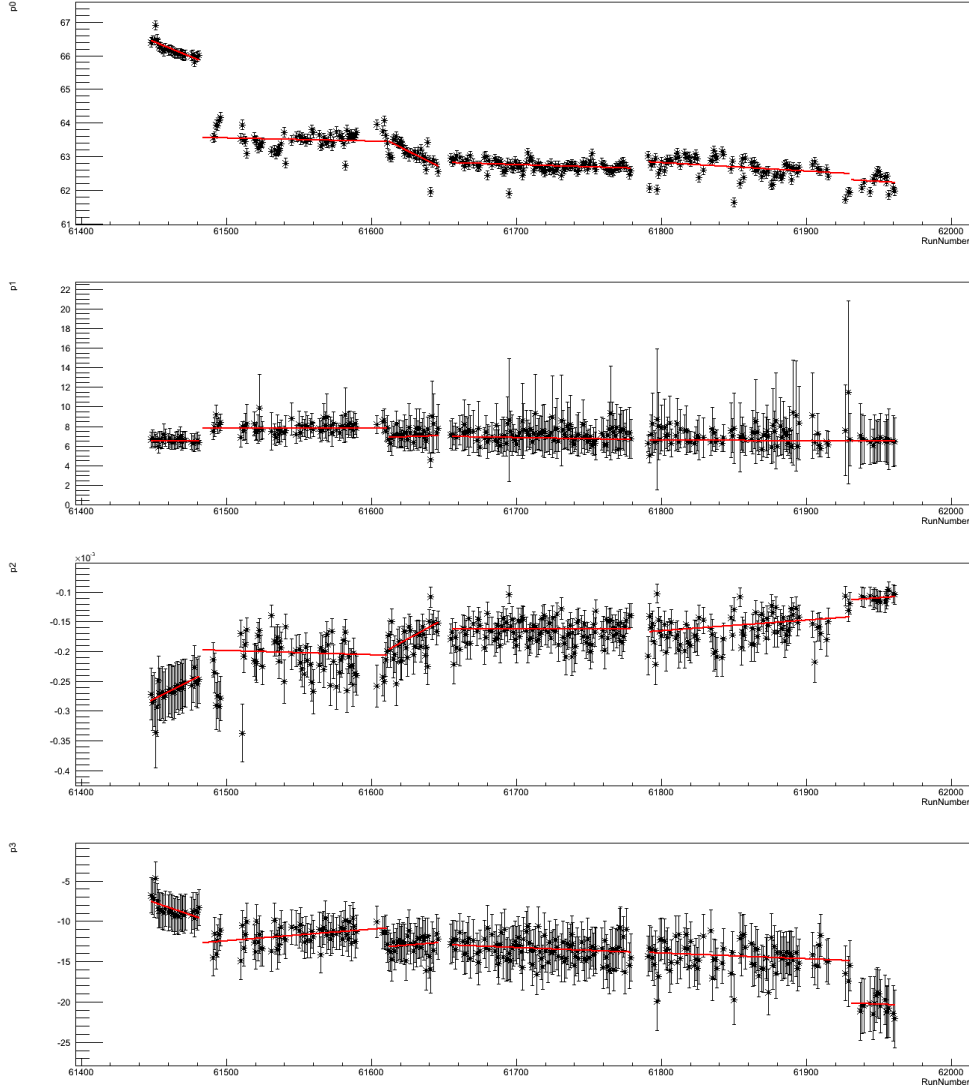


Figure B.1: The fit parameters: p_0 , p_1 , p_2 , and p_3 for the individual runs. The red lines represent their piece-wise fits.

$$TDC_{max/2}(z) = p_0 + p_1 * e^{p_2 * (z - p_3)^2} \quad (\text{B.11})$$

run range	p_0 p_2	p_1 p_3
61448 - 61481	$1.14312\text{e+03} - 1.75217\text{e-02} * r_N$ $-7.55131\text{e-02} + 1.22429\text{e-06} * r_N$	$3.27339\text{e+00} + 5.32577\text{e-05} * r_N$ $3.76627\text{e+03} - 6.14148\text{e-02} * r_N$
61483 - 61611	$1.21405\text{e+02} - 9.40705\text{e-04} * r_N$ $4.09308\text{e-03} - 6.97839\text{e-08} * r_N$	$3.89644\text{e+00} + 6.33813\text{e-05} * r_N$ $-9.04583\text{e+02} + 1.45062\text{e-02} * r_N$
61612 - 61646	$1.39733\text{e+03} - 2.16496\text{e-02} * r_N$ $-8.23774\text{e-02} + 1.33384\text{e-06} * r_N$	$-3.07845\text{e+02} + 5.10814\text{e-03} * r_N$ $-9.05752\text{e+02} + 1.44872\text{e-02} * r_N$
61655 - 61779	$1.45093\text{e+02} - 1.33438\text{e-03} * r_N$ $-5.10501\text{e-04} + 5.64359\text{e-09} * r_N$	$1.63746\text{e+02} - 2.54273\text{e-03} * r_N$ $4.26282\text{e+02} - 7.12408\text{e-03} * r_N$
61791 - 61930	$2.18243\text{e+02} - 2.51495\text{e-03} * r_N$ $-1.11909\text{e-02} + 1.78407\text{e-07} * r_N$	$4.92691\text{e+01} - 6.90443\text{e-04} * r_N$ $4.26297\text{e+02} - 7.12383\text{e-03} * r_N$
61931 - 61961)	$2.18152\text{e+02} - 2.51641\text{e-03} * r_N$ $-1.11766\text{e-02} + 1.78639\text{e-07} * r_N$	$4.92921\text{e+01} - 6.90070\text{e-04} * r_N$ $4.23668\text{e+02} - 7.16628\text{e-03} * r_N$

Table B.1: The parameters of $TDC_{max/2}$ used in EG6 experiment reconstruction codes.

- Drift paths' parametrization:

$$\Delta\phi(TDC, z) = \sum_{i=0}^4 p_i(z) * TDC^i \quad (\text{B.12})$$

Parameter	constant	$*z$	$*z^2$
p_0	0.14222	-6.52562e-05	4.06768e-06
p_1	-0.00147368	5.64924e-06	-7.31944e-07
p_2	0.000216222	6.25749e-09	1.8923e-08
p_3	-3.82450e-06	-6.29825e-09	-1.89627e-10
p_4	3.22973e-08	7.52017e-11	1.08564e-12

Table B.2: The drift paths extracted in the EG6 experiment.

APPENDIX C

The parametrization of the IC-photons energy corrections

- α parametrization

$$\alpha(x) = c_0 + c_2 \left[e^{-c_3(x-c_1)} - e^{-c_4(x-c_1)} \right], \quad (\text{C.1})$$

Fun_N	xmin	xmax	c_0	c_1	c_2	c_3	c_4
1	61510	61514	-0.00671929	61493	-0.00868856	-0.114874	-0.117953
2	61519	61525	-0.00160398	61585.7	-2.1e-09	0.38362	0.38362
3	61531	61545	-0.00956513	61876.8	-0.0295579	1.23958e-06	0.000704112
4	61546	61556	-0.000414459	61521.8	-0.0179471	-0.0316302	-0.030899
5	61558	61580	-0.00731749	61532.4	-0.465254	0.0200131	0.0193213
6	61581	61590	0.0604759	61561.7	-19.3314	0.0407449	0.0411026
7	61604	61608	-0.00320342	61521.1	-0.00074357	-0.018373	-0.0243743
8	61609	61622	-0.00205987	61649.1	5.94004e-05	0.0760846	-2.64412
9	61623	61637	-0.00153458	61640.7	-1.02541e-10	0.965545	0.959411
10	61638	61646	-0.000735223	61763.1	-0.00476067	0.0423013	0.0422956
11	61655	61675	-0.00123166	61561.1	-2.63733e-06	-0.159566	-0.159566
12	61678	61711	-0.00294886	61670.6	-0.0079126	0.052612	0.0252883
13	61712	61713	-0.00102705	61711.9	-0.0034062	-3.1972	-3.19763
14	61714	61724	-0.00109184	61731.2	-1.14221e-06	0.308061	-4.24803
15	61725	61729	-0.00915958	61716.6	-0.0240355	0.137179	0.0524492
16	61731	61779	-0.00295947	61669.4	0.0130552	0.00768358	0.0117274
17	61791	61796	-0.00117275	61791.9	-0.00210188	5.63266	5.63003
18	61797	61826	0.00155106	61787.7	-0.980189	0.0514066	0.0518518
19	61829	61843	-0.0015276	61826	-0.00204473	2.72258	0.275824
20	61848	61874	0.0265578	61973.2	-0.0249309	0.0010753	-0.186452
21	61876	61895	-0.00205642	61715.7	-3.3277e-05	-0.065808	-0.0658091
22	61904	61915	-0.00274984	62178.9	-0.107207	0.00976882	0.00977186
23	61925	61930	0.0064528	61924.8	-0.00849265	0.0278942	9.3268

Table C.1: α parametrization shown in figure 3.37.

- β parametrization

$$\beta(x) = p_0 + p_2 \left[e^{-p_3(x-p_1)} - e^{-p_4(x-p_1)} \right], \quad (\text{C.2})$$

Fun_N	xmin	xmax	p_0	p_1	p_2	p_3	p_4
1	61510	61514	0.139127	61508.7	-0.00705827	-0.127	-0.163719
2	61519	61525	0.144057	61553.1	6.44528e-05	0.384066	0.384069
3	61531	61545	-0.238301	61487	-1.28623	0.0260483	0.011476
4	61546	61556	0.0904474	61545.1	-0.0367149	2.10481	-0.0186192
5	61558	61580	0.095243	61543.5	-0.197639	0.0280817	0.015222
6	61581	61590	0.0643454	61557.1	-0.394422	0.0358816	0.0212999
7	61604	61608	0.138436	61605.4	-0.0142253	-0.0323464	-0.0103419
8	61609	61622	0.135047	61605.8	-0.00856825	0.157423	0.0474859
9	61623	61637	0.137445	61646.8	-1.46307e-05	0.273975	-0.0770047
10	61638	61646	0.141909	61651.9	-0.103873	0.00713496	0.000949948
11	61655	61675	0.127712	61652.8	-0.00969769	0.220956	0.00215349
12	61678	61711	0.137774	61697.7	-9.15967e-05	0.237965	-0.158587
13	61712	61713	0.124706	61655.1	-3.72443e-05	-0.0443564	-0.100321
14	61714	61724	0.138057	61726.8	-0.000274029	0.234	-4.45937
15	61725	61729	0.108381	61721.3	-0.0289603	0.77633	-0.00285553
16	61731	61779	0.113727	61726	-0.0236114	0.243927	-0.00196355
17	61791	61791	0.136619	0.0	0.0	0.0	0.0
18	61792	61796	0.138708	61914.5	1.07991e-09	0.181595	0.181612
19	61797	61825	0.137559	61839.6	-0.000312349	0.160791	0.159434
20	61826	61843	0.0359758	61810.5	-0.10032	0.215911	-0.000529924
21	61848	61874	0.116396	61891.7	-0.385562	-0.0563216	-0.0479573
22	61876	61915	0.105816	61872.2	-0.0312028	0.384691	-0.00145868
23	61925	61930	0.137809	61927.5	-0.00071665	0.620419	0.222406

Table C.2: β parametrization shown in figure 3.37.

Exclusive π^0 events selection

The exclusive selection of the experimental $e^4He\pi^0$ and $ep\pi^0$ events require the detection of only one good electron, one good π^0 in the topology ICIC or ICEC, and one good 4He track in the coherent channel or one good proton in the incoherent channel case. Furthermore, in order to ensure that this is a deep process we apply a set of initial requirements. The exclusivity of the reaction is ensured by a set of exclusivity cuts like for the DVCS channels. These requirements and exclusivity cuts are presented for the case of the coherent $e^4He\pi^0$ events are:

Initial criteria

These requirements are made to ensure that the selected events occur at the partonic level:

- High virtuality of the exchanged photon ($Q^2 > 1 \text{ GeV}^2$).
- High energy of the emitted π^0 ($E_{\pi^0} > 2 \text{ GeV}$).
- The invariant mass of the virtual photon and the target proton is greater than $2 \text{ GeV}^2/c^2$ in order to avoid the baryons resonances region.
- The transfer momentum squared ($-t$) between the initial target and the recoil one is greater than the minimum allowed one (t_{min}) defined by the kinematics of the incoming and the scattered electrons. The definition of t_{min} for each channel can be found in the corresponding DVCS channel selection presented previously.

Exclusivity requirements

The exclusivity of the selected $e^4He\pi^0$ events is done with the following cuts:

- The coplanarity cut ($\Delta\phi$) between the recoil 4He and the produced π^0 .
- The missing energy, mass and transverse momentum cuts in the configuration $e^4He\pi^0X$.
- The missing mass cut in the configuration e^4HeX .
- The missing mass cut in the configuration $e\pi^0X$.
- The cone angle cut between e^4HeX and the reconstructed π^0 .

The same procedure holds for the case of the incoherent $ep\pi^0$ events. In the following two subsections, the results of the two channels selection are presented.

D.1 $e^4He\pi^0$ exclusivity cuts

The events which pass the following exclusivity cuts are assumed to be good $e^4He\pi^0$ events.

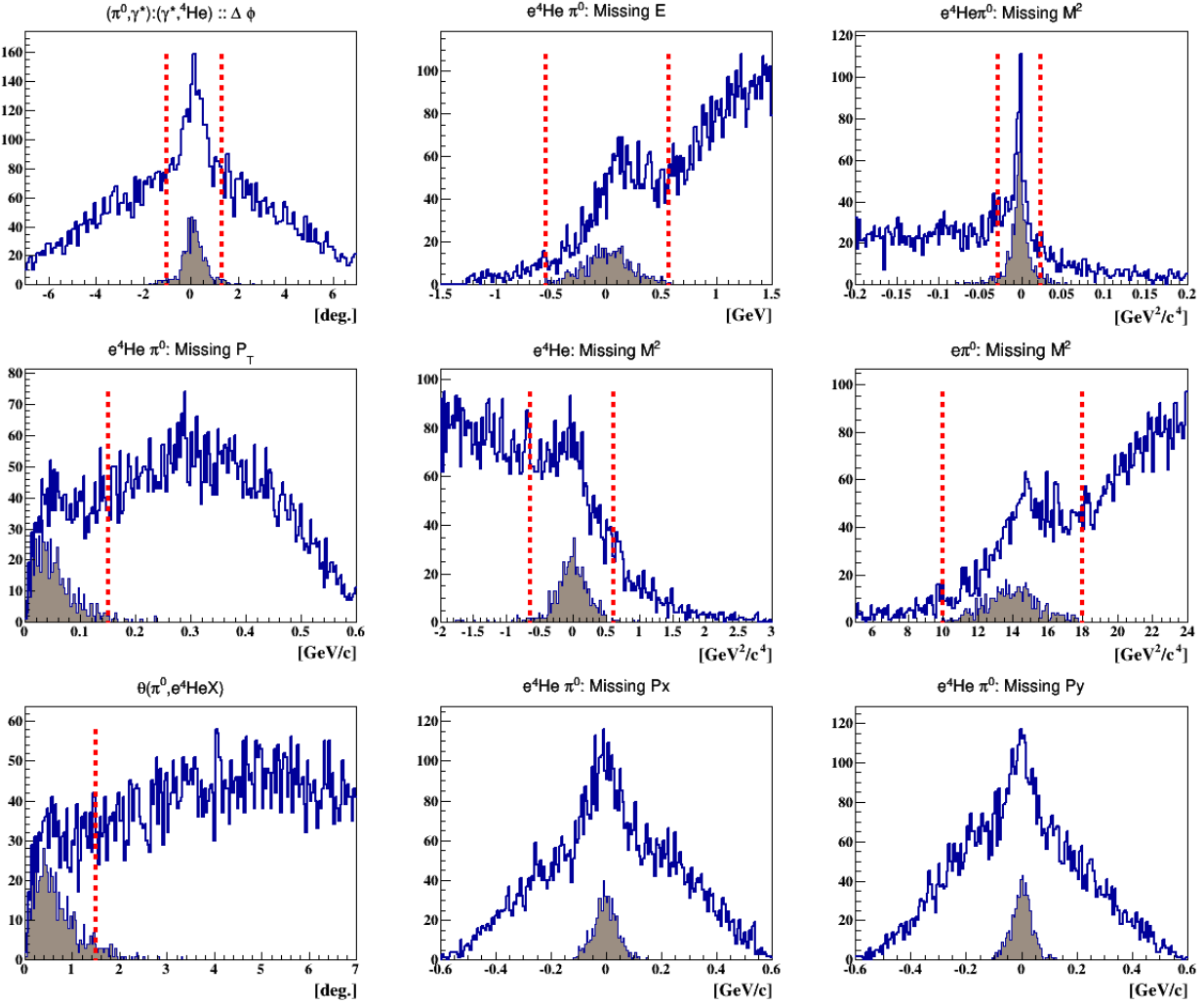


Figure D.1: The blue distributions represent all the $e^4He\pi^0$ events before the exclusivity cuts. The shaded distributions show the events which passed all the exclusivity cuts except for the quantity plotted. The red lines are 3σ cuts. The mean and sigma values of each distribution are listed in table E.2.

Comparison with simulation

As for the selection of the experimental $e^4He\pi^0$ events, the simulated events have to pass an equivalent set of exclusivity cuts in addition to the π^0 electroproduction criteria, presented at the beginning of this section. In this section, we show the comparison between the experimental and the simulated selected $e^4He\pi^0$ events as a function of the kinematic variables (Q^2 , x_B , $-t$), figure D.2, and as a function of the variables used for the exclusivity cuts, figure D.3.

Even with low experimental statistics, figures D.2 and D.3 show a good match between the simulation and the experimental $e^4He\gamma$ events for the different kinematic variables, which is

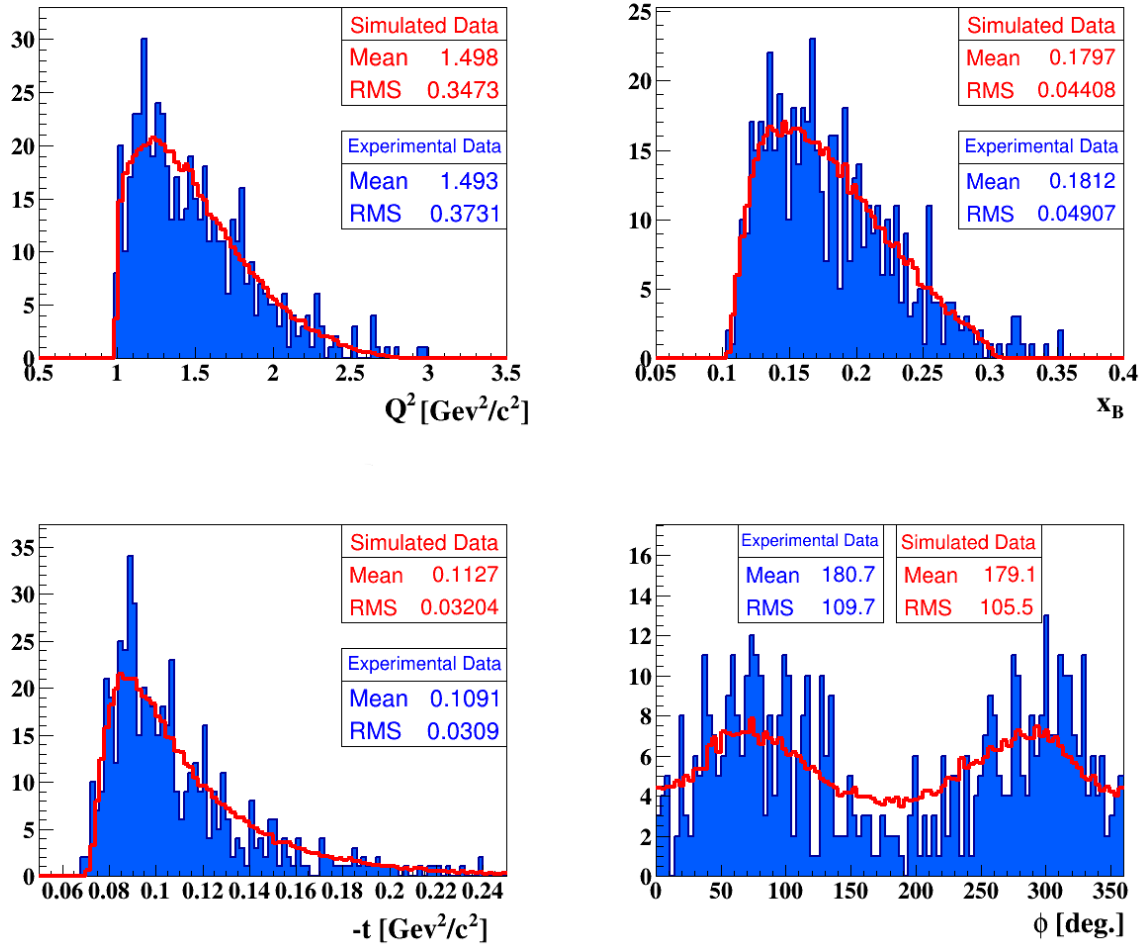


Figure D.2: Comparison between the simulated $e^4He\pi^0$ events (red lines) and the experimental events (blue shaded distributions) as a function of the kinematic variables: Q^2 , x_B , $-t$ and ϕ_h respectively from top to right to right and from top to bottom.

satisfying for our background subtraction goal.

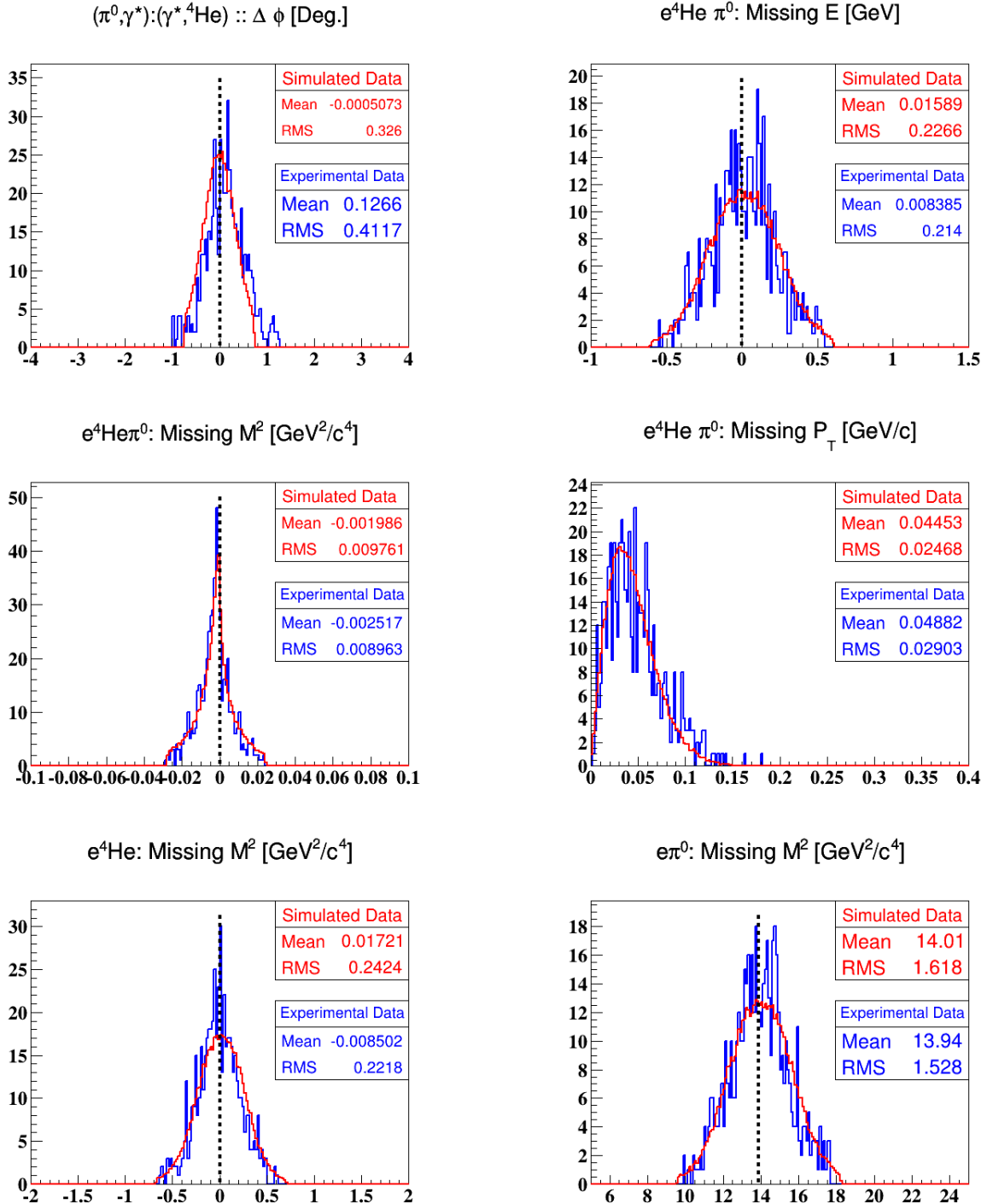


Figure D.3: Comparison between the simulated and experimental $e^{} {}^4\text{He}\gamma$ events in terms of the exclusivity variables. The vertical black line indicates the theoretically expected value for each exclusivity variable.

D.2 $ep\pi^0$ exclusivity cuts

The $ep\pi^0$ events which pass the initial deepness criteria and the exclusivity cuts, marked by the red vertical lines in the figure below, are considered as clean events.

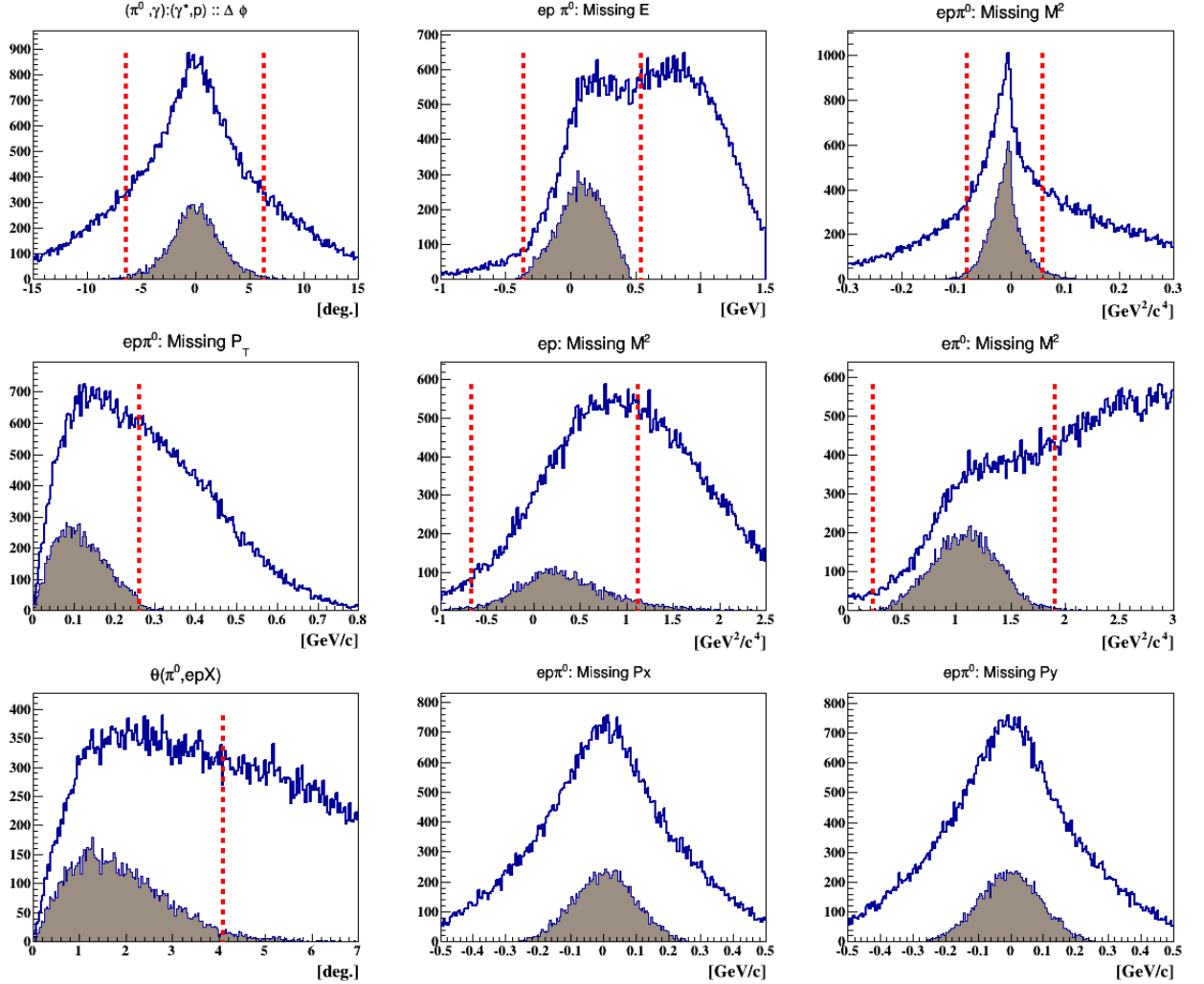


Figure D.4: The blue distributions represent all the $ep\pi^0$ events before any exclusive requirement. The shaded brown distributions show the events which passed all the exclusivity cuts except the quantity plotted. The vertical red lines represent 3σ cuts on the shaded distribution. The mean and sigma values of each distribution are listed in table E.4.

Comparison with simulation

In this section, the experimental selected $ep\pi^0$ events are compared to the Monte Carlo simulated events. Figure D.5 shows the comparison as a function of the kinematic variables. Figure D.6 shows the comparison in terms of the different exclusivity variables. One can see an agreement within some degrees of differences, which might come from the fact that our protons are bound ones and the physics of the nuclear process is not fully understood.

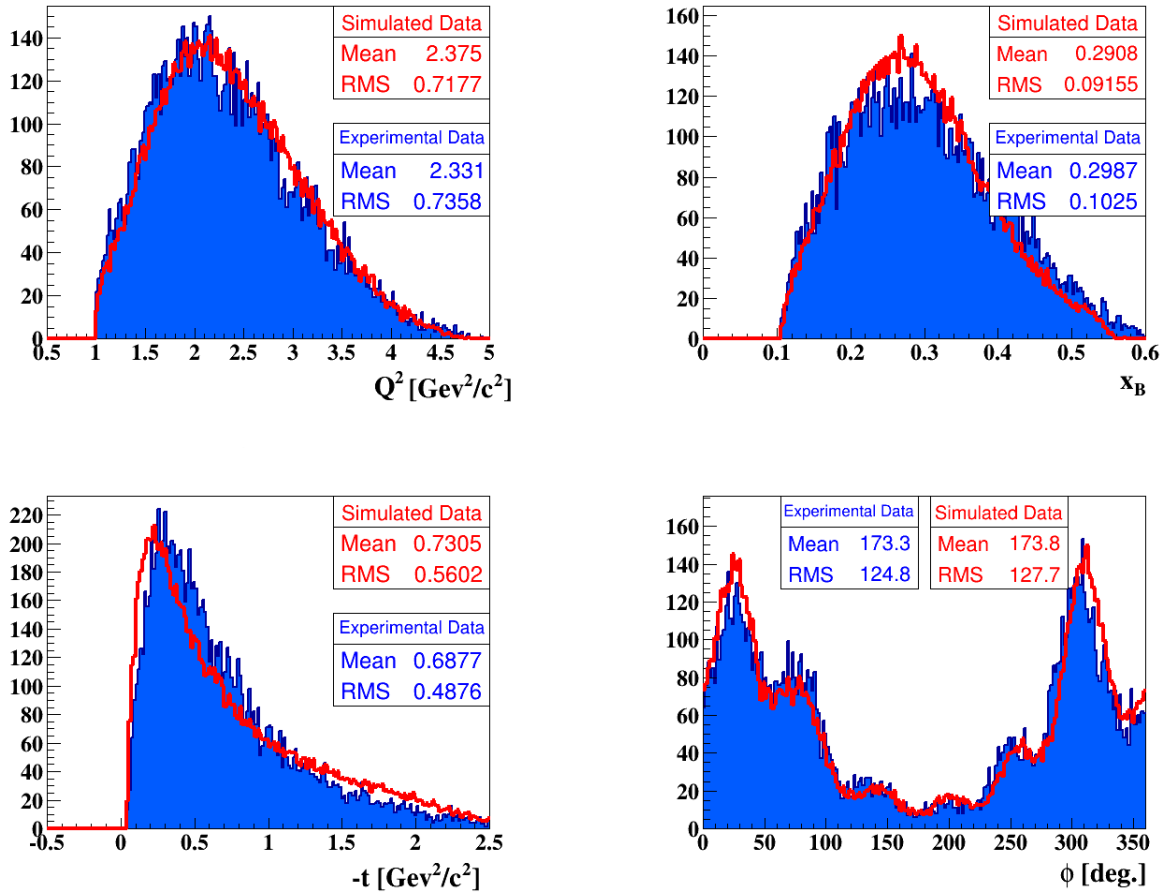


Figure D.5: Comparison between the Monte Carlo simulated $ep\pi^0$ events (red lines) and the experimental ones (blue shaded distributions) as a function of the kinematic variables: Q^2 , x_B , $-t$, and ϕ , respectively from top to right to right and from top to bottom.

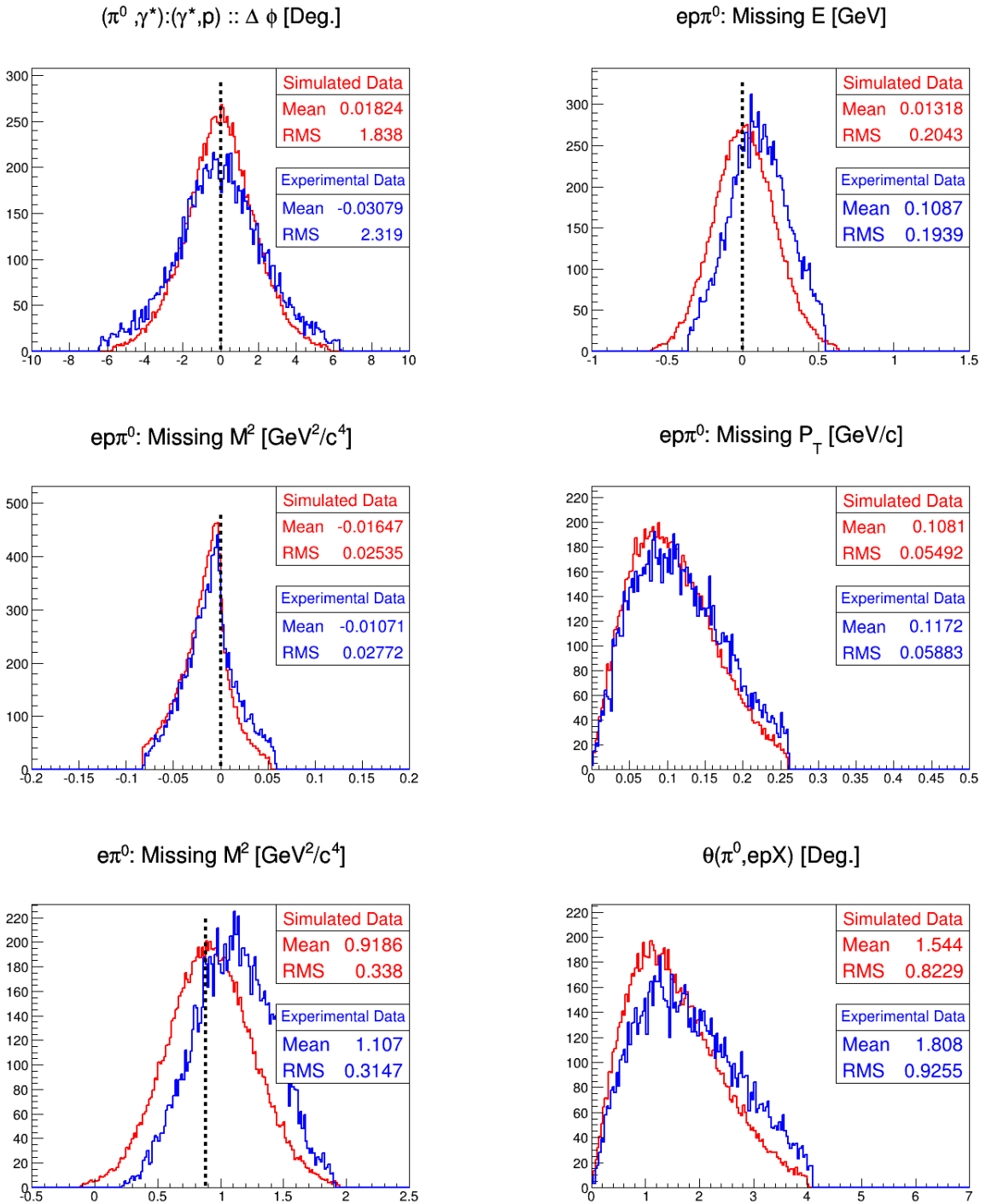


Figure D.6: Comparison between the simulated and experimental $e\pi^0$ DVCS events as a function of the variables used for the exclusivity cuts. The simulated distributions are normalized with respect to the experimental ones. The vertical black lines indicate the theoretically expected values.

APPENDIX E

Tables list of the exclusive distributions

- Exclusive $e^4He\gamma$ distributions

The quantity	mean	σ
$\Delta\phi$	1.86020e-01	4.64936e-01
$E_X (e^4He\gamma X)$	1.48023e-02	2.51854e-01
$M_X^2 (e^4He\gamma X)$	-2.98662e-03	9.28645e-03
$pt_X (e^4He\gamma X)$	4.14664e-02	4.24914e-02
$M_X^2 (e^4HeX)$	-3.45128e-02	2.28247e-01
$M_X^2 (e\gamma X)$	1.39930e+01	1.61245
$\theta (\gamma, e^4HeX)$	5.08070e-01	4.74883e-01
$px_X (e^4He\gamma X)$	-2.32102e-03	4.52945e-02
$py_X (e^4He\gamma X)$	-8.97351e-04	3.89937e-02

Table E.1: The mean and sigma values of the exclusive coherent quantities drawn in figure 4.4.

- Exclusive $e^4He\pi^0$ distributions

The quantity	mean	σ
$\Delta\phi$	1.41750e-01	3.84202e-01
$E_X (e^4He\pi^0 X)$	7.80328e-03	1.85770e-01
$M_X^2 (e^4He\pi^0 X)$	-2.31650e-03	8.65851e-03
$pt_X (e^4He\pi^0 X)$	4.36619e-02	3.25254e-02
$M_X^2 (e^4HeX)$	-1.30346e-02	2.07791e-01
$M_X^2 (e\pi^0 X)$	1.39835e+01	1.33781
$\theta (\pi^0, e^4HeX)$	5.30001e-01	3.44745e-01
$px_X (e^4He\pi^0 X)$	-3.79596e-03	4.20732e-02
$py_X (e^4He\pi^0 X)$	9.41010e-04	3.50393e-02

Table E.2: The mean and sigma values of the exclusive coherent quantities drawn in figure D.1.

- Exclusive $ep\gamma$ distributions

The quantity	mean	σ
$\Delta\phi$	4.22584e-02	1.39413
$E_X (ep\gamma X)$	6.27739e-02	1.34499e-01
$M_X^2 (ep\gamma X)$	-1.00889e-02	1.58503e-02
$pt_X (ep\gamma X)$	8.03008e-02	4.28511e-02
$M_X^2 (epX)$	2.40257e-01	3.66321e-01
$M_X^2 (e\gamma X)$	1.01266	2.03835e-01
$\theta (\gamma, epX)$	1.06788	6.76469e-01
$px_X (ep\gamma X)$	3.48024e-03	8.19527e-02
$py_X (ep\gamma X)$	-1.50911e-03	8.16219e-02

Table E.3: The mean and sigma values of the exclusive incoherent quantities drawn in figure 4.12.

- Exclusive $ep\pi^0$ distributions

The quantity	mean	σ
$\Delta\phi$	-3.25864e-02	2.11499
$E_X (ep\pi^0 X)$	9.23934e-02	1.50977e-01
$M_X^2 (ep\pi^0 X)$	-1.11900e-02	2.31963e-02
$pt_X (ep\pi^0 X)$	1.02247e-01	5.31387e-02
$M_X^2 (epX)$	2.27334e-01	2.98775e-01
$M_X^2 (e\pi^0 X)$	1.07125	2.79845e-01
$\theta (\pi^0, epX)$	1.42739	8.89072e-01
$px_X (ep\pi^0 X)$	2.19686e-03	9.01343e-02
$py_X (ep\pi^0 X)$	-1.30580e-03	9.05090e-02

Table E.4: The mean and sigma values of the exclusive $ep\pi^0$ quantities drawn in shaded brown in figure D.4.

APPENDIX F

 A_{LU} tables

$\langle Q^2 \rangle$	$\langle x_B \rangle$	$\langle -t \rangle$	$\langle \phi \rangle$	$A_{LU} \pm \text{stat.} \pm \text{syst.}$
1.143	0.136	0.096	24.3	$0.1327 \pm 0.1088 \pm 0.0257$
1.143	0.136	0.096	61.1	$0.3210 \pm 0.0932 \pm 0.0188$
1.143	0.136	0.096	98.9	$0.3709 \pm 0.1026 \pm 0.0403$
1.143	0.136	0.096	140.9	$0.2452 \pm 0.1517 \pm 0.0267$
1.143	0.136	0.096	178.4	$0.0225 \pm 0.1632 \pm 0.0278$
1.143	0.136	0.096	219.1	$-0.0526 \pm 0.1475 \pm 0.0248$
1.143	0.136	0.096	262.9	$-0.2642 \pm 0.1196 \pm 0.0389$
1.143	0.136	0.096	301.9	$-0.1761 \pm 0.0968 \pm 0.0263$
1.143	0.136	0.096	337.7	$-0.2791 \pm 0.1047 \pm 0.0343$
1.423	0.172	0.099	21.1	$0.1917 \pm 0.0892 \pm 0.0267$
1.423	0.172	0.099	56.6	$0.2819 \pm 0.0866 \pm 0.0250$
1.423	0.172	0.099	96.9	$0.4855 \pm 0.1291 \pm 0.0426$
1.423	0.172	0.099	139.9	$0.0996 \pm 0.1679 \pm 0.0250$
1.423	0.172	0.099	180.3	$0.1458 \pm 0.1906 \pm 0.0302$
1.423	0.172	0.099	218.7	$-0.1109 \pm 0.1853 \pm 0.0344$
1.423	0.172	0.099	263.1	$-0.3516 \pm 0.1371 \pm 0.0366$
1.423	0.172	0.099	302.2	$-0.4141 \pm 0.0842 \pm 0.0383$
1.423	0.172	0.099	338.2	$-0.2786 \pm 0.0836 \pm 0.0261$
1.902	0.224	0.107	21.4	$0.1803 \pm 0.0805 \pm 0.0234$
1.902	0.224	0.107	57.2	$0.3501 \pm 0.0824 \pm 0.0185$
1.902	0.224	0.107	96.2	$0.2701 \pm 0.1230 \pm 0.0173$
1.902	0.224	0.107	139.5	$0.3053 \pm 0.2390 \pm 0.0170$
1.902	0.224	0.107	178.2	$0.1028 \pm 0.2670 \pm 0.0126$
1.902	0.224	0.107	221.4	$-0.2118 \pm 0.2147 \pm 0.0152$
1.902	0.224	0.107	263.3	$-0.3060 \pm 0.1306 \pm 0.0260$
1.902	0.224	0.107	303.3	$-0.1384 \pm 0.0944 \pm 0.0207$
1.902	0.224	0.107	338.5	$-0.1633 \pm 0.0791 \pm 0.0163$

 Table F.1: The coherent A_{LU} in Q^2 bins

$\langle Q^2 \rangle$	$\langle x_B \rangle$	$\langle -t \rangle$	$\langle \phi \rangle$	$A_{LU} \pm \text{stat.} \pm \text{syst.}$
1.164	0.132	0.095	25.6	$0.0174 \pm 0.1440 \pm 0.0221$
1.164	0.132	0.095	61.6	$0.3478 \pm 0.0867 \pm 0.0198$
1.164	0.132	0.095	99.0	$0.3808 \pm 0.0948 \pm 0.0408$
1.164	0.132	0.095	141.7	$0.2943 \pm 0.1379 \pm 0.0333$
1.164	0.132	0.095	178.1	$0.0433 \pm 0.1519 \pm 0.0293$
1.164	0.132	0.095	218.5	$-0.0352 \pm 0.1316 \pm 0.0243$
1.164	0.132	0.095	262.7	$-0.2771 \pm 0.1050 \pm 0.0372$
1.164	0.132	0.095	300.7	$-0.2138 \pm 0.0836 \pm 0.0259$
1.164	0.132	0.095	335.2	$-0.2339 \pm 0.1221 \pm 0.0319$
1.439	0.17	0.099	22.9	$0.1579 \pm 0.0853 \pm 0.0230$
1.439	0.17	0.099	57.1	$0.1733 \pm 0.0880 \pm 0.0195$
1.439	0.17	0.099	96.3	$0.2259 \pm 0.1331 \pm 0.0295$
1.439	0.17	0.099	139.1	$0.2454 \pm 0.1758 \pm 0.0187$
1.439	0.17	0.099	180.1	$-0.1021 \pm 0.1918 \pm 0.0197$
1.439	0.17	0.099	218.9	$-0.2876 \pm 0.1909 \pm 0.0270$
1.439	0.17	0.099	263.9	$-0.2943 \pm 0.1360 \pm 0.0292$
1.439	0.17	0.099	302.5	$-0.3979 \pm 0.0921 \pm 0.0331$
1.439	0.17	0.099	338.1	$-0.2692 \pm 0.0834 \pm 0.0254$
1.844	0.225	0.107	20.1	$0.2626 \pm 0.0755 \pm 0.0248$
1.844	0.225	0.107	55.9	$0.4281 \pm 0.0887 \pm 0.0224$
1.844	0.225	0.107	96.4	$0.4925 \pm 0.1390 \pm 0.0271$
1.844	0.225	0.107	137.7	$-0.2736 \pm 0.2804 \pm 0.0166$
1.844	0.225	0.107	179.8	$0.8470 \pm 0.2497 \pm 0.0204$
1.844	0.225	0.107	224.7	$-0.0513 \pm 0.2811 \pm 0.0270$
1.844	0.225	0.107	262.8	$-0.3416 \pm 0.1694 \pm 0.0353$
1.844	0.225	0.107	304.5	$-0.1359 \pm 0.1025 \pm 0.0263$
1.844	0.225	0.107	339.8	$-0.1658 \pm 0.0770 \pm 0.0175$

Table F.2: The coherent A_{LU} in x_B bins

$\langle Q^2 \rangle$	$\langle x_B \rangle$	$\langle -t \rangle$	$\langle \phi \rangle$	$A_{LU} \pm \text{stat.} \pm \text{syst.}$
1.36	0.160	0.080	22.8	$0.2378 \pm 0.0928 \pm 0.0263$
1.36	0.160	0.080	57.6	$0.3014 \pm 0.0874 \pm 0.0243$
1.36	0.160	0.080	98.1	$0.4896 \pm 0.1118 \pm 0.0394$
1.36	0.160	0.080	139.3	$0.1965 \pm 0.1595 \pm 0.0252$
1.36	0.160	0.080	178.8	$0.0577 \pm 0.1923 \pm 0.0371$
1.36	0.160	0.080	222.6	$-0.1651 \pm 0.1640 \pm 0.0370$
1.36	0.160	0.080	265.6	$-0.3467 \pm 0.1339 \pm 0.0403$
1.36	0.160	0.080	300.0	$-0.2891 \pm 0.0928 \pm 0.0294$
1.36	0.160	0.080	339.3	$-0.1849 \pm 0.0856 \pm 0.0281$
1.507	0.179	0.094	21.1	$0.2481 \pm 0.0931 \pm 0.0267$
1.507	0.179	0.094	56.4	$0.3386 \pm 0.0828 \pm 0.0284$
1.507	0.179	0.094	97.5	$0.3467 \pm 0.1156 \pm 0.0307$
1.507	0.179	0.094	141.9	$0.1464 \pm 0.1887 \pm 0.0215$
1.507	0.179	0.094	179.5	$-0.2814 \pm 0.1864 \pm 0.0360$
1.507	0.179	0.094	218.5	$0.2104 \pm 0.1998 \pm 0.0147$
1.507	0.179	0.094	262.8	$-0.2399 \pm 0.1280 \pm 0.0283$
1.507	0.179	0.094	303.5	$-0.1989 \pm 0.0955 \pm 0.0286$
1.507	0.179	0.094	338.5	$-0.2098 \pm 0.0875 \pm 0.0201$
1.610	0.193	0.127	22.3	$0.0280 \pm 0.0909 \pm 0.0214$
1.610	0.193	0.127	60.7	$0.3582 \pm 0.0932 \pm 0.0204$
1.610	0.193	0.127	96.8	$0.2559 \pm 0.1269 \pm 0.0313$
1.610	0.193	0.127	139.9	$0.2207 \pm 0.1930 \pm 0.0203$
1.610	0.193	0.127	178.5	$0.5138 \pm 0.1832 \pm 0.0354$
1.610	0.193	0.127	217.5	$-0.2473 \pm 0.1664 \pm 0.0189$
1.610	0.193	0.127	260.9	$-0.2919 \pm 0.1295 \pm 0.0327$
1.610	0.193	0.127	303.4	$-0.2488 \pm 0.0892 \pm 0.0280$
1.610	0.193	0.127	336.8	$-0.2825 \pm 0.0901 \pm 0.0261$

Table F.3: The coherent A_{LU} in $-t$ bins

$\langle Q^2 \rangle$	$\langle x_B \rangle$	$\langle -t \rangle$	$\langle \phi \rangle$	$A_{LU} \pm \text{stat.} \pm \text{syst.}$
1.395	0.166	0.407	21.2	$0.0641 \pm 0.0456 \pm 0.0120$
1.395	0.166	0.407	62.1	$0.0820 \pm 0.0486 \pm 0.0156$
1.395	0.166	0.407	95.4	$0.2205 \pm 0.0488 \pm 0.0263$
1.395	0.166	0.407	139.8	$0.0623 \pm 0.0590 \pm 0.0158$
1.395	0.166	0.407	182.2	$0.0324 \pm 0.0736 \pm 0.0234$
1.395	0.166	0.407	219.4	$0.0042 \pm 0.0686 \pm 0.0150$
1.395	0.166	0.407	258.2	$-0.1746 \pm 0.0476 \pm 0.0226$
1.395	0.166	0.407	303.4	$-0.1058 \pm 0.0425 \pm 0.0196$
1.395	0.166	0.407	337.5	$-0.0506 \pm 0.0535 \pm 0.0142$
1.886	0.233	0.499	20.5	$-0.0108 \pm 0.0368 \pm 0.0124$
1.886	0.233	0.499	60.0	$0.0913 \pm 0.0499 \pm 0.0169$
1.886	0.233	0.499	95.9	$0.1217 \pm 0.0549 \pm 0.0202$
1.886	0.233	0.499	140.4	$0.1636 \pm 0.0825 \pm 0.0285$
1.886	0.233	0.499	180.2	$0.1547 \pm 0.0955 \pm 0.0146$
1.886	0.233	0.499	221.7	$-0.3104 \pm 0.0881 \pm 0.0430$
1.886	0.233	0.499	260.4	$-0.1210 \pm 0.0594 \pm 0.0180$
1.886	0.233	0.499	303.7	$-0.1937 \pm 0.0414 \pm 0.0198$
1.886	0.233	0.499	338.2	$0.0015 \pm 0.0460 \pm 0.0113$
2.338	0.29	0.521	20.8	$0.0995 \pm 0.0351 \pm 0.0135$
2.338	0.29	0.521	58.0	$0.1429 \pm 0.0506 \pm 0.0101$
2.338	0.29	0.521	95.0	$0.1229 \pm 0.0609 \pm 0.0176$
2.338	0.29	0.521	141.0	$0.0447 \pm 0.1034 \pm 0.0161$
2.338	0.29	0.521	182.4	$0.0946 \pm 0.1361 \pm 0.0236$
2.338	0.29	0.521	224.7	$0.0720 \pm 0.1129 \pm 0.0212$
2.338	0.29	0.521	260.8	$-0.2414 \pm 0.0623 \pm 0.0241$
2.338	0.29	0.521	303.4	$-0.2037 \pm 0.0417 \pm 0.0153$
2.338	0.29	0.521	339.1	$-0.0854 \pm 0.0419 \pm 0.0145$
3.098	0.379	0.65	20.0	$0.1025 \pm 0.0327 \pm 0.0147$
3.098	0.379	0.65	57.3	$0.0915 \pm 0.0501 \pm 0.0147$
3.098	0.379	0.65	94.4	$0.1381 \pm 0.0714 \pm 0.0281$
3.098	0.379	0.65	138.0	$0.1012 \pm 0.1458 \pm 0.0129$
3.098	0.379	0.65	179.9	$-0.4236 \pm 0.1925 \pm 0.0270$
3.098	0.379	0.65	226.6	$0.1298 \pm 0.1728 \pm 0.0273$
3.098	0.379	0.65	263.6	$-0.1795 \pm 0.0883 \pm 0.0214$
3.098	0.379	0.65	303.2	$-0.1856 \pm 0.0447 \pm 0.0221$
3.098	0.379	0.65	340.3	$-0.0677 \pm 0.0387 \pm 0.0141$

Table F.4: The incoherent A_{LU} in Q^2 bins

$\langle Q^2 \rangle$	$\langle x_B \rangle$	$\langle -t \rangle$	$\langle \phi \rangle$	$A_{LU} \pm \text{stat.} \pm \text{syst.}$
1.425	0.162	0.397	21.1	$0.1016 \pm 0.0470 \pm 0.0137$
1.425	0.162	0.397	63.0	$0.0703 \pm 0.0463 \pm 0.0165$
1.425	0.162	0.397	95.6	$0.1623 \pm 0.0454 \pm 0.0216$
1.425	0.162	0.397	140.1	$0.0485 \pm 0.0545 \pm 0.0149$
1.425	0.162	0.397	181.4	$0.0863 \pm 0.0664 \pm 0.0235$
1.425	0.162	0.397	219.2	$-0.0144 \pm 0.0642 \pm 0.0199$
1.425	0.162	0.397	258.4	$-0.1444 \pm 0.0451 \pm 0.0183$
1.425	0.162	0.397	303.3	$-0.0688 \pm 0.0413 \pm 0.0154$
1.425	0.162	0.397	337.1	$0.0020 \pm 0.0563 \pm 0.0105$
1.922	0.227	0.418	21.9	$0.0007 \pm 0.0390 \pm 0.0131$
1.922	0.227	0.418	59.7	$0.1077 \pm 0.0474 \pm 0.0161$
1.922	0.227	0.418	96.1	$0.1179 \pm 0.0521 \pm 0.0183$
1.922	0.227	0.418	140.9	$0.1508 \pm 0.0817 \pm 0.0246$
1.922	0.227	0.418	182.2	$0.0958 \pm 0.0979 \pm 0.0165$
1.922	0.227	0.418	222.7	$-0.2464 \pm 0.0867 \pm 0.0343$
1.922	0.227	0.418	260.2	$-0.1612 \pm 0.0543 \pm 0.0227$
1.922	0.227	0.418	303.2	$-0.2401 \pm 0.0387 \pm 0.0206$
1.922	0.227	0.418	336.9	$-0.0309 \pm 0.0460 \pm 0.0100$
2.354	0.287	0.492	20.9	$0.0567 \pm 0.0343 \pm 0.0198$
2.354	0.287	0.492	58.7	$0.1136 \pm 0.0488 \pm 0.0195$
2.354	0.287	0.492	94.5	$0.1973 \pm 0.0627 \pm 0.0188$
2.354	0.287	0.492	139.3	$0.1860 \pm 0.1161 \pm 0.0242$
2.354	0.287	0.492	180.5	$-0.2835 \pm 0.1568 \pm 0.0145$
2.354	0.287	0.492	225.8	$0.1616 \pm 0.1198 \pm 0.0140$
2.354	0.287	0.492	261.2	$-0.3132 \pm 0.0695 \pm 0.0272$
2.354	0.287	0.492	303.7	$-0.1591 \pm 0.0405 \pm 0.0178$
2.354	0.287	0.492	338.6	$-0.0642 \pm 0.0420 \pm 0.0101$
2.987	0.390	0.714	19.4	$0.0985 \pm 0.0315 \pm 0.0143$
2.987	0.390	0.714	55.4	$0.1165 \pm 0.0589 \pm 0.0148$
2.987	0.390	0.714	93.7	$0.1715 \pm 0.0944 \pm 0.0313$
2.987	0.390	0.714	135.2	$-0.0928 \pm 0.2481 \pm 0.0386$
2.987	0.390	0.714	181.8	$-0.1085 \pm 0.5511 \pm 0.0364$
2.987	0.390	0.714	230.1	$-0.2193 \pm 0.3567 \pm 0.0469$
2.987	0.390	0.714	265.3	$-0.0848 \pm 0.1166 \pm 0.0202$
2.987	0.390	0.714	303.4	$-0.2246 \pm 0.0520 \pm 0.0229$
2.987	0.390	0.714	341.2	$-0.0844 \pm 0.0378 \pm 0.0156$

Table F.5: The incoherent A_{LU} in x_B bins

$\langle Q^2 \rangle$	$\langle x_B \rangle$	$\langle -t \rangle$	$\langle \phi \rangle$	$A_{LU} \pm \text{stat.} \pm \text{syst.}$
1.823	0.213	0.145	22.0	$0.0968 \pm 0.0402 \pm 0.0135$
1.823	0.213	0.145	58.7	$0.1156 \pm 0.0471 \pm 0.0190$
1.823	0.213	0.145	96.9	$0.1270 \pm 0.0449 \pm 0.0179$
1.823	0.213	0.145	141.2	$0.1544 \pm 0.0598 \pm 0.0263$
1.823	0.213	0.145	180.5	$0.0308 \pm 0.0748 \pm 0.0150$
1.823	0.213	0.145	219.9	$-0.0366 \pm 0.0661 \pm 0.0182$
1.823	0.213	0.145	260.7	$-0.1370 \pm 0.0457 \pm 0.0195$
1.823	0.213	0.145	303.4	$-0.1286 \pm 0.0412 \pm 0.0137$
1.823	0.213	0.145	336.8	$-0.0421 \pm 0.0465 \pm 0.0100$
2.127	0.255	0.282	21.2	$0.0431 \pm 0.0396 \pm 0.0131$
2.127	0.255	0.282	60.3	$0.0441 \pm 0.0464 \pm 0.0125$
2.127	0.255	0.282	95.4	$0.2261 \pm 0.0521 \pm 0.0338$
2.127	0.255	0.282	141.0	$0.0325 \pm 0.0724 \pm 0.0178$
2.127	0.255	0.282	182.5	$-0.1014 \pm 0.0889 \pm 0.0298$
2.127	0.255	0.282	220.8	$0.0106 \pm 0.0867 \pm 0.0183$
2.127	0.255	0.282	259.1	$-0.1522 \pm 0.0562 \pm 0.0253$
2.127	0.255	0.282	303.6	$-0.1996 \pm 0.0411 \pm 0.0248$
2.127	0.255	0.282	338.2	$-0.1026 \pm 0.0497 \pm 0.0171$
2.308	0.284	0.490	20.4	$0.1388 \pm 0.0392 \pm 0.0154$
2.308	0.284	0.490	60.3	$0.1168 \pm 0.0472 \pm 0.0175$
2.308	0.284	0.490	94.0	$0.1236 \pm 0.0590 \pm 0.0147$
2.308	0.284	0.490	137.2	$0.0764 \pm 0.1034 \pm 0.0166$
2.308	0.284	0.490	182.5	$0.3871 \pm 0.1189 \pm 0.0392$
2.308	0.284	0.490	225.9	$-0.1565 \pm 0.1064 \pm 0.0125$
2.308	0.284	0.490	259.1	$-0.2829 \pm 0.0646 \pm 0.0234$
2.308	0.284	0.490	302.4	$-0.1768 \pm 0.0403 \pm 0.0162$
2.308	0.284	0.490	338.6	$-0.0512 \pm 0.0472 \pm 0.0178$
2.406	0.308	1.107	20.3	$0.0428 \pm 0.0336 \pm 0.0178$
2.406	0.308	1.107	57.7	$0.1460 \pm 0.0609 \pm 0.0108$
2.406	0.308	1.107	92.7	$0.1593 \pm 0.1114 \pm 0.0110$
2.406	0.308	1.107	133.6	$-0.1661 \pm 0.2523 \pm 0.0177$
2.406	0.308	1.107	176.7	$-0.7014 \pm 0.6435 \pm 0.0181$
2.406	0.308	1.107	224.8	$-0.5821 \pm 0.5513 \pm 0.0151$
2.406	0.308	1.107	263.1	$-0.1527 \pm 0.1123 \pm 0.0171$
2.406	0.308	1.107	304.4	$-0.1831 \pm 0.0480 \pm 0.0129$
2.406	0.308	1.107	340.1	$-0.0293 \pm 0.0400 \pm 0.0164$

Table F.6: The incoherent A_{LU} in $-t$ bins

Free proton beam-spin asymmetry interpolation

G.1 Fitting the experimentally measured asymmetries

Following the discussion in section 5.4, comparing the coherent and the incoherent beam-spin asymmetries to free proton asymmetries reveal new information about the nuclear medium modifications. To construct such ratio, the published free proton asymmetries [38] have been used in this analysis, see figure G.1. The measured free proton A_{LU} at $\phi = 90^\circ$ were fitted as a function of $-t$ for the different bins in x_B and Q^2 , figure G.1. Finally, the free proton asymmetries were calculated at the same measured incoherent and coherent $-t$ values from the t-dependence fit of the closest bin in x_B and Q^2 . The statistical errors on the calculated asymmetries were calculated using the fit errors.

G.2 Model-dependent extraction

The proton asymmetries have been adjusted using a dispersion calculation including a phenomenological GPD H only. The imaginary part of the amplitude is parameterized as in [52]. The real part of the amplitude is then obtained from the dispersion relation and the D-term as subtraction constant, parameterized as in [52]. The beam spin asymmetries mostly constrain the parameters of the imaginary part, and the unpolarized cross-section mostly constrain the D-term parameters. Figure G.2 presents the published free proton asymmetries with the model calculations, in solid red lines, and the interpolated free proton asymmetries at our measured coherent and incoherent kinematic values.

G.3 Summary

In this analysis we use the interpolated values from fitting the experimentally measured free proton asymmetries to construct the beam-spin asymmetry ratios, presented in section G.1. The differences between the beam-spin asymmetry ratios calculated using the free proton asymmetries fits, section G.1, and the model-dependent interpolated values, section G.2, were added as a systematic errors on the constructed beam-spin asymmetry ratios. Table G.1 presents the coherent and the incoherent A_{LU} ratios extracted using both methods and the associated systematic uncertainties.

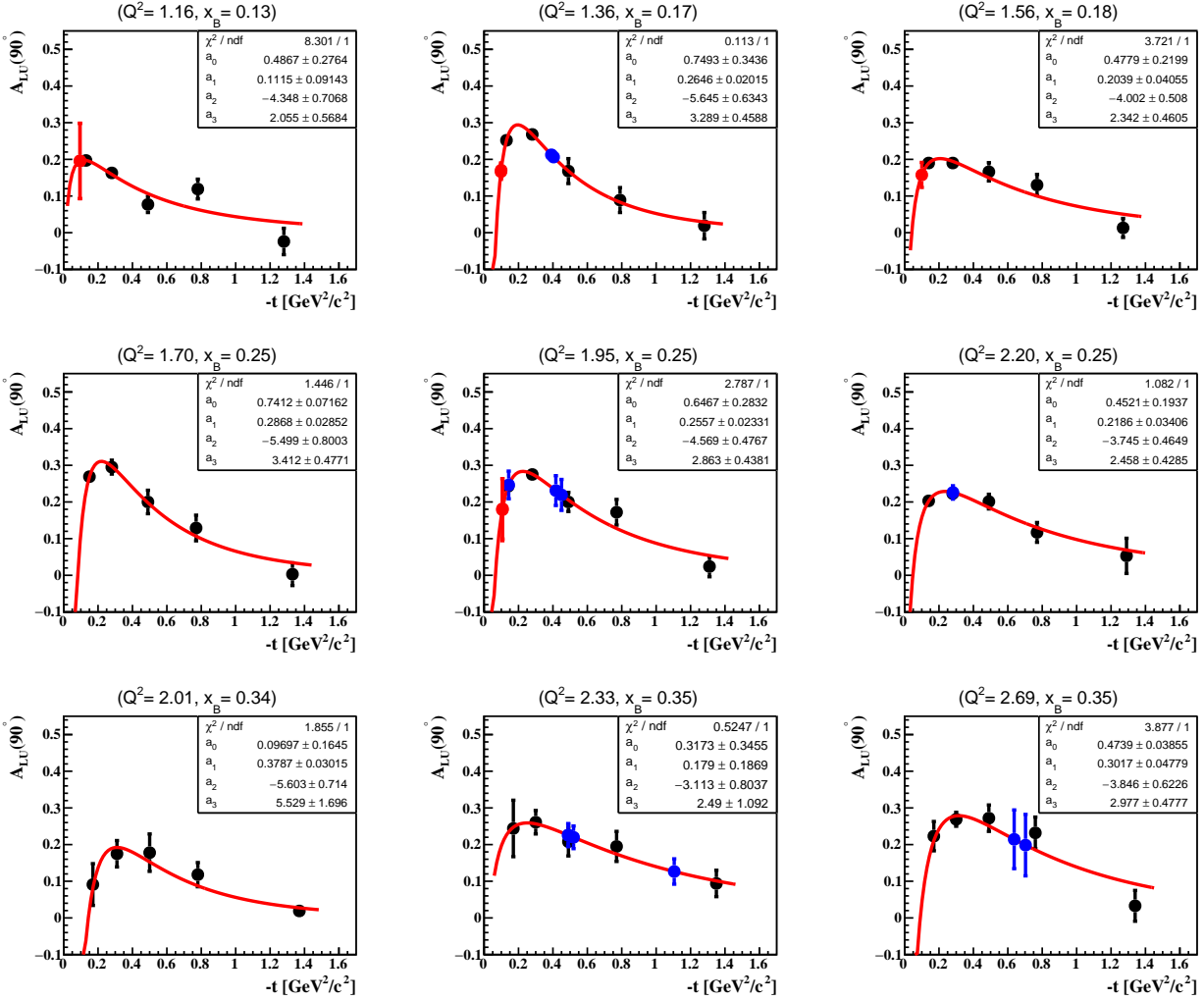


Figure G.1: Black circles are the free proton beam-spin asymmetries at $\phi = 90^\circ$ as a function of $-t$ in different (x_B, Q^2) bins as measured at CLAS-E1DVCS experiment. The solid red curves are fits to the free proton asymmetries in the form $a_0 * (\sqrt{t} - a_1) * e^{a_2 * \sqrt{t} - a_3}$. Blue points are the interpolated points corresponding for the incoherent points presented in this analysis. The red points stand for the extrapolated free proton asymmetries at the measured coherent kinematics.

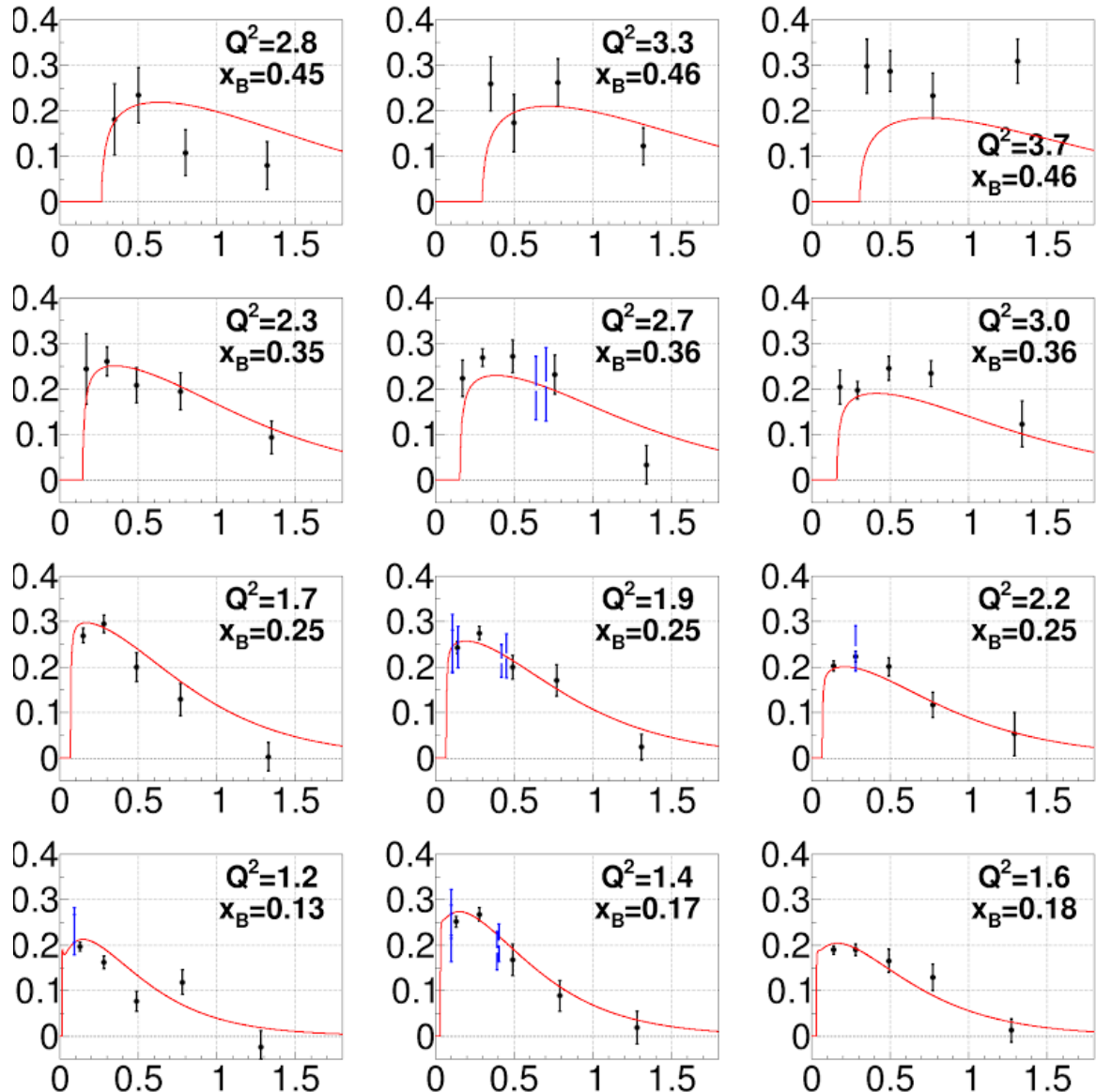


Figure G.2: The free proton beam-spin asymmetries at $\phi = 90^{\text{circ}}$ as a function of $-t$ in different (x_B, Q^2) bins as measured at CLAS-E1DVCS experiment. The solid red lines are the model calculations based on the kinematics of each bin. The blue points stand for the interpolated free proton asymmetries at the kinematics of our incoherent DVCS channels.

$(Q^2, x_B, -t)$	EG6 A_{LU} ± stat.	Exp. fit ± stat.	Exp. A_{LU} ratio	Model extr.	Model A_{LU} ratio
(1.395, 0.166, 0.407)	0.147 ± 0.023	0.206 ± 0.009	0.715 ± 0.117	0.205	0.717
(1.886, 0.233, 0.499)	0.153 ± 0.028	0.219 ± 0.042	0.702 ± 0.188	0.224	0.683
(2.338, 0.290, 0.521)	0.166 ± 0.032	0.219 ± 0.030	0.758 ± 0.182	0.217	0.764
(3.098, 0.379, 0.650)	0.132 ± 0.039	0.214 ± 0.080	0.619 ± 0.296	0.201	0.656
(1.425, 0.162, 0.397)	0.115 ± 0.022	0.212 ± 0.009	0.545 ± 0.106	0.188	0.611
(1.922, 0.227, 0.418)	0.182 ± 0.025	0.231 ± 0.040	0.790 ± 0.176	0.213	0.854
(2.354, 0.287, 0.492)	0.192 ± 0.030	0.225 ± 0.030	0.851 ± 0.178	0.217	0.884
(2.987, 0.390, 0.714)	0.149 ± 0.046	0.198 ± 0.083	0.754 ± 0.396	0.210	0.709
(1.823, 0.213, 0.145)	0.142 ± 0.023	0.246 ± 0.037	0.576 ± 0.131	0.243	0.584
(2.127, 0.255, 0.282)	0.155 ± 0.027	0.225 ± 0.018	0.688 ± 0.131	0.241	0.643
(2.308, 0.284, 0.490)	0.183 ± 0.034	0.225 ± 0.030	0.811 ± 0.188	0.219	0.835
(2.406, 0.308, 1.107)	0.170 ± 0.051	0.126 ± 0.034	1.343 ± 0.545	0.123	1.382
(1.143, 0.132, 0.096)	0.303 ± 0.051	0.195 ± 0.102	1.552 ± 0.857	0.244	1.241
(1.423, 0.170, 0.099)	0.364 ± 0.059	0.170 ± 0.020	2.137 ± 0.431	0.251	1.450
(1.902, 0.224, 0.107)	0.294 ± 0.060	0.181 ± 0.082	1.624 ± 0.808	0.235	1.251
(1.164, 0.132, 0.095)	0.319 ± 0.044	0.195 ± 0.102	1.633 ± 0.888	0.223	1.430
(1.439, 0.170, 0.099)	0.278 ± 0.078	0.166 ± 0.020	1.670 ± 0.518	0.243	1.144
(1.844, 0.225, 0.107)	0.319 ± 0.161	0.178 ± 0.084	1.788 ± 1.235	0.251	1.270
(1.493, 0.177, 0.1)	0.349 ± 0.029	0.157 ± 0.034	2.214 ± 0.515	0.245	1.424

Table G.1: A_{LU} ratios. The first three blocks stand for the incoherent bins in Q^2 , x_B , and $-t$, respectively. The last three blocks are for the coherent bins in Q^2 , x_B , and $-t$, respectively. The first column contains the mean value of the kinematical variables for each bin. The second column contains EG6 measured A_{LU} with the statistical error bars. The third column ("Exp. fit ± stat.") contains the interpolated free proton A_{LU} at EG6 kinematical values from fitting the free proton beam-spin asymmetries. The forth column ("Exp. A_{LU} ratio") stands for the calculated A_{LU} ratios using EG6 asymmetries and the fitted free proton asymmetries. The fifth column ("Model extr.") stands for the model-dependent extracted free proton asymmetries. The sixth column ("Model A_{LU} ratio") presents the calculated A_{LU} ratios using EG6 asymmetries and the model-dependent extracted free proton asymmetries.

Investigating the Fermi motion effects on the incoherent DVCS channel

In our DVCS analysis, we considered the initial proton of the incoherent channel to be at rest, while this is not totally true because of the Fermi motion. Does this assumption is a good approximation? What other options can be used to minimize this effect on the calculated exclusive quantities?

Figure H.1 presents the leading order handbag diagram of the incoherent DVCS channel off ${}^4\text{He}$, where the nucleus breaks and the DVCS occurs on a bound nucleon. Ideally, the transferred momentum squared (t) is defined using the initial and the final nucleons' 4-vectors as $(p - p')^2$. Then as a DVCS requirement, t has to be greater than a certain value (t_{min}), that is defined using the kinematics of the incoming and the scattered electrons. Due to the knowledge lack of the initial proton's momentum, this cut maybe inaccurate causes loosing some good DVCS events. In this work, we try to tackle this issue and check the stability of the reconstructed beam-spin asymmetry, as being our DVCS observable.

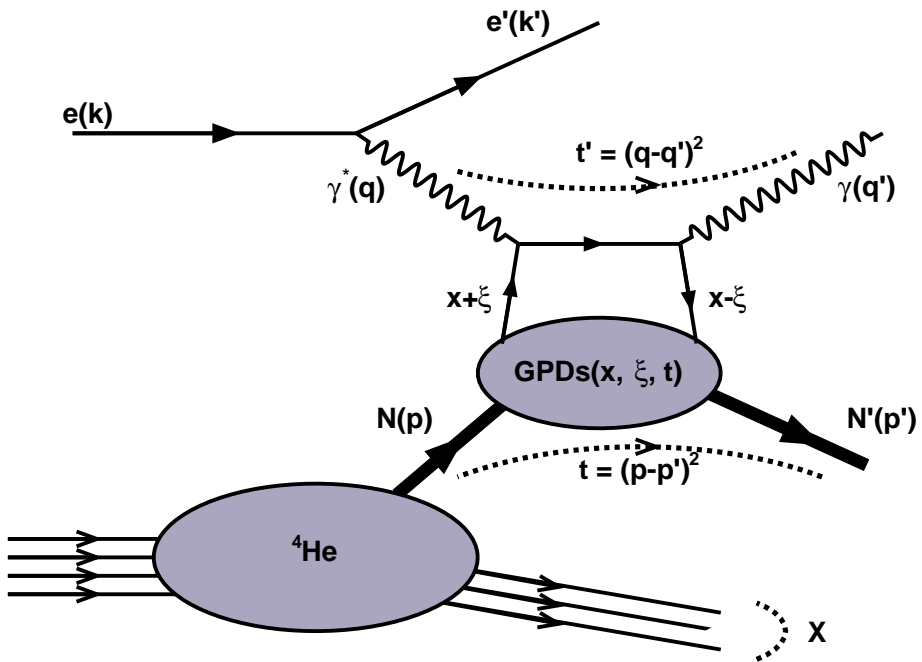


Figure H.1: Representation of the leading order handbag diagram of the incoherent DVCS process off ${}^4\text{He}$

Typically, the transferred momentum squared t is equal to the transferred momentum squared (t') defined between the virtual photon and the final-state real photon, as shown in Figure H.1. While defining the momentum transferred as t' is a good way to pass the Fermi motion effect on the initial bound proton,

it is more smeared than than t due to bigger energy resolutions of the photons. Figure H.2 shows the distributions of the coherent and the incoherent relative difference between t and t' . One can see that the coherent DVCS channel, the distributions is symmetric and centered at zero as expected due to our good knowledge on the initial ${}^4\text{He}$ target, while it is not exactly the case for the incoherent case due to the Fermi motion.

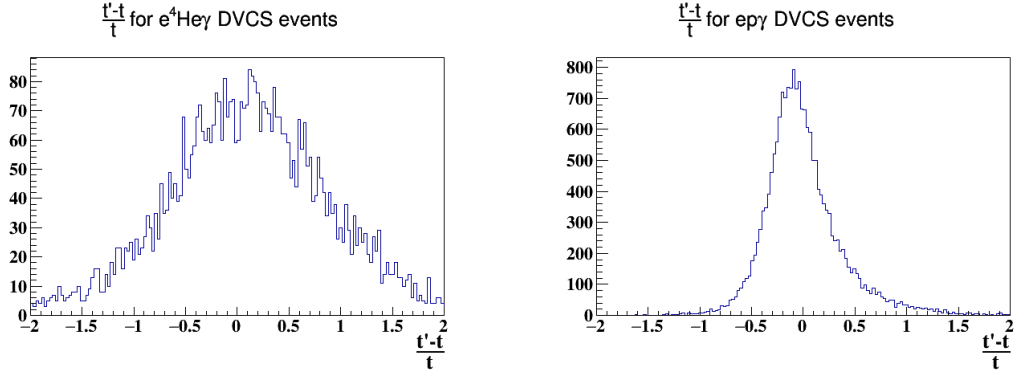


Figure H.2: On the left: the coherent relative difference between t and t' . On the right: the incoherent relative difference.

In the following, we check the effects of defining the transferred momentum squared as t and t' on the exclusive distributions and on the reconstructed beam-spin asymmetries. Figure H.3 presents the exclusive distributions of the incoherent DVCS events where the transferred momentum squared is defined as t , while it is define as t' in figure H.4. To minimize the smearing effects of t' on the exclusive distributions, 2σ exclusive cuts were optimized compared to 3σ cuts which were applied in the t case. In terms of collected statistics, the 2σ cuts using t' gave almost the same statistics using t . From comparing the exclusive distributions, especially the $ep\gamma$ missing energy and the missing mass squared, one sees that using t' gives more Gaussian missing energy distributions and cleaner missing mass squared distribution.

Conclusions

In summary, we have studied the effects of Fermi motion on the measured incoherent beam-spin asymmetries by defining the transferred momentum squared through the nucleons in one case and through the photons in the other case. In terms of collected statistics, 2σ exclusive cuts using the photons produced the same statistics as 3σ cuts. The exclusive distributions using t' , through the photons, have shown more acceptable distributions in terms of being more symmetric in some cases and cleaner on others. The reconstructed asymmetries in the two cases of defining the transferred momentum squared are compatible and while the given error bars. As a suggestion, we would like to consider the t' analysis as the final set for publications unless a major objections appear.

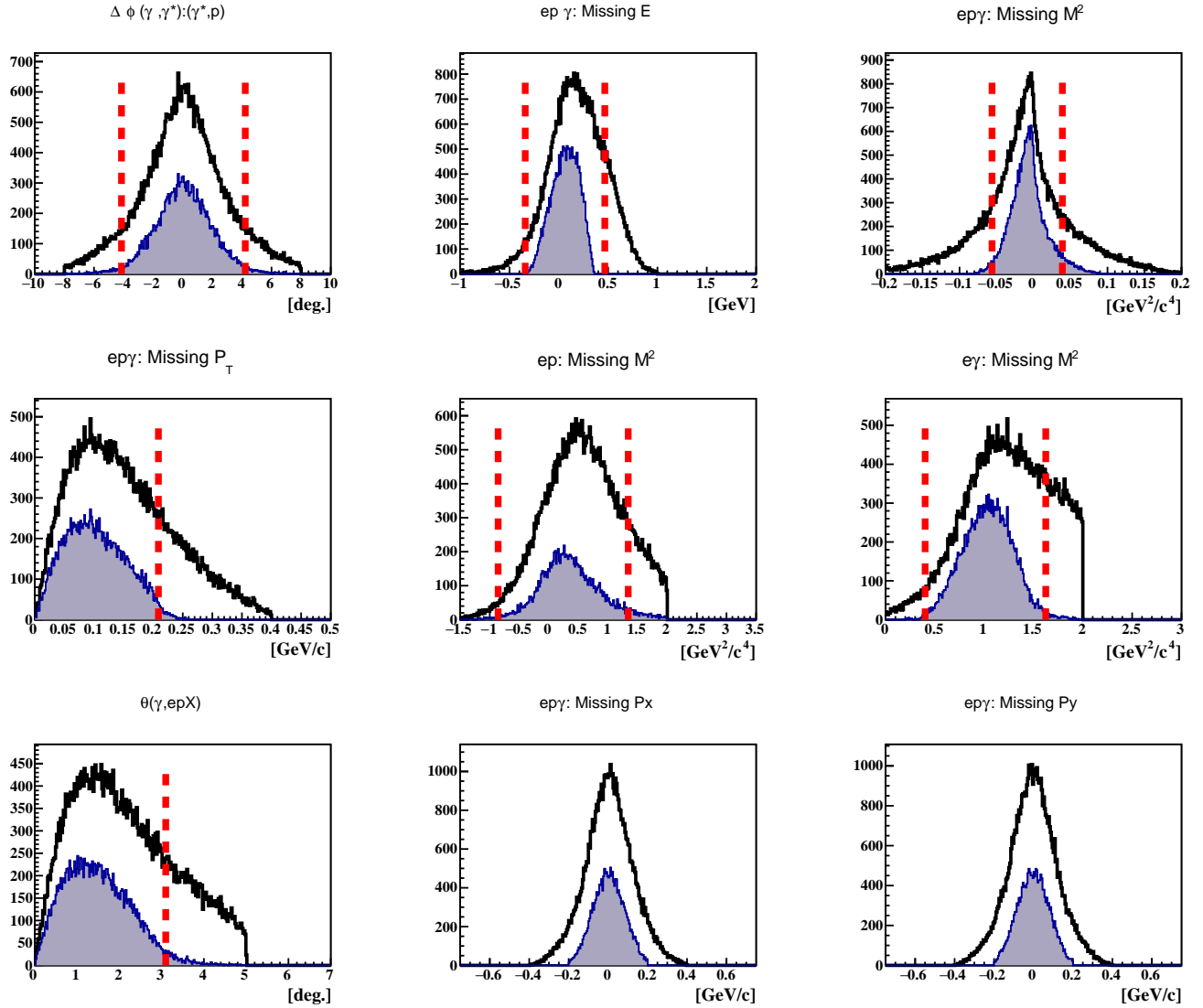


Figure H.3: The old set of exclusive cuts with $t > t_{min}$. The black distributions represent the incoherent DVCS events candidate. The shaded distributions represent the events which passed all the exclusivity cuts except the quantity plotted. The vertical red lines represent the applied exclusivity, 3σ cuts.

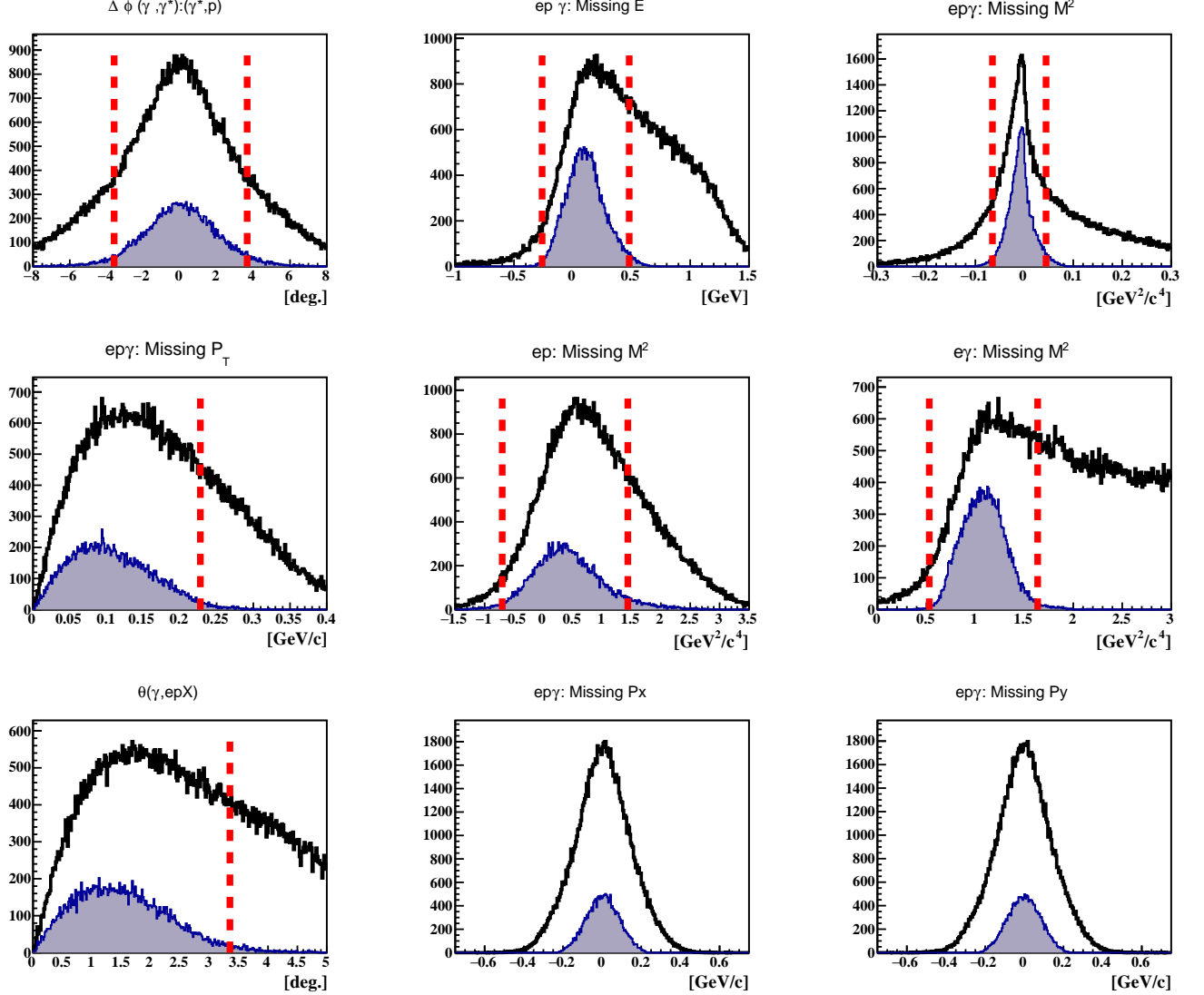


Figure H.4: New set of exclusive cuts with $t' > t_{min}$. The black distributions represent the incoherent DVCS events candidate. The shaded distributions represent the events which passed all the exclusivity cuts except the quantity plotted. The vertical red lines represent the applied exclusivity, 2σ cuts.

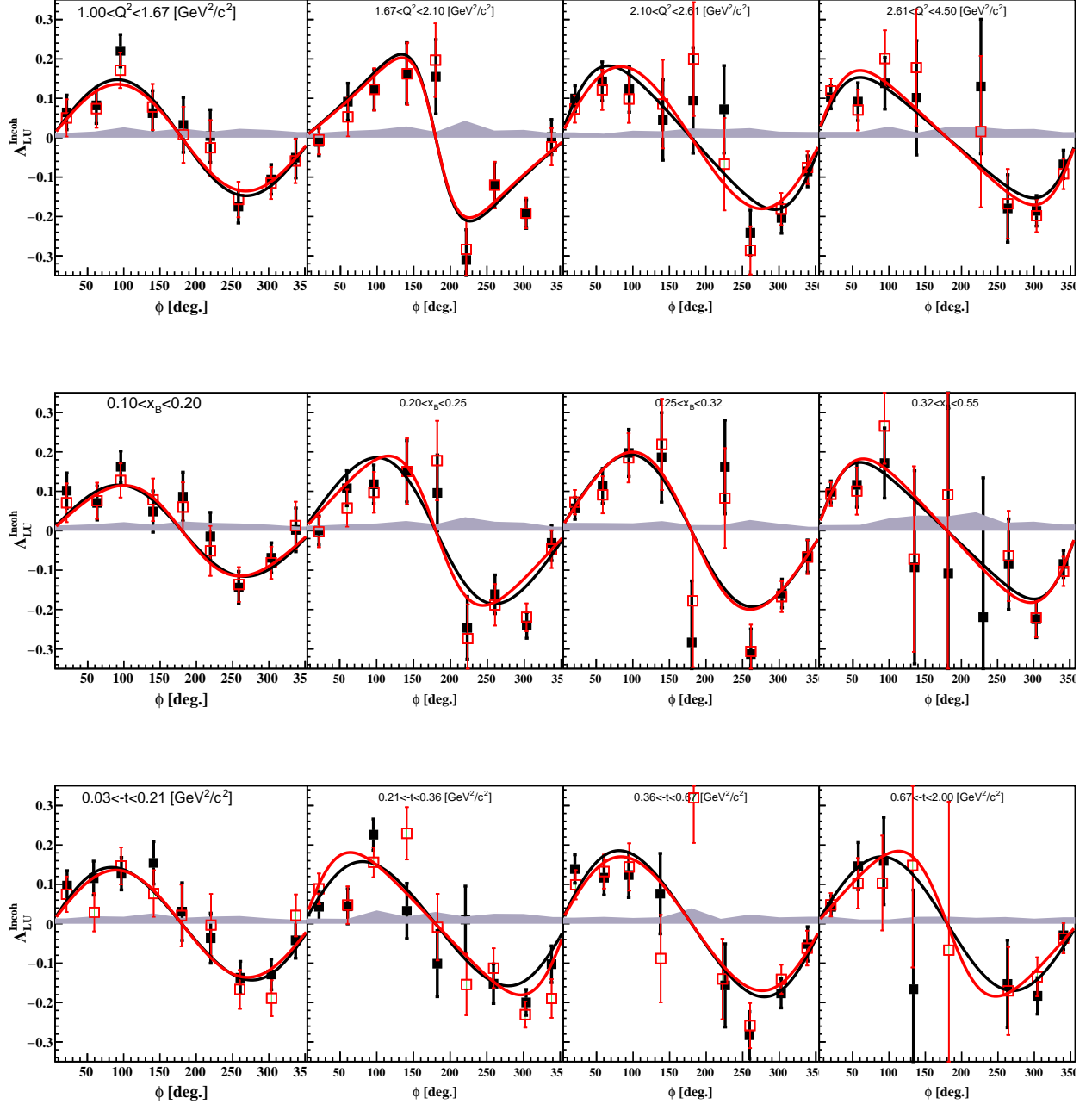


Figure H.5: The reconstructed incoherent A_{LU} as a function of the angle ϕ in Q^2 , x_B , and $-t$ bins, respectively from top to bottom using $t > t_{min}$ in black squares, and $t' > t_{min}$ in red squares.

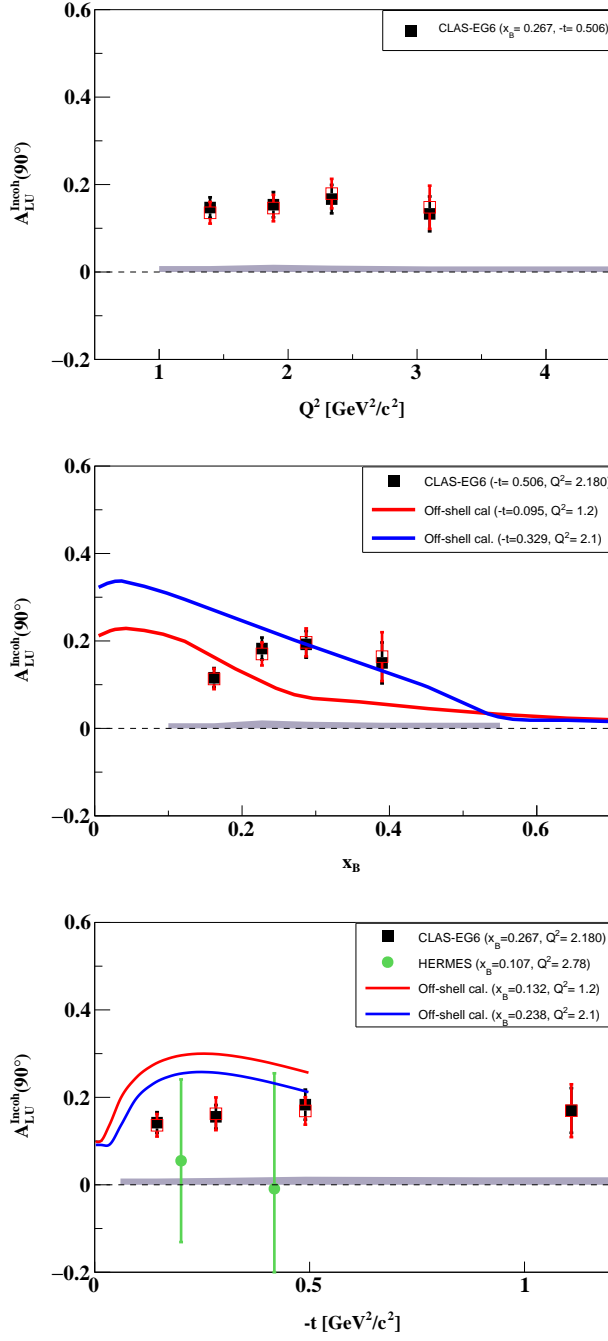


Figure H.6: The Q^2 (top), x_B (middle), and $-t$ -dependencies (bottom) of the incoherent A_{LU} at $\phi = 90^\circ$, using the $t > t_{min}$ cut and the corresponding exclusive cuts in black squares, and in red squares using the $t' > t_{min}$ and its exclusive cuts. The curves are theoretical calculations. On the bottom: the green circles are the HERMES $-A_{LU}$ (positron beam was used) inclusive measurements.

APPENDIX I

Binning the incoherent DVCS data to match the free proton DVCS published data

$\langle x_B \rangle$	$\langle Q^2 \rangle$	$\langle -t \rangle$	α	$\Delta\alpha$	β	$\Delta\beta$	χ^2
0.238	1.89	0.14	0.243	0.013	-0.02	0.09	1.0
0.249	1.95	0.28	0.275	0.014	-0.06	0.09	1.3
0.249	1.95	0.49	0.200	0.026	-0.36	0.15	1.3
0.248	1.94	0.77	0.172	0.035	0.01	0.31	0.3

Table I.1: Free proton DVCS published asymmetries associated with the incoherent $-t$ bins.

$\langle x_B \rangle$	$\langle Q^2 \rangle$	$\langle -t \rangle$	α	$\Delta\alpha$	β	$\Delta\beta$	χ^2
0.177	1.56	0.14	0.190	0.009	-0.03	0.12	2.3
0.249	1.95	0.28	0.275	0.014	-0.06	0.09	1.3
0.345	2.64	0.30	0.269	0.019	0.29	0.15	0.3
0.471	3.34	0.78	0.262	0.052	-0.23	0.25	0.9

Table I.2: Free proton DVCS published asymmetries associated with the 1250 incoherent Q^2 and x_B bins.

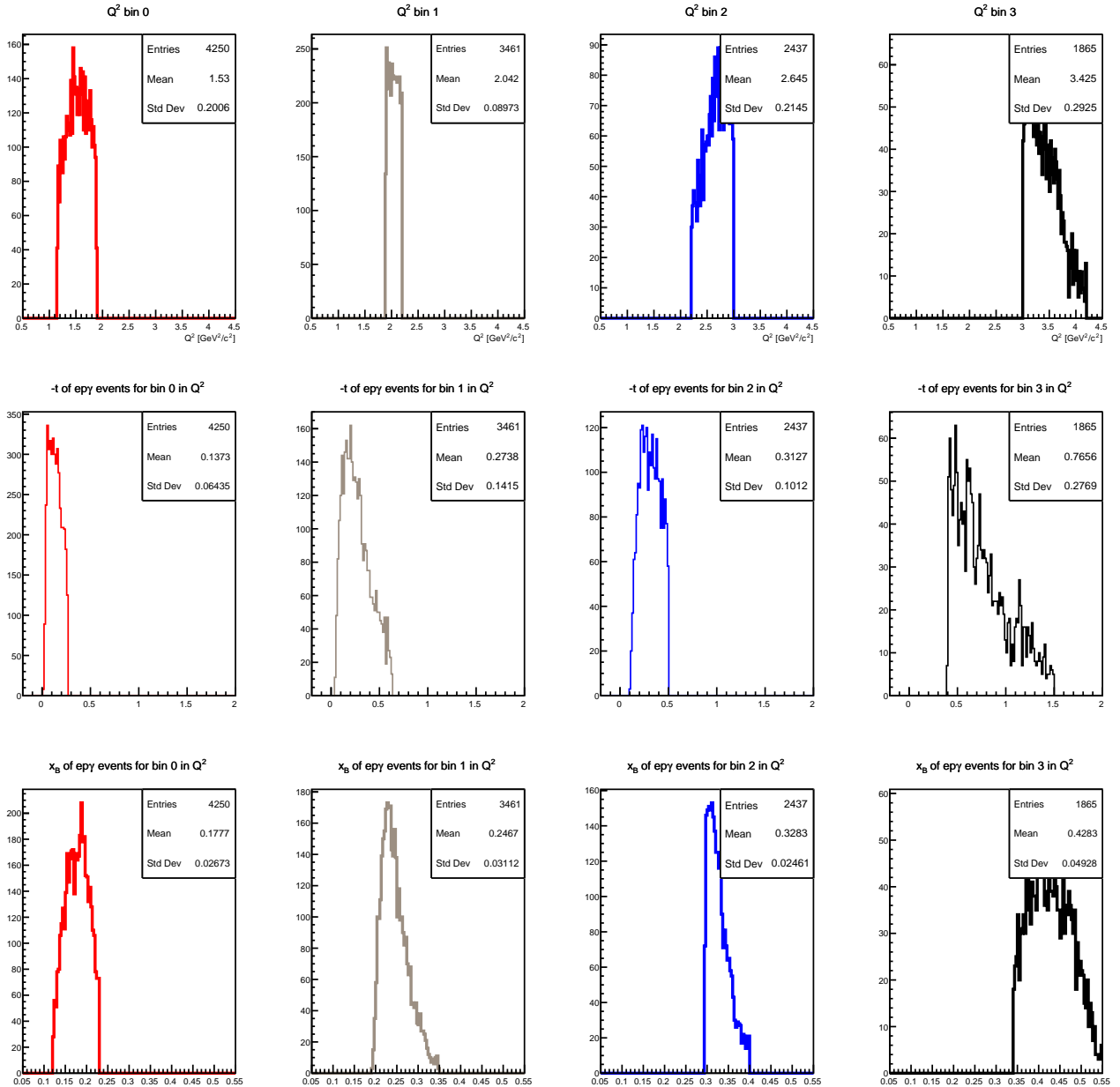


Figure I.1: First row: the four bins in Q^2 of the incoherent DVCS events. Second row: the associated distributions of t for the bins in Q^2 . Third row: the associated distributions of x_B for the bins in Q^2 .

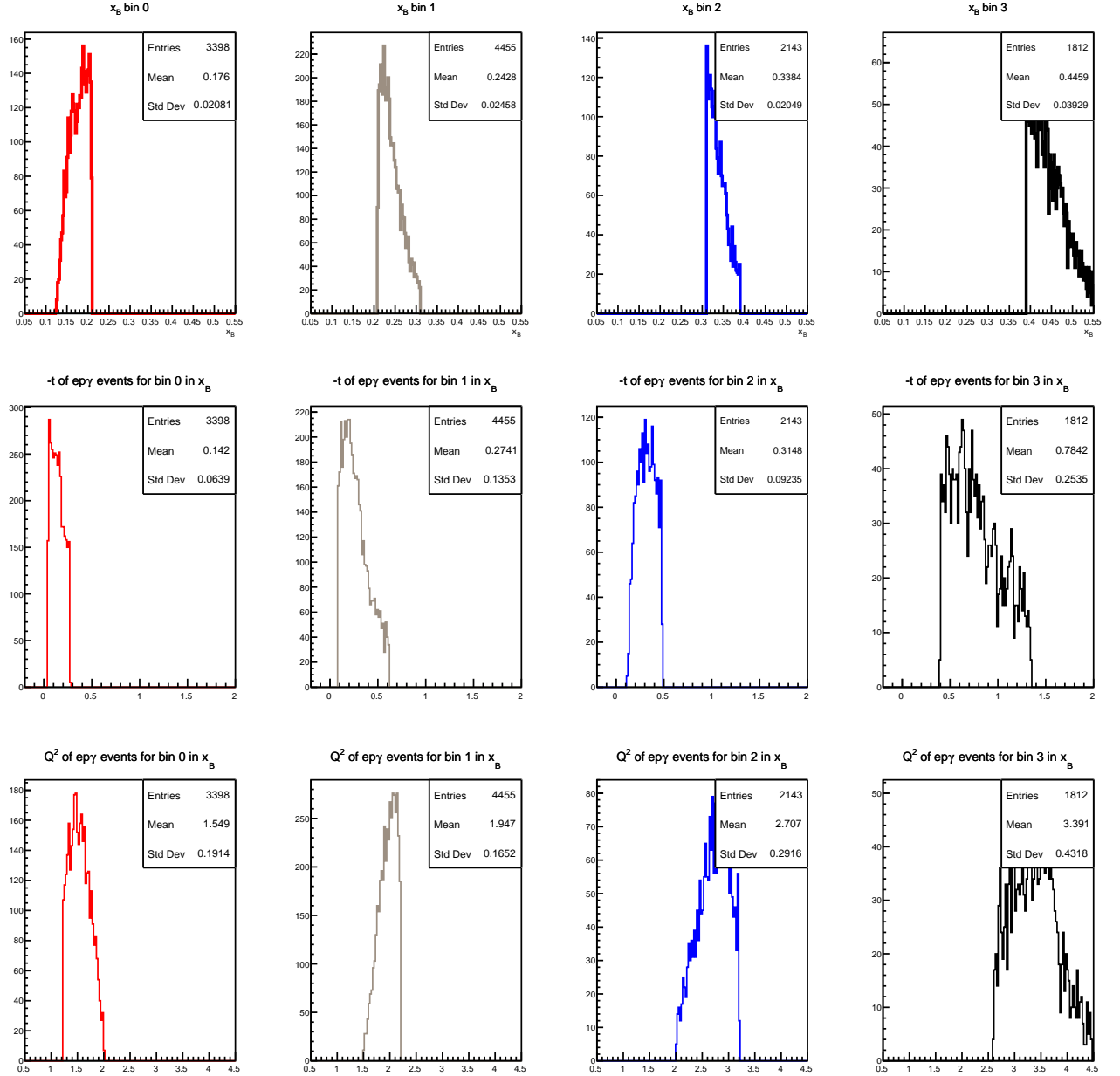


Figure I.2: First row: the four bins in x_B of the incoherent DVCS events. Second row: the associated distributions of t for the bins in x_B . Third row: the associated distributions of Q^2 for the bins in x_B .

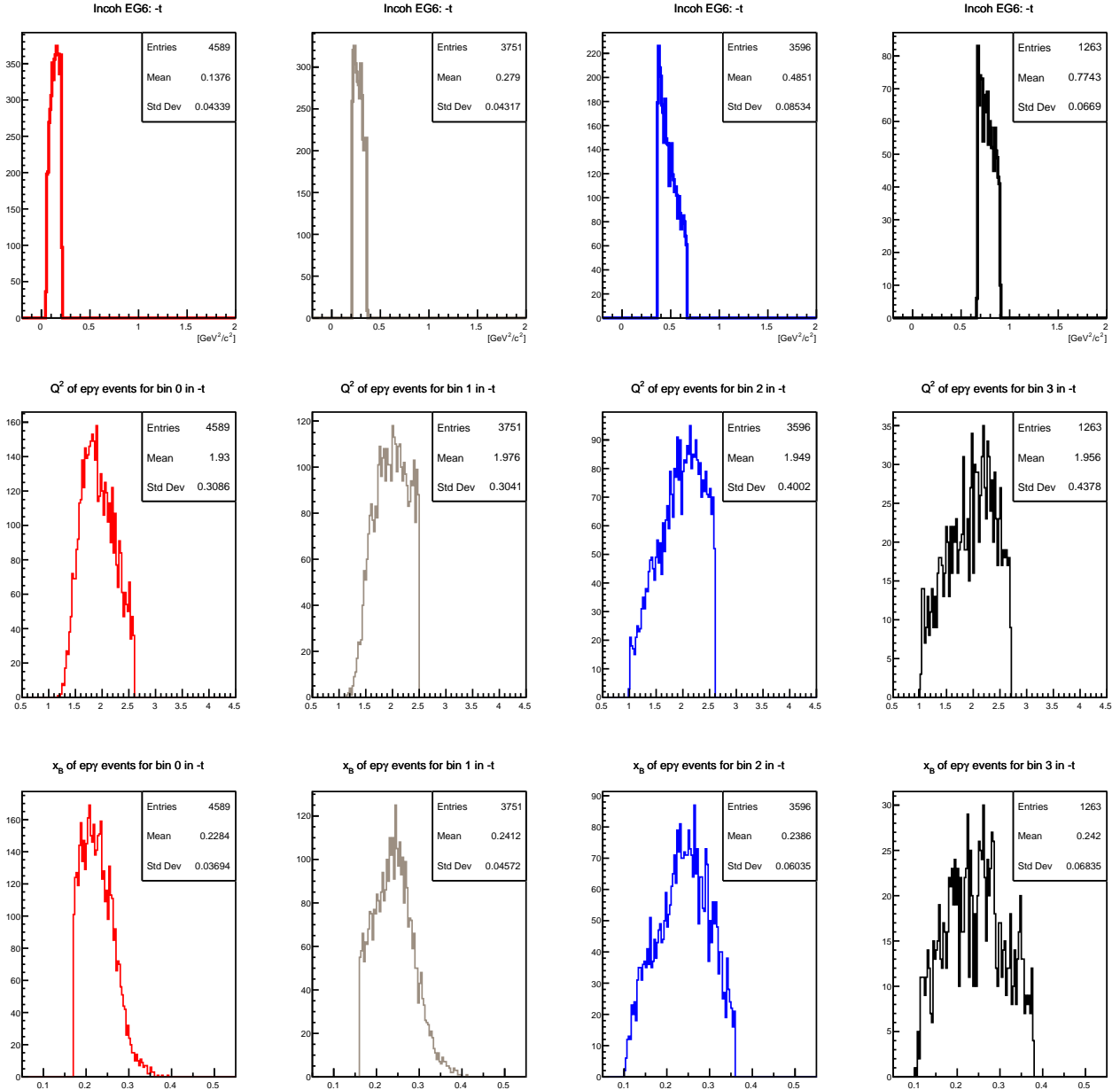


Figure I.3: First row: the four bins in t of the incoherent DVCS events. Second row: the associated distributions of Q^2 for the bins in t . Third row: the associated distributions of x_B for the bins in t .

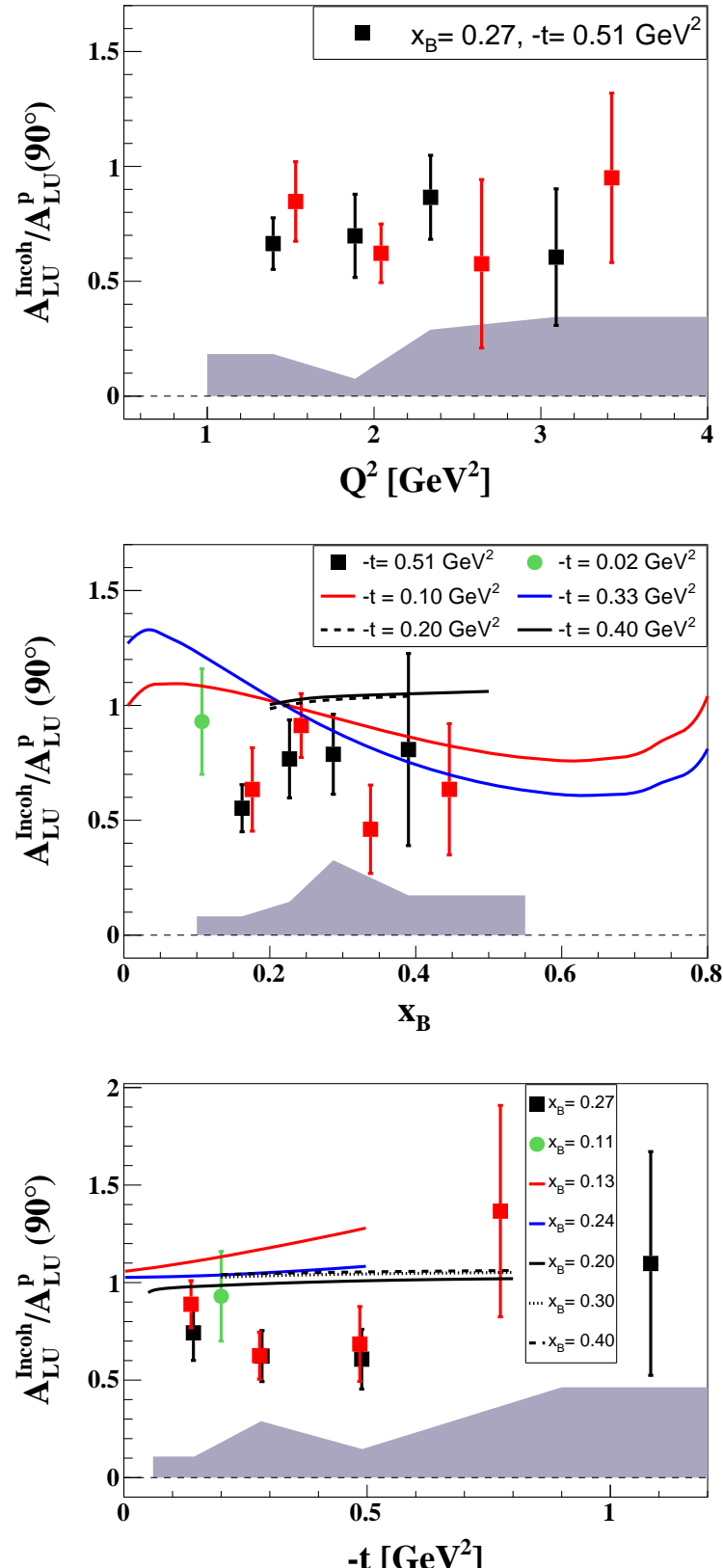


Figure I.4: The A_{LU} ratio between the bound and the free proton at $\phi = 90^\circ$, as a function of Q^2 (on the top), x_B (on the middle), and t (on the bottom). The black squares are our results using the interpolation method to get the free proton asymmetries at our kinematics, the red squares are our results using the method of tuning our kinematics to get kinematics similar to the published free proton from E1DVCS1 experiment. The gray band stands for the systematic errors calculated as the difference between the two extraction methods. The green circles are the HERMES inclusive measurement [18] results. The blue and red curves are from an on-shell calculations from S. Liuti and K. Taneja [16]. The solid and dashed black curves are from the off-shell calculations [14].

Bibliography

- [1] M. V. Polyakov, Generalized parton distributions and strong forces inside nucleons and nuclei, Phys. Lett. B 555, 57-62, 2003. (Cited on pages 5 and 7.)
- [2] S. Liuti and K. Taneja, Nuclear Medium Modifications of Hadrons from Generalized Parton Distributions, Phys. Rev. C 72, 034902; arXiv:0504027v2 [hep-ph], 2005. (Cited on pages 5, 9 and 11.)
- [3] A. Kirchner and D. Müller, Deeply virtual Compton scattering off nuclei, Eur. Phys. J. C32, 347-375, 2003. (Cited on pages 5, 7, 8 and 115.)
- [4] A. V. Belitsky and D. Müller, Refined analysis of photon leptoproduction off spinless target, Phys. Rev. D79, 014017; arXiv:0809.2890 [hep-ph], 2009. (Cited on pages 107 and 117.)
- [5] M. Vanderhaeghen, Gauge invariance of DVCS off an arbitrary spin hadron: the deuteron target case, Eur. Phys. J. A 8, 455, 2000. (Cited on page 5.)
- [6] S. Liuti, Exploring the transverse partonic structure of nuclei, Workshop on Hard Processes in Nuclei, ECT*, Trento, June 8-12, 2015. (Cited on page 6.)
- [7] R. F. Frosch et al., Structure of the He-4 Nucleus from Elastic Electron Scattering, Phys. Rev. 160, 874, 1967. (Cited on page 7.)
- [8] A. Camsonne et al. (Jefferson Lab Hall A Collaboration), JLab Measurement of the ${}^4\text{He}$ Charge Form Factor at Large Momentum Transfers, Phys. Rev. Lett. 112, 132503, 2014. (Cited on page 8.)
- [9] K. Hafidi et al., Deeply virtual Compton scattering off ${}^4\text{He}$, JLab proposal to PAC 33, 2007. (Cited on page 17.)
- [10] V. Guzey and M. Strikman, DVCS on spinless nuclear targets in impulse approximation, Phys. Rev. C 68, 015204; arXiv:0301216 [hep-ph], 2003. (Cited on page 8.)
- [11] V. Guzey, Neutron contribution to nuclear DVCS asymmetries, Phys. Rev. C 78, 025211; arXiv: 0801.3235 [nucl-th], 2008. (Cited on pages 8 and 159.)
- [12] I. V. Musatov and A. V. Radyushkin, Evolution and models for skewed parton distributions, Phys. Rev. D 61, 074027, 2000 (Cited on page 9.)
- [13] M. Guidal et al., Generalized Parton Distributions in the valence region from Deeply Virtual Compton Scattering, arXiv:1303.6600v1 [hep-ph], 2013. (Cited on page 9.)
- [14] V. Guzey, A.W. Thomas and K. Tsushima, Medium modifications of the bound nucleon GPDs and incoherent DVCS on nuclear targets, Phys. Lett. B 673, 9-14; arXiv:0806.3288 [nucl-th], 2009. (Cited on pages 9, 10, 114, 115 and 155.)
- [15] D. H. Lu et al., In-medium electron-nucleon scattering, Phys. Lett. B 417, 217, 1998. (Cited on page 9.)
- [16] S. Liuti and K. Taneja, Microscopic Description of Deeply Virtual Compton Scattering off Spin-0 Nuclei, Phys.Rev. C 72, 032201; arXiv:0505123v1 [hep-ph], 2005. (Cited on pages 9, 108, 110, 112, 114, 115, 116 and 155.)
- [17] J. Gomez et al., Measurement of the A-dependence of deep inelastic electron scattering. Phys. Rev. D 49, 4348-4372, 1994. (Cited on page 11.)
- [18] A. Airapetian et al. (HERMES Collaboration), Nuclear-mass dependence of beam-helicity and beam-charge azimuthal asymmetries in DVCS, Phys. Rev. C 81, 035202, 2010. (Cited on pages 11, 12, 110, 112, 114, 115, 116 and 155.)
- [19] B.A. Mecking et al., The CEBAF large acceptance spectrometer, Nucl. Inst. and Meth. A 503, 513-553, 2003. (Cited on page 43.)

- [20] M.D. Mestayer et al., The CLAS drift chamber System, Nucl. Inst. and Meth. A 449, 81, 2000. (Cited on page 50.)
- [21] G. Adams et al., The CLAS Cerenkov detector, Nucl. Inst. and Meth. A 465, 414, 2001. (Cited on page 48.)
- [22] E.S. Smith et al., The time-of-flight system for CLAS, Nucl. Inst. and Meth. A 432, 265, 1999. (Not cited.)
- [23] M. Amarian et al., The CLAS forward electromagnetic calorimeter, Nucl. Inst. and Meth. A 460, 239, 2001. (Not cited.)
- [24] Hyon-Suk Jo, Etude de la Diffusion Compton Profondément Virtuelle Sur le Nucléon avec le Détecteur CLAS de Jefferson Lab: Mesure des Sections Efficaces polarisées et non polarisées, IPNO-Thesis, 2007. (Cited on pages 13 and 15.)
- [25] S. Tkachenko et al., Measurement of the nearly free neutron structure function using spectator tagging in inelastic $^2H(e, e' p)X$ scattering with CLAS, Phys. Rev. C 89, 045206, 2014. (Cited on pages 17 and 22.)
- [26] The PubChem Project. USA: National Center for Biotechnology Information, dimethyl ether - PubChem Public Chemical Database, <http://pubchem.ncbi.nlm.nih.gov/compound/8254>. (Cited on page 18.)
- [27] N. Baillie et al., BoNus Experiment Analysis Note, CLAS internal analysis note, <https://www.jlab.org/Hall-B/secure/bonus/publication/BonusAnal110117.pdf> (Cited on page 19.)
- [28] J. Beringer et al. (Particle Data Group), Particle detectors at accelerators, Phys. Rev. D 86, 010001, pages: 339-368, 2012. (Cited on pages 19 and 33.)
- [29] S. Biagi, Monte Carlo simulation of electron drift and diffusion in counting gases under the influence of electric and magnetic fields, Nucl. Inst. and Meth. in Phy. Res. A 421, pp. 234-240, 1999. (Cited on page 29.)
- [30] N. Baltzell, New TPC Noise Reduction, https://clasweb.jlab.org/rungroups/lowq/wiki/index.php/New_TPC_Noise_Reduction (Not cited.)
- [31] M. Osipenko et al., Matching between the electron candidate track and the Cherenkov counter hit, CLAS-NOTE-020, 2004. (Cited on page 48.)
- [32] J. Beringer et al. (Particle Data Group), Electronic energy loss by heavy particles, Phys. Rev. D 86, 010001, 2012. (Cited on page 34.)
- [33] F.X. Girod, Diffusion Compton profondément virtuelle avec le détecteur CLAS pour une étude des distributions de partons généralisées, Ph.D-Thesis, 2006. (Cited on pages 55 and 61.)
- [34] C.Ciofi degli Atti and S.Simula, Realistic model of the nucleon spectral function in few- and many-nucleon systems, Phys. Rev. C 53, 1689. (Cited on page 61.)
- [35] CLAS collaboration, CLAS GEANT3 simulation, http://nuclear.unh.edu/~maurik/gsim_info.shtml. (Cited on page 62.)
- [36] Y. Perrin, Etude de la structure partonique du noyau d'hélium, Ph.D thesis, 2012. (Cited on page 104.)
- [37] C. Moody and N. Baltzell, IC depth corrections for CLAS-EG6 experiment, https://clasweb.jlab.org/rungroups/lowq/wiki/index.php/IC_Depth_Correction_Invetsigation_Creating_a_new_depth_correction. (Cited on page 71.)
- [38] F.X. Girod et al. (CLAS Collaboration), Measurement of Deeply Virtual Compton Scattering Beam-Spin Asymmetries, Phys. Rev. Lett. 100, 162002, 2008. (Cited on pages 107, 113 and 141.)
- [39] H.S. Jo et al. (CLAS Collaboration), Cross sections for the exclusive photon electroproduction on the proton and Generalized Parton Distributions, arXiv:1504.02009v1 [hep-ex], 2015. (Cited on page 113.)

- [40] B. Guegan, Study of Generalized Parton Distributions and Deeply Virtual Compton Scattering on the nucleon with the CLAS and CLAS12, Ph.D-thesis, 2013. (Not cited.)
- [41] N. Saylor, A Measurement of Unpolarized Cross Sections and Polarized Cross Section Differences of Deeply Virtual Compton Scattering on the Proton at Jefferson Laboratory using CLAS, Ph.D-thesis, 2013. (Not cited.)
- [42] J. M. Grames et al., Unique electron polarimeter analyzing power comparison and precision spin-based energy measurement, Phys. Rev. Spec. Topics - Accelerators and Beams, Vol.7 , 042802, 2004. (Cited on page 98.)
- [43] A.V. Afanasev, M.I. Konchatnij and N.P. Merenkov, Single-spin asymmetries in the Bethe-Heitler process $e^- + p \rightarrow e^- + \gamma + p$ from QED radiative corrections, J. of Exp. and Theo. Phys. 102(2), 220-233, 2006. (Cited on page 98.)
- [44] Private communication with V. Guzey based on his model presented in [11]. (Cited on pages 115 and 116.)
- [45] EG1-DVCS TN027, https://clasweb.jlab.org/rungroups/eg1-dvcs/wiki/index.php/Technical_Notes. (Cited on page 71.)
- [46] RTPC Alignment Calibration for EG6, CLAS-NOTE 2013-007, <https://misportal.jlab.org/ul/Physics/Hall-B/clas/viewFile.cfm/2013-007.pdf?documentId=705>. (Cited on page 21.)
- [47] Beam XY-Position at the Target for CLAS/EG6, CLAS-NOTE 2013-008, <https://misportal.jlab.org/ul/Physics/Hall-B/clas/viewFile.cfm/2013-008.pdf?documentId=711>. (Not cited.)
- [48] F.X. Girod et al. (CLAS Collaboration), Measurement of Deeply Virtual Compton Scattering Beam-Spin Asymmetries, CLAS Note, 2007-026, 2007. (Cited on page 107.)
- [49] Private communications with V. Guzey based on reference [11]. (Cited on page 113.)
- [50] Private communications with M. Guidal based on reference: M. Guidal, M. V. Polyakov, A. V. Radyushkin and M. Vanderhaeghen, Nucleon form-factors from generalized parton distributions, Phys. Rev. D 72, 054013, [hep-ph/0410251], 2005. (Cited on page 113.)
- [51] Private communications with S. Liuti based on: J. O. Gonzalez-Hernandez, S. Liuti, G. R. Goldstein and K. Kathuria, Interpretation of the Flavor Dependence of Nucleon Form Factors in a Generalized Parton Distribution Model, Phys. Rev. C 88, no. 6, 065206, arXiv:1206.1876 [hep-ph], 2013. (Cited on page 113.)
- [52] K. Kumericki, S. Liuti, H. Moutarde, GPD phenomenology and DVCS fitting - Entering the high-precision era, arXiv:1602.02763 [hep-ph], 2016. (Cited on page 141.)

